8-1-2014

Mars-Relevant Phosphate Minerals and Implications for Martian Habitability

Christopher Adcock
University of Nevada, Las Vegas, adcockc2@gmail.com

MARS-RELEVANT PHOSPHATE MINERALS AND IMPLICATIONS FOR MARTIAN HABITABILITY

by

Christopher T. Adcock

Bachelor of Science in Earth and Planetary Sciences
University of New Mexico
1995

Masters of Science in Geology
Oklahoma State University
2004

A dissertation submitted in partial fulfillment
of the requirements for the

Doctor of Philosophy - Geoscience

Department of Geoscience
College of Sciences
The Graduate College

University of Nevada, Las Vegas
August 2014

UNLV
UNIVERSITY OF NEVADA LAS VEGAS

THE GRADUATE COLLEGE

We recommend the dissertation prepared under our supervision by

Christopher Adcock

entitled

Mars-Relevant Phosphate Minerals and Implications for Martian Habitability

is approved in partial fulfillment of the requirements for the degree of

Doctor of Philosophy - Geosciences

Department of Geoscience

Elisabeth Hausrath, Ph.D., Committee Chair

Eugene Smith, Ph.D., Committee Member

Adam Simon, Ph.D., Committee Member

Oliver Tschauner, Ph.D., Additional Committee Member

Henry Sun, Ph.D., Additional Committee Member

Paul Forster, Ph.D., Graduate College Representative

Kathryn Hausbeck Korgan, Ph.D., Interim Dean of the Graduate College

August 2014

ABSTRACT

Mars-Relevant Phosphate Minerals and Implications for Martian Habitability

by

Christopher T. Adcock

Dr. Elisabeth Hausrath, Examination Committee Chair
Assistant Professor of Geoscience
University of Nevada, Las Vegas

This dissertation is comprised of three studies focused on martian phosphate availability, with an introductory chapter introducing and linking the three studies. Chapter two is on the subject of merrillite synthesis. Merrillite is an extraterrestrial Ca-phosphate mineral similar to the mineral whitlockite and is found as a dominant primary phosphate mineral in martian meteorites. The chapter includes methods of whitlockite and merrillite synthesis as well as a detailed characterization of the produced minerals and a mechanism by which charge balance can be maintained when merrillite is synthesized through dehydrogenation of whitlockite.

Chapter three presents the results of kinetic and thermodynamic studies on the Mars-relevant minerals chlorapatite and merrillite, as well as the more terrestrially-relevant minerals whitlockite and fluorapatite. The results of these studies indicate that the dominant primary Ca-phosphate minerals on Mars possess higher solubilities that could lead to more than twice the phosphate concentration in solution. Dissolution rates for the Mars-relevant minerals derived in the study, when combined with the higher martian phosphorus abundance, could result in phosphate release rates of up to 45x faster for a given set of aqueous conditions on Mars when compared to Earth. The implications of the results for past or present martian habitability are discussed.

In Chapter four, reactive transport modeling was applied to investigate the transport and mobility of phosphate under martian conditions. The kinetic and thermodynamic data derived in Chapter three were combined with Mars mission data, results from an investigation of Mars analog basalts at Craters of the Moon National Monument in Idaho, and previously published data to inform a reactive transport code and model dissolution profiles measured by Mars Exploration Rover (MER) Spirit in Wishstone class rocks. The modeling results suggest phosphate release into near-neutral waters occurred at some point in the past at Gusev Crater on Mars with positive implications for past martian habitability.

ACKNOWLEDGEMENTS

A Ph.D. is a tremendous undertaking for an individual and a task I do not believe a single individual can accomplish alone. Thus, it is unfortunate that this dissertation allows for only a single author. In fact, it is somewhat misleading. While the work contained herein is my own, it certainly would never have been completed without the help, support, and contributions of many individuals. The list of those I need to acknowledge is a long one, and I apologize that I will fail to mention everyone - I am sure.

Eugene Smith may be the main reason I even attempted a Ph.D. He encouraged me to apply and encouraged me thereafter. Always a kind word or point of view. It is unlikely I would have attended UNLV if not for him. Christopher Tacker, Dan Harlov, and Adam Simon were instrumental in helping me successfully synthesize chlorapatite. Not an easy task. Without their help this project would have traveled a much different path. Adam Simon was also always very supportive of all of my work. A great conversation with Henry Sun is the reason I can consider Astrobiology as part of my degree. Astrobiology is a "field between fields" and thus difficult - and I look forward to exploring it further. Paul Forster and Oliver Tschauner went beyond the call in helping me with much of the work that would become Chapter Two of this document, and did so more in my interest than theirs I believe. I learned (and am still learning) a great deal from both of them. I have no doubt my future work will involve one or both of them. I have been blessed that most of the above folks are members of my committee.

Elisabeth Hausrath has been my committee chair. I don't really have the room here to express my thanks to her. She is always positive, supportive, and understanding.

I swear she even smiles when she is angry. She encouraged me to keep going, made time for me when I needed it, and is a friend. She listened to my ideas and never simply dismissed them. I hope to have many future projects together.

In doing this research I had an office. And, in that office, I had office-mates. Office-mates are like siblings after awhile. We argued and fussed, we had fun together, we joked with each other and commiserated - we competed with each other often. We also helped each other often, and not simply with school or research work. Seth Gainey, Mike Steiner, Fritz Freudenberger, Valerie Tu, Britney Downs, Julie Baumeister - I thank you all for the great conversations, debates, technical support, and a list of other things too long to include. I also want to thank Brenda Buck, who helped me get my mind back into research science after 5 years of consulting and applied science. And she did that in a single class on soils. Scott Nowicki deserves my thanks as well. His views on what education should be and how I should approach my own career were invaluable. He also helped me keep a finger on my broader interest and I regret we didn't have more time for thought provoking discussions.

Finally, there is my family. My parents and in-laws were always willing to help out Denise, Miranda, and myself. Both sides of Denise's and my families were very supportive and understanding. As for my wife Denise, I am not an easy person to get along with. It is a testament to her, far more then myself, that our marriage made it through this Ph.D. I can't say anything more encompassing than that.

And then there is Miranda Jane Tillery Adcock (a.k.a. Pandora or Panda), my daughter. When I started this she couldn't walk. Now she has finished kindergarten. She is no small part of the reason I attempted a Ph.D. I do not know if one dedicates a

dissertation, but if they do, this one is for Miranda, because it has been a true adventure. I do not know what you will be when you "grow up" Miranda, but let it be adventurous. Remember the words of the crew of the Galaxy Quest, "Never give up, never surrender". Just try to plan a little better than they did.

Lastly I have to thank all of the sources of funding that made this research even possible. This material is based upon work supported by the National Aeronautics and Space Administration (NASA) Mars Fundamental Research Program grant NNX10AP58G and NASA grant no. NNX10AN23H issued through the NASA training grant National Space Grant College and Fellowship Program to E. M. Hausrath, as well as Nevada Space Grant Consortium fellowships to C. T. Adcock, a GSA research grant to C. T. Adcock, and by a cooperative agreement through the National Nuclear Security Administration under the Stewardship Science Academic Alliances program through DOE Cooperative Agreement #DE-NA0001982 to P. M. Forster and O. Tschauner. The Advanced Light Source was used as part of this work and is supported by the Director, Office of Science, Office of Basic Energy Sciences, of the U.S. Department of Energy under Contract No. DE-AC02-05CH11231. C. T. Adcock also received funding from the UNLV Graduate and Professional Student Association and the UNLV Department of Geoscience.

On to the science...

TABLE OF CONTENTS

LIST OF TABLES

LIST OF FIGURES

CHAPTER ONE

INTRODUCTION AND OVERVIEW

The possibility of the development and persistence of life on Mars has been a topic of scientific interest for centuries (e.g. Huygens, 1698). In the last five decades, dozens of unmanned missions to the planet have returned data that have significantly reshaped the general understanding of Mars and its potential to have harbored life, past or present. The present day martian surface has been revealed as a generally inhospitable, cold, dry, and radiation-bombarded environment. However, Mars also possesses abundant geomorphic and mineralogical evidence of significant surface and near-surface waters in the past (Carr, 1996; Squyres et al., 2004; Baker, 2006; Milliken et al., 2008; Treiman, 2008; Murchie et al., 2009; Milliken et al., 2010; Grotzinger et al., 2013; Williams et al., 2013; Gainey et al., 2014). Provided the availability of bio-essential chemistry, these aqueous environments may have been habitable places conducive to the origin and development of life. Further, present day water in the form of ice currently exists on Mars (Squyres et al., 1992) and liquid water may exist in the subsurface (Malin and Edgett, 2000). If these more localized environments also posses the necessary bio-essential chemistry, habitable niches for martian life might still persist.

Phosphate is among the nutrients considered critical for all known life (Johnston et al., 1934; Miller and Urey, 1959; Wald, 1962, 1964; Madigan et al., 2000). The ion is a component in ATP, DNA, RNA, phospholipid cell membranes and required in a number of fundamental biochemical reactions (Madigan et al., 2000; Pasek and Kee, 2011). Phosphorus, either as phosphate or a more reduced species such as phosphite,

may have also been crucial in pre-biotic reactions that led to the origin of life on Earth (Schwartz, 2006; Powner et al., 2009; Pasek and Kee, 2011). Thus, the availability of phosphate may be a determining factor for an environment to be suitable to maintain life (i.e. habitable). In fact, in long term ecosystems on Earth, phosphate availability is often a biologically limiting factor (Chadwick et al., 1999). If life ever arose on Mars, the availability of phosphorus likely played a significant role.

Though Mars is rich in phosphate (5-10x Earth) (Wanke and Dreibus, 1988; Brückner et al., 2008; Ming et al., 2008; Adcock et al., 2013), the presence of phosphate alone is not equivalent to phosphate availability. Unlike other bioessential nutrients, phosphate has no significant volatile phase and remains locked in phosphate-bearing minerals within rocks until water/rock interactions release it into the environment (Filippelli, 2002). The goal of the research presented here, therefore, is to investigate the mobility and transport of phosphate on Mars and assess martian phosphate availability and the implications for martian habitability in the past, present and, if we choose to make extended visits to Mars, the future. The bioessential nature of phosphate requires that any long term visits to the planet have a secure source of the nutrient. Further, because phosphate is released primarily through aqueous processes, phosphate mobility and transport have implications for past aqueous conditions on Mars. The chapters that follow document three studies focused on the study of martian phosphate mobility and transport.

Chapter two focuses on the synthesis and characterization of the Mars-relevant phosphate mineral merrillite [$Ca_9(Na,Fe,Mg)(PO_4)_7$], as well as the similar mineral whitlockite [$Ca_9(Fe,Mg)(PO_3OH)(PO_4)_6$]. Merrillite is an extraterrestrial Ca-phosphate

mineral similar to whitlockite and is found as a dominant primary phosphate mineral in martian meteorites (McSween and Treiman, 1998). Though merrillite has been previously synthesized (e.g. Gopal and Calvo, 1972; Gopal et al., 1974; Hughes et al., 2008), this study developed methods to produce relatively large quantities of end-member Fe-, Mg- and mixed Fe/Mg-merrillite in an economical manner. The synthesized minerals were also characterized in detail by electron microprobe, single-crystal X-ray diffraction, and synchrotron X-ray diffraction, which allowed for the development of a potential mechanism by which merrillite maintains charge balance during the dehydrogenation of whitlockite. The developed methods are documented in chapter two along with the characterization results of the synthesized materials, including atomic structures of the minerals. This chapter in the form of a manuscript, was accepted and published in American Mineralogist in a July 2014 issue (Adcock et al., 2014).

Chapter three documents the results of thermodynamic and kinetic experiments performed on fluorapatite, synthetic chlorapatite, and the synthetic whitlockite and merrillite produced by methods documented in chapter two. On Earth, the most common primary phosphate mineral is fluorapatite [$Ca_5(PO_4)_3F$]. The dissolution of fluorapatite in igneous rocks is a major source of inorganic phosphate available for biological reactions, and because it is biologically important, it has been well studied (Valsami-Jones et al., 1998; Welch et al., 2002; Guidry and Mackenzie, 2003; Köhler et al., 2005; Chaïrat et al., 2007; Harouiya et al., 2007). In contrast, meteorite evidence suggests that the most abundant primary phosphate minerals on Mars are Cl-rich apatite [$Ca_5(PO_4)_3Cl$] and the mineral merrillite [$Ca_9(Na,Fe,Mg)(PO_4)_7$], an extraterrestrial mineral similar to whitlockite [$Ca_9(Fe,Mg)(PO_3OH)(PO_4)_6$] (McSween and Treiman, 1998). Few kinetic

(e.g. dissolution rates) and thermodynamic (e.g. solubility) data exist for these Mars-relevant minerals. The experiments conducted in chapter three allowed for the derivation of dissolution rates laws and solubilities for these Mars-relevant minerals. The resulting data indicate faster dissolution rates for the Mars-relevant minerals that, when the overall higher phosphorus abundance on Mars is taken into consideration, could lead to phosphate release rates as much as 45 times faster on Mars for a given set of aqueous conditions. Solubility measurements of the Mars-relevant minerals also suggest final concentrations of phosphate in aqueous systems on Mars could be as much as twice that of Earth for a given set of conditions. The potential implications for phosphate availability and martian abiogenesis are discussed. This chapter, in the form of a manuscript, was accepted and published in the journal Nature Geoscience (Adcock et al., 2013).

Finally, in chapter four the measured thermodynamic and kinetic data derived in chapter three are applied to Mars-specific reactive transport modeling of Wishstone class martian rocks to model phosphate transport under martian conditions. The Mars Exploration Rover (MER) Spirit encountered Wishstone class rocks in the Columbia Hills of Gusev Crater. Alpha particle X-ray spectrometry (APXS) was performed on two rocks of this class (i.e. Wishstone and Champagne) and Mini-TES data indicate that the rock class is common among the float rocks of Columbia Hills. Comparisons of APXS brushed surface analyses and analyses taken on fresh surfaces of the rocks, after treatment with Spirit's Rock Abrasion Tool (RAT), indicate the loss of Ca and P from the rocks in ratios consistent with a Ca-phosphate mineral. Reactive transport modeling was performed to investigate the conditions under which these somewhat unique profiles

might have formed. The findings of this study indicate that a period of near-neutral aqueous conditions may have persisted at Gusev Crater at some point in the past. This has positive implications for the potential origin and development of life on Mars. This chapter has been submitted for publication to a peer reviewed planetary science journal.

CHAPTER TWO

SYNTHESIS AND CHARACTERIZATION OF THE MARS-RELEVANT PHOSPHATE MINERALS FE- AND MG-WHITLOCKITE AND MERRILLITE AND A POSSIBLE MECHANISM THAT MAINTAINS CHARGE BALANCE DURING WHITLOCKITE TO MERRILLITE TRANSFORMATION

This chapter was originally published in American Mineralogist in July, 2014.

Citation: Adcock, C.T., Hausrath, E.M., Forster, P.M., Tschauner, O., and Sefein, K.J. (2014) Synthesis and characterization of the Mars-relevant phosphate minerals Fe- and Mg-whitlockite and merrillite and a possible mechanism that maintains charge balance during whitlockite to merrillite transformation. American Mineralogist, 99, 1221-1232.

Abstract

Merrillite [$Ca_9NaMg(PO_4)_7$] occurs as a dominant primary Ca-phosphate mineral in martian meteorites and therefore presumably also on Mars. The mineral is an important phase in exploring differences in geologic processes between Earth and Mars, and also has astrobiological implications due to its potential role as a significant source of the bio-essential nutrient phosphate. Merrillite does not occur terrestrially as a discrete mineral phase, making it difficult to obtain for Mars-relevant studies. It can, however, be synthesized from a similar terrestrial mineral, whitlockite (natural or synthetic), through dehydrogenation. Here we present methods for synthesizing relatively large quantities (0.5 g or greater per batch) of coarse crystalline (75 μm+) Mg-whitlockite, Fe-whitlockite, mixed Fe/Mg-whitlockites, and from these synthesized minerals produce Mg-merrillite, ferrous and ferric Fe-merrillite and ferrous and ferric mixed Fe/Mg-

merrillite. Chemistry and atomic structures of synthesized Fe- and mixed Fe/Mg-whitlockite and ferrous and ferric Fe- and mixed Fe/Mg-merrillite resulting from single-crystal X-ray diffraction, infra-red spectroscopy, and electron microprobe analyses are presented. We also present a mechanism for maintaining charge balance during the formation of merrillite from whitlockite. Our results shed light on these mineral structures for future martian studies, and provide methods for creating coarse crystalline merrillite for use in Mars-relevant thermodynamic, kinetic, soil/dust simulant, crystallographic, astrobiological, and other studies.

Introduction

Merrillite is an anhydrous calcium phosphate mineral that occurs in lunar samples and meteorites, including martian meteorites (Jolliff et al., 1993; McSween et al., 1996; Xie et al., 2002; Terada et al., 2003). The IMA formula for merrillite is $Ca_9NaMg(PO_4)_7$, though merrillite can also be iron-bearing (Jolliff et al., 2006). Synthetic merrillite also lacks Na^+ and charge balance is maintained by additional Ca^{2+} [i.e. $Ca_{9.5}Mg(PO_4)_7$] . Merrillite is of particular interest to martian studies because it is the dominant primary phosphate mineral in martian meteorites (McSween et al., 1996; McSween and Treiman, 1998), and thus presumably also on Mars. This is in contrast to Earth where fluorapatite [$Ca_5(PO_4)_3F$] is the dominant terrestrial primary phosphate mineral and the nearest analog to merrillite, the mineral whitlockite [$Ca_9Mg(PO_3OH)(PO_4)_6$], occurs as a component of teeth and bones in vertebrates, but outside of biological systems is a rare alteration product of phosphate pegmatites. Merrillite is also the major carrier of Rare Earth Elements (REE) in martian meteorites (McSween et al., 1996; McSween and Treiman,

1998; Shearer et al., 2011a) and likely one of the major sources of the phosphorus observed in phosphorus rich martian soils and dust (Goetz et al., 2005; Greenwood and Blake, 2006; Brückner et al., 2008). Phosphate minerals such as merrillite and apatite are thought to react in late stage martian magmas (McCubbin and Nekvasil, 2008; Filiberto and Treiman, 2009a; Gross et al., 2013b), and their presence and intergrowth relationships with each other within martian rocks (or meteorites) can be useful indicators of crystallization and melt evolution, including the evolution of both water and halogen budgets over time (Patiño Douce and Roden, 2006; Patiño Douce et al., 2011; Gross et al., 2013a; Gross et al., 2013b). Such use of merrillite/apatite intergrowth relationships may also be applicable to other differentiated bodies outside of Mars (Shearer et al., 2011b). Phosphate minerals have also been shown to be altered in acid vapor environments, potentially recording important characteristics of the reacting environment (Lane et al., 2008; Hausrath et al., 2013; Hausrath and Tschauner, 2013). In addition, phosphate is a required component in fundamental biologic reactions as well as considered critical to reactions that may have led to life on Earth (Gulick, 1955; Westheimer, 1987; Schwartz, 2006). The alteration of phosphate minerals such as merrillite has important implications for phosphate availability and the potential for martian abiogenesis and development of life on that planet (Adcock et al., 2013). Thus merrillite is an important phase in exploring the differences in petrogenesis, mantle evolution, surface processes and other geologic processes between Earth, Mars, and possibly other bodies (McSween et al., 1996; Treiman, 2003; Shearer et al., 2011a).

The importance of merrillite in martian processes makes a readily available source of the mineral desirable for laboratory study. However, single-phase natural

merrillite only occurs in extraterrestrial materials and thus studies requiring merrillite must obtain the mineral directly from meteorites or lunar samples, or through synthesis. Here we present, methods for producing fairly large quantities of crystalline Fe/Mg-bearing merrillite for use in Mars-relevant studies, the chemistry and atomic arrangements of the synthetic minerals, and a proposed mechanism for maintaining charge balance during the formation of merrillite from whitlockite.

Background

Merrillite was first described in meteorites by Merrill (1915; 1917). Wherry (1917) was the first to suggest applying "merrillite" as the name of the extraterrestrial mineral. Merrillite is chemically and structurally similar to the terrestrially occurring mineral whitlockite; in fact, though merrillite is not found terrestrially as a discrete mineral phase outside of biological systems, it does occur as a minor component within whitlockite, with which it forms a solid solution (Hughes et al., 2008). In biological systems, merrillite forms in dental calculi and urinary stones (Dorozhkin and Epple, 2002). The similarities of merrillite and whitlockite have resulted in overlapping use of the mineral names within the literature, though they are not strictly the same mineral. Whitlockite was first described by Frondel (1941) as a late stage calcium phosphate mineral associated with pegmatites. Frondel and Prien (1946) later applied the term "whitlockite" to synthetic tricalcium phosphate [β-$Ca_3(PO_4)_2$ or commonly β-TCP] because of chemical and structural similarities of that phase. The similarity of merrillite, whitlockite, and β-TCP led Fuchs (1962) to argue, based primarily on powder X-ray diffraction data, that the three phases were the same and that the term "merrillite" should

be abandoned in favor of "whitlockite". Subsequent research conclusively demonstrated that merrillite and β-TCP, while isostructural and very similar to whitlockite, are distinct, and lack the required hydrogen of whitlockite (Gopal and Calvo, 1972; Dowty, 1977; Rubin, 1997; Hughes et al., 2008). Dowty (1977) suggested "merrillite" as the more appropriate name for the hydrogen-free form found in meteorites. However, because of the historical usage of "whitlockite" and the difficulty of confirming the hydrous or anhydrous nature of the phases, the term "whitlockite" continues to be occasionally used synonymously or interchangeably when describing merrillite (e.g. Ruszala and Kostiner, 1980; Jolliff et al., 1993; McSween et al., 1996; Terada et al., 2003; Orlova et al., 2009). This is especially the case in biomedical fields where synthetic merrillite compounds, such as β-TCP, are important in bio-ceramics and are often referred to as whitlockite or β-whitlockite (e.g. Jarcho et al., 1979; Lagier and Baud, 2003). In this paper, as in some other studies that discuss both merrillite and whitlockite (e.g. Hughes et al., 2006; Jolliff et al., 2006) the term "merrillite" is used to describe the anhydrous extraterrestrial (and synthetic) Ca-phosphate mineral, and the term "whitlockite" to refer to the hydrogenated terrestrial mineral form.

The most common method of synthesizing merrillite powder is solid state sintering, which involves heating relevant powdered calcium phosphate chemistry to >1025 °C. The method typically requires several cycles of regrinding the material during the synthesis process (e.g. Lazoryak et al., 1996; Belik et al., 2002; Orlova et al., 2009), and therefore produces a very fine powder. This general method is used to produce synthetic Ca-endmember merrillite materials including commercially available β-TCP powders and ceramics. The same methods have been used to synthesize other types of

merrillite powders (Teterskii et al., 2007; Orlova et al., 2009), including Mg-merrillite and ferric Fe-merrillite (Lazoryak et al., 1996). A drawback to this general method is that it produces only very fine powders, which may not be preferred for some studies (e.g. dissolution kinetics, crystallography, soil simulants). The commercial version is also an endmember lacking in Fe or Mg and thus chemically dissimilar to the merrillite commonly found in lunar samples or martian meteorites (Jolliff et al., 2006).

Another method of synthesizing merrillite is through the heating of whitlockite to >1000 °C for at least 24 hours to drive off the "essential hydrogen" (Gopal and Calvo, 1972; Hughes et al., 2008). This method has the advantage of being simple to perform and has been applied to both synthetic Mg-whitlockite and natural whitlockite crystals to produce crystalline merrillite rather than powders. However, natural terrestrial whitlockite is itself uncommon and generally restricted to small quantities associated with pegmatites. Thus, in order to synthesize quantities of high purity crystalline Mg- and Fe-merrillite for use in Mars-related kinetic, thermodynamic, astrobiological, or other studies, the synthesis of Mg- and Fe-whitlockite in large quantity is required.

Whitlockite can be synthesized by the Rowles method (Rowles, 1968) which involves hydrolysis of brushite in magnesium chloride solution to create Mg-whitlockite. The method can create pure Mg-whitlockite crystalline material and large output masses (500+ g). The crystalline material generated by this method is very fine with specific surface areas (SSA) of 3-7 m^2/g (geometrically equivalent to 0.3-0.6 μm diameter average particle size)(Hamad and Heughebaert, 1986) making it of limited usefulness in kinetic, simulant, crystallographic, or other studies where coarser crystalline material is preferred. Hydrothermal methods, however, can create coarser crystalline material.

Gopal et al. (1974) synthesized coarse, up to 500 μm per side, crystalline Mg-whitlockite using such a method. The method required the pre-synthesis and processing of a calcium phosphate gel and a large (6mm x 100mm) single-use gold tube to contain the reagents during heating to 300 °C, making it less practical for synthesizing in quantity. Hughes et al. (2008) inadvertently produced a small amount (i.e. "a few crystals") of Mg-whitlockite by similar methods while hydrothermally recrystallizing hydroxyapatite [$Ca_5(PO_4)_3OH$]. Their method involved first synthesizing hydroxyapatite powder from a calcium phosphate solution and suspending it in 10ml of distilled water with the pH adjusted to 2.79 using phosphoric acid. The resulting suspension was sealed in a reusable 23ml Teflon lined acid digestion vessel and heated to 240 °C for 5 days. The output mass from the hydrothermal treatment consisted mainly of elongate, recrystallized hydroxyapatite along with a small number of large, well-formed, Mg-whitlockite crystals. The apparent cause of whitlockite synthesis was Mg contamination from an undetermined source. Here we present methods based on Hughes et al. (2008) to generate large quantities of single phase Mg-whitlockite and, from that whitlockite, Mg-merrillite by intentionally supplying Mg^{2+} to the synthesis. We also developed methods to generate large amounts of crystalline Fe-whitlockite, as well as mixed Fe/Mg-whitlockites, and ferrous, ferric, and mixed Fe/Mg-merrillites. Atomic parameters are presented for ferrous, ferric, and mixed merrillite and Fe- and mixed whitlockite, as well as a proposed mechanism for maintaining charge balance during the formation of merrillite from whitlockite.

Methods

Whitlockite synthesis

Based on preliminary experiments (Table S1 in Appendix I), the following synthesis methods were developed for Mg- and Fe-whitlockite production: a solution containing 90ml of high purity (18.2 MΩ) water, laboratory grade hydroxyapatite (Spectrum, reagent grade), and either magnesium nitrate hexahydrate for Mg-whitlockite (J.T. Baker, ACS grade) or troilite for Fe-whitlockite (Alfa Aesar, Fe[II]S 99%) were combined in a 125ml Parr acid digestion vessel (Parr #4748) with an acid washed Teflon liner. Specific volumes and masses are contained in Table 1. Once the solution was mixed, it was acidified to pH <2.8 with concentrated phosphoric acid (Alfa Aesar, ACS grade). The vessel was then sealed and incubated in an oven at 240 °C for 7 days. At the end of 7 days, the vessel was removed from the oven and quenched in a water bath in an effort to prevent any further reaction. After cooling, the vessel was opened and the solution decanted leaving the solids. Solid material was rinsed from the vessel using ethanol, allowed to air dry for 24 hours, weighed, and inspected by optical microscopy for preliminary phase identification. Impurities, first determined by powder XRD and then optically by morphology thereafter, were typically hydroxyapatite and monetite ($CaHPO_4$). In the case of Fe-bearing whitlockite, additional opaque materials presumed to be Fe-phases occurred in quantities too minor for powder XRD analysis. These impurities were primarily confined to the <75 μm fraction and output masses were brush sieved on 200 mesh screen to remove that size fraction. Crystals were confirmed as Mg- or Fe-whitlockite by Scanning Electron Microscopy (SEM) with Energy Dispersive

Spectroscopy (EDS), Electron Microprobe Analysis (EMP), Powder X-ray Diffraction (XRD), and Single Crystal X-ray Diffraction (SC-XRD).

Based on results from endmember experiments described above, mixed Fe/Mg-whitlockites were also successfully synthesized by combining both troilite and magnesium nitrate hexahydrate (J.T. Baker ACS grade, and Alfa Aesar Fe[II]S 99%, respectively) in the solution used within a single synthesis experiment. Table 1 contains the specific masses and volumes used to produce the mixed Fe/Mg-whitlockite that was further characterized in this study and it includes sodium (as NaCl) as part of the solution. Subsequent experiments indicated that the addition of NaCl in this method has no observable effect and can be omitted (see Results and Discussion, and Appendix I Supplementary Discussion and Table S1), but it is included in Table 1 as this was the material further characterized in this study. Outside of solution chemistry, all other parameters used in mixed Fe/Mg-whitlockite synthesis were the same as for the endmember whitlockite synthesis (e.g. temperature, acidity, incubation time). Impurities found in mixed Fe/Mg synthesis batches (typically large polycrystalline aggregates, hydroxyapatite and opaque phases as determined optically) were primarily confined to the <75 μm and >150 μm fractions and output masses were brush sieved to isolate the 75-150 μm size fraction. Remaining crystalline material was confirmed as Fe/Mg-whitlockite by EMP and SC-XRD.

Merrillite synthesis

Merrillite can be synthesized from whitlockite (natural or synthetic) by dehydrogenation through heating to >1000 °C for at least 24 hours (Gopal et al., 1974;

Hughes et al., 2008). In this study, crystalline Mg-merrillite was synthesized from synthetic Mg-whitlockite by heating to 1055 °C (+/-5 °C) for a minimum of 24 hours in a loosely covered 10ml Pt crucible nested within a larger (100ml) alumina crucible for easier handling. After heating, the crucibles were removed and allowed to air cool. After cooling, resulting materials, typically white to clear in color, were removed from the crucible using a synthetic brush.

Crystalline ferric Fe-merrillite was synthesized in an identical manner as the Mg-merrillite described above, in a Pt crucible in ambient atmosphere. The process produces an orange/red colored material. Ferrous Fe-merrillite was synthesized in an evacuated (10^{-3} Torr) sealed SiO_2 tube in place of the Pt crucible to inhibit oxidation of Fe from ferrous to ferric in the Fe-whitlockite. Tubes were purged with argon three times to remove oxygen before final evacuation and sealing. SiO_2 glass wool (average 4 μm diameter) was used to prevent the loss of material from the tubes during purge and evacuation cycles. Whitlockite heat treated in this manner ranged in color from white/translucent to black and nearly opaque.

Mixed Fe/Mg-merrillite was synthesized both in a 10 ml Pt crucible in ambient atmosphere, and also in a triple argon purged evacuated (10^{-3} Torr) sealed SiO_2 tube to inhibit oxidation of the Fe in the Mg-Fe whitlockite, both as described above. Resulting materials from all merrillite syntheses were analyzed by optical microscopy, EMP and SC-XRD to confirm the phases. Oxidation of Fe during merrillite synthesis can mask detection of dehydrogenation by SC-XRD, so Fe-containing phases were additionally analyzed by Infrared Spectroscopy (IR). As with the Fe-endmember whitlockite treated

in the same manner, the output material ranged in color from white/translucent to black and nearly opaque.

Analytical Methods

Powder X-ray Diffraction (XRD) analyses were performed in the UNLV Geoscience XXL facility. Samples of synthesized Mg- and Fe-whitlockite, as well as impurities from synthesis, were powdered by hand in an agate mortar and pestle and subjected to powder XRD in a Panalytical X'pert Pro diffractometer using Cu Kα radiation. Scans were run at 45 Kv and 40 mA from 5-75° 2θ in continuous mode with step-size of 0.0084° and scan rate of 0.06° sec^{-1}. Patterns were identified and confirmed using Panalytical's X'pert Pro High Score Plus software.

Optical microscopy was used to identify synthesized phases based on crystal habit/morphology and previous XRD analyses. These identifications were carried out with a Barska tri-ocular stereomicroscope with a magnification range of 7x to 45x. An adaptor mounted Canon XTi camera was used for all optical photomicrographs.

Scanning Electron Microscopy (SEM) in secondary electron imaging mode (SEI) and Energy Dispersive Spectrometry (EDS) was carried out on a JEOL 5600 SEM at the UNLV Electron Microanalysis and Imaging Laboratory (EMiL). Operating conditions were 20 KeV and a 20 mm working distance. Analyses by Electron Microprobe (EMP) wavelength dispersive spectroscopy (WDS) were carried out in a JEOL JXA-8900 at the UNLV EMiL facility on polished epoxy mounts. Analysis conditions were 20 KeV and 10 nA using a 10 μm beam. Analyses were standardized using Smithsonian mineral

standards of olivine (Mg, Fe) and apatite (Ca, P)(Jarosewich, 2002), and Harvard (Amelia) albite (Na)(McGuire et al., 1992).

Single Crystal X-ray Diffraction (SC-XRD) analyses were carried out using a Bruker APEXII single crystal diffractometer. An appropriate crystal was selected under paratone oil on a polarizing microscope and attached to a Kapton mount. A full sphere of data was collected with the sample cooled to 100 K using an Oxford nitrogen cryostream. An absorption correction utilized the Bruker software SADABS, structure solution was performed using a beta-version of SHELXT, and refinement was carried out using a combination of SHELX (Sheldrick, 2007) and OLEXII (Dolomanov et al., 2009). Bond valence calculations from SC-XRD data were conducted using VALIST (Wills, 1999).

Infrared (IR) spectra were obtained with a Digilab FTS 7000 series FT-infrared spectrometer on powdered samples using a photo-acoustic chamber attachment. Analyses were performed under ambient conditions at 2.5 KHz and a resolution of 8 cm^{-1} for 64 total scans. Data were collected over the range of 400 to 4000 cm^{-1}. Carbon black was used to obtain a background versus subsequent spectra.

Synchrotron X-ray diffraction experiments were conducted on two samples (a red ferric Fe/Mg-merrillite crystal and a dark colored ferrous Fe/Mg-merrillite crystal) at the superconducting bending magnet beamline 12.2.2 at the Advanced Light Source (ALS), Lawrence Berkeley National Laboratory, with the goal of identifying any trace fine-grained phases within the merrillite. Primary beam energy was 20.000 keV and a MAR345 image plate detector was utilized. Detector parameters were calibrated and corrected for geometric distortions based on a LaB_6 NIST powder diffraction standard using the Fit2D software (Hammersley et al., 1996). The X-ray beam at beamline 12.2.2

of the ALS is focused by Kirkpatrick-Baesz mirrors vertically and horizontally to 10 x 15 μm^2. Crystal samples were mounted on the tips of quartz glass fibers of 30 μm diameter and centered on the phi rotation axis. Exposures were taken over 160 s while the samples were oscillated by +/-40 degrees around the phi axis. Recorded images were integrated using Fit2D (Hammersley et al., 1996). We first used Fit2D to mask strong reflections from merrillite and any remaining minor untransformed whitlockite in the diffraction image frames and integrated the remaining patterns. Integrated patterns were still dominated by merrillite reflections and less intense whitlockite reflections. The contributions from both these phases were fitted by a Le Bail refinement (Le Bail, 2005). Remaining reflections were then identifiable as fine-grained inclusions. We used the first strong diffraction peaks of these fine-grained inclusions for a search in the American Mineralogist database (Downs and Hall-Wallace, 2003) and commercial data bases (ICSD) for identifying possible inclusion phases (Bergerhoff and Brown, 1987).

Results and Discussion

Optimization of Whitlockite Synthesis

Results of preliminary Mg-whitlockite experiments indicated that the concentration of solids in solution (g/L) was a strong control on Mg-whitlockite formation (Appendix I Table S1). Concentrations of greater than approximately 22 g/L produced primarily monetite ($CaHPO_4$) and hydroxyapatite (HAP) crystalline material rather than whitlockite. Concentrations of less than 22 g/L, including the 14.5 g/L used in the finalized method, produced yields consisting primarily of well formed crystals of Mg-whitlockite confirmed by morphology, SEM EDS, powder XRD, and SC-XRD

(Figures 1A and 2A). Solution concentrations of significantly less than 14.5 g/L (e.g. 11.1 g/L) produced whitlockite, but in smaller amounts (Appendix I Table S1). Variations in incubation time (5-14 days) indicated that most crystal growth occurred in the first 7 to 8 days. Longer incubation times (up to 14 days) did not produce significantly larger crystals. Variations in pH from 2.1 to 2.8 did not appear to have any significant effect. Scaling up from 23ml vessels to 125ml vessels had no effect as long as solution concentrations were maintained. Temperature (i.e. 240 °C) was not varied and represented the highest safe temperature rated for the vessels used. The ratio of HAP to magnesium nitrate hexahydrate (3.33: 1) was not varied significantly, but minor changes (2.93:1 to 3.52:1) had no noticeable effect on syntheses. Overall yields from multiple batches of Mg-whitlockite synthesis using the final method had an average yield of >700 mg (Appendix I Table S1). The <75μm fraction was removed to minimize impurities (i.e. monetite and hydroxyapatite); this fraction averaged <2% of the total output mass. Imperfections within some crystals, mainly in the larger size fraction, were apparent optically, but centralized clusters of inclusions similar to those seen by Hughes at al. (2008), while present, were uncommon. Most crystals (>80%) were over 150 μm and the largest crystals were 2mm. Polycrystalline aggregates of whitlockite occurred in the >75 μm fraction but the majority of the material were single crystals. EMP analyses of synthesized crystals (Table 2) confirmed Mg-whitlockite stoichiometry as $Ca_{9.0}Mg_{0.9}(PO_3OH)(PO_4)_6$.

Attempts to synthesize Fe-whitlockite using $FeCl_2$ as the source of Fe failed to produce the mineral in amounts detectable by optical microscopy, even at total solid in solution concentrations as low as 12.0 g/L. Instead, crystal morphologies consistent with

monetite and recrystallized HAP were produced as well as minor opaques (presumably Fe phases). The subsequent use of Fe(II)S as the source of Fe did produce Fe-whitlockite. Aggregate and hydroxyapatite production were minimized by decreasing the concentration of solids in solution from an initial 16.1 g/L to < 12.0 g/L. To minimize iron sulfide phases, the ratio of hydroxyapatite to Fe(II)S in solution was increased from ~9:1 (near stoichiometric ideal) to between 16:1 and 20:1 in an effort to "starve" the system of Fe. Yields from Fe-whitlockite syntheses using the final method described in the methods section averaged >500 mg of largely well formed whitlockite crystals (Figs. 1B and 2B, Appendix I Table S1). Impurities (i.e. iron sulfides, hydroxyapatite, and monetite) mainly occurred in the <75 μm fraction which could be removed through sieving. The <75 μm fraction accounted for 33% of the total output mass on average. Inter-crystalline Fe-films were apparent optically in some aggregates (Fig. 1C). Some Fe-whitlockite crystals themselves contained minor intra-crystalline Fe-film deposits (determined optically) on earlier growth surfaces (Fig. 1B), with the crystals separable by picking. Minor amounts of Mg (0.14 wt. % as MgO) were also detected in Fe-whitlockites by EMP (Table 2). Like Hughes et al. (2008), the source of Mg is unknown, but is most likely from trace impurities in the reagents used. EMP analyses of synthesized crystals (Table 2) confirmed synthetic Fe-whitlockite stoichiometry as $Ca_{9.0}Fe_{1.0}(P_{1.0}O_3OH)(PO_4)_6$.

While Mg- and Fe-endmember whitlockite (and the merrillite synthesized from them) represent closer analogs to naturally occurring minerals than a phase like β-$Ca_3(PO_4)_2$, mixed Fe/Mg phases are closer analogs still. Two early experiments to produce mixed Fe/Mg-whitlockite failed to produce any significant whitlockite

(Appendix I Table S1). With understanding gained from further endmember experiments, another set of experimental conditions was tested with a lower solution concentration (13.0 g/L as opposed to >17 g/L for the earlier attempts). This experiment included a source of Na^+ as part of the solution (included in the solution concentration noted above). Though Na^+ does not generally occur in whitlockite, the ion does occur in a specific Ca^{2+} site in natural merrillite, including merrillite found in martian meteorites where Na^+ content can be as high as 2 wt.% (Jolliff et al., 2006). The batch produced Fe/Mg mixed whitlockite (Figs. 1D and 2C) along with impurities of hydroxyapatite and monetite, and large (>150 μm) polycrystalline aggregates. Most impurities were in the >150 μm and <75 μm size fractions, leaving the 75-150 μm size fraction the purest. This fraction comprised 39% of the total output mass. EMP analyses showed no incorporation of Na^+ into any of the synthesized material and an average stoichiometry of $Ca_{9.0}Fe_{0.7}Mg_{0.3}(PO_3OH)(PO_4)_6$ (Table 2). The whitlockite seems to preferentially incorporate Mg, as the whitlockite from this batch had a Fe to Mg molar ratio of ~7:3 but the molar ratio of Fe to Mg in the reactants added was ~9:3. EMP analyses of results from additional mixed Fe/Mg-whitlockite synthesis experiments support this observation (Appendix I Table S2). It is also of note that the mixed Fe/Mg-whitlockite synthesis experiments had a higher failure rate than those of the endmembers, even after finding a generally successful set of conditions. Further investigation might yield the source of the failures or better refine the method. The lack of Na^+ incorporated within the whitlockite synthesized in these experiments suggests it may not be possible to incorporate the ion into the structure under hydrothermal conditions. Thus, mixed Fe/Mg-merrillite subsequently synthesized from the mixed Fe/Mg-whitlockite would also lack the sodium

generally found in martian and lunar merrillite. Further investigation to determine conditions that favor Na^+ substitution in merrillite are warranted as they could potentially reveal important information about the specific martian environments in which merrillite forms. Nevertheless, sodium-free mixed Fe/Mg-bearing merrillite represents a better analog to martian merrillite than pure endmember phases. EMP analyses revealed standard deviations of Fe and Mg contents were slightly higher than those of endmember synthesized material (Table 2). However, the minor increase in inhomogeneity should not limit the usefulness of the material for most studies.

Merrillite Synthesis

Merrillite and whitlockite structures are too similar to be easily distinguished by powder XRD, thus heat-treated materials were analyzed by SC-XRD and EMP to determine if the whitlockite to merrillite transformation had occurred. In the case of Mg-merrillite, SC-XRD (discussed in more detail below under Crystallography) confirmed synthesis had occurred and EMP analyses of the resulting Mg-merrillite (Table 2) indicated a stoichiometry of $Ca_{9.4}Mg_{1.1}(PO_4)_{7.0}$, compared to $Ca_{9.0}Mg_{0.9}(PO_3OH)(PO_4)_6$ of the starting Mg-whitlockite. The higher stoichiometric value for Ca^{2+} results from Ca substitution for charge balance due to dehydrogenation. Dehydrogenation is also the likely cause of higher observed totals for EMP analyses of Mg-merrillite versus the Mg-whitlockite used to synthesize it (99.35% versus 98.02% respectively). The synthesized Mg-merrillite maintained the crystallinity and morphology of the starting whitlockite material (Fig. 1E).

Fe-merrillite synthesis proved more complex than Mg-merrillite synthesis due to the apparent oxidation of ferrous Fe^{2+} to ferric Fe^{3+} when heated in open air. Fe-whitlockite samples heat-treated in open air (i.e. in the Pt crucible) changed color from white to orange or yellow. Like the Mg-merrillite, EMP analyses of the heat treated material showed overall totals rise from 98.15% for the original whitlockite to 98.80% for the heat treated material (with Fe calculated as FeO, see Table 2 and associated table notes), likely due to the loss of H^+ during heating. However, EMP analyses also indicated a stoichiometry that did not significantly change from the Fe-whitlockite of $Ca_{9.0}Fe_{1.0}(PO_4)_{7.0}$. This EMP result, and the color change, suggested oxidation of Fe^{2+} to Fe^{3+} to produce a ferric Fe-merrillite phase balancing the change in charge due to the loss of H^+ as shown below:

$$Ca_9Fe^{2+}(PO_3OH)(PO_4)_6 \rightarrow Ca_9Fe^{3+}(PO_4)_7. \quad (1)$$

Bond valence calculations (Skowron and Brown, 1990) and Fe – O bond lengths (Table 3) based on SC-XRD analyses of the heat treated material were also consistent with Fe^{3+}. To confirm dehydrogenation, IR analyses were performed on both the unreacted Fe-whitlockite and the heat-treated Fe-merrillite to determine the presence or absence of O–H bonds (Fig. 3A). The IR spectra show a large reduction in absorption between the starting material and the heat-treated material over the range of 3330 to 2570 cm^{-1} where a broad feature is associated with an O–H stretch (White, 1990; Belik et al., 2002). There is also an O–H absorption peak at 2380 cm^{-1} (Belik et al., 2002) which disappears between the starting whitlockite material and the samples heated treated in the Pt crucible open to the atmosphere (Fig. 3A), further supporting the conclusion that the material is ferric (Fe^{3+}) Fe-merrillite. Previous research using solid state methods has also produced

a ferric Fe-merrillite (e.g. Lazoryak et al., 1996; Belik et al., 2002), although the material in those experiments was a fine powder.

In order to prevent Fe oxidation and promote the formation of ferrous Fe-merrillite, Fe-whitlockite was heated to 1055 °C in triple argon purged evacuated fused SiO_2 tubes instead of the open air Pt crucible. After heat treatment, EMP analyses indicated a stoichiometry of $Ca_{9.2}Fe_{1.0}Mg_{0.1}(P_{1.0}O_4)_7$ and overall totals rose compared to the starting material (Table 2). Bond valence calculations performed using VALIST (Wills, 1999) and Fe–O bond lengths (Table 3) from SC-XRD data are consistent with an Fe oxidation state of 2+, indicating that the phase is ferrous. However, IR results showed a remaining peak at 2380 cm^{-1} indicating that full dehydrogenation did not occur during the heat treatment (Fig. 3A). Thus the resulting phase consists of ferrous Fe-merrillite containing some whitlockite. Extending the incubation time at 1055 °C to three days had no effect on the IR results. The result of heat treating the Fe-whitlockite in a sealed SiO_2 appears to be ~80-90% transformation to merrillite based on SC-XRD and is discussed in more detail in the Crystallography section. The incomplete dehydrogenation of the ferrous merrillite may be the result of changing partial pressure due to H^+ loss in the sealed system and warrants further exploration. Many of the heat treated crystals were darker in color suggesting the formation of other, possibly Fe-containing phases, although BSE and EMP analyses were unable to detect a separate phase within crystals or a color dependent difference in chemistry.

Formation of mixed Fe/Mg-merrillite followed similar trends to that of endmember Fe-merrillite synthesis, with samples heated in open air oxidizing to Fe^{3+}/Mg-merrillite and samples heated in an evacuated SiO_2 tube forming Fe^{2+}/Mg-

merrillite. Fe/Mg-whitlockite heat treated in a Pt crucible in open air showed a rise in EMP totals over the starting material beyond that attributable only to total calculations based on Fe_2O_3 rather than FeO (Table 2 and associated table notes). IR analyses, as described above (Fig. 3B), indicated dehydrogenation had occurred. Bond valence calculations based on SC-XRD data showed that Fe had oxidized to Fe^{3+}, and EMP analyses of the reacted material showed a stoichiometry of $Ca_{9.2}Fe_{0.7}Mg_{0.4}(P_{1.0}O_4)_7$ compared to the unreacted whitlockite of $Ca_{9.0}Fe_{0.7}Mg_{0.3}(P_{1.0}O_3OH)(PO_4)_6$ indicating Ca mobility to balance the change in charge due to the loss of H^+ had occurred. Heat treatment also caused a color change in the material from white/translucent to red/orange.

Dehydrogenation of mixed Fe/Mg-whitlockite by heating in an evacuated fused SiO_2 tube resulted in crystalline material that varied in color from clear translucent to nearly opaque dark black. SC-XRD analysis performed on a clear crystal indicated it to be Fe^{2+}/Mg-merrillite that contained some whitlockite. Fe – O distances determined by SC-XRD indicate that the Fe had not significantly oxidized. A smaller, sharp O-H absorption peak at 2380 cm^{-1} remained (Fig. 3B) indicating that the phase contained some whitlockite. Similar to the ferrous endmember Fe-merrillite extending the incubation time to three days had no effect on the IR results. Estimates of the merrillite/whitlockite content are discussed in more detail in the Crystallography section, but indicate that most of the mixed Fe/Mg-reacted material is merrillite (~70%). The color change observed in post heat treatment crystals, as with the Fe-merrillite treated in a SiO_2 tube, suggested the possible formation of another phase. However, as with the similarly treated endmember Fe-whitlockite, BSE and EMP analyses were unable to detect a separate phase within the crystals or a difference in chemistry between lighter or darker colored material.

Surface deposits or films on crystals of synthesized endmember and mixed merrillite crystals are apparent under SEM imaging (Figs. 2D to 2F) and by optical microscopy (e.g. Fig. 1E). Large (> 150 μm) Mg-merrillite crystals were completely covered with the film, which is generally sub-micron in thickness. The amount of coverage appeared to decrease with decreasing grain size (i.e. smaller crystals exhibited less complete or thinner coverage). In contrast, deposits on Fe^{2+}-bearing crystals rarely covered the entire crystal surface and in the case of ferric Fe-merrillite, most crystals showed no coating (Fig. 1F). SC-XRD analyses did not detect a second phase, although SC-XRD analysis would be unlikely to detect such small amounts of a second phase. The surface textures also lack any morphology that would suggest crystallinity and thus may be amorphous. The coatings were also not detectable in EMP prepared samples due to their sub-micron thickness and similar chemistry. EDS in SEM of the reacted surfaces indicated that the surface deposits were mainly Ca and P with no evidence of Mg or Fe, and therefore suggest that they may be the result of some form of diffusion to the surface during heating.

In an attempt to determine what additional phases might be present in the merrillite samples, two samples were analyzed by synchrotron XRD; a translucent red-colored crystal of the Fe/Mg-merrillite heat treated in open air (ferric Fe/Mg-merrillite), and a crystal containing a hazy grey to black core within a clear crystal matrix of Fe/Mg-merrillite heat treated in a SiO_2 tube (ferrous Fe/Mg merrillite). Specimens were 100 to 150 μm in diameter. In both cases, diffraction patterns exhibited three distinct sets of features: reflections that belong to multiple domains of merrillite, reflections that belong

to domains from whitlockite, and Debye fringes from very fined grained (grain size < 1μm) inclusions. Thus the samples were not true single crystals.

Modeled and observed patterns of the red-colored ferric Fe/Mg-merrillite sample along with the residual of the fit appear in Figure 4A. In addition to the expected merrillite and whitlockite, monetite and a minor amount of holtedahlite [$Mg_2(PO_4)(OH)$] were also identified. Holtedahlite occurs as a fine grained phase which generated a smooth powder diffraction pattern. With the given experimental settings and based on the observed peak profiles the average grain size of holtedahlite is less than 1 μm and more than 100 nm. Since the diffraction signals from whitlockite, merrillite, and monetite were not powderous, a Reitveld analysis for phase quantification could not be conducted. However, the strength of the diffraction signal of holtedahlite indicates that it is significantly less than merrillite, whitlockite, and monetite.

The ferrous Fe/Mg-merrillite specimen with the grey-black core region was composed of a solid solution whitlockite/merrillite matrix (>3 micron grain size) containing small amounts of monetite and an additional unidentified fine grained (< 1μm) phase. Limited diffraction data are consistent with a Na-bearing Ca-ferrate, although a confident identification is not possible and oxidized Fe would be surprising in the ferrous Fe/Mg-merrillite. The observed pattern with the whitlockite/merrillite contributions masked and modeled patterns of monetite, a Na-bearing Ca-Ferrate, and the residual of the fit appear in Figure 4B.

Presumably, some of these additional phases may also occur in the endmember merrillite materials, though we were not able to confirm that as part of the current study. Synchrotron diffraction patterns of monetite might explain the calcium and phosphorus

phase observed as films on crystals. SC-XRD analyses did not detect monetite, holtedahlite or another unidentified phase, but the technique and sample selection criteria are designed to refine single structures from single crystals and are not applicable to detecting minor phases that exhibit reflections from multiple domains or powder fringe patterns.

The mechanism by which calcium balances the charge imbalance due to the loss of H^+ from whitlockite and increases the stoichiometric Ca in non-ferric merrillite is unclear. Gopal and Calvo (1972) and Gopal et al. (1974), who synthesized merrillite from both natural and synthetic Mg-whitlockite, present no mechanism. Hughes et al. (2008), who synthesized merrillite from synthetic Mg-whitlockite, suggest Ca-rich reagents entrained in the synthetic whitlockite crystals yielded Ca sufficient to counter the charge imbalance due to H^+ loss, with the Ca presumably diffusing through the crystal. However, this mechanism fails to explain enhanced Ca concentrations in the whitlockite to merrillite dehydrogenation experiments of Gopal and Calvo (1972) who used natural whitlockite, which would contain no entrained reagents.

The apparent enrichment of Ca relative to phosphate during the whitlockite to merrillite transformation could take place through the formation of additional phases that either diffuse to the surface or are dispersed and difficult to detect within the bulk crystals. This would be consistent with the synchrotron diffraction data that indicate additional phases were present within Fe/Mg-merrillites. An additional phase or phases, like the holtedahlite or Fe-bearing phase indicated by synchrotron diffraction, would be required in order to take up extra Mg or Fe made available during the transformation from whitlockite to merrillite. Synchrotron diffraction data from the ferric Fe/Mg-

merrillite heat treated open to atmosphere indicated holtedahlite as the only additional crystalline phase beyond monetite, which would take up remaining Mg. It is plausible that if the Fe is oxidizing during transformation as per Equation 1, an additional Fe-bearing phase may not necessarily form. However, in the case of the ferrous Fe/Mg-merrillite treated in the SiO_2 sealed tube, both Fe- and Mg-bearing additional phases would be expected and synchrotron diffraction data only indicate a possible Fe-bearing crystalline phase. It is possible that an undetected amorphous Mg-phase is taking up the excess Mg, and that a similar Fe-bearing phase may also form to take up any excess Fe in the Ferric merrillite that is not accounted for by oxidation (Equation 1). Candidates for such a phase include Fe- and Mg- pyrophosphates [$X_2(P_2O_7)$ where X is Mg or Fe], which can be produced in high temperature metal/phosphate systems and can be amorphous (Bensalem et al., 1997; Lee et al., 2012). These Fe- and Mg-pyrophosphate phases may also act as transitional phases – for example, a hypothetical Mg-pyrophosphate may be a transitional phase to the holtedahlite observed by synchrotron XRD (Equation 2), which would explain why holtedahlite was detected in one sample, but no Mg-containing phase in the other:

$$Mg_2(P_2O_7) + 2\ H_2O \rightarrow\ Mg_2(PO_4)(OH) + H_3PO_4\,. \qquad (2)$$

A general reaction reflecting the transformation from whitlockite to merrillite may therefore include either holtedahlite or an amorphous metal pyrophosphate, and be represented by:

$$\textit{Whitlockite} + \textit{Heat} \rightarrow \textit{Merrillite} + \textit{Monetite} + \textit{Additional Phase(s)} + H_3PO_4 + H_2O,$$

where non-merrillite phases take up any remaining chemistry resulting from the whitlockite-to-merrillite transformation. A balanced example that includes both monetite and pyrophosphate as the metal phosphate is:

$$24\ Ca_9X(PO_3OH)(PO_4)_6 \rightarrow\ 22\ Ca_{9.5}X(PO_4)_7\ +7\ Ca(HPO_4) + X_2(P_2O_7) + 5\ H_3PO_4 + H_2O. \quad (3)$$

Equations similar to 1, 2, or 3, or combinations thereof, are consistent with the observations of this study and allow for a mechanism of charge balance that does not require entrained synthesis reagents. Such a mechanism would better explain the transformation of natural whitlockite to merrillite confirmed by Gopal and Calvo (1972), where no entrained reagents from synthesis were present.

Crystallography

The atomic parameters of Mg-whitlockite and Mg-merrillite synthesized by conceptually similar methods to those used here have been previously measured by SC-XRD and discussed (Gopal et al., 1974; Hughes et al., 2008), and therefore we only focus on differences between the Fe- and Fe/Mg-whitlockite and merrillite structures determined in this work. The structures of Fe-whitlockite and ferric Fe-merrillite have been previously refined using powder XRD diffraction (Corlett and Keppler, 1966; Keppler, 1968; Lazoryak et al., 1996; Belik et al., 2002). Belik et al. (2002) utilized neutron powder XRD and located two deuterium sites for Fe–whitlockite; hydrogen cannot be located by SC-XRD methods. Since significantly more accuracy is possible with single crystal XRD, we report the structures of Fe-whitlockite and ferric Fe-merrillite here (Table 4). Atomic parameters of synthetic ferrous Fe-merrillite, and mixed Fe/Mg-merrillite do not appear to be in the literature, and we present atomic coordinates and full listing of bond distances as Tables S3 and S4 in Appendix I. A .cif file containing all six crystal structures is also in Appendix I.

Broadly speaking, the six crystal structures determined (Fe- and Fe/Mg-whitlockite, as well as ferrous and ferric Fe- and Fe/Mg-merrillite)(Table 4) are similar with differences related mainly to the chemistry. The position of the proton has previously been established as protonating the phosphate group located on the 3-fold axis (labeled P3 in this work). Protonated phosphates point in the opposite direction compared to non-protonated phosphates. Modeling of this disorder for the synthetic Fe-whitlockite found 89.0% of P3 on the inverted site; 100% should be inverted if the structure were fully protonated. It is possible that some protons occupy other sites in the structure, some Fe^{3+} is present, minor merrillite is present, or a combination of the three. Small amounts of merrillite within natural whitlockite and synthetic Mg-whitlockite have been previously noted (Hughes et al., 2008).

Heat treating the Fe-whitlockite in a Pt crucible open to the atmosphere yields an Fe-merrillite sample where 97.1% of the P3 are not on the inverted site, in agreement with essentially full conversion to merrillite. This does not require 2.9% protonation – it is possible that a fraction of the P3 phosphate remains inverted after deprotonation. The observed Fe – O distances (Table 3) are highly sensitive to the oxidation state of the iron. We find distances in the Fe-whitlockite sample (Fe – O bond lengths of ~2.03 Å), and in the ferric merrillite sample (Fe – O bond length of ~2.10 Å) that match expected metal – oxygen distances for Fe^{2+} and Fe^{3+}, respectively. Note that the approximate difference of 0.1 Å between Fe for Fe^{2+} and Fe^{3+} is larger by roughly a factor of 50 than standard deviations on these bond distances (Table 3). Bond valence calculations are normally only an approximate method of identifying oxidation state as bond distances can be influenced by a variety of structural features in a specific compound. In this particular

instance, bond valence calculations are more conclusive as the crystal structures and compositions are very similar to each other. While the observed bond distances as well as the bond valence calculations clearly suggest primarily Fe^{2+} in the Fe-whitlockite and ferrous merrillite, and primarily Fe^{3+} in ferric merrillite, they only indicate which oxidation state is predominant in each structure, not the relative amounts of Fe^{2+} and Fe^{3+}.

Heating the Fe-whitlockite samples in evacuated SiO_2 tubes apparently prevented some oxidation of Fe^{2+} to Fe^{3+}, as evidenced by little change in the measured Fe – O bond distances (Table 3). Charge balance in the merrillite is maintained by the migration of Ca^{2+} cation sites to around where protons are found in the whitlockite form. The Ca is distributed over two sites, Ca4A and Ca4B, with refined occupancies of 14.8 and 29.6%, respectively. As it is not possible from crystallography to assign elements to partially occupied sites such as these, we infer that they are likely Ca based on its increase in microprobe data (Table 2) and the bonding environments for both sites. Table 3 includes bond distances for these sites, all of which are longer than expected for Fe^{2+}. In addition, the environments are quite irregular, which would be unfavorable for d^6 Fe but not unusual for Ca^{2+}. As 50% occupancy of a divalent cation site would provide sufficient charge balance to replace that lost by full dehydrogenation, these occupancies are consistent with 88.8% conversion to merrillite. Of the P3 phosphates, 23.9% are inverted, which is consistent with a modestly higher degree of protonation than suggested by the Ca^{2+} occupancies, though some of the P3 phosphate may have remained inverted after deprotonation. The Ca^{2+} occupancies of the Fe-whitlockite heat treated in a sealed SiO_2 tube, together with P3 observations, indicate ~80-90% conversion to merrillite.

There was no evidence of significant electron density on or around these sites in the Fe-whitlockite and Fe-merrillite heat treated in a Pt crucible.

The mixed Fe/Mg-whitlockite sample refined to a similar overall structure as the pure Fe-whitlockite. Refinement of the Fe/Mg ratio yielded a 63.7% Fe occupancy, with the balance Mg, in general agreement with the microprobe results (Table 2). The Fe/Mg ratios refined for the two heated samples refined to 75.4% (Pt crucible) and 64.6% (SiO_2 tube). Inter-crystal standard deviations on this ratio determined by microprobe were high, so it is quite possible that this value varies some from crystal to crystal. P3 phosphates are inverted 84.0% of the time, suggesting the whitlockite is 16% merrillite already, and the Fe – O distances are consistent with Fe^{2+}. The sample heated in air ended up with 6.5% of the P3 site inverted, suggesting near complete conversion to merrillite structure, and the Fe – O distances are consistent with Fe^{3+}.

Results of heating mixed Fe/Mg samples in sealed SiO_2 tubes were also quite similar to the pure Fe case. Fe – O distances are consistent with Fe^{2+}, and 30.9% of the P3 phosphate group are inverted, indicating that the sample is largely merrillite. Two Ca sites with similar environments and occupancies (9.8% and 26.4%) were also found.

Implications for Martian Studies

Merrillite is a potentially important indicator of martian geologic processes, including the evolution of halogen and water content over time in martian magmas. A deeper understanding of the relationship of merrillite formation to halogen and water content in melts may hold clues to parts of the martian igneous and hydrologic cycles. The relationship of merrillite/whitlockite to apatite in melts may also hold important

clues to the evolution of not only martian magmas, but those of other differentiated bodies including Earth and asteroids. The phosphate in martian soils and dust may also be present as merrillite, making the mineral of interest to martian surface process studies and, as a major source of bio-essential phosphate, studies pertaining to martian habitability. Access to a supply of synthetic, coarse crystalline whitlockite and merrillite of various chemistries and an understanding of the conditions under which these phases can be formed, as presented here, will likely aid in facilitating a number of these studies as well as further investigations into more fundamental thermodynamic and kinetic parameters of the minerals. Complete dehydrogenation of ferrous merrillite in this study may have been hindered by the sealed tube used. A flow through apparatus may eventually prove more successful, and while Na^+ incorporation into merrillite may not be possible under hydrothermal conditions, a high temperature approach may yield success. Future efforts in producing completely dehydrogenated ferrous merrillite as well as incorporating Na^+ into synthetic merrillite are warranted as the conditions under which these are achieved may reveal further insights into the natural environments, martian or otherwise, in which these minerals form.

Acknowledgements

This material is based upon work supported by the National Aeronautics and Space Administration (NASA) Mars Fundamental Research Program grant NNX10AP58G to E. M. Hausrath, a Nevada Space Grant Consortium fellowship to C. T. Adcock, a GSA research grant to C. T. Adcock, and by a cooperative agreement through the National Nuclear Security Administration under the Stewardship Science Academic

Alliances program through DOE Cooperative Agreement #DE-NA0001982 to P. M. Forster and O. Tschauner. The authors thank David Hatchett and Keith Lawler for IR spectroscopy support, as well as Ravhi Kumar, Darius Roohani, and Michael Steiner for aid in synthesis experiments. The comments and advice of Francis McCubbin and Justin Filiberto who reviewed the manuscript were greatly appreciated and improved many aspects of the final manuscript. We also express our appreciation to Eugene Smith, Henry Sun, Sean Mulcahy, Valerie Tu, William Kerlin, and Seth Gainey for technical assistance and discussion which improved this paper. The Advanced Light Source is supported by the Director, Office of Science, Office of Basic Energy Sciences, of the U.S. Department of Energy under Contract No. DE-AC02-05CH11231.

Table 1. Masses and volumes used in finalized whitlockite synthesis methods

Synthetic Mineral	*$MgNO_3$ (g)*	*FeS (g)*	*NaCl (g)[a]*	*HAP (g)[b]*	*Total solid Mass (g)*	*H_2O (ml)*	*Solids in Solution (g/L)*
Mg-whitlockite	0.300 (±0.003)	-	-	1.000 (±0.003)	1.300	90	14.4
Fe-whitlockite	-	0.055 (±0.005)		1.000 (±0.003)	1.055	90	11.7
Fe/Mg-whitlockite	0.050 (±0.003)	0.050 (±0.005)	0.067 (±0.005)	1.000 (±0.003)	1.167	90	13.0

[a]*Later experiments showed NaCl to have no effect on synthesis.* [b]*HAP = hydroxyapatite.*

Table 2. Chemical analyses of whitlockite and merrillite by electron microprobe in wt%.

	Mg-whitlockite		*Mg-merrillite*	
CaO	47.61	(0.20)	48.89	(0.21)
P_2O_5	46.85	(0.27)	46.38	(0.32)
MgO	3.54	(0.14)	4.06	(0.12)
FeO	0.02	(0.03)	0.02	(0.03)
Na_2O	B.D.		B.D.	
[a]H_2O	0.86		-	
Total	98.02	(0.34)	99.35	(0.36)
n	17		16	
Stoic.	$Ca_{9.0}Mg_{0.9}(PO_3OH)(PO_4)_6$		$Ca_{9.4}Mg_{1.1}(PO_4)_{7.0}$	

	Fe-whitlockite		*Ferric Fe-merrillite (Pt cruc.)*		*Ferrous Fe-merrillite (SiO_2 tube)*	
CaO	46.00	(0.45)	46.37	(0.27)	47.00	(0.19)
P_2O_5	45.26	(0.47)	46.02	(0.50)	45.42	(0.46)
MgO	0.14	(0.03)	0.34	(0.07)	0.39	(0.10)
[b]Fe_2O_3	-		6.74	-	-	
FeO	6.75	(0.27)	-		6.85	(0.18)
Na_2O	B.D		B.D.		B.D.	
[a]H_2O	0.86		-		-	
Total	98.15	(0.63)	99.47	(0.45)	99.65	(0.53)
n	18		17		20	
Stoic.	$Ca_{9.0}Mg_{0.9}(PO_3OH)(PO_4)_6$		$Ca_{9.0}Fe_{0.9}Mg_{0.1}(PO_4)_{7.0}$		$Ca_{9.2}Fe_{1.0}Mg_{0.1}(PO_4)_{7.0}$	

	Fe/Mg-whitlockite		*Ferric Fe/Mg-merrillite (Pt cruc.)*		*Ferrous Fe/Mg-merrillite (SiO_2 tube)*	
CaO	46.54	(0.59)	46.79	(0.33)	47.09	(0.22)
P_2O_5	45.83	(0.36)	45.96	(0.39)	45.40	(0.38)
MgO	1.00	(0.20)	1.29	(0.09)	1.20	(0.16)
[b]Fe_2O_3	-		4.98	-	-	
FeO	4.62	(0.71)	-		5.68	(0.23)
Na_2O	B.D.		B.D.		B.D.	
[a]H_2O	0.86		-		-	
Total	97.99	(0.49)	99.02	(0.60)	99.36	(0.48)
n	15		13		19	
Stoic.	$Ca_{9.0}Fe_{0.7}Mg_{0.3}(PO_3OH)(PO_4)_6$		$Ca_{9.1}Fe_{0.7}Mg_{0.3}(PO_4)_{7.0}$		$Ca_{9.2}Fe_{0.9}Mg_{0.3}(PO_4)_{7.0}$	

Parenthetical values are 1 standard deviation. n = number of analyses averaged chemistry is based on. B.D. = below detection.

[a]H_2O is based on ideal whitlockite (Hughes et al., 2008) and is not included in the EMP totals.

[b]Fe was measured assuming Fe^{2+} and recalculated to Fe^{3+} with total and resulting stoichiometry adjusted accordingly. For ferric Fe-merrillite, the original FeO wt. % = 6.07 with a standard deviation of 0.13, analysis total of 98.80, and calculated stoichiometry of $Ca_{9.1}Fe_{0.9}Mg_{0.1}(PO_4)_{7.0}$. For Ferric Fe/Mg-merrillite the original FeO wt. % = 4.48 with a standard deviation of 0.08, analysis total of 98.53, and calculated stoichiometry of $Ca_{9.2}Fe_{0.7}Mg_{0.4}(PO_4)_{7.0}$. NOTE: It is not possible by microprobe alone to actually determine Fe^{2+}/Fe^{3+} content and these values are estimates.

Table 3. Select bond lengths discussed in text for synthetic minerals Å.

		Fe-whitlockite	Fe/Mg-whitlockite	Ferric Fe-merrillite (Pt cruc.)	Ferrous Fe-merrillite (SiO_2 tube)	Ferric Fe/Mg-merrillite (Pt cruc.)	Ferrous Fe/Mg-merrillite (SiO_2 tube)
Fe(1)-	O(4)	2.1131(16)	2.1067(13)	2.046(2)	2.122(3)	2.048(2)	2.104(2)
	O(4)#1	2.1130(16)	2.1068(13)	2.046(2)	2.122(3)	2.048(2)	2.104(2)
	O(4)#2	2.1130(16)	2.1068(13)	2.046(2)	2.122(3)	2.048(2)	2.104(2)
	O(5)	2.0893(16)	2.0806(12)	2.011(2)	2.108(3)	2.023(2)	2.092(2)
	O(5)#1	2.0893(16)	2.0806(12)	2.011(2)	2.108(3)	2.023(2)	2.092(2)
	O(5)#2	2.0893(16)	2.0806(12)	2.011(2)	2.108(3)	2.023(2)	2.092(2)
Ca(4A)-	O(6)#18	NA	NA	NA	2.736(5)	NA	2.758(6)
	O(6)#19	NA	NA	NA	2.736(5)	NA	2.758(6)
	O(7)#18	NA	NA	NA	2.541(4)	NA	2.541(4)
	O(7)#19	NA	NA	NA	2.541(4)	NA	2.541(4)
Ca(4B)-	O(6)#18	NA	NA	NA	2.516(3)	NA	2.518(2)
	O(6)#19	NA	NA	NA	2.516(3)	NA	2.518(2)
	O(7)#18	NA	NA	NA	2.846(5)	NA	2.851(4)
	O(7)#19	NA	NA	NA	2.846(5)	NA	2.851(4)

Parenthetical values are standard deviations. "Pt cruc." denotes merrillite produced in a platinum crucible in open air. "SiO_2 Tube" denotes merrillite produced using a triple argon purged and seal glass tube. Only Fe-O and Ca-O bonds discussed in text appear in table. A full table of bond lengths appears in deposit item Table S4.

Table 4. Single crystal X-ray diffraction refinement statistics.

Mineral	Fe-whitlockite	Fe/Mg-whitlockite	Ferric Fe-merrillite (Pt cruc.)	Ferrous Fe-merrillite (SiO_2 tube)	Ferric Fe/Mg-merrillite (Pt cruc.)	Ferrous Fe/Mg-merrillite (SiO_2 tube)
Emp. formula	$Ca_9FeHO_{28}P_7$	$Ca_9Fe_{0.64}HMg_{0.36}O_{28}P_7$	$Ca_9FeH_{0.02}O_{28}P_7$	$Ca_{9.44}FeH_{0.12}O_{28}P_7$	$Ca_9Fe_{0.75}Mg_{0.25}O_{28}P_7$	$Ca_{9.36}Fe_{0.65}H_{0.28}Mg_{0.35}O_{28}P_7$
Formula wt.	1082.37	1070.93	1081.38	1099.12	1073.59	1084.98
a (Å)	10.3510(7)	10.3499(4)	10.3278(11)	10.3453(6)	10.3301(13)	10.3392(7)
c (Å)	37.059(2)	37.0715(16)	37.050(4)	37.118(2)	37.062(5)	37.081(2)
Volume ($Å^3$)	3438.6(4)	3439.1(2)	3422.4(8)	3440.3(5)	3425.1(10)	3432.8(5)
Density (calc.) (Mg/m^3)	3.136	3.103	3.148	3.183	3.123	3.149
Reflections collected	17516	17609	17589	11475	17501	17513
Independent reflections	2352	2355	2334	2238	2338	2342
R(int)	0.0221	0.0202	0.0248	0.0236	0.0249	0.0213
parameters	140	142	140	146	143	153
Goodness-of-fit on F2	1.148	1.085	1.095	1.078	1.053	1.085
Final R indices [I>2sigma(I)]						
R1	0.0185	0.0154	0.0172	0.0204	0.0171	0.0157
wR2	0.0552	0.041	0.0454	0.0517	0.0483	0.0411
R indices (all data)						
R1	0.0185	0.0155	0.0175	0.0211	0.0178	0.016
wR2	0.0553	0.0411	0.0455	0.0521	0.0489	0.0414
Largest diff. e $Å^{-3}$						
peak	0.361	0.315	0.372	0.590	0.787	0.472
hole	-1.913	-0.956	-1.092	-1.032	-0.366	-0.425

Note: 5.1° to 61.0° 2Θ range, temperature 100 K, space group R3c. Parenthetical values are standard deviations.

Figures

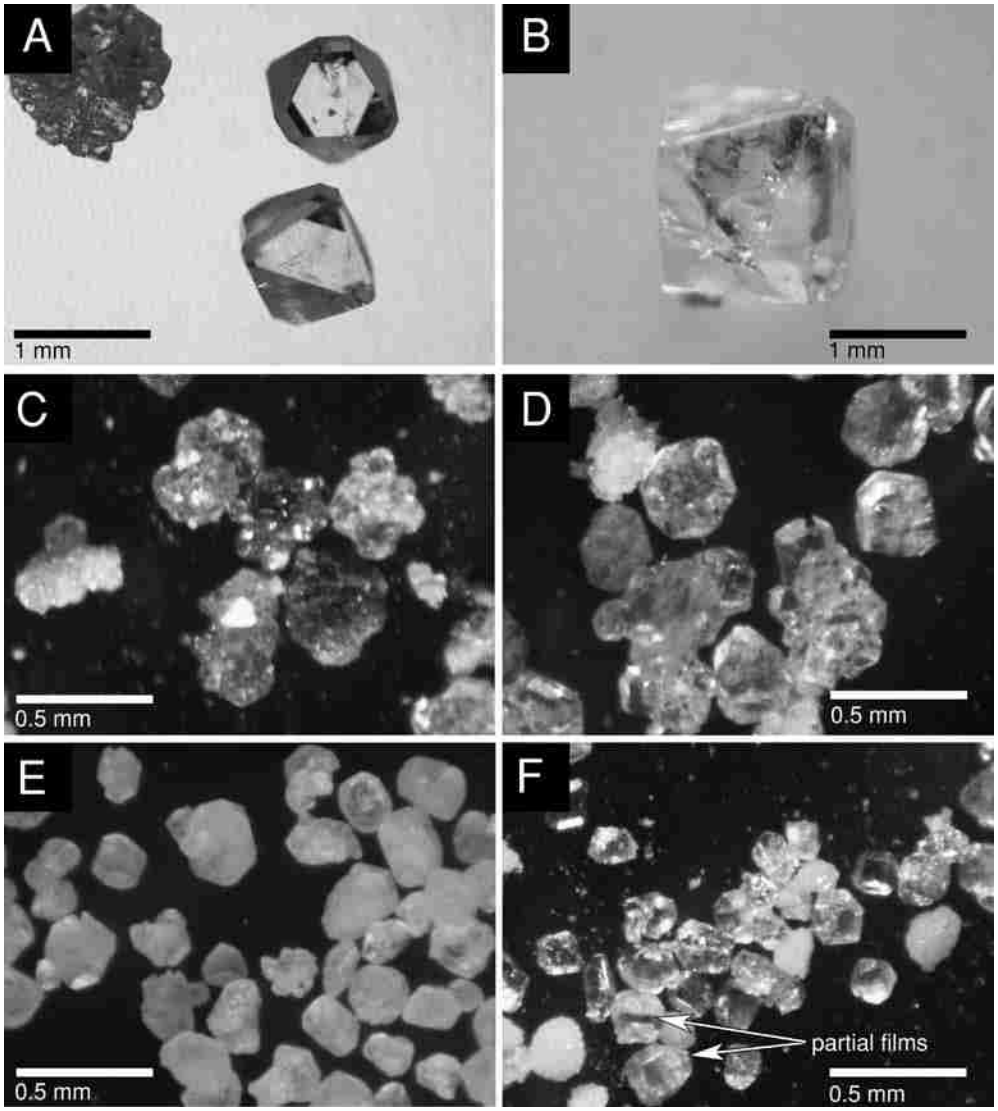

Figure 1. Optical images of synthesized phases. A) Mg-whitlockite single crystals with a polycrystalline aggregate in the upper left corner. B) Fe-whitlockite single crystal. Dark color inside crystal suggests some intra-crystalline iron film on growth faces. C) Fe-whitlockite polycrystalline aggregates. Darker colors in some aggregates from inter-crystalline iron films. D) Mixed Fe/Mg-whitlockite single crystals. E) Mg-merrillite showing the hazy surface texture due to a thin film deposit post heat treatment. The extent of coverage appeared to decrease with decreasing grain size (i.e. smaller crystals exhibited less complete or thinner coverage). F) Ferric Fe-merrillite crystals showing the incomplete hazy surface texture post heat treatment on some crystals (arrows). Deposits on the minerals rarely covered the entire crystalline surface. "White crystals" in this image are polycrystalline aggregates.

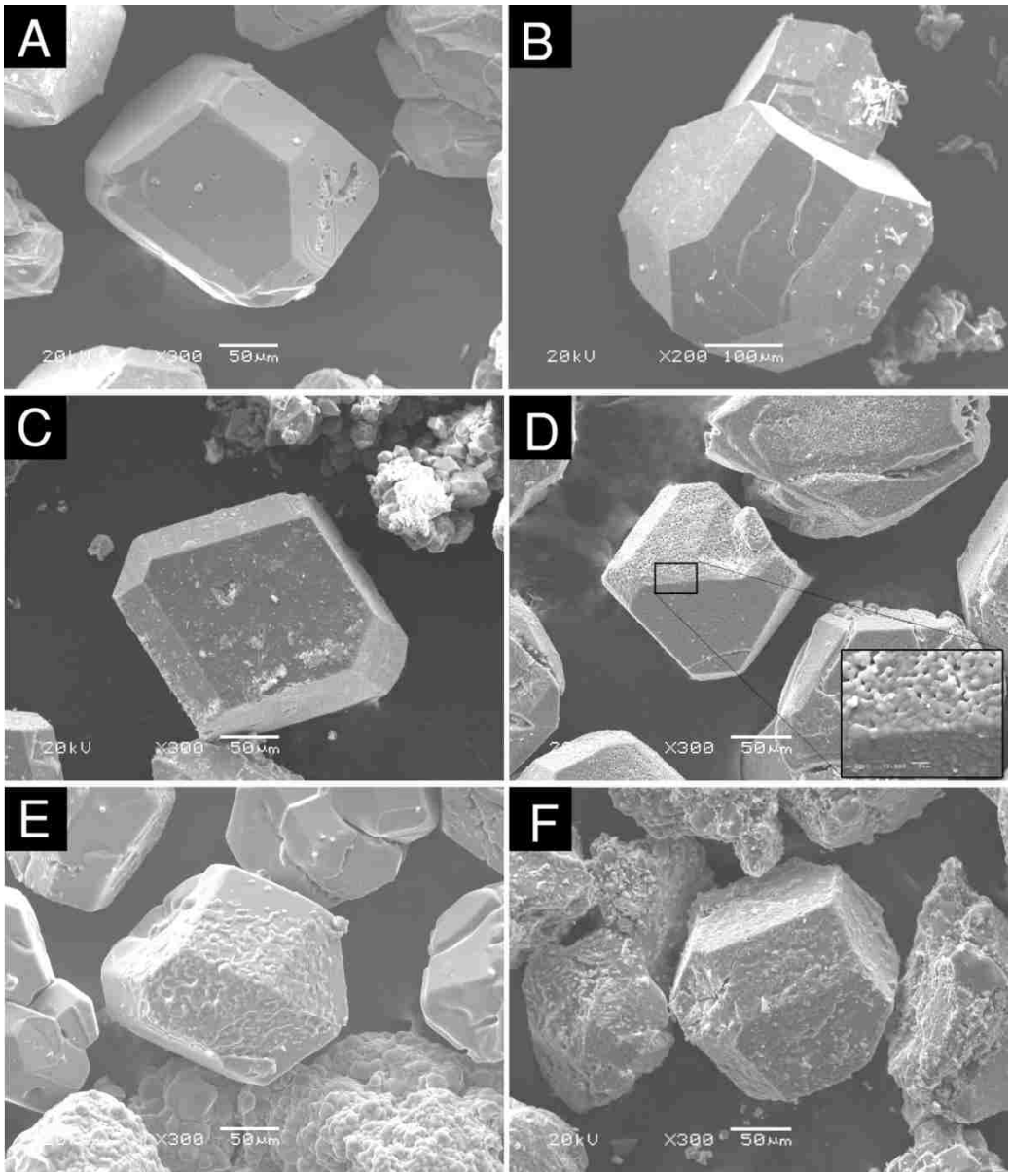

Figure 2. Scanning Electron Microscope images of synthesized materials. A) SEM SEI image of synthesized Mg-whitlockite. **B)** SEM SEI image of synthetic twinned Fe-whitlockite. **C)** SEM SEI image of synthesized Fe/Mg-whitlockite. **D)** SEM SEI with inset (taken at 3000x) showing coating developed on Mg-merrillite crystal during synthesis. Most Mg-merrillite crystals were completely covered, although smaller grains exhibited less complete or thinner coverage. **E)** SEM SEI image of Ferric Fe-merrillite showing coating developed during synthesis. In contrast to Mg-merrillite, the deposit on the mineral rarely covered the entire crystalline surface and in some cases crystal showed no coating, consistent with discussion of our proposed mechanisms. **F)** SEM SEI image of ferrous Fe-merrillite showing coating developed during synthesis.

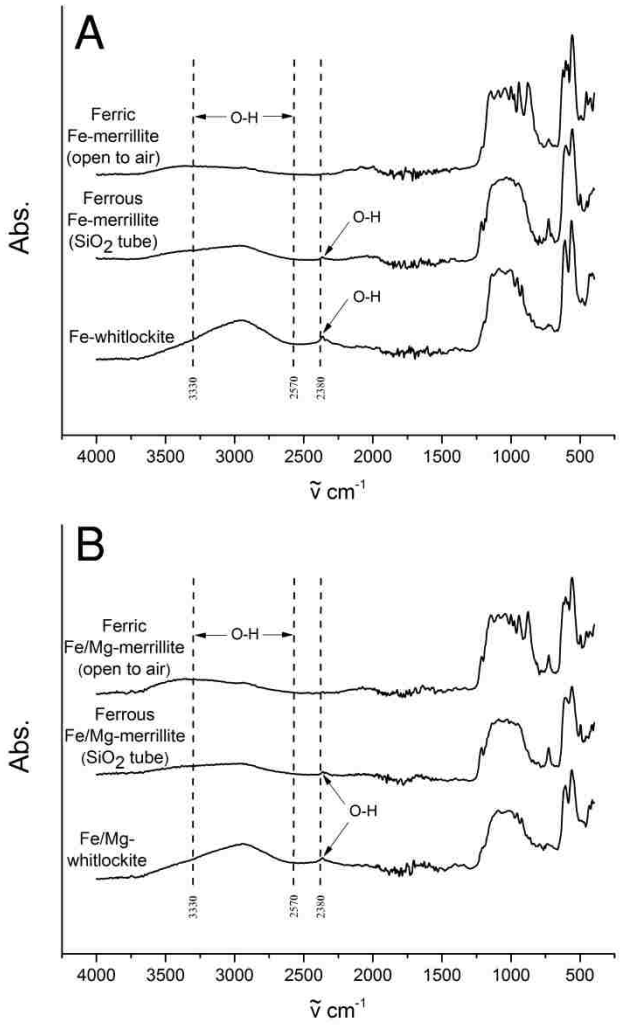

Figure 3. IR Spectra of whitlockite and merrillite A) Fe-whitlockite, ferrous merrillite treated in a SiO2 tube, and ferric merrillite treated open to atmosphere. **B)** Fe/Mg-whitlockite, ferrous Fe/Mg-merrillite heat treated in a SiO2 tube, and ferric Fe/Mg-merrillite heat treated open to atmosphere. Whitlockite data show an apparent absorption from 3330 to 2570 cm-1 where a broad O-H stretch feature exists. The absorbance is mainly absent in material treated in a Pt crucible exposed to air (ferric Fe- and Fe/Mg-merrillite), with some absorption in the O-H stretching band present in material treated in a sealed SiO2 tube (ferrous Fe- and Fe/Mg-merrillite) including a peak at 2380 cm-1. Spectra offset for clarity.

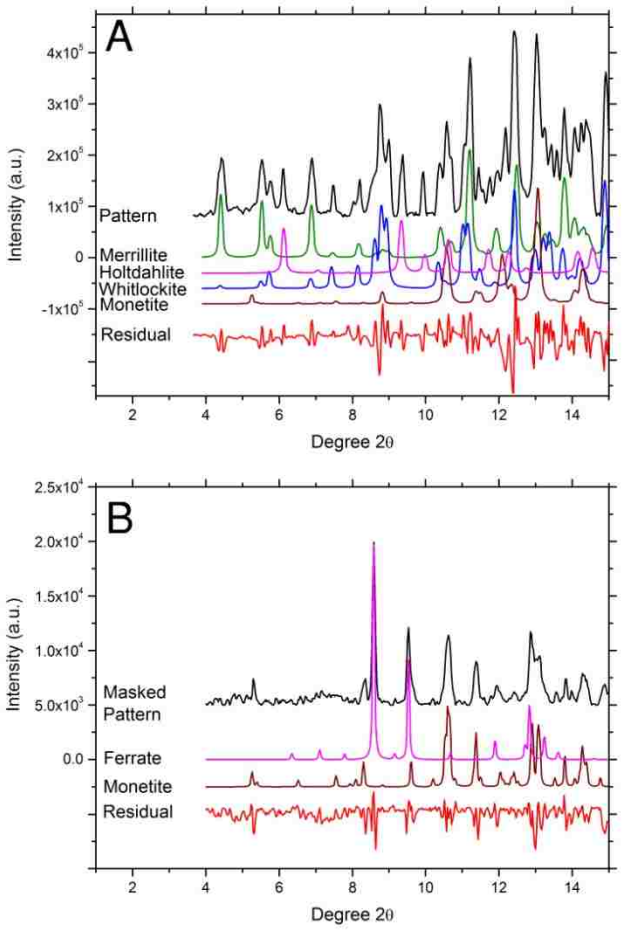

Figure 4. Synchrotron X-ray diffraction. A) Observed and modeled patterns of the red-colored ferric Fe/Mg-merrillite sample along with the residual of the fit. Beyond the expected whitlockite/merrillite observed in the crystal, monetite and holtedahlite also appear to be present. **B)** Similar data for a dark-colored ferrous merrillite crystal with whitlockite/merrillite pattern data masked out. This crystal also contained monetite and an additional unconfirmed phase with structure similar to a ferrate.

CHAPTER THREE

READILY AVAILABLE PHOSPHATE FROM MINERALS IN EARLY AQUEOUS ENVIRONMENTS ON MARS.

This chapter was originally published in Nature Geoscience in September, 2013.

Citation: Adcock, C., Hausrath, E., and Forster, P. (2013) Readily available phosphate from minerals in early aqueous environments on Mars. Nature Geoscience, 6(10), 824-827.

Abstract

Given the presence of essential chemistry, the processes that led to life on Earth may have also occurred on Mars. Phosphate is among the chemical nutrients thought to be essential for life and low prebiotic availability of phosphate may have been a complicating factor in terrestrial abiogenesis. A similar hurdle may have potentially confronted the development of life on Mars. Here we present dissolution rates, phosphate release rates and solubilities of phosphate minerals found in martian rocks as determined from laboratory measurements. Our findings indicate phosphate release rates and phosphate concentrations in solution are higher on Mars than Earth for a given set of conditions.

Introduction

If the chemistry essential to life was present in water containing environments on Mars, the processes that led to life on Earth may have also occurred on the red planet (Miller and Urey, 1959). Phosphate is one of the chemical nutrients thought to be

essential for life and is also considered critical to reactions that may have led to life on Earth (Westheimer, 1987; Schwartz, 2006). However, low prebiotic availability of phosphate may have been a complicating factor in terrestrial abiogenesis (Gulick, 1955; Schwartz, 2006), suggesting that a similar hurdle may have confronted the development of life on Mars. Phosphate available for biological reactions can be introduced into aqueous environments through dissolution of primary phosphate minerals during water–rock interactions, but little is known about the dissolution of the dominant phosphate minerals found in martian meteorites and presumably on Mars (McSween and Treiman, 1998; McCubbin and Nekvasil, 2008; Filiberto and Treiman, 2009b; McCubbin et al., 2012). Here we present dissolution rates, phosphate release rates and solubilities of phosphate minerals found in martian rocks as determined from laboratory measurements. Our experimental findings predict phosphate release rates during water–rock interactions on Mars that are as much as 45 times higher than on Earth and phosphate concentrations of early wet martian environments more than twice those of Earth. We suggest that available phosphate may have mitigated one of the hurdles to abiogenesis on Mars.

Phosphate possesses many attributes that exclusively suit the ion for biotic and prebiotic roles, including stabilizing adenosinetriphosphate (ATP), deoxyribonucleic acid (DNA), ribonucleic acid (RNA) and contributing to the amphiphilic character of phospholipids that make them ideal components of cell membranes (Westheimer, 1987). In DNA, for example, the phosphate bond configuration and resulting net negative charge act to ionize and protect the macromolecule from hydrolysis, qualities required for cell containment and the persistence of genetic material (Westheimer, 1987). The hydrolysis half-life of phosphate-based DNA is of the order of millions of years, its stability making

it ideal for retaining genetic information (Schroeder et al., 2006). In contrast, DNA-type diesters based on anions similar to phosphate, such as arsenate, sulfate, silicate, or orthovanadate, possess half-lives of the order of days at most, which is not sufficient for the faithful reproduction of genetic material (Westheimer, 1987; Schroeder et al., 2006). No terrestrial organism has been observed to persist in an environment completely devoid of phosphate. Phosphate availability is also considered essential for prebiotic reactions that eventually led to terrestrial life (Miller and Urey, 1959). Phospholipid polymers have been observed to abiotically form in water and self-assemble into bilayers that may have acted as precursors to present biological cell membranes (Hargreaves et al., 1977). Phosphate has also been shown to be key in reactions leading to abiotic formation of RNA, both in the RNA itself and acting as a catalyst and pH buffer, which may have been a step towards a so-called RNA world and a possible precursor to present DNA-using life (Powner et al., 2009). Phosphate availability for prebiotic reactions is considered critical enough that the low solubility of phosphate minerals resulting in low concentrations of phosphate in prebiotic terrestrial waters and the relatively poor reactivity of phosphate towards organic compounds, may have been a hurdle for the origin of life (that is, the so-called phosphate problem)(Keefe and Miller, 1995; Schwartz, 2006). Numerous studies have proposed plausible mechanisms for the synthesis of organophosphates using agents such as cyanamide, salts of phosphoric acid, or heating in the presence of aluminum phosphate (Schwartz, 2006), thus addressing the poor reactivity. However, all of these mechanisms require phosphate availability. The fundamental necessity of aqueous phosphate availability has led to a number of studies suggesting mechanisms to enhance global or local P concentrations, including the introduction of more soluble reduced P

species by volcanism, meteorites, or lightning (Yamagata et al., 1991; Schwartz, 2006; Pasek and Lauretta, 2008; Pasek and Block, 2009). Whatever mechanism allowed for terrestrial abiogenesis, the phosphate problem underlines the crucial nature of phosphate in biotic and probably prebiotic reactions. Given the possible similarity of past and perhaps present environments on Mars and the chemical attributes of phosphate that make it essential for terrestrial life, if life arose on Mars, phosphate availability probably played a critical role (Miller and Urey, 1959).

Mars is phosphate rich (five to ten times more than Earth) as evidenced from martian meteorites and alpha particle X-ray spectrometry rock analyses by the Mars Exploration Rovers (Appendix II, Table S5). However, the presence of phosphate is not equivalent to phosphate availability. Phosphate has no significant volatile phase under terrestrial or martian conditions. Phosphate is first introduced and made bioavailable in an environment through the dissolution of primary phosphate minerals in igneous rocks during rock-water interactions.

Dissolution of phosphate-containing minerals has probably occurred on Mars. Alpha particle X-ray spectrometry analyses from Mars Exploration Rover Spirit indicate a loss of Ca and P from the surfaces of high-P rocks such as Wishstone at Gusev Crater (Gellert et al., 2006), suggesting dissolution of a Ca- and P-containing mineral. The dissolution rate of primary phosphate minerals from rocks such as Wishstone controls the rate of introduction of phosphate into aqueous and therefore potentially habitable environments and the solubility of these minerals controls equilibrium phosphate concentrations. Thus, fundamental thermodynamic and kinetic data (for example, solubility and dissolution rates) from Mars-relevant phosphate minerals can be applied to

interpret phosphate release as part of a conceptual model of martian phosphate mobility. Such application of fundamental kinetic and thermodynamic data is extensively used to interpret natural systems (Drever, 2005).

The dissolution rates and solubility of fluorapatite, $Ca_5(PO_4)_3F$, the most common primary phosphate mineral on Earth, are well studied (Valsami-Jones et al., 1998; Welch et al., 2002; Guidry and Mackenzie, 2003; Chaïrat et al., 2007; Harouiya et al., 2007). In contrast, few kinetic and thermodynamic data exist for merrillite, $Ca_9NaMg(PO_4)_7$ [an extraterrestrial variety of whitlockite, $Ca_9Mg(PO_3OH)(PO_4)_6$] and Cl-rich apatite, $Ca_5(PO_4)_3(Cl; F)$, the dominant primary phosphate minerals in martian meteorites (McSween and Treiman, 1998). Therefore, to better understand martian phosphate release and availability, we measured chlorapatite, merrillite and whitlockite dissolution rates over a range of pH values using the initial rate method and carried out solubility experiments (see Appendix II Supplementary Methods).

Fluorapatite dissolution rates and solubility were also measured to determine the relative differences in dissolution rates and equilibrium concentrations between the Mars-relevant primary phosphate minerals and fluorapatite. Although mineral dissolution rates measured in the laboratory often cannot be directly extrapolated to the field, relative differences in dissolution rates between minerals can, allowing for comparison of the rate of phosphate release during water-rock interactions in terrestrial versus martian environments.

Mineral dissolution was measured in duplicate or triplicate experiments for each mineral over a pH range of 2 to 5 in 35 individual batch experiments. Results indicate higher Ca and P release rates for chlorapatite, whitlockite and merrillite than for

fluorapatite (Fig. 5 and Supplementary Sheets S1-S35 of Appendix II). Ca: P release ratios are generally stoichiometric or close to stoichiometric in experiments (Appendix II Supplementary Sheets S1-S35). Mineral dissolution rates for individual experiments were determined through linear regression analysis of cumulative calcium release over time (Appendix II Supplementary Methods) and are compiled in Supplementary Table S6 of Appendix II.

Rate laws for each mineral were developed by applying linear regression to log dissolution rates of averaged batch experiments versus pH (Table 5 and Appendix II Supplementary Sheets S1-S35). The resulting pH dependence of mineral dissolution was fit to:

$$log\, R = log\, k_{H+} - n_{H+} pH,$$

where R is the mineral dissolution rate (in mol m^{-2} s^{-1}), k_{H+} is the intrinsic rate constant in units of mol m^{-2} s^{-1} and n_{H+} is the reaction order with respect to H+ (Table 6). To compare our results for well-studied fluorapatite with dissolution rates from the literature, our mineral dissolution rates of fluorapatite were plotted against results from previous studies (Valsami-Jones et al., 1998; Welch et al., 2002; Guidry and Mackenzie, 2003; Chaïrat et al., 2007; Harouiya et al., 2007). Our fluorapatite dissolution rates all fall within half an order of magnitude of previously published data. Our derived value of k_{H+} for the fluorapatite rate law is within error of a previously published rate law, and our value of n_{H+} is within 10% of a previously published rate law (Appendix II, Fig. S2)(Chaïrat et al., 2007).

Comparison of chlorapatite, merrillite, whitlockite and fluorapatite dissolution rates indicates that chlorapatite dissolves more rapidly than fluorapatite over the entire pH range of the experiments, and merrillite and whitlockite exhibit faster dissolution than

fluorapatite over the pH range of 2 to 4.5 (Fig. 6a), although, owing to mineral stoichiometry, P release is greater over the entire pH range for these minerals (Fig. 6b). The rapid dissolution of whitlockite and merrillite relative to fluorapatite is probably the result of significant structural differences between the two mineral types. In contrast, similar dissolution rates of whitlockite and merrillite are probably owing to the very similar mineral structures that differ mainly by the higher calcium in the merrillite used in these experiments and slight structural differences resulting from dehydrogenation of whitlockite (Appendix II Supplementary Methods). The faster dissolution of chlorapatite relative to fluorapatite may be the result of somewhat weaker bonds in chlorapatite from incorporating the larger Cl^- ion into the anion column sites of the mineral. The approximately equal dependence on pH of fluorapatite and chlorapatite dissolution is similar to that of other minerals that form solid solution series such as celestite/anglesite/barite and the olivine series (Wogelius and Walther, 1992; Dove and Czank, 1995). However, a change in structure from *P63=m* hexagonal structure (fluorapatite) to *P21=b* monoclinic structure (chlorapatite) occurs at the Cl endmember (Hughes et al., 1989) and enthalpy data suggest nonlinearity may exist along the Cl-F join (Hovis and Harlov, 2010). Nonetheless, dissolution and solubility data presented here should represent upper and lower bounds and be useful in approximating dissolution of mixed F^- and Cl^- apatites that have been observed in martian meteorites (McCubbin and Nekvasil, 2008; McCubbin et al., 2012).

Mineral dissolution rates are generally expressed in terms of moles of mineral released per unit of time (Fig. 6a); however, differences in mineral stoichiometry result in more moles of phosphate released per mole of merrillite or whitlockite than per mole of

apatite. The mineral dissolution rates and stoichiometry measured here indicate phosphate release from whitlockite and merrillite that is 1.9 to 4.8 times greater than fluorapatite over the measured pH range. Over the same pH range, phosphate release from chlorapatite ranges from 2.2 to 4.1 times higher than fluorapatite (Fig. 6b). Factoring in the approximate order of magnitude greater presence of phosphate minerals inferred from the P content of bulk Mars versus Earth (Appendix II Table S5), rates of phosphate introduction into martian environments during rock-water interactions could be >45 times that of Earth.

Solubility experiments carried out on the minerals (Table 6 and Appendix II Supplementary Methods) indicate that equilibrium concentrations of Ca and P from chlorapatite, whitlockite, and merrillite are significantly greater than from fluorapatite (Fig. 7). Solubility product constant (K_{sp}) values for fluorapatite from our experiments generally agree with previous studies (Appendix II Table S7) lending confidence to the method. The solubility experiments also allowed for calculation of dissolution rates under near-neutral conditions (pH ~7; Appendix II Supplementary Methods and Fig. S3), which indicate that phosphate release from chlorapatite, merrillite and whitlockite dissolution remain higher than from fluorapatite under neutral conditions as well as acidic (Appendix II Fig. S4). Although Earth and Mars have probably possessed both alkaline and acidic aqueous environments (Ehlmann et al., 2008), and the pH necessary for crucial prebiotic reactions is not known for either Earth or potentially Mars, it is not unlikely that prebiotic reactions that lead to abiogenesis occur in a specific pH range (for example, the abiotic synthesis of RNA requires pH buffering) (Powner et al., 2009). Therefore, under such expected similar pH environments, the greater phosphate release from the Mars-

relevant minerals relative to fluorapatite would be important in alleviating any shortage of phosphate.

The higher solubilities of Mars-relevant primary phosphate minerals and faster dissolution rates measured here suggest higher phosphate concentrations in solution and that phosphate removed from solution by prebiotic, biotic, or abiotic reactions would be replaced rapidly, effectively increasing phosphate availability in situations of rapid uptake or removal. Phosphate is but one bioessential component and the fundamental data presented here do not specifically replicate conditions in a particular martian environment. However, the faster dissolution rates of Mars-relevant dominant primary phosphate minerals, higher concentrations of phosphate minerals in the martian crust and higher final phosphate concentrations in solution from Mars-relevant phosphate minerals all suggest higher phosphate availability on Mars relative to Earth. The results suggest that the phosphate problem may be much less significant on Mars than on Earth, possibly mitigating one of the hurdles faced by potential martian abiogenesis.

Methods

Dissolution rates of synthetic chlorapatite, whitlockite, merrillite and natural fluorapatite were measured by the initial rate method in batch dissolution experiments (Rimstidt and Newcomb, 1993). This method, where a rate is determined under conditions at the onset of far-from-equilibrium batch experiments, has been demonstrated to yield results comparable to other experimental methods (Rimstidt and Newcomb, 1993). A graphical representation of the method is included as Appendix II Fig. S1. Solubility experiments were carried out in pure water using previously published

methods (Zhu et al., 2009). Detailed materials, methods, data analysis and any associated references are provided in Appendix II Supplementary Methods.

Acknowledgments

This material is based on work supported by NASA under grant no. NNX10AN23H issued through the NASA training grant National Space Grant College and Fellowship Program to Elisabeth M. Hausrath, a Nevada Space Grant Consortium fellowship to Christopher T. Adcock, Mars Fundamental Research Program grant NNX10AP58G to Elisabeth M. Hausrath and GSA research grant to Christopher T. Adcock. The authors thank A. Simon, C. Tacker, D. Harlov, K. Sefein and D. Roohani for assistance in mineral synthesis. We also express our appreciation to E. Smith, H. Sun, O. Tschauner, V. Tu, S. Gainey and B. Myers for technical assistance and discussion, which improved this paper.

Tables

Table 5. Log mineral dissolution rates and accompanying pH values.

Mineral	Initial pH	*n**	Ave. log *R* (mol m^{-2} s^{-1})
Whitlockite	2	2	-6.43
Whitlockite	3	2	-7.20
Whitlockite	4	2	-8.46
Whitlockite	5	2	-9.17
Merrillite	2	2	-6.49
Merrillite	3	2	-7.22
Merrillite	4	2	-8.20
Merrillite	5	2	-9.25
Chlorapatite	2	2	-6.27
Chlorapatite	3	2	-6.66
Chlorapatite	4	2	-8.15
Chlorapatite	5	2	-8.81
Fluorapatite	2	3	-6.64
Fluorapatite	3	3	-7.58
Fluorapatite	4	3	-8.39
Fluorapatite	5	2	-9.09

**n = number of experiments average is based on.*

Table 6. Dissolution rate constants (log k_{H+}), pH dependence (n_{H+}), and final concentrations from solubility experiments with calculated K_{sp} values.

Mineral	*Dissolution rate experiments*	
	log k_{H+} (mol m^{-2} s^{-1})	n_{H+}
Merrillite	-4.56 ±0.192	-0.92 ±0.052
Whitlockite	-4.50 ±0.274	-0.95 ±0.075
Chlorapatite	-4.28 ±0.524	-0.91 ±0.143
Fluorapatite	-5.07 ±0.138	-0.82 ±0.038

	Solubility experiments[a]			
	Ca mmol*	**P mmol***	**pH**	**Log K_{sp}**
Merrillite	0.0358 ±0.0005	0.0254 ±0.0010	6.6	-39
Whitlockite	0.0490 ±0.0008	0.0368 ±0.0014	6.8	-39
Chlorapatite	0.0466 ±0.0012	0.0226 ±0.0009	6.9	-22
Fluorapatite	0.0224 ±0.0007	0.0109 ±0.0012	6.5	-27

Range values are standard errors (dissolution) or standard deviations (solubility).
[a]Reactions: Merrillite; $Ca_{9.5}Mg(PO_4)_7 + 7H^+ = 9.5Ca^{2+} + Mg^{2+} + 7HPO_4^{2-}$,
Whitlockite; $Ca_9Mg(PO_3OH)(PO_4)_6 + 6H^+ = 9Ca^{2+} + Mg^{2+} + 7HPO_4^{2-}$,
Chlorapatite; $Ca_5(PO_4)_3Cl + 3H^+ = 5Ca^{2+} + 3HPO_4^{2-} + Cl$,
Fluorapatite; $Ca_5(PO_4)_3F + 3H^+ = 5Ca^{2+} + 3HPO_4^{2-} + F^-$.
**average of 3 analyses*

Figures

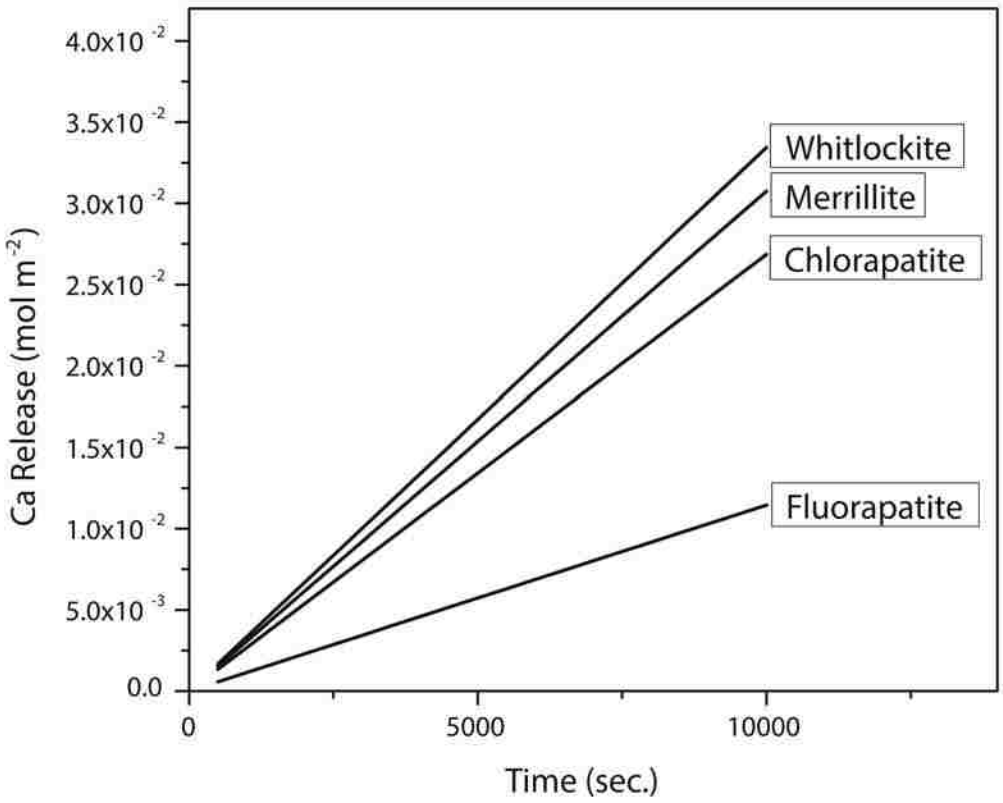

Figure 5. Calcium release over time. Initial calcium release over time (average of linear fits of duplicate or triplicate experiments) at pH 2 for chlorapatite, whitlockite, merrillite and fluorapatite. Relative release rates are representative of all pH conditions tested here, where chlorapatite, whitlockite, and merrillite all exhibit faster Ca and P release rates than fluorapatite.

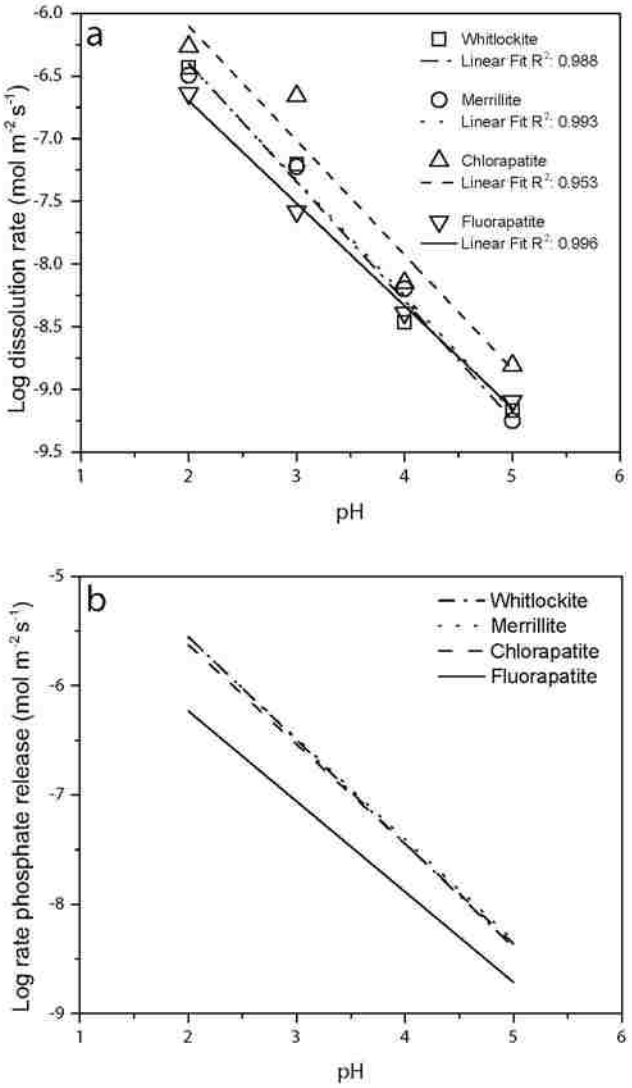

Figure 6. Mineral dissolution rates and phosphate release rates. a, Log mineral dissolution rates versus pH for whitlockite, merrillite, chlorapatite and fluorapatite. Plotted points are the average of two or more dissolution experiments (Appendix II Table S6). Lines are derived from regression analyses and represent measured rate laws. **b**, Log rates of phosphate release versus pH based on measured mineral dissolution rates and stoichiometric release. Plots show that Mars-relevant minerals chlorapatite, whitlockite and merrillite all release phosphate at significantly higher rates than fluorapatite during dissolution under these conditions.

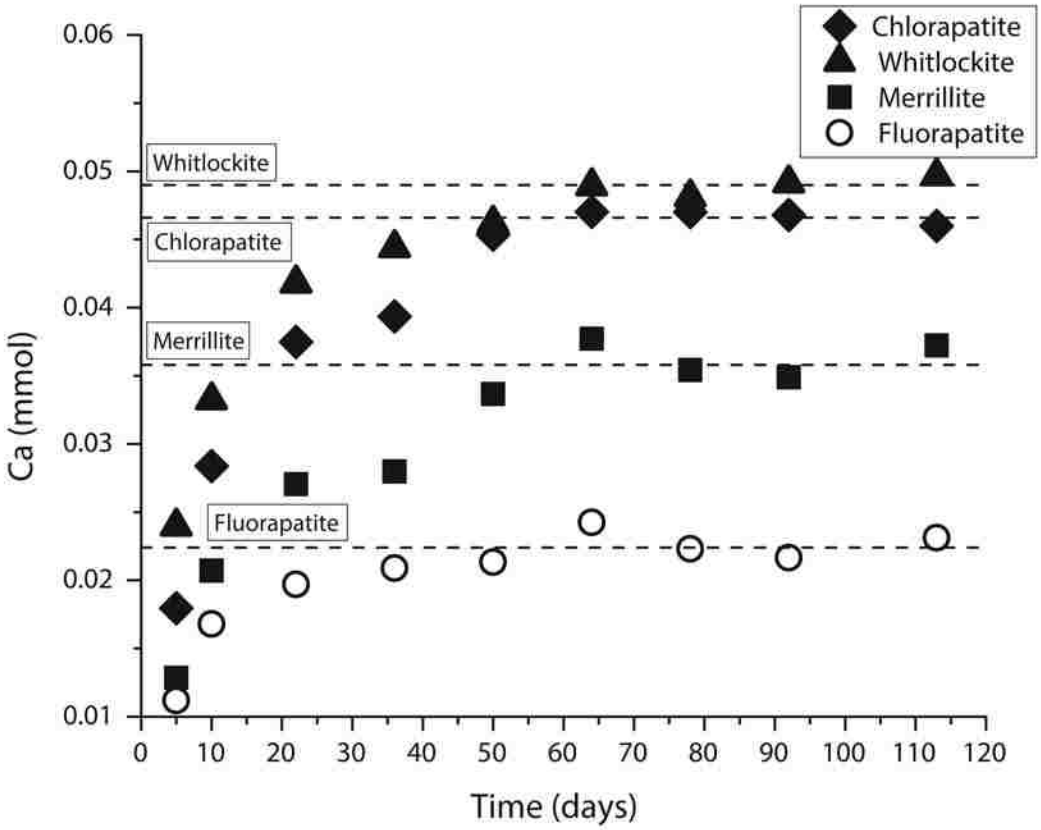

Figure 7. Calcium concentrations over time in solubility experiments. Values are averages of duplicate experiments for each mineral. Plot shows that Ca concentrations over time are higher for chlorapatite, merrillite and whitlockite, versus fluorapatite. Labeled dashed lines represent final concentrations based on three point averages. Phosphate release follows the same trends. Experiment conducted at 25 °C under neutral conditions. End pH values were 6.9, 6.6, 6.8 and 6.5 for chlorapatite, merrillite, whitlockite and fluorapatite, respectively.

CHAPTER FOUR

WEATHERING PROFILES IN HIGH-P ROCKS AT GUSEV CRATER, MARS, SUGGEST DISSOLUTION OF PHOSPHATE MINERALS INTO NEAR-NEUTRAL WATERS

Abstract

Abundant evidence indicates that significant surface and near-surface liquid water has existed on Mars in the past. Evaluating the potential for habitable environments on Mars requires an understanding of the chemical and physical conditions that prevailed in such aqueous environments. Among the geologic features that may hold evidence of past environmental conditions on Mars are dissolution profiles, such as those in the high-P bearing Wishstone class rocks. The dissolution profiles of these rocks indicate the loss of a Ca-phosphate mineral occurred during past aqueous interactions, and the high-P content of these rocks makes them of astrobiological interest because the phosphorus released from them during aqueous interactions is among the elements thought to be required for life. In this work, we used Mars mission data, laboratory-derived kinetic and thermodynamic data, and data from terrestrial analogs for Mars rocks, including our own observations of potential martian high-P analog basalts from Craters of the Moon National Monument (COTM), to model a conceptualized Wishstone class rock using the reactive transport code CrunchFlow. Our results suggest that the weathering profiles in Wishstone class rocks are consistent with dissolution of minerals from a rock containing

multiple Ca-phosphate minerals into near-neutral environments that may have been conducive to life on Mars.

Introduction

Although abundant geologic and mineralogical data indicate that Mars experienced a period of significant and regionally widespread surface and near-surface liquid water (Carr, 1996; Christensen et al., 2000; Bibring et al., 2005; Baker, 2006; Bibring et al., 2006; Clark et al., 2007; Michalski and Dobrea, 2007; Ehlmann et al., 2008; Milliken et al., 2008; Mustard et al., 2008; Murchie et al., 2009; Wray et al., 2009; Milliken et al., 2010; Grotzinger et al., 2013; Williams et al., 2013; Gainey et al., 2014), the specific characteristics of these past waters, such as pH, remain largely unknown. There is evidence of acidic aqueous interactions on Mars, such as the discovery of jarosite at Meridiani Planum (Elwood Madden et al., 2004; Klingelhöfer et al., 2004) and the stratigraphic relationship of Fe-sulfates with opaline silica in young martian deposits in the same area (Milliken et al., 2008), both indicators of a period of acidic aqueous conditions. However, at the Phoenix Lander site, soil/mineral experiments suggest more neutral or slightly alkaline conditions may have prevailed (Hecht et al., 2009) and mineralogical findings at Gale Crater by MSL also suggest a neutral pH environment at that location (Grotzinger et al., 2013). Recent work focused on Comanche rock class outcrops has suggested that the area of Columbia Hills in Gusev Crater on Mars may have experience periodic flooding of mildly acidic to near neutral waters (Ruff et al., 2014), while other studies suggest more acidic aqueous interactions in Gusev (Gellert et

al., 2004; Arvidson et al., 2006; Hurowitz et al., 2006a). It is likely that Mars possessed a diversity of aqueous environmental conditions that evolved over time.

Weathering profiles, persistence of primary minerals, and mineral alteration products of martian rocks can be indicators of the chemical and physical aqueous conditions under which they were formed, such as pH and duration of water/rock interaction (Elwood Madden et al., 2004; Klingelhöfer et al., 2004; Papike et al., 2006; Stopar et al., 2006; Olsen and Rimstidt, 2007; Hausrath et al., 2008a; Hausrath et al., 2008b; Elwood Madden et al., 2009; Hecht et al., 2009; Hausrath et al., 2011; Grotzinger et al., 2013; Hausrath and Olsen, 2013; Gainey et al., 2014). Numerical modeling is a technique which has been extensively applied to such indicators in order to quantitatively interpret past aqueous conditions which may have prevailed on Mars (Elwood Madden et al., 2004; Tosca et al., 2005; Chevrier, 2006; Zolotov and Mironenko, 2007; Hausrath et al., 2008a; McAdam et al., 2008; Schwenzer and Kring, 2008; Hausrath and Olsen, 2013). Here we apply reactive transport modeling to model dissolution profiles in Wishstone class float rocks on Mars.

Wishstone class rocks were encountered by the Mars Exploration Rover (MER) Spirit in the Columbia Hills of Gusev Crater on Mars and two rocks of the class, Wishstone and Champagne, were analyzed with the full MER Spirit science package, including Alpha Particle X-ray Spectroscopy (APXS). APXS analyses by MER Spirit of this rock class indicate a decrease in Ca and P at the rock surfaces, suggesting alteration of the rocks by mineral dissolution. Ca and P are the only elements to show appreciable loss, and Ca/ P ratios at the rock surfaces compared to Ca/ P ratios in the interior suggest that a Ca-phosphate mineral, likely apatite or merrillite, though the ratios also allow for a

secondary mineral like brushite (Hurowitz et al., 2006a; Ming et al., 2006), is the only mineral that has seen significant dissolution from the rocks during past aqueous interactions. This somewhat unusual profile may be indicative of specific aqueous conditions, shedding light on past martian weathering conditions. This rock class is of further astrobiological interest because P is a bioessential nutrient and the release of P from martian rocks has implications for past martian habitability.

Previous work has suggested Wishstone class dissolution profiles could be the result of highly acidic weathering. Hurowitz et al. (2006a), based on fluorapatite dissolution kinetics, suggested leaching driven by repeated episodic exposure to volcanically derived acidic fogs might result in the profiles measured by APXS. Gellert et al. (2004), also suggested acidic conditions based on laboratory observations of meteorites interacting with dilute acid solutions. Here, in order to investigate the aqueous conditions under which Wishstone class rocks may have weathered and released phosphate into the environment, with implications both for potentially widespread weathering conditions on Mars and for mobility of the important nutrient P on Mars, we used reactive transport modeling to quantitatively interpret Wishstone weathering profiles. We used Mars mission data, laboratory derived kinetic and thermodynamic data, and data from terrestrial analogs, including the high-P basalts at Craters of the Moon National Monument (COTM), to inform our model. Our results suggest the weathering profiles in Wishstone class rocks may indicate dissolution of phosphate minerals by near neutral waters, with important implications for past weathering conditions on Mars, as well as a better understanding of P release into aqueous martian environments.

Methods

High-P Wishstone Class Rocks

Wishstone class rocks comprise the dominant population of float rocks encountered by Spirit on the northwest flank of Husband Hill and are common among the float rocks of Cumberland Ridge (Arvidson et al., 2006; Squyres et al., 2006). Miniature Thermal Emission Spectrometer (MiniTES) classified over 95 Wishstone class rocks at Columbia Hills (Ruff et al., 2006), although only two rocks, Wishstone and Champagne, were subjected to the full MER Spirit analysis package. No source or outcrop for the rocks has been identified and, though a number of studies suggest plausible mineralogies for the class based on differing assumptions (Hurowitz et al., 2006b; McSween, 2006; McSween et al., 2006; Ming et al., 2006; McSween et al., 2008; Ming et al., 2008; Usui et al., 2008), the MER science package allowed for only limited direct mineralogy measurements by Mini-TES or by Mossbauer of Fe-containing phases. Alpha Particle X-ray Spectroscopy (APXS) of two Wishstone class rocks (i.e. Wishstone and Champagne) showed them to be typified by high P (~5% as P_2O_5), and low Cr (below detection limit) (Gellert et al., 2006; Ming et al., 2006). The P in the rocks is considered high for common basaltic rock (Ming et al., 2006; Squyres et al., 2006), though terrestrially rare phoscorite-carbonatite complex rocks are high in P, and the high-P basalt flows at Craters of the Moon National Monument in Idaho, USA, have also been suggested as plausible analogs for the martian rocks (Ming et al., 2008; Usui et al., 2008). Images from Spirit's Microscopic Imager (MI) show some angular grains present in the rocks, thus, the rocks have also been suggested as pyroclastic in origin or possibly a breccia resulting from

impact processes (Squyres et al., 2006). With these uncertainties in mind, whenever possible we chose modeling inputs that were appropriate for a plausible range of Wishstone mineralogies and formation mechanisms.

To provide additional constraints for the model inputs of a Wishstone class rock and inform other parameters of the modeling, we examined petrographic thin sections of basalts from Craters of the Moon National Monument in Idaho (COTM) by Scanning Electron Microscopy (SEM) (Appendix III supplementary information and accompanying Figs. S5-S12, and Appendix IV). These high-P-bearing basalts (up to 2.9 wt% as P_2O_5) (Kuntz et al., 1992) have been suggested as analogs to high-P rocks on Mars such as Wishstone class (Usui et al., 2008). Insights gained from investigating COTM rocks were used in conjunction with other data to inform the model on secondary minerals, porosity, and specific surface areas of minerals as discussed below (detailed methods and results of COTM observations are contained in Appendix III supplementary information, and Appendix IV).

Model inputs for mineralogy of a conceptualized Wishstone class rock were based on CIPW norm calculations of McSween et al. (2006) from MER Spirit APXS which included information from Mossbauer measurements (Table 7). To simplify the model, minerals present in the CIPW norm calculations at less than 5 wt% were not incorporated into the model, ilmenite and magnetite were combined into a single mineral, and feldspars were also input as a single mineral with an intermediate composition (An_{25}).

Analyses by APXS of an "as is" surface, brushed surfaces, and Rock Abrasion Tool (RAT) treated surfaces of Wishstone class rocks indicated less Ca and P in the surface of the rocks than the interior (Gellert et al., 2006; Brückner et al., 2008) (Table

8). Ratios of Ca and P between rock surfaces and interiors are consistent with the loss of a Ca-phosphate mineral and suggest a Ca-phosphate mineral as the only mineral substantially lost from the rocks due to alteration (Hurowitz et al., 2006a; Ming et al., 2006). Martian meteorite data indicate that the dominant primary phosphate minerals on Mars are Cl-apatite and merrillite (McSween and Treiman, 1998), often found coexisting in martian meteorites, although fluorapatite (the dominate primary phosphate mineral on Earth) also occurs in some martian meteorites with chlorapatite (McCubbin and Nekvasil, 2008). Ca/ P ratio differences in APSX analyses are also reasonably consistent with apatite and merrillite. We therefore configured models with merrillite, chlorapatite, and fluorapatite each as the only Ca-P-bearing mineral, as well as models that included both chlorapatite and merrillite within the model.

The Ca/ P ratios in APXS data of Wishstone class rocks are also reasonably consistent with brushite, a secondary phosphate mineral (Hurowitz et al., 2006a). Because brushite is a secondary mineral and observations of Wishstone class rocks suggests them be less altered than other Columbia Hills materials, brushite is not favored as the source of P in Wishstone class (Ming et al., 2006). Thus, brushite has not been considered in CIPW mineralogy norms of Wishstone class rocks or other petrologic interpretations of the rocks (Gellert et al., 2004; McSween et al., 2006; Ming et al., 2006; McSween et al., 2008; Ming et al., 2008; Usui et al., 2008). The mineral is also rare on Earth and has not been detected in either martian meteorites or on Mars. The presence of brushite in Wishstone class rocks as more than an alteration product in the near surface, would limit Wishstone class petrogenesis to sedimentary or impact breccias derived from a very brushite rich (10 wt %+) source area, or a secondary process that generated

brushite within the rocks while preserving other primary minerals, scenarios that seem unlikely. For this reason, brushite dissolution is not considered further in this paper.

A fit of MiniTES data indicate up to 10% basalt glass may be present in Wishstone class rocks along with 10% phosphate minerals (Ruff et al., 2006). Phosphate is incompatible and can be concentrated in basalt glasses. Thus, a high-P basalt glass could be a Ca-P-containing phase within Wishstone class rocks along with another Ca-phosphate mineral (or multiple Ca-phosphate minerals). Glass kinetics and thermodynamics vary significantly as a function of glass composition, which itself is highly variable (Hamilton, 1999; Wolff-Boenisch et al., 2004). Thus, a Wishstone glass could be the phase dissolving from the rocks, or be a resistant phase which accounts for the P concentration on brushed surfaces analyzed by APXS. However, the 10% phosphate minerals in the MiniTES fit would account for nearly all of the P measured by APXS in Wishstone class. Further, if a glass does play a significant role in the measured profiles of Wishstone class, the Ca/ P ratio in the glass would have to roughly match that of a Ca-phosphate mineral and the P concentrations would have to be very high (as much as 25 wt% P_2O_5 in the glass to account for the dissolving phase or a resistant phase contributing to the higher P concentrations within the rock). In addition, if the glass is the dissolving component, any remaining chemistry outside of the Ca and P in the glass would have to be consistent with the bulk rock to produce the profiles measured in Wishstone class by APXS. For these reasons we did not include a glass component in finalized models. The possibility of a glass within Wishstone class as one of the P-bearing phases is, however, still plausible.

Since Wishstone class rocks have been previously suggested to be impact breccias, pyroclastics, or extrusive igneous rocks (Arvidson et al., 2006; Squyres et al., 2006), initial porosity values were set to 5% based on image analysis of COTM basalt (Appendix III supplementary information), and data for volcanic breccias (Rejeki et al., 2005; Benning, 2008), tuffs (Keller, 1960; Rejeki et al., 2005), terrestrial basalts (Davis, 1969; Freeze and Cherry, 1977; Sato et al., 1997; Rejeki et al., 2005), lunar basalts (Kiefer et al., 2012; Macke et al., 2012), and brecciated basalt or fractured basalt (Freeze and Cherry, 1977) (Table 9). We varied porosity from 3% to 10% in early modeling and found that porosity variations alone did not significantly change the relative dissolution depths of minerals.

Tortuosity (T) is a measure of the complexity of permeable paths within rocks. Though it can be calculated in a number of ways, in the modeling code used in this study (Crunchflow, discussed below) the value is equivalent to:

$$T = \frac{D_e}{D_w},$$

where D_e is the effective diffusion coefficient and D_w is the coefficient in pure water (Steefel, 2008; Steefel, 2009). Values derived from experimental data on both basalt and volcanic breccias range from 5.76×10^{-3} to 3.56×10^{-6} (Sato et al., 1997; Benning, 2008). We chose an intermediate value of 1×10^{-4}. Varying the tortuosity over 2 orders of magnitude in preliminary models changed the absolute depths of the reaction fronts but did not change the relative positions of the reaction fronts.

Mineral dissolution rates and solubilities were sourced from the literature (Table 10). In order to account for Al immobility, a generalized Al-bearing amorphous-like phase based on kaolinite/halloysite kinetics and thermodynamics was allowed to

precipitate in the models (Table 10). This phase is not listed in Table 7 because it is a precipitate rather than an initial component in the rock. Phosphate was also allowed to sorb to mineral surfaces in the model, after Dzombak and Morel, (1990). Solubility values for Ca-phosphate minerals were varied by +/- 2 orders of magnitude, based on variations in measured solubilities for fluorapatite in the literature (+/- 5 orders of magnitude, Oelkers et al., 2009). This variation showed some change in the overall depth of dissolution of Ca-phosphate minerals in preliminary modeling profiles, suggesting a component of diffusion-limited dissolution exists in the models (see Appendix III Figs. S13 and S14 for a general description of model output profiles and the effects of solubility on Ca-phosphate minerals respectively). Finalized models were run with measured values (Adcock et al., 2013).

Mineral dissolution rates are generally normalized to mineral surface areas. To estimate mineral surface areas for this study, grain size measurements taken from the COTM Kimama lava flow thin sections were used to derive grain diameters for the minerals ilmenite, plagioclase, and fluorapatite (Appendix III supplementary information). Kimama does not contain appreciable pyroxene, however, pyroxenes and plagioclase in both Blue Dragon and Minidoka COTM basalts are roughly the same size, so we assumed pyroxene grain sizes to be similar to plagioclase for modeling. We also assumed merrillite and chlorapatite grain sizes to be similar to fluorapatite in Kimama thin sections. The relative grain sizes followed feldspar ~ pyroxene > ilmenite > Ca-phosphate mineral. The geometric (A_{geo}) specific surface area (SSA) was then determined for the minerals using:

$$A_{geo} = \frac{6V_m}{W_m D},$$

where V_m is the molar volume in $m^3\ mol^{-1}$, W_m is the molar mass in $g\ mol^{-1}$, and D is the grain diameter in meters (Rimstidt et al., 2012). Most laboratory-derived dissolution rates (including those used as inputs in this study) normalize dissolution rates to surface areas determined by gas sorption using the Brunauer, Emmett, and Teller method (BET) (Brunauer et al., 1938). The relationship between gas sorption-measured surface areas and geometrically calculated surface areas (the roughness) is expressed as:

$$\lambda = \frac{A_{BET}}{A_{geo}},$$

where λ is a unit-less roughness coefficient, A_{BET} is the specific surface area as measured by BET in $m^2\ g^{-1}$, and A_{geo} is the geometrically calculated specific surface area also in units of $m^2\ g^{-1}$. Geometric SSA's calculated for minerals were multiplied by roughness coefficient values from the literature (White et al., 1994; Brantley and Mellott, 2000; Adcock et al., 2013) to approximate BET SSAs. The mineral surface area that interacts with aqueous solutions (i.e. the total reactive surface area) is considered the largest source of uncertainty in field calculations of mineral dissolution rates (White, 2002). Previous research has shown that the mineral surface actually in contact with weathering fluids during rock/water interactions may only be 0.1 to 10% of the measurable mineral surface area (Velbel, 1993). In order to approximate this effect in our modeling, we chose an intermediate value of 5% and applied it to our mineral surface area, shown in Table 10. Varying the surface areas over 2 orders of magnitude did not change the relative positions of reaction fronts in model output.

During chemical weathering, some component of surface retreat is expected as porosity develops to a point where the rock is no longer competent. CrunchFlow is capable of incorporating surface retreat or erosion at a specific rate, however there is no

current option for surface retreat based on porosity due to chemical weathering. Based on observed maximum total porosities for altered or fractured basalt (Freeze and Cherry, 1977; Sak et al., 2004; Navarre-Sitchler et al., 2009) and typical porosities of unconsolidated sediments (Davis, 1969; Freeze and Cherry, 1977), we considered 50% porosity as a reasonable threshold for surface retreat in our models, and applied the surface retreat component into results after modeling. We also considered physical erosion beyond that associated with surface retreat from chemical weathering based on the observation that many of the rocks at Gusev Crater are ventifacts and Wishstone itself has rounded edges, some faceting, and streaking of RAT surfaces (Greeley et al., 2006)(Appendix III Figs. S15 and S16).

Reactive Transport Modeling

The dissolution profiles that form in rocks, including Wishstone class rocks, are the result of a combination of chemical (e.g. mineral kinetics, thermodynamics, solution pH) and physical (e.g. reactive surface area, porosity, tortuosity, mineralogy) conditions at work during water/rock interactions. Reactive transport modeling is a tool that can incorporate the effects of multiple chemical and physical parameters during aqueous interactions, produce dissolution profiles in model space (see Appendix III Fig. S13 as an example), and constrain the conditions under which specific dissolution profiles may form, such as those observed in Wishstone class rocks.

Modeling in this study was conducted using the reactive transport code CrunchFlow written by Carl Steefel (Steefel, 2010). The code allows for a global implicit reactive transport modeling approach (GIMRT) in which transport and

multicomponent reactions are simultaneously solved (Steefel and Lasaga, 1994; Steefel and MacQuarrie, 1996; Steefel, 2009). CrunchFlow has been used in a number of previous water/rock interaction studies, including those applied to Mars (Giambalvo et al., 2002; Knauss et al., 2005; Maher et al., 2006; Hausrath et al., 2008a; Dontsova, 2009; Maher et al., 2009; Navarre-Sitchler et al., 2011; Shen et al., 2011; Beisman et al., 2013; Hausrath and Olsen, 2013).

In order to investigate the solution which interacted with high-P rocks on Mars, we constructed a model using CrunchFlow with the conceptualized Wishstone class rock in contact with waters of variable pH on the martian surface. The water contacting the rock during rock-water interactions was modeled as a low ionic strength solution with the initial pH adjusted for each corresponding model over a range of 2 to 8. Partial pressures for oxygen and CO_2 were set to present day martian atmospheric pressures. Solution temperature was set to 1 °C.

Models were conceptualized as a column of 150 cells of 50 μm depth representing the rock Wishstone from surface to interior, and were run for up to 100,000 years of water-rock interaction. Models included a Dirichlet boundary for aqueous and gaseous species at the interaction surface. Total surface area is calculated by CrunchFlow using a shrinking sphere model (Levenspiel, 1972; Lasaga, 1998), and all parameters (surface area, mineral volumes, surface area, porosity and others) are updated by CrunchFlow at the end of each time iteration.

Results and Discussion

Understanding the persistence and characteristics of liquid water is important in assessing the habitability of Mars. Weathering profiles that develop within rocks during rock/water-interactions can be indicators of the aqueous conditions under which they were formed. Profiles in martian Wishstone class rocks, which indicate dissolution mainly restricted to Ca-phosphate mineralogy (Hurowitz et al., 2006a; Ming et al., 2006) are of particular interest. Not only are these somewhat unusual profiles likely indicative of specific past martian aqueous conditions, but phosphate is a required nutrient for all known life and phosphorus (as phosphate or a more reduced species such as phosphite) was likely required for the origin of terrestrial life (Westheimer, 1987; Schwartz, 2006; Powner et al., 2009; Pasek and Kee, 2011). Thus the profiles in Wishstone rocks could not only yield insight into alteration under martian conditions, but also the characteristics of release of a nutrient essential for both the origin and persistence of life.

In previous studies the profiles of Wishstone rocks have been suggested to be the result of acidic chemical weathering, possibly by volcanically derived acid fogs, based either on kinetic values for fluorapatite dissolution or the observation of apatite dissolution from meteorites by dilute acids in the laboratory (Gellert et al., 2004; Hurowitz et al., 2006a). The use of reactive transport modeling allows the consideration of multiple factors affecting mineral dissolution, including kinetics, thermodynamics, porosity, tortuosity, and specific surface area, both simultaneously and quantitatively.

Model output from CrunchFlow is generated at user-defined modeling times (e.g. at 100,000 years of modeling) and includes modeled values correlated with cells (i.e. depths in this study) of bulk chemistry, mineralogy, surface area, and porosity within the

conceptualized rock, as well as gas concentrations, pore-water chemistry, pH, and the saturation state of solution. Because the output data are correlated with cell values (i.e. depths into the modeled rock), they can be easy plotted as a function of depth. Mineral volume output data plotted against cell depth, for example, represents modeled mineral dissolution profiles within a rock from the original "surface" of the rock down to unaltered (or less altered) “corestone”. These model generated profiles can be compared to APXS data of Wishstone on Mars, as well as analyzed using knowledge obtained from terrestrial weathering profiles. In such plots mineral dissolution front depths are represented by curves in mineral volume fraction lines (see Appendix III Fig. S13).

Model outputs in this study showed a number of overall trends consistent with the kinetic and thermodynamic properties of the modeled mineralogy of Wishstone class. For instance, in all modeled profiles, the trend of overall deeper dissolution of minerals with decreasing pH from neutral to acidic is present (Fig. 8 and Appendix III Figs. S17 to S20). This is consistent with the kinetics and thermodynamics of the minerals used in the models which all tend toward faster dissolution rates and higher solubilities with decreasing pH. The depth of 50% developed porosity in models, our threshold for surface retreat due to chemical weathering, follows the same trend of increasing depth with more acidic pH values (Fig. 8).

Similarly, comparing models containing different Ca-phosphate minerals (merrillite, fluorapatite, and chlorapatite), the relative dissolution depth results between the three primary Ca-phosphate phases are in agreement with laboratory-measured dissolution rates and solubilities of the minerals (Table 10)(Adcock et al., 2013). In all pH cases modeled, fluorapatite shows the shallowest dissolution of the three Ca-

phosphate minerals (Fig. 9 and Appendix III Figs. S17-S19). Chlorapatite shows the deepest dissolution fronts of the Ca-phosphate minerals at a given pH, and merrillite is intermediate between chlorapatite and fluorapatite (Fig. 9), although in pH 7 and 8 models, merrillite and fluorapatite dissolution fronts are somewhat similar (Appendix III Figs. S17 and S19). For chlorapatite- and merrillite-bearing models, the Ca-phosphate mineral dissolution depth exceeded the depth of the chemical weathering surface retreat in all but the pH 2 models. In the pH = 2 models, the surface retreat due to enhanced porosity (> 50%) is deeper than the loss of merrillite and matched the depth of chlorapatite dissolution. Fluorapatite-bearing models showed the same trend, however, surface retreat from chemical weathering also exceeded fluorapatite mineral dissolution depth at pH 3. Models containing two Ca-phosphate minerals (i.e. chlorapatite + merrillite) showed the same overall trends as single Ca-phosphate mineral models, with dissolution depth of a particular Ca-phosphate mineral, at a given pH and modeling time, generally matching that of the same Ca-phosphate in the single phosphate mineral models.

All models (including models with two Ca-phosphate minerals) showed significant plagioclase dissolution, beyond the surface retreat from chemical weathering, over the entire pH range with fronts being deep but also relatively gradual in shape (Appendix III Figs. S17- S20). Comparatively sharp ilmenite dissolution fronts were also apparent over the entire pH range, but generally shallow in depth at pH 5 or higher. With the exception of pH 2, the depth of estimated surface retreat from chemical weathering exceeded or coincided with the dissolution front depth for illmenite, effectively removing the fronts from the overall dissolution profiles in the rock. Hypersthene showed no

significant dissolution except in models with pH <5, and in all models the surface retreat due to developed porosity exceeded any significant hypersthene dissolution (Appendix III Figs. S17-S20).

In chlorapatite models run at pH > 3 and merrillite at pH 5-6, the Ca-phosphate minerals show the most significant dissolution with depth and were completely dissolved from the rock before any other mineral. The significant plagioclase dissolution is accompanied by precipitation of the secondary Al-bearing phase at all but pH 2 and 8. This plagioclase dissolution behavior is not inconsistent with terrestrial observations of natural systems where plagioclase has been observed to be the first mineral to dissolve from rocks or exhibit relatively rapid dissolution suggesting solubility as well as kinetics may play an important role in controlling mineral weathering (White, 2008; Brantley and White, 2009; Maher et al., 2009; Navarre-Sitchler et al., 2009; Navarre-Sitchler et al., 2011). Therefore, in low-porosity rocks such as these, and others on Mars, significant dissolution of plagioclase is consistent with what we would expect from interaction of rock surfaces with liquid water.

In addition to surface retreat assumed to occur due to porosity developed from chemical weathering, additional surface erosion is also likely. Many profiles on Earth and Mars show a significant component of physical surface erosion has occurred to modify profiles (Hausrath et al., 2008a). A number of rocks at Gusev crater are fluted or faceted ventifacts or show signs of physical weathering (Greeley et al., 2006; Greeley et al., 2008), including Wishstone which shows some evidence of both faceting and rounded edges (Appendix III Fig. S15). Further, RATed surfaces on Wishstone also showed "streaking" (Greeley et al., 2008) which is an indicator of present day physical abrasion

or weathering (Appendix III Fig. S16). Thus ongoing physical erosion, in addition to surface retreat due to chemical weathering, is expected for Wishstone class rocks.

Incorporating an additional component of physical erosion could yield modeled profiles consistent with the partial loss of Ca and P from the profiles measured by APXS for models containing chlorapatite or merrillite at pH 4-7 (see Fig. 10). Though some dissolution of plagioclase exceeds or matches that of the merrillite and chlorapatite at these pH values, the presence of the secondary phase could potentially mask plagioclase dissolution from elemental-only analytical techniques such as APXS. Figure 10 includes a τ plot of Al content normalized to Ti that shows Al concentrations remain relatively stable despite the plagioclase dissolution. This is also the case for other elements including Si, indicating that even in profiles with significant plagioclase dissolution, APXS data might detect only dissolution of a Ca- and P-containing mineral. However, because of the very similar brushed concentrations of P measured by APXS at the surfaces of both Wishstone and Champagne (Wishstone = 2.64 wt% and Champagne = 2.63 wt% as P_2O_5, both of which represent ~ 50 % of the P_2O_5 measured at depth) (Table 8), in models that contained a single Ca-phosphate mineral, physical erosion fronts would have to precisely intercept the Ca-phosphate reaction fronts in both Wishstone and Champagne rocks at the same point, a scenario that seems unlikely (Fig. 10). In contrast, in models with multiple Ca-phosphate minerals, as would be expected from martian meteorite observations which commonly have a mixture of apatite and merrillite or possibly mixture of chlorapatite and fluorapatite (McSween and Treiman, 1998; McCubbin and Nekvasil, 2008), a range of physical erosion depths could yield similar concentrations measured by APXS if only one Ca-phosphate mineral were fully dissolved

from the rock at the brushed/eroded surface, but both minerals were present in the interior at the RATed depth 3mm+ deeper. This scenario is diagramed in Figure 11 with merrillite and chlorapatite and the accompanying τ plot. Chlorapatite + merrillite models run at initial pH values of 4 to 7 produce profiles that fit this scenario. However, the greatest separation between the two phosphate mineral fronts, and thus the most available leeway for variation in physical erosion depth between rocks while still possessing profiles consistent with APXS measurements, occurs at pH 6 (Appendix III Table S9). Thus, for chlorapatite + merrillite bearing models, profiles produced under pH 6 conditions are the most plausibly consistent with Wishstone as measured by APXS.

While reactive transport models such as those used in this study are numerical approximations that by necessity contain assumptions and simplification, and different assumptions or input might yield different results, the models presented here reasonably approximate dissolution in Wishstone-type rocks on Mars with the available data. The models of this study suggest the dissolution profiles in Wishstone class rocks are best explained if Wishstone class rocks contain more than one Ca-phosphate mineral, a likely scenario based on martian meteorites (McSween and Treiman, 1998; McCubbin and Nekvasil, 2008). Further, the modeled profiles here suggest that the profiles measured by APXS indicate alteration of Wishstone class rocks by mildly acidic to neutral waters, with pH 6 models allowing the best fit. These conditions are consistent with resent research that indicates mildly acidic to near neutral (pH 5-6) waters may have been episodically present in Gusev Crater at Columbia hills in the form of an ephemeral lake, based on observations and modeling applied to Comanche rocks in the Columbia hills (Ruff et al., 2014).

Though the pH conditions most favorable to life are not conclusively known, certain potentially prebiotic reactions and the stability of some bio-molecules are favored under more neutral rather than acidic conditions (Lindahl, 1993; Madigan et al., 2000; Knoll et al., 2005; Powner et al., 2009). The modeling results in this study suggest that more neutral aqueous conditions may have prevailed at some point in the past at Gusev Crater, rather than more acidic conditions such as wide-spread acid vapor alteration (Settle, 1979; Banin et al., 1997; Tosca et al., 2004; Golden et al., 2005; Hurowitz et al., 2006a; Yen et al., 2008; Hausrath et al., 2013). These results are in agreement with recent observation and modeling of other rocks in Gusev Crater (Ruff et al., 2014), with positive implications for past martian habitability.

Conclusions

Weathering profiles can be used as indicators of past aqueous conditions, preserving characteristics such as the duration of liquid water, pH, temperature, and other factors. In Wishstone class rocks on Mars, profiles measured by MER Spirit APXS suggest the loss of a Ca-phosphate mineral has occurred during past aqueous interactions. These profiles have previously been suggested as an indicator of chemical weathering by highly acidic fogs or possibly dilute acidic waters. In this study, models which contained multiple Ca-phosphate minerals, initial pH values of 4-7, and a component of physical erosion produced profiles similar to those apparent in Wishstone class rocks on Mars, with pH 6 models being the most consistent with the APSX-measured data. These modeling results suggest that past environmental conditions at Gusev Crater may have included aqueous dissolution into mildly acidic to neutral conditions.

Though the exact range of required conditions under which life can originate are unknown, certain potentially prebiotic reactions and the stability of some bio-molecules are favored under more neutral conditions (Lindahl, 1993; Madigan et al., 2000; Knoll et al., 2005; Powner et al., 2009). In addition, phosphate is a bioessential nutrient and phosphorus, either as phosphate or a more reduced species such as phosphite, is considered crucial in pre-biotic reactions that may have led to the origin of life on Earth. The results of this study, which indicate the possible dissolution of phosphate minerals by near neutral waters on Mars, therefore have positive implications for potentially habitable environments on Mars.

Acknowledgements

This research is based on work supported by a Mars Fundamental Research Program grant no. NNX10AP58G to E. Hausrath. Additional support was provided from a Nevada Space Grant Consortium fellowship and GSA research grant to C. Adcock. The authors thank A. Simon, E. Smith, H. Sun, P. Forster, O. Tschauner, V. Tu, S. Gainey, and M. Steiner for assistance related to this work.

Tables

Table 7. Mineralogy and volume fraction used in model.

Mineral	McSween et al. 2006 Wt. %	This study Wt%**	Mineral Volume Fraction	Mineral Volume Fraction with 5% porosity
Feldspars*	57.6	59.3	0.679	0.646
Albite	42.9			
Anorthite	10.4			
Orthoclase	3.4			
Illmenite	5.0	14.0	0.089	0.084
Corundum	2.4			
Magnetite	7.6			
Hypersthene (OPX)	13.5	13.9	0.109	0.103
Ca-phosphate mineral	12.5	12.9	0.123	0.117
Olivine	1.9			
Porosity				0.05
Totals	99.6	100	1	1

**Total Feldspars (Feldspars were combined into a single mineral of representative composition)*
***Minerals comprising <5 wt.% were not included in the model. Ilmenite and magnetite were combined into a single mineral "Ilmenite". Wt% values were then renormalized to 100% before mineral volume fractions were calculated.*

Table 8. APXS Ca and P analyses of Wishstone and Champagne on Mars.

	Champagne					Wishstone				
	Depth	Oxide wt. %		Elemental wt. %		Depth	Oxide wt. %		Elemental wt. %	
	(mm)	CaO	P_2O_5	Ca	P	(mm)	CaO	P_2O_5	Ca	P
Surface	0.00	6.67	1.79	4.77	0.78	-	-	-	-	-
Brushed	0.00	6.59	2.64	4.71	1.15	0.00	6.86	2.63	4.90	1.15
RAT 1*	-	8.78	5.07	6.28	2.21	3.18	8.89	5.19	6.35	2.26
RAT 2	3.95	8.75	5.05	6.25	2.20	-	-	-	-	-
Loss		2.16	2.41	1.54	1.05		2.03	2.56	1.45	1.12

**Champagne received two RAT operations and analyses (included in table). No depth has been reported for Champagne RAT 1. Only one RAT operation was performed on Wishstone.*

Table 9. Porosities of basalts, tuff and breccias relevant to Wishstone.

Rock Type	Porosity (%)	Reference
Terrestrial Welded Tuff	5-14	Keller, 1960; Rejeki et al., 2005
Terrestrial Basalt	0.1-11.4	Davis, 1969; Freeze and Cherry, 1977; Sato et al., 1990; Rejeki et al., 2005
Craters of The Moon Basalts	0.1 -7.5	This study.
Lunar Basalt	2-11	Macke et al., 2012
Brecciated Basalt	10	Freeze and Cherry, 1977
Volcanic Breccia	4-19	Rejeki et al., 2005; Benning, 2008
Lunar Impact/Regolith Breccia	5-12	Macke et al., 2012

Table 10. Thermodynamic data, kinetic data, and specific surface areas used in modeling

Mineral	Reaction Stoichiometry	Log K (298 K)	Log k_{H+}	n_{H+}	Log_{OH-}	n_{OH-}	Ea (kcal/mol)	Surface Area ($m^2 g^{-1}$)
Plagioclase (An_{25})	$Ca_{0.25}Na_{0.75}Al_{1.25}Si_{2.75}O_8 + 5H^+ = 1.25Al^{3+} + 0.75Na^+ + 0.25Ca^{2+} + 2.75SiO_2 + 2.5H_2O$	8.17[a]	-9.22[f]	0.408[f]	-9.24[f]	0.38[f]	14.8425[d]	7.66×10^{-3}
Hypersthene	$FeMgSi_2O_6 + 4\ H^+ = + Mg^{2+} + Fe^{2+} + 2SiO_2 + 2H_2O$	11.3269[b]	-9.02[d]	0.6[d]	-12.72[d]	0.00[d]	19.11132[d]	6.07×10^{-3}
Ilmenite	$FeTiO_3 + 2H^+ + H_2O = Fe^{2+} + Ti(OH)_4$	0.9046[b]	-8.35[d]	0.421[d]	-11.16[d]	0.00[d]	9.053989[d]	9.44×10^{-3}
Phosphate mineral								
Merrillite	$Ca_{9.5}Mg(PO_4)_7 + 7H^+ = 9.5Ca^{2+} + Mg^{2+} + 7HPO4^{2-}$	-39.1[c]	-4.56[c]	0.924[c]				3.10×10^{-3}
Chlorapatite	$Ca_5(PO_4)_3Cl + 3H^+ = 5Ca^{2+} + 3HPO_4^{2-} + Cl^-$	-21.3[c]	-4.28[c]	0.912[c]			11[e]	3.85×10^{-3}
Fluorapatite	$Ca_5(PO_4)_3F + 3H^+ = 5Ca^{2+} + 3HPO_4^{2-} + F^-$	-26.5[c]	-5.07[c]	0.817[c]			11[e]	4.89×10^{-3}
Brushite	$CaHPO_4 \cdot 2(H_2O) = Ca2+ + HPO_4^{2-} + 2H_2O$	6.55[b]	-4.14	0.541[g]			3.8[h]	3.10×10^{-3}
Secondary phase	$Al_2Si_2O_5(OH)_4 + 6H+ = 2Al^{3+} + 2SiO_2 + 5H_2O$	12.55[i]	-13.2[j]	0.55[j]	-15.4[j]	0.00[j]	15.0	7.66×10^{-3}

[a] *Based on work by Maher et al. (2009) for An_{25}.*
[b] *Lawrence Livermore National Laboratory thermochemical modeling database (Thermo.com.V8.R6.230) (Delany and Lundeen, 1990; Johnson et al., 2000).*
[c] *Adcock et al., (2013).*
[d] *Palandri and Kharaka (2004) from compiled mineral data by Schott and Berner (1985) and White et al. (1994) .*
[e] *Harouiya et al. (2007).*
[f] *Plagioclase kinetics derived based on data compiled by Bandstra and Brantley (2008) from multiple sources of dissolution rates for albite and anorthite (i.e. Chou and Wollast, 1984; Knauss and Wolery, 1986; Holdren and Speyer, 1987; Casey et al., 1991; Rose, 1991; Amrhein and Suarez, 1992; Stillings and Brantley, 1995; Hodson, 2003) and data on the non-linear relationship between Ca and Na content and dissolution rates from Blum and Stillings (1995).*
[g] *Estimated value based on the kaolinite Ksp from Maher et al. (2009) increased 4 orders of magnitude to approximate a precursor phases like halloysite (Steefel and Van Cappellen, 1990; Yang and Steefel, 2008)*
[h] *Based on kaolinite dissolution kinetics of Huertas et al. (1999) for proton promoted and neutral range dissolution slowed 1 order of magnitude to account for slower precipitation kinetics based on Yang and Steefel (2008)*

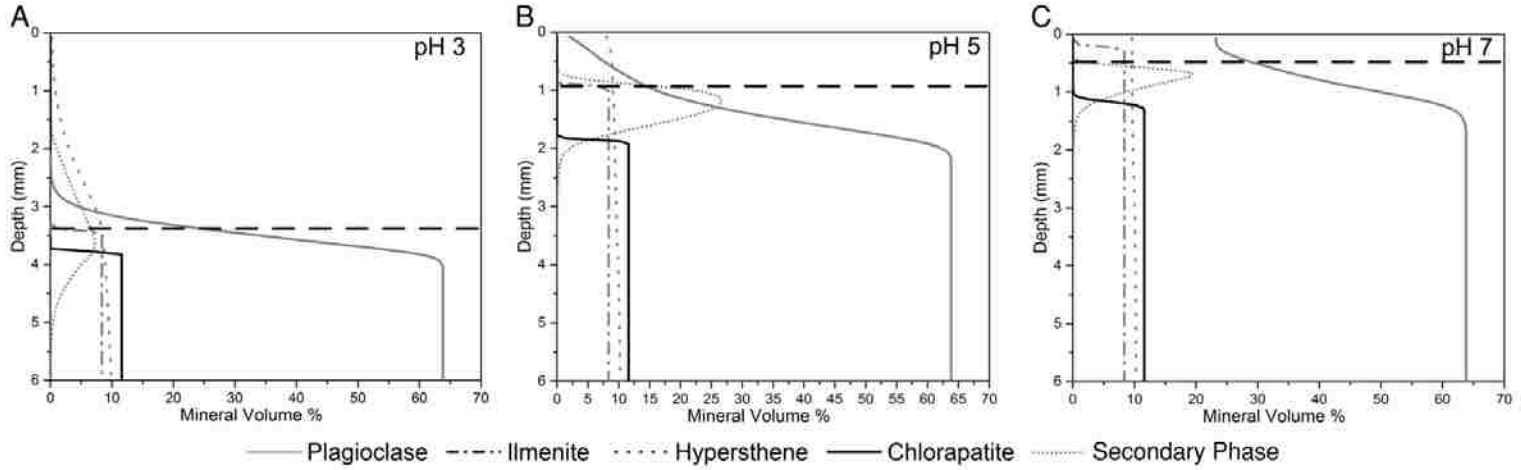

Figure 8. Modeled dissolution profiles (100 k.y. models at pH values of 3, 5 and 7) of a Wishstone-type rock containing chlorapatite as the Ca-phosphate mineral. Dashed horizontal lines represent estimated surface retreat due to chemical and physical weathering of the rocks based on 50% porosity. The overall trend of deeper dissolution of minerals with decreasing pH is consistent with the thermodynamics and kinetics of the minerals in the modeled rock. Dissolution profiles of the non-phosphate minerals at a given modeled pH were similar in all models regardless of the Ca-phosphate mineral used in the modeled rock.

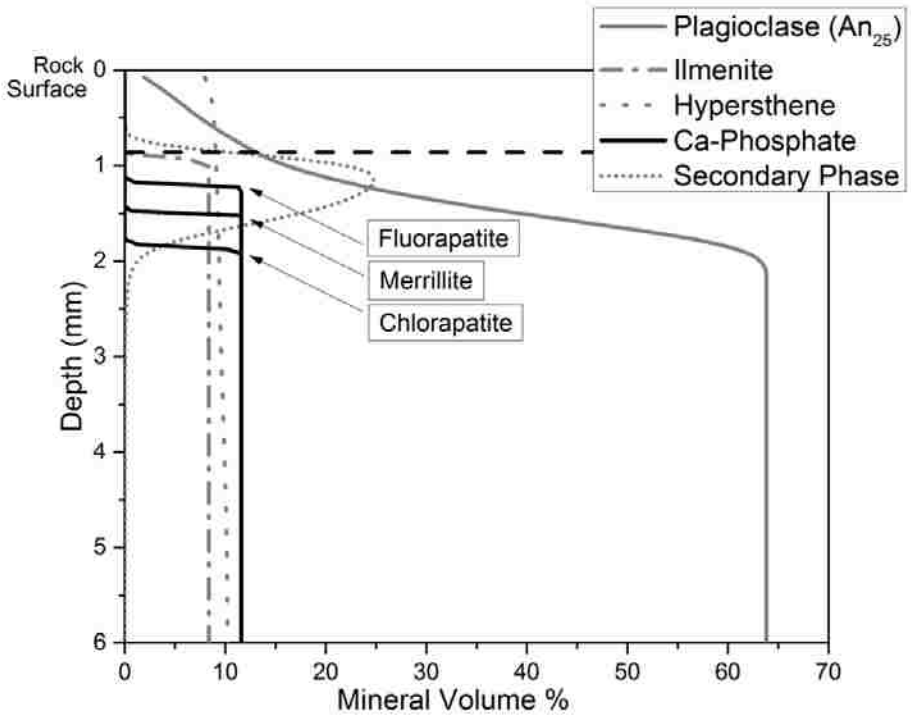

Figure 9. Comparison of different modeled Ca-phosphate minerals weathering at pH 6 with 100 k.y. of model time. Dashed horizontal line represents surface retreat of the rocks based on 50% porosity Dissolution profiles for minerals other than the Ca-phosphate and depth of surface retreat do not significantly change between models, thus only those from the chlorapatite model are shown. Figure shows chlorapatite dissolution to the greatest depth and fluorapatite to the shallowest, with merrillite in between. This is consistent with thermodynamic and kinetic data for these minerals (Adcock et al., 2013)

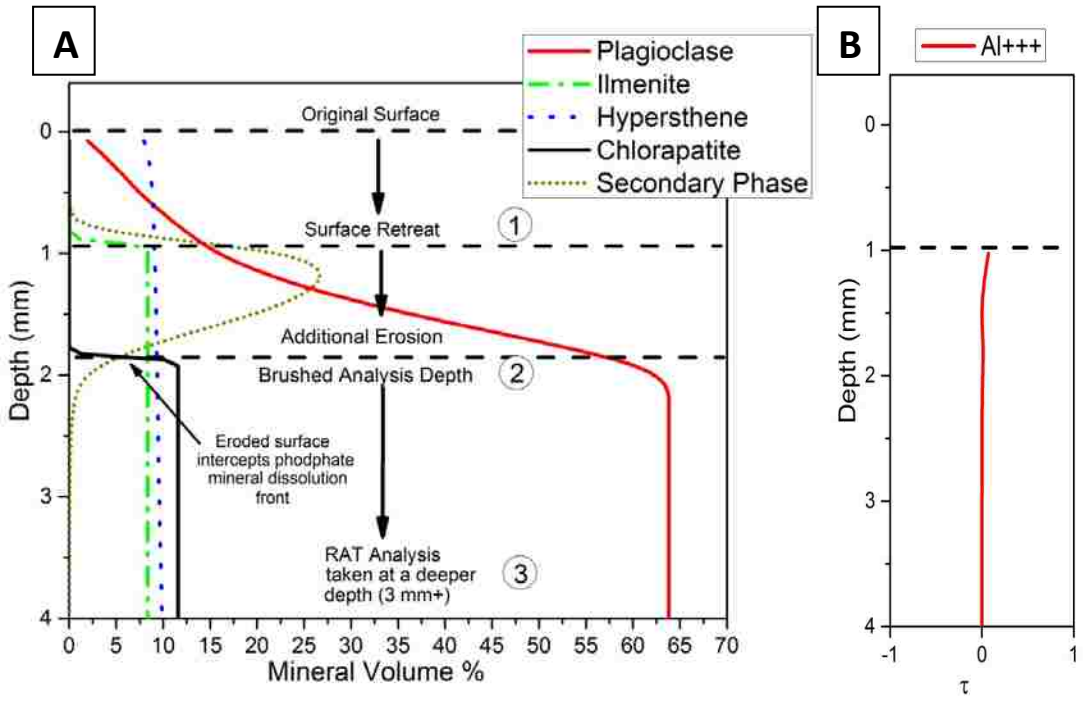

Figure 10. Output dissolution profile for chlorapatite-bearing model at pH 5 for 100 k.y. A) 1. Surface retreat from the original rock surface based on 50% developed porosity. Note that the surface retreat overtakes the dissolution front of ilmenite, effectively removing it from the rock dissolution profile. **2.** A component of additional erosion lowers the rock surface even more and generates a profile consistent with APXS brushed surface data for both Wishstone and Champagne, however, the depth of the physical erosion must intercept the Ca-phosphate dissolution front in exactly the same place in both rocks to remain consistent with the APXS data. **3.** At an additional depth (3 mm+) reached after use of the RAT, another APXS analysis is taken in relatively unweathered rock. **B)** τ plot of Al normalized to Ti concentration where 0 = parent concentration for Al and -1 = complete depletion. Plot shows that despite plagioclase dissolution Al remains relatively immobile. This is due to the formation of the Al-bearing secondary phase.

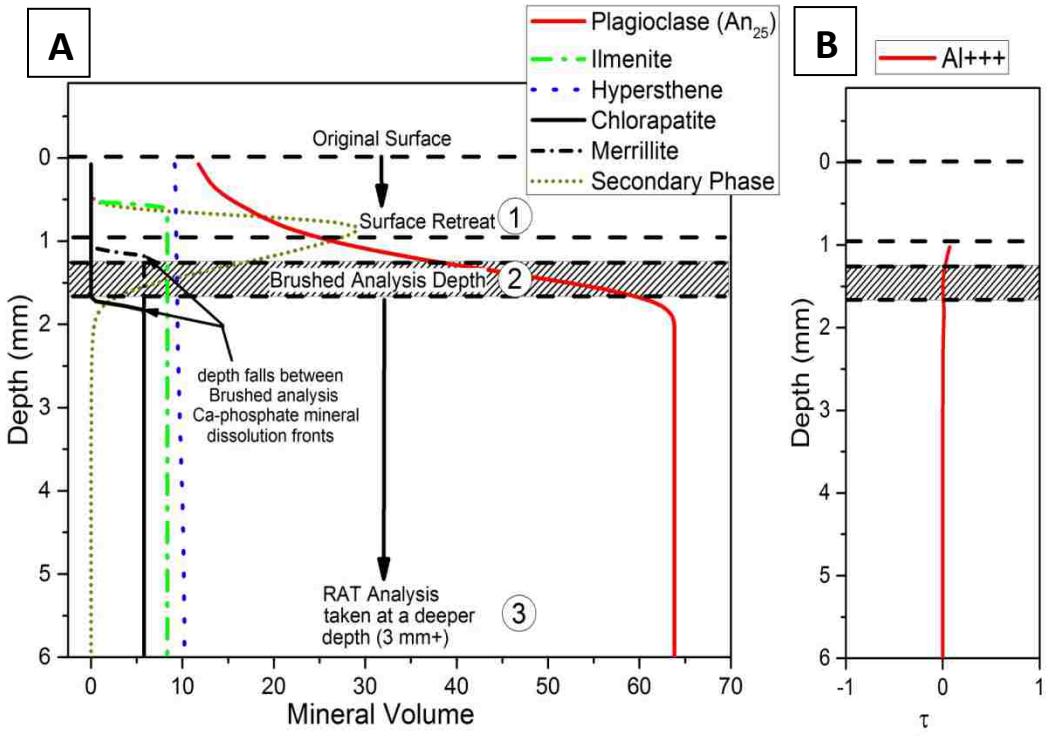

Figure 11. Two mineral dissolution model scenario from a chlorapatite/merrillite bearing model at pH 6 for 100 k.y. A) 1. Surface retreat from the original rock surface based on 50% developed porosity. Note that the surface retreat overtakes the dissolution front of ilmenite, effectively removing it from the rock dissolution profile. 2) A component of additional erosion lowers the rock surface even more (shaded area) overtaking the merrillite dissolution front but leaving the chlorapatite front, thus an APXS brushed surface analysis would indicate some but not all Ca-phosphate mineral loss. 3) At an additional depth (3 mm+) reached after use of the RAT, another APXS analysis is taken in relatively unweathered rock which would show the full phosphorus content of the rock. **B)** τ plot of Al normalized to Ti concentration where 0 = parent concentration for Al and -1 = complete depletion. Plot shows that despite plagioclase dissolution Al remains relatively immobile. This is due to the formation of the Al-bearing secondary phase.

APPENDIX I

SUPPLEMENTARY INFORMATION FOR CHAPTER TWO

Contents

Supplementary Discussion

Effects of parameter variation during whitlockite synthesis.

In order to synthesize Mg-whitlockite, the Hughes et al. (2008) experiment was replicated, but Mg^{2+} was intentionally supplied to the system in the form of magnesium nitrate hexahydrate ($Mg(NO_3)_2 \cdot 6H_2O$) (J. T. Baker, ACS grade). To simplify the method, 40 mesh reagent grade calcium hydroxyapatite (HAP) powder (Spectrum, reagent grade) was used rather than pre-synthesizing this phase. The ratio of HAP to magnesium nitrate hexahydrate by mass was generally 3.33: 1 to provide sufficient Mg^{2+} based on whitlockite stoichiometry, but not excess Mg^{2+} that might lead to the formation of additional Mg phases. Variables during the preliminary experiments included incubation time at 240 °C (5-14 days), adjusted pH (2.1 to 2.8), and the total concentration of solids used in the experiments (6.7 to 90 g/L). Early experiments were run in 23 ml Teflon lined acid digestion vessels (Parr 4749) and later scaled up to 125 ml vessels (Parr 4748). Preliminary experiments were carried out with the goal of first producing Mg-whitlockite crystals, and then refining the synthesis method for phase purity, larger crystal size, and sufficient output mass to carry out crystallographic and chemical characterization as well as supply Mg-whitlockite for use in the synthesis of Mg-merrillite.

Insight gained during synthesis of Mg-whitlockite was used to develop a procedure for Fe-whitlockite synthesis. Initially, $FeCl_2$ was used as a source of Fe^{2+} in

place of the $Mg(NO_3)_2 \cdot 6H_2O$ used in Mg-whitlockite synthesis. After experiments using $FeCl_2$ failed to produce significant whitlockite, Fe(II)S was utilized as the Fe^{2+} source and whitlockite crystals were produced along with hydroxyapatite and opaque phases (presumably Fe phases). Variables during the preliminary experiments included incubation time at 240 °C (5-9 days), and total concentration of solids (9.0 to 17.8 g/L). In addition, the production of iron sulfide phases prompted varying the ratio of HAP to Fe(II)S from 9.6:1 (near stoichiometric ideal) to 28.6:1 by mass to limit their formation. The pH value was not significantly varied from 2.8 as results from Mg-whitlockite synthesis indicated it had no effect.

Although endmember whitlockite and merrillite are useful for different studies, natural whitlockite and merrillite generally contain both Mg^{2+} and Fe^{2+}. We therefore applied the results of endmember synthesis experiments to synthesize non-endmember whitlockites and from them mixed Fe/Mg-merrillite. Variables included the ratio of Mg and Fe, as well as the concentration of total solids in solution (10.2 to 17.8 g/L). Sodium (as NaCl) was also included in some experiments. Though sodium is not typical within terrestrial whitlockite, it is present in most natural merrillite, particularly martian merrillite, in what is a partially filled calcium site in synthetic merrillite (Jolliff et al., 2006). The methods documented in the accompanying paper are those which successfully produced the material characterized and used for mixed Fe/Mg-merrillite synthesis in this study and include sodium (as NaCl), however, sodium was not incorporated into the whitlockite structure in any of multiple attempts. Additional experiments showed sodium to neither inhibit nor aid the production of mixed Mg/Fe-

whitlockite. Appendix I Table S1 contains parameter values for all whitlockite synthesis experiments in this study, including those used to make mixed Fe/Mg-whitlockite and subsequent Fe/Mg-merrillite.

Table S1. Batch parameters for whitlockite synthesis experiments.

ID	Vessel Size	$MgNO_3 \cdot 6H_2O$ (g)	$FeCl_2$ (g)	FeS (g)	NaCl (g)	HAP (g)	Mass Tot (g)	DI (mL)	g/L*	pH start	Days	pH end	Mass Out (g)	Note
Mg-1	23 ml	0.0153				0.0518	0.0671	10	6.7	2.70	5	-	-	Whit.
Mg-2	23 ml	0.2210				0.7716	0.9926	11	90.2	2.78	5	-	-	Monetite
Mg-3	23 ml	0.0159				0.0519	0.0678	10	6.8	2.66	10	2.80	0.016	Whit.
Mg-4	23 ml	0.0461				0.1541	0.2002	10	20.0	2.69	11	2.80	0.113	Whit.
Mg-5	23 ml	0.1093				0.3630	0.4723	13.5	35.0	2.81	14	2.16	0.189	Monetite
Mg-6	23 ml	0.2190				0.7280	0.9470	13.5	70.1	2.80	14	1.92	0.607	Monetite
Mg-7	125 ml	0.4599				1.5432	2.0031	90	22.3	2.80	7	2.09	1.150	Monetite
Mg-8	125 ml	0.4588				1.5423	2.0011	90	22.2	2.78	6	1.85	1.320	Monetite
Mg-9	125 ml	0.4595				1.5452	2.0047	90	22.3	2.80	5	1.86	1.370	Monetite
Mg-10	125 ml	0.4601				1.5426	2.0027	90	22.3	2.77	5	1.85	1.300	Monetite
Mg-11	125 ml	0.4595				1.5423	2.0018	90	22.2	2.80	5	1.90	1.220	Monetite
Mg-12	125 ml	0.2298				0.7709	1.0007	90	11.1	2.70	7	2.10	0.240	Whit.
Mg-13	125 ml	0.3890				1.2813	1.6703	90	18.6	2.79	5	2.01	0.834	Crypto-xtal mix
Mg-14	23 ml	0.0158				0.0512	0.0670	10	6.7	2.10	7	1.85	0.030	Whit.
Mg-15	23 ml	0.2006				0.0000	0.2006	10	20.1	2.70	5	2.12	0.125	Whit.
Mg-16	125 ml	0.3004				1.0014	1.3018	90	14.5	2.77	7	1.70	1.131	Whit.
Mg-17	125 ml	0.3000				1.0000	1.3000	90	14.4	2.76	7	1.84	0.899	Whit.
Mg-18	125 ml	0.3000				1.0000	1.3000	90	14.4	2.74	7	-	-	Whit.
Mg-19	125 ml	0.3000				1.0000	1.3000	90	14.4	2.78	7	-	-	Whit.
Mg-22	125 ml	0.3004				1.0000	1.3004	90	14.4	2.72	7	1.78	0.800	Whit.
Mg-23	125 ml	0.3000				1.0070	1.3070	90	14.5	2.79	7	2.10	0.555	Whit.
Mg-24	125 ml	0.3000				1.0000	1.3000	80	16.3	2.74	7	2.11	0.588	Leaked/Failed
Mg-25	125 ml	0.3004				1.0007	1.3011	90	14.5	2.73	7	1.97	0.510	Whit.
Mg-26	125 ml	0.3005				1.0011	1.3016	90	14.5	2.70	7	1.98	0.480	Whit.
Mg-27	125 ml	0.3003				1.0010	1.3013	90	14.5	2.79	7	1.81	0.720	Whit.
Mg-28	125 ml	0.3000				1.0000	1.3000	90	14.4	2.78	7	1.88	0.699	Whit.
Mg-29	125 ml	0.3000				1.0000	1.3000	90	14.4	2.65	7	1.74	0.702	Whit.
Mg-31	125 ml	0.3026				1.0004	1.3030	90	14.5	2.65	12	1.76	0.810	Whit.
Mg-32	125 ml	0.3016				1.0006	1.3022	90	14.5	2.69	12	1.77	0.710	Whit.
Mg-33	125 ml	0.2997				1.0012	1.3009	90	14.5	2.71	12	1.72	0.730	Whit.
Mg-34	125 ml	0.2994				0.9996	1.299	90	14.4	2.74	6	1.78	0.770	Whit.
Mg-35	125 ml	0.3013				0.9998	1.3011	90	14.5	2.80	6	1.75	0.720	Whit.
Mg-36	125 ml	0.2997				1.0009	1.3006	90	14.5	2.75	6	1.74	0.810	Whit.
Mg-37	125 ml	0.3004				1.0005	1.3009	90	14.5	2.68	7	1.89	0.730	Whit.
Mg-38	125 ml	0.3002				1.0001	1.3003	90	14.4	2.72	7	1.82	0.700	Whit.
Mg-39	125 ml	0.3003				1.0001	1.3004	90	14.4	2.40	7	1.78	0.760	Whit.
Mg-40	125 ml	0.3004				1.0004	1.3008	90	14.5	2.74	8	1.89	0.665	Whit.
Mg-41	125 ml	0.2994				0.9999	1.2993	90	14.4	2.78	8	1.82	0.706	Whit.
Mg-42	125 ml	0.3008				1.0002	1.301	90	14.5	2.75	8	1.78	0.825	Whit.
Mg-44	125 ml	0.3002				1.0012	1.3014	90	14.5	2.73	7	-	0.632	Whit.

Table S1 continued. Batch parameters for whitlockite synthesis experiments.

ID	Vessel Size	$MgNO_3 \cdot 6H_2O$ (g)	$FeCl_2$ (g)	FeS (g)	NaCl (g)	HAP (g)	Mass Tot (g)	DI (mL)	g/L*	pH start	Days	pH end	Mass Out (g)	Note
Mg-45	125 ml	0.3003				1.0008	1.3011	90	14.5	2.76	7	1.83	0.676	Whit.
Mg-46	125 ml	0.3005				1.0005	1.3010	90	14.5	2.74	7	1.77	0.775	Whit.
Mg-47	125 ml	0.2998				1.0003	1.3001	90	14.4	2.74	7	1.77	0.723	Whit.
Mg-48	125 ml	0.2998				1.0005	1.3003	90	14.4	2.76	7	1.76	0.726	Whit.
Mg-49	125 ml	0.2990				1.0000	1.2990	90	14.4	2.75	7	1.69	0.813	Whit.
Mg-50	125 ml	0.3002				1.0001	1.3003	90	14.4	2.66	8	1.80	0.627	Whit.
Mg-51	125 ml	0.3003				1.0001	1.3004	90	14.4	2.73	8	1.73	0.734	Whit.
Mg-52	125 ml	0.3001				1.0000	1.3001	90	14.4	2.75	8	1.68	0.776	Whit.
Mg-53	125 ml	0.3008				1.0000	1.3008	90	14.5	2.66	6	1.84	0.594	Whit.
Mg-54	125 ml	0.3009				1.0003	1.3012	90	14.5	2.79	6	1.75	0.690	Whit.
Mg-55	125 ml	0.3412				1.0006	1.3418	90	14.9	2.76	6	1.74	0.715	Whit.
Mg-56	125 ml	0.3003				0.9994	1.2997	90	14.4	2.69	7	1.85	0.702	Whit.
Mg-57	125 ml	0.3002				0.9995	1.2997	90	14.4	2.76	7	1.74	0.715	Whit.
Mg-58	125 ml	0.2999				1.0003	1.3002	90	14.4	2.74	7	1.70	0.734	Whit.
Mg-59	125 ml	0.3002				0.9998	1.3000	90	14.4	2.77	7	1.83	0.460	Whit.
Mg-60	125 ml	0.2998				0.9998	1.2996	90	14.4	2.74	7	1.85	0.437	Whit.
Mg-61	125 ml	0.3003				1.0012	1.3015	90	14.5	2.74	7	1.83	0.566	Whit.
Fe-1	23 ml		0.0287			0.2307	0.2594	16	16.2	2.68	9	2.26	0.148	No Whit.
Fe-2	23 ml		0.0290			0.2311	0.2601	16	16.3	2.77	9	2.20	0.143	No Whit.
Fe-3	23 ml	0.0356	0.0173			0.2312	0.2841	16	17.8	2.74	8	2.11	0.114	No Whit.
Fe-4	23 ml	0.0357		0.0129		0.2311	0.2797	16	17.5	2.77	8	2.00	0.173	minor Whit.
Fe-5	23 ml			0.0249		0.2334	0.2583	16	16.1	2.75	8	1.80	-	aggregates Whit.
Fe-6	23 ml			0.0183		0.1739	0.1922	16	12.0	2.74	8	1.80	-	Cleaner Whit
Fe-7	125 ml			0.0763		0.7300	0.8063	90	9.0	2.76	7	2.06	0.427	Fe-Whit.
Fe-8	125 ml			0.0769		1.0012	1.0781	90	12.0	2.77	7	2.10	0.520	Fe-Whit.
Fe-9	125 ml			0.0600		0.9994	1.0594	90	11.8	2.78	7	2.05	0.630	Fe-Whit.
Fe-10	125 ml			0.0500		1.0001	1.0501	90	11.7	2.77	7	2.17	0.520	Fe-whit+agg.
Fe-11	125 ml			0.0347		1.0009	1.0356	90	11.5	2.78	7	1.87	0.500	
Fe-12	125 ml			0.0392		1.0000	1.0392	90	11.5	2.69	7	1.96	0.471	Lg xtals Fe-whit.
Fe-13	125 ml			0.0450		1.0000	1.0450	90	11.6	2.74	7	1.87	0.785	Lg xtals Fe-whit.
Fe-14	125 ml			0.0767		1.0008	1.0775	90	12.0	2.75	7	1.90	0.731	Fe-whit+agg.
Fe-15	125 ml			0.1003		1.0004	1.1007	90	12.2	2.72	7	1.92	0.846	Fe-Whit.
Fe-16	125 ml			0.0349		0.9999	1.0348	90	11.5	2.69	7	1.89	0.609	Fe-Whit.
Fe-17	125 ml		0.0800			1.0003	1.0803	90	12.0	2.75	7	1.94	0.451	No-Whit.
Fe-18	125 ml			0.0849		1.1003	1.1852	90	13.2	2.75	7	1.89	0.726	Fe-Whit.
Fe-19	125 ml			0.1101		1.2004	1.3105	90	14.6	2.68	7	1.97	0.845	Fe-whit+agg.
Fe-20	125 ml			0.0549		1.0004	1.0553	90	11.7	2.76	7	1.95	0.419	Fe-Whit.
Fe-21	125 ml			0.0558		1.0001	1.0559	90	11.7	2.69	7	1.92	0.452	Fe-Whit.
Fe-22	125 ml			0.0544		1.0004	1.0548	90	11.7	2.71	7	1.96	0.444	Fe-Whit.

Table S1 continued. Batch parameters for whitlockite synthesis experiments.

ID	Vessel Size	$MgNO_3 \cdot 6H_2O$ (g)	$FeCl_2$ (g)	FeS (g)	NaCl (g)	HAP (g)	Mass Tot (g)	DI (mL)	g/L*	pH start	Days	pH end	Mass Out (g)	Note
Mix-1	125ml	0.0500		0.0500	0.0667	1.0000	1.1667	90	13.0	2.64	7	2.05	0.761	Whit.
Mix-2	125ml	0.1000		0.0500		1.0000	1.1500	90	12.8	2.73	7	2.15	0.694	Whit.
Mix-3	125ml	0.1000			0.1000	1.0000	1.2000	90	13.3	2.78	7	-	-	No Whit.
Mix-4	125ml	0.1000		0.0495		0.9997	1.1492	90	12.8	2.78	7	2.2	0.688	No Whit. (HAP)
Mix-5	125ml	0.1103		0.0403		1.0000	1.1506	90	12.8	2.70	7	2.01	0.821	No Whit. (HAP)
Mix-6	125ml	0.1207		0.0305		1.0005	1.1517	90	12.8	2.78	7	2.27	0.591	Rare Whit.
Mix-7	125 ml	0.0505		0.0499	0.0668	1.0000	1.1672	90	13.0	2.75	7	1.8	0.811	Whit.
Mix-8	125 ml	0.0505		0.0499		1.0005	1.1009	90	12.2	2.74	7	1.84	0.915	Whit.
Mix-9	125 ml	0.1505		0.0500		1.2000	1.4005	90	15.6	2.78	7	2.1	0.974	No Whit.
Mix-10	125 ml	0.1000		0.0500		1.0000	1.1500	90	12.8	2.72	7	2.05	0.700	Rare Whit.
Mix-11	125 ml	0.0800		0.0400		0.8000	0.9200	90	10.2	2.78	7	2.04	0.550	Rare Whit.
Mix-12	125 ml	0.0900		0.0300		0.8000	0.9200	90	10.2	2.78	7	2.02	-	Minor Whit.
Mix-13	125 ml	0.0500		0.0501		1.0002	1.1003	90	12.2	2.75	7	1.89	0.799	Whit. (lg)
Mix-14	125 ml	0.0399		0.0601		0.9999	1.0999	90	12.2	2.78	7	-	0.765	Whit.
Mix-15	125 ml	0.0600		0.0400		1.0000	1.1000	90	12.2	2.77	7	2.04	0.707	Whit.
Mix-16	125 ml	0.0501		0.0500	0.0601	1.0001	1.1603	90	12.9	2.77	7	1.99	0.785	Whit. well fm.
Mix-17	125 ml	0.0251		0.0501		0.9000	0.9752	90	10.8	2.76	7	-	0.556	Whit.
Mix-18	125 ml	0.0300		0.0700		1.0000	1.1000	90	12.2	2.77	7	2.01	0.644	Whit.
Mix-19	125 ml	0.0351		0.0501		1.0001	1.0853	90	12.1	2.77	7	1.98	0.689	Whit.
Mix-20	125 ml	0.0350		0.0502		1.0000	1.0852	90	12.1	2.78	7	1.96	0.674	A.W./Whit.
Mix-21	125 ml	0.0901		0.0302		0.9002	1.0205	90	11.3	2.78	7	2.2	0.470	Rare Whit.

Vessel Size = the volume of the Teflon lines Parr reaction vessel used. All chemistry weights are in grams. Mass Tot = Total mass of solids in grams used in the experiment. DI = volume of 18 MΩ water used in experiment. g/L = ratio of total mass of solids (g) in solution (L). pH Start = the adjusted pH at the start of the experiment. Days = number of days of incubation. pH end = measured pH at end of experiment. Mass Out = total mass (g)of material recovered after experiment including impurities. Abbreviations in notes: Whit.=whitlockite, agg. = polycrystalline aggregates, lg = large, HAP = hydroxyapatite, well fm. = well formed crystals. Crypto-xtal mix = mix of microcrystalline phases. A.W. = reaction vessel underwent additional cleaning including additional acid washing to investigate any affect on nucleation.

Table S2. Microprobe analyses of Mg/Fe-whitlockite synthesized with varied Fe: Mg ratios.

	Mg/Fe-Whitlockite Synthesis Experiment ID					
	Mix-6		***Mix-21***		***Mix-1***	
CaO	48.40	(0.26)	47.73	(1.31)	46.54	(0.59)
P_2O_5	45.83	(0.28)	45.59	(0.92)	45.83	(0.36)
MgO	3.43	(0.32)	2.63	(0.05)	1	(0.20)
FeO	0.18	(0.24)	1.92	(2.51)	4.62	(0.71)
Na_2O	B.D.	-	B.D.	-	B.D.	-
H_2O[a]	0.86	-	0.86	-	0.86	-
Total	98.69	(0.42)	98.73	(0.79)	98.85	(0.49)
n	11		7		18	
Stoic.	$Ca_{9.2}Fe_{0.0}Mg_{0.9}(PO_3OH)(PO_4)_{5.9}$		$Ca_{9.1}Fe_{0.3}Mg_{0.7}(PO_3OH)(PO_4)_{5.9}$		$Ca_{9.0}Fe_{0.7}Mg_{0.3}(PO_3OH)(PO_4)_6$	
Fe:Mg Soln.[b]	0.74		0.98		2.91	
Fe:Mg Prod.[c]	0.00		0.43		2.33	

Parenthetical values are 1 standard deviation. n = number of analyses averaged chemistry is based on. B.D. = below detection.
[a]H_2O is based on ideal whitlockite (Hughes et al., 2008) and is included in these EMP totals.
[b]The molar ratio of Fe: Mg added to the solution of the experiment.
[c]The molar ratio of Fe: Mg in the stoichiometry of the resulting whitlockite.

Table S3. Atomic parameters for synthesized whitlockite and merrillite.

Atom	Fe-whitlockite	Fe/Mg-whitlockite	Ferric Fe-merrillite (Pt cruc.)	Ferrous Fe-merrillite (SiO_2 tube)	Ferric Fe/Mg-merrillite (Pt cruc.)	Ferrous Fe/Mg-merrillite (SiO_2 tube)
Fe(1)	$Fe_{1.00}$	$Fe_{0.637}$	$Fe_{1.00}$	$Fe_{1.00}$	$Fe_{0.754}$	$Fe_{0.646}$
x	0.6667	0.6667	0.6667	0.6667	0.6667	0.6667
y	0.3333	0.3333	0.3333	0.3333	0.3333	0.3333
z	0.1137(1)	0.1138(1)	0.1151(1)	0.1142(1)	0.1149(1)	0.1150(1)
U(eq)	0.008(1)	0.003(1)	0.005(1)	0.006(1)	0.002(1)	0.004(1)
Mg(1)		$Mg_{0.363}$			$Mg_{0.246}$	$Mg_{0.354}$
x	NA	0.6667	NA	NA	0.6667	0.6667
y	NA	0.3333	NA	NA	0.3333	0.3333
z	NA	0.1138(1)	NA	NA	0.1149(1)	0.1150(1)
U(eq)	NA	0.002	NA	NA	0.002	0.004
Ca(1)	$Ca_{1.00}$	$Ca_{1.00}$	$Ca_{1.00}$	$Ca_{1.00}$	$Ca_{1.00}$	$Ca_{1.00}$
x	0.7191(1)	0.7192(1)	0.7224(1)	0.7245(1)	0.7226(1)	0.7239(1)
y	0.8534(1)	0.8534(1)	0.8547(1)	0.8571(1)	0.8548(1)	0.8566(1)
z	0.2150(1)	0.2150(1)	0.2140(1)	0.2133(1)	0.2140(1)	0.2144(1)
U(eq)	0.005(1)	0.004(1)	0.004(1)	0.005(1)	0.004(1)	0.005(1)
Ca(2)	$Ca_{1.00}$	$Ca_{1.00}$	$Ca_{1.00}$	$Ca_{1.00}$	$Ca_{1.00}$	$Ca_{1.00}$
x	0.5125(1)	0.5122(1)	0.5081(1)	0.5099(1)	0.5088(1)	0.5103(1)
y	0.0542(1)	0.0537(1)	0.0442(1)	0.0502(1)	0.0451(1)	0.0509(1)
z	0.1792(1)	0.1793(1)	0.1798(1)	0.1785(1)	0.1796(1)	0.1794(1)
U(eq)	0.005(1)	0.005(1)	0.004(1)	0.005(1)	0.004(1)	0.006(1)
Ca(3)	$Ca_{1.00}$	$Ca_{1.00}$	$Ca_{1.00}$	$Ca_{1.00}$	$Ca_{1.00}$	$Ca_{1.00}$
x	1.1580(1)	1.1573(1)	1.1483(1)	1.1495(1)	1.1489(1)	1.1506(1)
y	0.8643(1)	0.8646(1)	0.8714(1)	0.8731(1)	0.8709(1)	0.8717(1)
z	0.1080(1)	0.1080(1)	0.1072(1)	0.1064(1)	0.1071(1)	0.1074(1)
U(eq)	0.012(1)	0.011(1)	0.006(1)	0.015(1)	0.007(1)	0.016(1)
P(2)	$P_{1.00}$	$P_{1.00}$	$P_{1.00}$	$P_{1.00}$	$P_{1.00}$	$P_{1.00}$
x	0.4761(1)	0.4761(1)	0.4745(1)	0.4713(1)	0.4746(1)	0.4725(1)
y	-0.0162(1)	-0.0160(1)	-0.0175(1)	-0.0201(1)	-0.0174(1)	-0.0193(1)
z	0.0827(1)	0.0827(1)	0.0841(1)	0.0820(1)	0.0837(1)	0.0830(1)
U(eq)	0.005(1)	0.004(1)	0.003(1)	0.005(1)	0.003(1)	0.005(1)
P(1)	$P_{1.00}$	$P_{1.00}$	$P_{1.00}$	$P_{1.00}$	$P_{1.00}$	$P_{1.00}$
x	0.8606(1)	0.8601(1)	0.8562(1)	0.8602(1)	0.8564(1)	0.8601(1)
y	0.6848(1)	0.6841(1)	0.6761(1)	0.6794(1)	0.6767(1)	0.6798(1)
z	0.1464(1)	0.1464(1)	0.1459(1)	0.1455(1)	0.1458(1)	0.1464(1)
U(eq)	0.004(1)	0.004(1)	0.003(1)	0.004(1)	0.003(1)	0.005(1)
P(3A)	$P_{0.890}$	$P_{0.840}$	$P_{0.029}$	$P_{0.239}$	$P_{0.065}$	$P_{0.309}$
x	0.3333	0.3333	0.3333	0.3333	0.3333	0.3333
y	-0.3333	-0.3333	-0.3333	-0.3333	-0.3333	-0.3333
z	0.1934(1)	0.1934(1)	0.2178(1)	0.2138(1)	0.2170(1)	0.2146(1)
U(eq)	0.005(1)	0.005(1)	0.004(1)	0.005(1)	0.005(1)	0.006(1)
P(3B)	$P_{0.110}$	$P_{0.160}$	$P_{0.971}$	$P_{0.761}$	$P_{0.935}$	$P_{0.691}$
x	0.3333	0.3333	0.3333	0.3333	0.3333	0.3333
y	-0.3333	-0.3333	-0.3333	-0.3333	-0.3333	-0.3333
z	0.2160(2)	0.2165(1)	0.1952(13)	0.1932(2)	0.1933(5)	0.1936(1)
U(eq)	0.005	0.005	0.004	0.005	0.005	0.004(1)
O(10A)	$O_{0.890}$	$O_{0.840}$	$O_{0.029}$	$O_{0.239}$	$O_{0.065}$	$O_{0.309}$
x	0.3333	0.3333	0.3333	0.3333	0.3333	0.3333
y	-0.3333	-0.3333	-0.3333	-0.3333	-0.3333	-0.3333

Atom	Fe-whitlockite	Fe/Mg-whitlockite	Ferric Fe-merrillite (Pt cruc.)	Ferrous Fe-merrillite (SiO_2 tube)	Ferric Fe/Mg-merrillite (Pt cruc.)	Ferrous Fe/Mg-merrillite (SiO_2 tube)
z	0.1508(1)	0.1508(1)	0.2594(1)	0.2555(2)	0.2586(1)	0.1523(2)
U(eq)	0.013(1)	0.012(1)	0.006(1)	0.009(1)	0.007(1)	0.015(3)
O(10B)	$O_{0.110}$	$O_{0.160}$	$O_{0.970}$	$O_{0.761}$	$O_{0.935}$	$O_{0.691}$
x	0.3333	0.3333	0.3333	0.3333	0.3333	0.3333
y	-0.3333	-0.3333	-0.3333	-0.3333	-0.3333	-0.3333
z	0.2568(8)	0.2579(3)	0.1549(15)	0.1520(2)	0.1511(8)	0.2560(2)
U(eq)	0.013	0.004(2)	0.007	0.009	0.007	0.011(1)
O(6)	$O_{1.00}$	$O_{1.00}$	$O_{1.00}$	$O_{1.00}$	$O_{1.00}$	$O_{1.00}$
x	0.5657(2)	0.5658(1)	0.5682(2)	0.5602(3)	0.5677(2)	0.5620(2)
y	-0.0877(2)	-0.0872	-0.0826(2)	-0.0930(3)	-0.0831(2)	-909(2)
z	0.0696(1)	0.0695(1)	0.0696(1)	0.0684(1)	0.0691(1)	0.0694(1)
U(eq)	0.008(1)	0.007(1)	0.006(1)	0.016(1)	0.006(1)	0.013(1)
O(9)	$O_{1.00}$	$O_{1.00}$	$O_{1.00}$	$O_{1.00}$	$O_{1.00}$	$O_{1.00}$
x	0.3533(2)	0.3526(1)	0.3444(2)	0.3420(3)	0.3436(2)	0.3431(3)
y	-0.1832(2)	-0.1834(1)	-0.1866(2)	-0.1882(3)	-0.0187(2)	-0.1876(2)
z	0.2056(1)	0.2054(1)	0.2050(1)	0.2018(1)	0.2044(1)	0.2030(1)
U(eq)	0.009(1)	0.008(1)	0.007(1)	0.016(1)	0.009(1)	0.017(1)
O(8)	$O_{1.00}$	$O_{1.00}$	$O_{1.00}$	$O_{1.00}$	$O_{1.00}$	$O_{1.00}$
x	0.3344(2)	0.3345(1)	0.3365(2)	0.3317(3)	0.3356(2)	0.3325(2)
y	-0.0606(2)	-0.0606(1)	-0.0552(2)	-0.0575(3)	-0.0559(2)	-0.0579(2)
z	0.0604(1)	0.0604(1)	0.0606(1)	0.0594(1)	0.0605(1)	0.0604(1)
U(eq)	0.006(1)	0.005(1)	0.005(1)	0.006(1)	0.005(1)	0.006(1)
O(5)	$O_{1.00}$	$O_{1.00}$	$O_{1.00}$	$O_{1.00}$	$O_{1.00}$	$O_{1.00}$
x	0.5754(2)	0.5756(1)	0.5763(2)	0.5746(3)	0.5762(2)	0.5750(2)
y	0.1551(2)	0.1556(1)	0.1589(2)	0.1516(3)	0.1582(2)	0.1529(2)
z	0.0774(1)	0.0778(1)	0.0808(1)	0.0781(1)	0.0803(1)	0.0792(1)
U(eq)	0.007(1)	0.007(1)	0.005(1)	0.009(1)	0.004(1)	0.010(1)
O(2)	$O_{1.00}$	$O_{1.00}$	$O_{1.00}$	$O_{1.00}$	$O_{1.00}$	$O_{1.00}$
x	0.8747(2)	0.8737(1)	0.8599(2)	0.8660(3)	0.8613(2)	0.8670(2)
y	0.7381(2)	0.7360(1)	0.7100(2)	0.7168(3)	0.7119(3)	0.7198(3)
z	0.1068(1)	0.1068(1)	0.1058(1)	0.1054(1)	0.1057(1)	0.1063(1)
U(eq)	0.009(1)	0.009(1)	0.006(1)	0.010(1)	0.007(1)	0.013(1)
O(3)	$O_{1.00}$	$O_{1.00}$	$O_{1.00}$	$O_{1.00}$	$O_{1.00}$	$O_{1.00}$
x	1.0193(2)	1.0188(1)	1.0161(2)	1.0204(2)	1.0161(2)	1.0203(2)
y	0.7337(2)	0.7330(1)	0.7289(2)	0.7308(3)	0.7291(2)	0.7311(2)
z	0.1598(1)	0.1597(1)	0.1589(1)	0.1580(1)	0.1590(1)	0.1590(1)
U(eq)	0.007(1)	0.006(1)	0.006(1)	0.007(1)	0.006(1)	0.007(1)
O(1)	$O_{1.00}$	$O_{1.00}$	$O_{1.00}$	$O_{1.00}$	$O_{1.00}$	$O_{1.00}$
x	0.7795(2)	0.7792(1)	0.7803(2)	0.7857(3)	0.7800(2)	0.7846(2)
y	0.7504(2)	0.7499(1)	0.7482(2)	0.7538(3)	0.7486(2)	0.7528(2)
z	0.1674(1)	0.1672(1)	0.1665(1)	0.1657(1)	0.1663(1)	0.1667(1)
U(eq)	0.008(1)	0.007(1)	0.006(1)	0.009(1)	0.007(1)	0.009(1)
O(4)	$O_{1.00}$	$O_{1.00}$	$O_{1.00}$	$O_{1.00}$	$O_{1.00}$	$O_{1.00}$
x	0.7675(2)	0.7671(1)	0.7619(2)	0.7656(3)	0.7623(2)	0.7655(2)
y	0.5128(2)	0.5122(1)	0.5034(2)	0.5096(3)	0.5041(2)	0.5093(2)
z	0.1506(1)	0.1506(1)	0.1519(1)	0.1523(1)	0.1516(1)	0.1524(1)
U(eq)	0.007(1)	0.007(1)	0.005(1)	0.007(1)	0.005(1)	0.008(1)
O(7)	$O_{1.00}$	$O_{1.00}$	$O_{1.00}$	$O_{1.00}$	$O_{1.00}$	$O_{1.00}$

Atom	Fe-whitlockite	Fe/Mg-whitlockite	Ferric Fe-merrillite (Pt cruc.)	Ferrous Fe-merrillite (SiO_2 tube)	Ferric Fe/Mg-merrillite (Pt cruc.)	Ferrous Fe/Mg-merrillite (SiO_2 tube)
x	0.4261(2)	0.4260(1)	0.4214(2)	0.4176(3)	0.4222(3)	0.4189(2)
y	-0.0543(2)	-0.0550(1)	-0.0610(2)	-0.0657(3)	-0.0616(2)	-0.0650(3)
z	0.1219(1)	0.1219(1)	0.1227(1)	0.1208(1)	0.1224(1)	0.1218(1)
U(eq)	0.009(1)	0.008(1)	0.006(1)	0.014(1)	0.008(1)	0.0015(1)
Ca(4A)				$Ca_{0.148}$		$Ca_{0.098}$
x	NA	NA	NA	0.3333	NA	0.3333
y	NA	NA	NA	-0.3333	NA	-0.3333
z	NA	NA	NA	0.1360(1)	NA	0.1041(3)
U(eq)	NA	NA	NA	0.011(1)	NA	0.019(3)
Ca(4B)				$Ca_{0.296}$		$Ca_{0.264}$
x	NA	NA	NA	0.3333	NA	0.3333
y	NA	NA	NA	-0.3333	NA	-0.3333
z	NA	NA	NA	0.1028(3)	NA	0.1369(1)
U(eq)	NA	NA	NA	0.013(3)	NA	0.007(1)

Parenthetic values are standard deviations. Pt cruc. = merrillite produced by heating in open air in a platinum crucible. SiO_2 tube = merrillite produced in a triple argon purged and sealed silica glass tube.

Table S4. Bond lengths for synthesized whitlockite and merrillite in angstroms.

		Fe-whitlockite	Fe/Mg-whitlockite	Ferric Fe-merrillite (Pt cruc.)	Ferrous Fe-merrillite (SiO_2 tube)	Ferric Fe/Mg-merrillite (Pt cruc.)	Ferrous Fe/Mg-merrillite (SiO_2 tube)
Ca(1)-	O(1)	2.3062(14)	2.3115(11)	2.308(2)	2.313(3)	2.310(2)	2.3128(19)
	O(2)#6	2.4348(17)	2.4268(13)	2.340(2)	2.386(3)	2.345(2)	2.385(2)
	O(3)#8	2.4482(15)	2.4548(11)	2.468(2)	2.456(2)	2.467(2)	2.4568(19)
	O(5)#7	2.4401(14)	2.4445(11)	2.511(2)	2.449(3)	2.506(2)	2.449(2)
	O(5)#9	2.4724(14)	2.4763(11)	2.495(2)	2.487(3)	2.484(2)	2.485(2)
	O(6)#7	2.7753(15)	2.7703(11)	2.740(2)	2.849(3)	2.741(2)	2.823(2)
	O(8)#9	2.5050(14)	2.5065(11)	2.470(2)	2.469(2)	2.474(2)	2.4742(19)
	O(9)#2	2.4570(14)	2.4530(11)	2.409(2)	2.437(3)	2.409(2)	2.437(2)
Ca(2)-	O(1)#14	2.6522(15)	2.6481(11)	2.638(2)	2.627(3)	2.631(2)	2.630(2)
	O(10B)#15	2.717(7)	2.699(3)	2.5360(11)	2.544(2)	2.578(2)	2.542(2)
	O(2)	2.5441(15)	2.5465(11)	2.586(2)	2.475(3)	2.492(2)	2.469(2)
	O(2)#14	2.4649(14)	2.4675(11)	2.492(2)	2.377(2)	2.389(2)	2.3720(18)
	O(3)	2.3727(14)	2.3736(11)	2.388(2)	2.564(2)	2.5518(12)	2.5888(17)
	O(6)#1	2.3934(15)	2.4009(12)	2.458(2)	2.484(3)	2.463(2)	2.468(2)
	O(7)#13	2.5186(16)	2.5251(12)	2.609(2)	2.573(3)	2.610(2)	2.567(2)
	O(8)#13	2.3717(15)	2.3762(11)	2.418(2)	2.399(3)	2.412(2)	2.3957(19)
	O(9)#16	2.9456(15)	2.9483(11)	2.899(2)	2.998(3)	2.926(2)	2.994(3)
Ca(3)-	O(1)#1	2.6373(15)	2.6345(11)	2.634(2)	2.681(3)	2.638(2)	2.669(2)
	O(3)#2	2.6570(14)	2.6507(11)	2.602(2)	2.633(2)	2.602(2)	2.6348(18)
	O(4)#1	2.4591(14)	2.4612(11)	2.501(2)	2.439(2)	2.497(2)	2.4444(19)
	O(4)#2	2.4278(14)	2.4313(11)	2.463(2)	2.414(3)	2.458(2)	2.4191(19)
	O(6)#12	2.4604(14)	2.4616(11)	2.473(2)	2.450(3)	2.468(2)	2.449(2)
	O(7)	2.3600(15)	2.3633(11)	2.345(2)	2.407(3)	2.350(2)	2.401(2)
	O(8)#11	2.3685(14)	2.3691(11)	2.378(2)	2.368(2)	2.374(2)	2.3675(18)
	O(9)	2.3782(14)	2.3748(11)	2.320(2)	2.358(3)	2.327(2)	2.360(2)
Ca(4A)-	O(6)#18	NA	NA	NA	2.736(5)	NA	2.758(6)
	O(6)#19	NA	NA	NA	2.736(5)	NA	2.758(6)
	O(7)#18	NA	NA	NA	2.541(4)	NA	2.541(4)
	O(7)#19	NA	NA	NA	2.541(4)	NA	2.541(4)
Ca(4B)-	O(6)#18	NA	NA	NA	2.516(3)	NA	2.518(2)
	O(6)#19	NA	NA	NA	2.516(3)	NA	2.518(2)
	O(7)#18	NA	NA	NA	2.846(5)	NA	2.851(4)
	O(7)#19	NA	NA	NA	2.846(5)	NA	2.851(4)
Fe(1)-	O(4)	2.1131(16)	2.1067(13)	2.046(2)	2.122(3)	2.048(2)	2.104(2)
	O(4)#1	2.1130(16)	2.1068(13)	2.046(2)	2.122(3)	2.048(2)	2.104(2)
	O(4)#2	2.1130(16)	2.1068(13)	2.046(2)	2.122(3)	2.048(2)	2.104(2)
	O(5)	2.0893(16)	2.0806(12)	2.011(2)	2.108(3)	2.023(2)	2.092(2)
	O(5)#1	2.0893(16)	2.0806(12)	2.011(2)	2.108(3)	2.023(2)	2.092(2)
	O(5)#2	2.0893(16)	2.0806(12)	2.011(2)	2.108(3)	2.023(2)	2.092(2)
P(1)-	O(1)	1.5281(15)	1.5257(11)	1.528(2)	1.528(3)	1.530(2)	1.528(2)
	O(2)	1.5484(16)	1.5456(13)	1.521(2)	1.532(3)	1.523(2)	1.535(2)
	O(3)	1.5393(14)	1.5382(11)	1.535(2)	1.537(2)	1.535(2)	1.5377(18)
	O(4)	1.5512(16)	1.5497(12)	1.562(2)	1.546(3)	1.561(2)	1.546(2)
P(2)-	O(5)	1.5538(16)	1.5552(12)	1.588(2)	1.556(3)	1.583(2)	1.558(2)
	O(6)	1.5261(15)	1.5260(12)	1.527(2)	1.537(3)	1.526(2)	1.531(2)
	O(7)	1.5284(15)	1.5256(12)	1.516(2)	1.529(3)	1.520(2)	1.529(2)

	O(8)	1.5385(15)	1.5381(11)	1.544(2)	1.543(2)	1.546(2)	1.5422(19)
P(3A)-	O(10A)	1.582(3)	1.578(3)	1.540(4)	1.530(3)	1.57(3)	1.530(7)
	O(9)	1.5297(14)	1.5291(11)	1.5366(19)	1.493(3)	1.518(6)	1.500(2)
	O(9)#18	1.5298(14)	1.5292(11)	1.5366(19)	1.493(3)	1.518(6)	1.500(2)
	O(9)#19	1.5298(14)	1.5292(11)	1.5366(19)	1.493(3)	1.518(6)	1.500(2)
P(3B)-	O(10B)	1.51(3)	1.534(14)	1.49(3)	1.546(7)	1.543(5)	1.535(6)
	O(9)	1.512(3)	1.5187(16)	1.507(12)	1.526(2)	1.534(2)	1.5209(19)
	O(9)#18	1.512(3)	1.5187(16)	1.507(12)	1.526(2)	1.534(2)	1.5209(19)
	O(9)#19	1.512(3)	1.5187(16)	1.507(12)	1.526(2)	1.534(2)	1.5209(19)

Parenthetic values are standard deviations. Pt cruc. = merrillite produced by heating in open air in a platinum crucible. SiO_2 tube = merrillite produced in a triple argon purged and sealed silica glass tube.

CIF Files to accompany Chapter Two

Fe-whitlockite

```
data_FeWhitlockite_0m_b

_chemical_formula_sum
 ' Ca9 Fe H O28 P7'
_chemical_formula_weight         1082.37
_chemical_compound_source        'synthetic'
_symmetry_cell_setting           trigonal
_symmetry_space_group_name_H-M    R3c
_chemical_name_mineral           whitlockite

loop_
 _symmetry_equiv_pos_as_xyz
 'x, y, z'
 '-y, x-y, z'
 '-x+y, -x, z'
 '-y, -x, z+1/2'
 '-x+y, y, z+1/2'
 'x, x-y, z+1/2'
 'x+2/3, y+1/3, z+1/3'
 '-y+2/3, x-y+1/3, z+1/3'
 '-x+y+2/3, -x+1/3, z+1/3'
 '-y+2/3, -x+1/3, z+5/6'
 '-x+y+2/3, y+1/3, z+5/6'
 'x+2/3, x-y+1/3, z+5/6'
 'x+1/3, y+2/3, z+2/3'
 '-y+1/3, x-y+2/3, z+2/3'
 '-x+y+1/3, -x+2/3, z+2/3'
 '-y+1/3, -x+2/3, z+7/6'
 '-x+y+1/3, y+2/3, z+7/6'
 'x+1/3, x-y+2/3, z+7/6'

_cell_length_a                10.3510(7)
_cell_length_b                10.3510(7)
_cell_length_c                37.059(2)
_cell_angle_alpha              90.00
_cell_angle_beta               90.00
_cell_angle_gamma               120.00
_cell_volume                  3438.6(4)
_cell_formula_units_Z          6
_cell_measurement_temperature    100(2)
_exptl_crystal_density_diffrn    3.136
_exptl_crystal_density_method    'not measured'
_exptl_crystal_F_000           3216
_exptl_absorpt_coefficient_mu    3.294
_exptl_absorpt_correction_type    multi-scan
_exptl_absorpt_correction_T_min   0.6768
```

```
_exptl_absorpt_correction_T_max   0.7466
_exptl_absorpt_process_details    "SADABS"

_diffrn_ambient_temperature       100(2)
_diffrn_radiation_wavelength      0.71073
_diffrn_radiation_type            MoK\a
_diffrn_radiation_source          'fine-focus sealed tube'
_diffrn_radiation_monochromator   graphite
_diffrn_reflns_number             17516
_diffrn_reflns_av_R_equivalents   0.0221
_diffrn_reflns_av_sigmaI/netI     0.0128
_diffrn_reflns_limit_h_min        -14
_diffrn_reflns_limit_h_max        14
_diffrn_reflns_limit_k_min        -14
_diffrn_reflns_limit_k_max        14
_diffrn_reflns_limit_l_min        -52
_diffrn_reflns_limit_l_max        52
_diffrn_reflns_theta_min          2.52
_diffrn_reflns_theta_max          30.50
_reflns_number_total              2352
_reflns_number_gt                 2341
_reflns_threshold_expression      >2sigma(I)

_computing_structure_solution     'SHELXS-97 (Sheldrick, 2008)'
_computing_structure_refinement   'SHELXL-97 (Sheldrick, 2008)'

_refine_special_details
;
 Refinement of F^2^ against ALL reflections.  The weighted R-factor wR and
 goodness of fit S are based on F^2^, conventional R-factors R are based
 on F, with F set to zero for negative F^2^. The threshold expression of
 F^2^ > 2sigma(F^2^) is used only for calculating R-factors(gt) etc. and is
 not relevant to the choice of reflections for refinement.  R-factors based
 on F^2^ are statistically about twice as large as those based on F, and R-
 factors based on ALL data will be even larger.
;

_refine_ls_structure_factor_coef  Fsqd
_refine_ls_matrix_type            full
_refine_ls_weighting_scheme       calc
_refine_ls_weighting_details
 'calc w=1/[\s^2^(Fo^2^)+(0.0372P)^2^+2.0977P] where P=(Fo^2^+2Fc^2^)/3'
_atom_sites_solution_primary      intrinsic
_atom_sites_solution_secondary    difmap
_atom_sites_solution_hydrogens    none
_refine_ls_hydrogen_treatment     none
_refine_ls_extinction_method      none
_refine_ls_extinction_coef        ?
_refine_ls_abs_structure_details
 'Flack H D (1983), Acta Cryst. A39, 876-881'
_refine_ls_abs_structure_Flack    0.00(4)
_refine_ls_number_reflns          2352
_refine_ls_number_parameters      140
```

```
_refine_ls_number_restraints     1
_refine_ls_R_factor_all          0.0186
_refine_ls_R_factor_gt           0.0185
_refine_ls_wR_factor_ref         0.0552
_refine_ls_wR_factor_gt          0.0552
_refine_ls_goodness_of_fit_ref   1.148
_refine_ls_restrained_S_all      1.148
_refine_ls_shift/su_max          0.001
_refine_ls_shift/su_mean         0.000

loop_
 _atom_site_label
 _atom_site_type_symbol
 _atom_site_fract_x
 _atom_site_fract_y
 _atom_site_fract_z
 _atom_site_U_iso_or_equiv
 _atom_site_adp_type
 _atom_site_occupancy
 _atom_site_symmetry_multiplicity
 _atom_site_calc_flag
 _atom_site_refinement_flags
 _atom_site_disorder_assembly
 _atom_site_disorder_group
Fe1 Fe 0.6667 0.3333 0.113741(17) 0.00771(9) Uani 1 3 d S . .
Ca1 Ca 0.71906(5) 0.85343(4) 0.215037(11) 0.00506(9) Uani 1 1 d . . .
Ca3 Ca 0.51246(4) 0.05420(5) 0.179244(10) 0.00547(8) Uani 1 1 d . . .
Ca2 Ca 1.15795(5) 0.86426(4) 0.107990(13) 0.01161(9) Uani 1 1 d . . .
P2 P 0.47612(6) -0.01616(6) 0.082656(13) 0.00455(10) Uani 1 1 d . . .
P1 P 0.86055(6) 0.68479(6) 0.146444(12) 0.00450(10) Uani 1 1 d . . .
P3A P 0.3333 -0.3333 0.19345(3) 0.0051(2) Uani 0.890(3) 3 d SP . .
P3B P 0.3333 -0.3333 0.2160(2) 0.005 Uiso 0.110(3) 3 d SP . .
O10A O 0.3333 -0.3333 0.15077(9) 0.0130(7) Uani 0.890(3) 3 d SP . .
O10B O 0.3333 -0.3333 0.2568(8) 0.013 Uiso 0.110(3) 3 d SP . .
O6 O 0.56574(16) -0.08767(16) 0.06961(4) 0.0076(3) Uani 1 1 d . . .
O9 O 0.35329(15) -0.18316(15) 0.20559(4) 0.0087(3) Uani 1 1 d . . .
O8 O 0.33437(16) -0.06065(15) 0.06044(4) 0.0061(2) Uani 1 1 d . . .
O5 O 0.57543(15) 0.15508(17) 0.07742(4) 0.0074(3) Uani 1 1 d . . .
O2 O 0.87474(16) 0.73809(18) 0.10685(4) 0.0086(3) Uani 1 1 d . . .
O3 O 1.01933(15) 0.73373(15) 0.15978(4) 0.0069(3) Uani 1 1 d . . .
O1 O 0.77948(16) 0.75035(16) 0.16736(4) 0.0078(3) Uani 1 1 d . . .
O4 O 0.76750(15) 0.51279(17) 0.15058(4) 0.0072(3) Uani 1 1 d . . .
O7 O 0.42614(17) -0.05431(17) 0.12192(4) 0.0092(3) Uani 1 1 d . . .

loop_
 _atom_site_aniso_label
 _atom_site_aniso_U_11
 _atom_site_aniso_U_22
 _atom_site_aniso_U_33
 _atom_site_aniso_U_23
 _atom_site_aniso_U_13
 _atom_site_aniso_U_12
Fe1 0.00759(13) 0.00759(13) 0.0080(2) 0.000 0.000 0.00379(7)
```

Ca1 0.00526(18) 0.00538(16) 0.00496(18) -0.00048(13) -0.00005(13) 0.00297(14)
Ca3 0.00491(17) 0.00649(17) 0.00489(16) 0.00131(13) 0.00019(14) 0.00277(14)
Ca2 0.01178(19) 0.00726(18) 0.00855(18) -0.00144(14) 0.00505(16) -0.00068(14)
P2 0.00460(19) 0.0051(2) 0.0044(2) -0.00043(17) -0.00058(17) 0.00278(17)
P1 0.0050(2) 0.0050(2) 0.0039(2) -0.00033(17) 0.00015(17) 0.00285(16)
P3A 0.0046(3) 0.0046(3) 0.0061(5) 0.000 0.000 0.00229(13)
O10A 0.0147(10) 0.0147(10) 0.0095(14) 0.000 0.000 0.0073(5)
O6 0.0098(6) 0.0092(6) 0.0069(6) -0.0011(5) -0.0010(5) 0.0073(5)
O9 0.0090(6) 0.0059(6) 0.0123(6) 0.0016(4) 0.0032(5) 0.0044(5)
O8 0.0052(6) 0.0072(6) 0.0055(5) -0.0004(5) -0.0008(4) 0.0027(5)
O5 0.0057(6) 0.0065(7) 0.0101(6) -0.0013(5) -0.0006(5) 0.0031(5)
O2 0.0096(6) 0.0131(7) 0.0039(6) 0.0004(5) 0.0008(5) 0.0064(5)
O3 0.0054(6) 0.0079(6) 0.0065(5) 0.0006(5) -0.0002(4) 0.0025(5)
O1 0.0104(6) 0.0087(6) 0.0071(6) -0.0017(5) 0.0004(5) 0.0069(5)
O4 0.0057(6) 0.0049(6) 0.0103(6) -0.0002(5) -0.0008(5) 0.0021(5)
O7 0.0106(7) 0.0132(7) 0.0051(6) -0.0013(5) 0.0002(5) 0.0068(6)

Fe/Mg-whitlockite

data_FeMgWhitlockite__0m_b

_chemical_formula_sum
'Ca9 Fe0.64 H Mg0.36 O28 P7'
_chemical_formula_weight 1070.93
_chemical_compound_source 'synthetic'
_symmetry_cell_setting trigonal
_symmetry_space_group_name_H-M R3c
_chemical_name_mineral whitlockite

loop_
_symmetry_equiv_pos_as_xyz
'x, y, z'
'-y, x-y, z'
'-x+y, -x, z'
'-y, -x, z+1/2'
'-x+y, y, z+1/2'
'x, x-y, z+1/2'
'x+2/3, y+1/3, z+1/3'
'-y+2/3, x-y+1/3, z+1/3'
'-x+y+2/3, -x+1/3, z+1/3'
'-y+2/3, -x+1/3, z+5/6'
'-x+y+2/3, y+1/3, z+5/6'
'x+2/3, x-y+1/3, z+5/6'
'x+1/3, y+2/3, z+2/3'
'-y+1/3, x-y+2/3, z+2/3'
'-x+y+1/3, -x+2/3, z+2/3'
'-y+1/3, -x+2/3, z+7/6'
'-x+y+1/3, y+2/3, z+7/6'
'x+1/3, x-y+2/3, z+7/6'

_cell_length_a 10.3499(4)

```
_cell_length_b                  10.3499(4)
_cell_length_c                  37.0715(16)
_cell_angle_alpha               90.00
_cell_angle_beta                90.00
_cell_angle_gamma               120.00
_cell_volume                    3439.1(2)
_cell_formula_units_Z           6
_cell_measurement_temperature     100(2)
_exptl_crystal_density_diffrn     3.103
_exptl_crystal_density_method     'not measured'
_exptl_crystal_F_000            3186
_exptl_absorpt_coefficient_mu     3.084
_exptl_absorpt_correction_type    multi-scan
_exptl_absorpt_correction_T_min   0.6997
_exptl_absorpt_correction_T_max   0.7466
_exptl_absorpt_process_details    "SADABS"

_diffrn_ambient_temperature       100(2)
_diffrn_radiation_wavelength      0.71073
_diffrn_radiation_type            MoK\a
_diffrn_radiation_source          'fine-focus sealed tube'
_diffrn_radiation_monochromator   graphite
_diffrn_reflns_number             17609
_diffrn_reflns_av_R_equivalents   0.0202
_diffrn_reflns_av_sigmaI/netI     0.0113
_diffrn_reflns_limit_h_min        -14
_diffrn_reflns_limit_h_max        14
_diffrn_reflns_limit_k_min        -14
_diffrn_reflns_limit_k_max        14
_diffrn_reflns_limit_l_min        -52
_diffrn_reflns_limit_l_max        52
_diffrn_reflns_theta_min          2.52
_diffrn_reflns_theta_max          30.51
_reflns_number_total              2355
_reflns_number_gt                 2336
_reflns_threshold_expression      >2sigma(I)

_computing_structure_solution     'SHELXS-97 (Sheldrick, 2008)'
_computing_structure_refinement   'SHELXL-97 (Sheldrick, 2008)'

_refine_special_details
;
 Refinement of F^2^ against ALL reflections.  The weighted R-factor wR and
 goodness of fit S are based on F^2^, conventional R-factors R are based
 on F, with F set to zero for negative F^2^. The threshold expression of
 F^2^ > 2sigma(F^2^) is used only for calculating R-factors(gt) etc. and is
 not relevant to the choice of reflections for refinement.  R-factors based
 on F^2^ are statistically about twice as large as those based on F, and R-
 factors based on ALL data will be even larger.
;

_refine_ls_structure_factor_coef  Fsqd
_refine_ls_matrix_type            full
```

```
_refine_ls_weighting_scheme      calc
_refine_ls_weighting_details
 'calc w=1/[\s^2^(Fo^2^)+(0.0267P)^2^+0.9683P] where P=(Fo^2^+2Fc^2^)/3'
_atom_sites_solution_primary     intrinsic
_atom_sites_solution_secondary    difmap
_atom_sites_solution_hydrogens    none
_refine_ls_hydrogen_treatment     none
_refine_ls_extinction_method      none
_refine_ls_extinction_coef       ?
_refine_ls_abs_structure_details
 'Flack H D (1983), Acta Cryst. A39, 876-881'
_refine_ls_abs_structure_Flack    0.00(9)
_refine_ls_number_reflns         2355
_refine_ls_number_parameters      142
_refine_ls_number_restraints      1
_refine_ls_R_factor_all          0.0155
_refine_ls_R_factor_gt           0.0154
_refine_ls_wR_factor_ref         0.0411
_refine_ls_wR_factor_gt          0.0410
_refine_ls_goodness_of_fit_ref    1.145
_refine_ls_restrained_S_all       1.145
_refine_ls_shift/su_max          0.001
_refine_ls_shift/su_mean         0.000

loop_
 _atom_site_label
 _atom_site_type_symbol
 _atom_site_fract_x
 _atom_site_fract_y
 _atom_site_fract_z
 _atom_site_U_iso_or_equiv
 _atom_site_adp_type
 _atom_site_occupancy
 _atom_site_symmetry_multiplicity
 _atom_site_calc_flag
 _atom_site_refinement_flags
 _atom_site_disorder_assembly
 _atom_site_disorder_group
Fe1 Fe 0.6667 0.3333 0.113848(16) 0.00310(17) Uani 0.637(4) 3 d SP . .
Mg1 Mg 0.6667 0.3333 0.113848(16) 0.003 Uiso 0.363(4) 3 d SP . .
Ca1 Ca 0.71923(3) 0.85341(3) 0.215018(8) 0.00441(7) Uani 1 1 d . . .
Ca3 Ca 0.51225(3) 0.05368(3) 0.179264(8) 0.00492(6) Uani 1 1 d . . .
Ca2 Ca 1.15730(4) 0.86455(3) 0.107972(10) 0.01143(7) Uani 1 1 d . . .
P2 P 0.47608(5) -0.01597(5) 0.082739(10) 0.00369(8) Uani 1 1 d . . .
P1 P 0.86008(4) 0.68408(5) 0.146408(9) 0.00373(7) Uani 1 1 d . . .
P3A P 0.3333 -0.3333 0.19339(2) 0.00472(18) Uani 0.840(2) 3 d SP . .
P3B P 0.3333 -0.3333 0.21651(13) 0.005 Uiso 0.160(2) 3 d SP . .
O10A O 0.3333 -0.3333 0.15081(7) 0.0124(5) Uani 0.840(2) 3 d SP . .
O10B O 0.3333 -0.3333 0.2579(3) 0.004(2) Uiso 0.160(2) 3 d SP . .
O6 O 0.56579(12) -0.08715(12) 0.06953(3) 0.0068(2) Uani 1 1 d . . .
O9 O 0.35257(12) -0.18341(11) 0.20545(3) 0.0080(2) Uani 1 1 d . . .
O8 O 0.33451(12) -0.06062(11) 0.06045(3) 0.00537(19) Uani 1 1 d . . .
O5 O 0.57559(11) 0.15558(13) 0.07776(3) 0.0066(2) Uani 1 1 d . . .
```

O2 O 0.87366(12) 0.73603(14) 0.10680(3) 0.0089(2) Uani 1 1 d . . .
O3 O 1.01881(12) 0.73302(12) 0.15970(3) 0.00611(19) Uani 1 1 d . . .
O1 O 0.77921(12) 0.74988(12) 0.16719(3) 0.00655(19) Uani 1 1 d . . .
O4 O 0.76708(11) 0.51224(13) 0.15058(3) 0.0066(2) Uani 1 1 d . . .
O7 O 0.42597(13) -0.05502(13) 0.12187(3) 0.0084(2) Uani 1 1 d . . .

loop_
 _atom_site_aniso_label
 _atom_site_aniso_U_11
 _atom_site_aniso_U_22
 _atom_site_aniso_U_33
 _atom_site_aniso_U_23
 _atom_site_aniso_U_13
 _atom_site_aniso_U_12
Fe1 0.00305(19) 0.00305(19) 0.0032(3) 0.000 0.000 0.00153(10)
Ca1 0.00469(14) 0.00469(12) 0.00420(14) -0.00059(10) -0.00019(10) 0.00260(11)
Ca3 0.00442(13) 0.00589(13) 0.00431(13) 0.00130(10) 0.00028(11) 0.00246(11)
Ca2 0.01162(15) 0.00662(14) 0.00774(14) -0.00155(11) 0.00505(12) -0.00168(11)
P2 0.00385(15) 0.00397(17) 0.00383(17) -0.00036(13) -0.00039(13) 0.00238(13)
P1 0.00386(16) 0.00425(16) 0.00315(17) -0.00030(13) 0.00000(14) 0.00207(13)
P3A 0.0038(2) 0.0038(2) 0.0066(5) 0.000 0.000 0.00189(10)
O10A 0.0142(8) 0.0142(8) 0.0089(12) 0.000 0.000 0.0071(4)
O6 0.0088(5) 0.0082(5) 0.0062(4) -0.0003(4) -0.0001(4) 0.0064(4)
O9 0.0073(5) 0.0048(4) 0.0119(5) 0.0014(3) 0.0033(4) 0.0032(4)
O8 0.0050(5) 0.0058(5) 0.0047(4) -0.0007(3) -0.0011(3) 0.0023(4)
O5 0.0052(4) 0.0047(5) 0.0097(5) -0.0019(4) -0.0012(4) 0.0022(4)
O2 0.0092(5) 0.0167(6) 0.0035(5) 0.0014(4) 0.0009(4) 0.0084(4)
O3 0.0045(5) 0.0071(5) 0.0058(4) 0.0004(4) 0.0000(4) 0.0023(4)
O1 0.0085(5) 0.0074(5) 0.0060(4) -0.0010(4) 0.0008(4) 0.0056(4)
O4 0.0047(5) 0.0051(5) 0.0097(5) -0.0001(4) -0.0010(4) 0.0022(4)
O7 0.0089(5) 0.0127(5) 0.0047(4) -0.0007(4) 0.0002(4) 0.0063(4)

Fe-merrillite heat treated open to air

data_FeMerrilliteAir_0m_a

_chemical_formula_sum
 ' Ca9 Fe H0.02 O28 P7'
_chemical_formula_weight 1081.38
_space_group_crystal_system trigonal
_space_group_IT_number 161
_chemical_compound_source 'synthetic'
_symmetry_space_group_name_H-M R3c
_chemical_name_mineral merrillite

loop_
 _space_group_symop_operation_xyz
 'x, y, z'
 '-y, x-y, z'
 '-x+y, -x, z'
 '-y, -x, z+1/2'

'-x+y, y, z+1/2'
'x, x-y, z+1/2'
'x+2/3, y+1/3, z+1/3'
'-y+2/3, x-y+1/3, z+1/3'
'-x+y+2/3, -x+1/3, z+1/3'
'-y+2/3, -x+1/3, z+5/6'
'-x+y+2/3, y+1/3, z+5/6'
'x+2/3, x-y+1/3, z+5/6'
'x+1/3, y+2/3, z+2/3'
'-y+1/3, x-y+2/3, z+2/3'
'-x+y+1/3, -x+2/3, z+2/3'
'-y+1/3, -x+2/3, z+7/6'
'-x+y+1/3, y+2/3, z+7/6'
'x+1/3, x-y+2/3, z+7/6'

_cell_length_a 10.3278(11)
_cell_length_b 10.3278(11)
_cell_length_c 37.050(4)
_cell_angle_alpha 90
_cell_angle_beta 90
_cell_angle_gamma 120
_cell_volume 3422.4(8)
_cell_formula_units_Z 6
_cell_measurement_temperature 100(2)
_exptl_crystal_density_diffrn 3.148
_exptl_crystal_F_000 3210
_exptl_crystal_size_max 0.07
_exptl_crystal_size_mid 0.07
_exptl_crystal_size_min 0.07
_exptl_absorpt_coefficient_mu 3.310
_exptl_absorpt_correction_type multi-scan
_exptl_absorpt_correction_T_min 0.6943
_exptl_absorpt_correction_T_max 0.7466
_exptl_absorpt_process_details "SADABS"

_diffrn_ambient_temperature 100(2)
_diffrn_radiation_wavelength 0.71073
_diffrn_radiation_type MoK\a
_diffrn_reflns_number 17589
_diffrn_reflns_av_unetI/netI 0.0139
_diffrn_reflns_av_R_equivalents 0.0248
_diffrn_reflns_limit_h_min -14
_diffrn_reflns_limit_h_max 14
_diffrn_reflns_limit_k_min -14
_diffrn_reflns_limit_k_max 14
_diffrn_reflns_limit_l_min -52
_diffrn_reflns_limit_l_max 52
_diffrn_reflns_theta_min 2.529
_diffrn_reflns_theta_max 30.506
_diffrn_reflns_theta_full 25.242
_diffrn_measured_fraction_theta_max 0.998
_diffrn_measured_fraction_theta_full 0.996
_diffrn_reflns_Laue_measured_fraction_max 0.998

```
_diffrn_reflns_Laue_measured_fraction_full   0.996
_diffrn_reflns_point_group_measured_fraction_max   0.998
_diffrn_reflns_point_group_measured_fraction_full  0.996
_reflns_number_total            2334
_reflns_number_gt               2283
_reflns_threshold_expression      'I > 2\s(I)'
_reflns_Friedel_coverage         0.994
_reflns_Friedel_fraction_max      0.998
_reflns_Friedel_fraction_full     0.997

_computing_structure_refinement   'SHELXL-2013 (Sheldrick, 2013)'

_refine_special_details
;
 Refined as a 2-component inversion twin.
;
_refine_ls_structure_factor_coef  Fsqd
_refine_ls_matrix_type           full
_refine_ls_weighting_scheme      calc
_refine_ls_weighting_details
'w=1/[\s^2^(Fo^2^)+(0.0264P)^2^+4.0671P] where P=(Fo^2^+2Fc^2^)/3'
_atom_sites_solution_primary     intrinsic
_atom_sites_solution_secondary    diffmap
_atom_sites_solution_hydrogens    .
_refine_ls_hydrogen_treatment     undef
_refine_ls_extinction_method      none
_refine_ls_extinction_coef        .
_refine_ls_abs_structure_details
;
 Refined as an inversion twin.
;
_refine_ls_abs_structure_Flack    0.56(2)
_chemical_absolute_configuration  ?
_refine_ls_number_reflns         2334
_refine_ls_number_parameters      140
_refine_ls_number_restraints      2
_refine_ls_R_factor_all          0.0175
_refine_ls_R_factor_gt           0.0172
_refine_ls_wR_factor_ref         0.0455
_refine_ls_wR_factor_gt          0.0454
_refine_ls_goodness_of_fit_ref    1.095
_refine_ls_restrained_S_all      1.094
_refine_ls_shift/su_max          0.000
_refine_ls_shift/su_mean         0.000

loop_
 _atom_site_label
 _atom_site_type_symbol
 _atom_site_fract_x
 _atom_site_fract_y
 _atom_site_fract_z
 _atom_site_U_iso_or_equiv
 _atom_site_adp_type
```

```
 _atom_site_occupancy
 _atom_site_site_symmetry_order
 _atom_site_calc_flag
 _atom_site_refinement_flags_posn
 _atom_site_refinement_flags_adp
 _atom_site_refinement_flags_occupancy
 _atom_site_disorder_assembly
 _atom_site_disorder_group
Fe1 Fe 0.6667 0.3333 0.11505(2) 0.00519(13) Uani 1 3 d S T P . .
Ca1 Ca 0.72237(6) 0.85471(6) 0.21403(2) 0.00411(12) Uani 1 1 d . . . . .
Ca3 Ca 0.50813(6) 0.04416(7) 0.17985(2) 0.00416(11) Uani 1 1 d . . . . .
Ca2 Ca 1.14831(6) 0.87139(6) 0.10715(2) 0.00557(12) Uani 1 1 d . . . . .
P2 P 0.47448(9) -0.01749(9) 0.08408(2) 0.00319(14) Uani 1 1 d . . . . .
P1 P 0.85624(8) 0.67612(9) 0.14590(2) 0.00331(13) Uani 1 1 d . . . . .
P3A P 0.3333 -0.3333 0.1952(13) 0.004 Uiso 0.029(3) 3 d DS U P . .
P3B P 0.3333 -0.3333 0.21780(3) 0.0038(3) Uani 0.971(3) 3 d S T P . .
O10A O 0.3333 -0.3333 0.25937(11) 0.0065(7) Uani 0.971(3) 3 d S T P . .
O10B O 0.3333 -0.3333 0.1549(15) 0.007 Uiso 0.029(3) 3 d DS U P . .
O6 O 0.5682(2) -0.0826(2) 0.06956(5) 0.0056(4) Uani 1 1 d . . . . .
O9 O 0.3444(2) -0.1866(2) 0.20504(5) 0.0075(4) Uani 1 1 d . . . . .
O8 O 0.3365(2) -0.0552(2) 0.06064(5) 0.0046(4) Uani 1 1 d . . . . .
O5 O 0.5763(2) 0.1589(2) 0.08082(5) 0.0046(4) Uani 1 1 d . . . . .
O2 O 0.8599(2) 0.7100(2) 0.10584(6) 0.0056(4) Uani 1 1 d . . . . .
O3 O 1.0161(2) 0.7289(2) 0.15893(5) 0.0056(4) Uani 1 1 d . . . . .
O1 O 0.7803(2) 0.7482(2) 0.16651(5) 0.0061(4) Uani 1 1 d . . . . .
O4 O 0.7619(2) 0.5034(2) 0.15187(5) 0.0051(4) Uani 1 1 d . . . . .
O7 O 0.4214(2) -0.0610(2) 0.12267(6) 0.0063(4) Uani 1 1 d . . . . .

loop_
 _atom_site_aniso_label
 _atom_site_aniso_U_11
 _atom_site_aniso_U_22
 _atom_site_aniso_U_33
 _atom_site_aniso_U_23
 _atom_site_aniso_U_13
 _atom_site_aniso_U_12
Fe1 0.00518(18) 0.00518(18) 0.0052(3) 0.000 0.000 0.00259(9)
Ca1 0.0040(3) 0.0042(2) 0.0041(2) -0.00028(19) 0.00020(19) 0.00209(19)
Ca3 0.0042(3) 0.0043(2) 0.0036(2) 0.00061(19) -0.0001(2) 0.00182(19)
Ca2 0.0052(2) 0.0045(2) 0.0052(2) 0.0001(2) 0.0017(2) 0.0011(2)
P2 0.0032(3) 0.0027(3) 0.0035(3) 0.0000(2) -0.0002(3) 0.0014(2)
P1 0.0034(3) 0.0032(3) 0.0033(3) -0.0003(2) 0.0000(3) 0.0016(2)
P3B 0.0027(3) 0.0027(3) 0.0059(6) 0.000 0.000 0.00136(17)
O10A 0.0068(10) 0.0068(10) 0.0060(16) 0.000 0.000 0.0034(5)
O6 0.0066(9) 0.0066(9) 0.0055(8) -0.0004(7) 0.0001(7) 0.0046(8)
O9 0.0067(9) 0.0045(9) 0.0115(10) 0.0024(7) 0.0028(8) 0.0029(8)
O8 0.0044(9) 0.0043(8) 0.0046(8) -0.0001(7) -0.0008(7) 0.0019(7)
O5 0.0036(8) 0.0036(9) 0.0064(9) 0.0005(7) -0.0001(7) 0.0015(7)
O2 0.0064(9) 0.0078(9) 0.0035(9) 0.0005(7) 0.0004(7) 0.0042(8)
O3 0.0042(9) 0.0068(9) 0.0048(8) 0.0007(7) -0.0002(7) 0.0020(7)
O1 0.0079(9) 0.0070(9) 0.0054(8) -0.0011(7) 0.0005(7) 0.0051(8)
O4 0.0043(9) 0.0035(9) 0.0064(9) 0.0000(7) -0.0005(7) 0.0011(7)
O7 0.0076(9) 0.0059(9) 0.0051(8) 0.0010(7) 0.0007(7) 0.0032(8)
```

Fe-merrillite heat treated in an SiO_2 sealed tube

```
data_FeMerrilliteQTZ_0m_a

_chemical_formula_sum
 ' Ca9.44 Fe H0.12 O28 P7'
_chemical_formula_weight        1099.12
_chemical_name_mineral          merrillite
_space_group_crystal_system     trigonal
_space_group_IT_number          161
_chemical_compound_source       'synthetic'
_symmetry_space_group_name_H-M    R3c

loop_
 _space_group_symop_operation_xyz
 'x, y, z'
 '-y, x-y, z'
 '-x+y, -x, z'
 '-y, -x, z+1/2'
 '-x+y, y, z+1/2'
 'x, x-y, z+1/2'
 'x+2/3, y+1/3, z+1/3'
 '-y+2/3, x-y+1/3, z+1/3'
 '-x+y+2/3, -x+1/3, z+1/3'
 '-y+2/3, -x+1/3, z+5/6'
 '-x+y+2/3, y+1/3, z+5/6'
 'x+2/3, x-y+1/3, z+5/6'
 'x+1/3, y+2/3, z+2/3'
 '-y+1/3, x-y+2/3, z+2/3'
 '-x+y+1/3, -x+2/3, z+2/3'
 '-y+1/3, -x+2/3, z+7/6'
 '-x+y+1/3, y+2/3, z+7/6'
 'x+1/3, x-y+2/3, z+7/6'

_cell_length_a                10.3453(6)
_cell_length_b                10.3453(6)
_cell_length_c                37.118(2)
_cell_angle_alpha               90
_cell_angle_beta                90
_cell_angle_gamma                120
_cell_volume                  3440.3(5)
_cell_formula_units_Z           6
_cell_measurement_temperature     100(2)
_exptl_crystal_density_diffrn     3.183
_exptl_crystal_F_000            3264
_exptl_crystal_size_max          .05
_exptl_crystal_size_mid          .05
_exptl_crystal_size_min          .05
_exptl_absorpt_coefficient_mu     3.392
_exptl_absorpt_correction_type    multi-scan
_exptl_absorpt_correction_T_min   0.6939
_exptl_absorpt_correction_T_max   0.7466
```

```
_exptl_absorpt_process_details    "SADABS"

_diffrn_ambient_temperature      100(2)
_diffrn_radiation_wavelength     0.71073
_diffrn_radiation_type           MoK\a
_diffrn_refIns_number            11475
_diffrn_refIns_av_unetI/netI     0.0178
_diffrn_refIns_av_R_equivalents  0.0236
_diffrn_refIns_limit_h_min       -14
_diffrn_refIns_limit_h_max       14
_diffrn_refIns_limit_k_min       -14
_diffrn_refIns_limit_k_max       14
_diffrn_refIns_limit_l_min       -45
_diffrn_refIns_limit_l_max       52
_diffrn_refIns_theta_min         2.524
_diffrn_refIns_theta_max         30.488
_diffrn_refIns_theta_full        25.242
_diffrn_measured_fraction_theta_max  1.000
_diffrn_measured_fraction_theta_full  0.999
_diffrn_refIns_Laue_measured_fraction_max    1.000
_diffrn_refIns_Laue_measured_fraction_full   0.999
_diffrn_refIns_point_group_measured_fraction_max   1.000
_diffrn_refIns_point_group_measured_fraction_full  0.999
_refIns_number_total             2238
_refIns_number_gt                2189
_refIns_threshold_expression     'I > 2\s(I)'
_refIns_Friedel_coverage         0.994
_refIns_Friedel_fraction_max     1.000
_refIns_Friedel_fraction_full    1.000


_computing_structure_refinement   'SHELXL-2013 (Sheldrick, 2013)'


_refine_special_details
;
 Refined as a 2-component inversion twin.
;
_refine_ls_structure_factor_coef  Fsqd
_refine_ls_matrix_type           full
_refine_ls_weighting_scheme      calc
_refine_ls_weighting_details
'w=1/[\s^2^(Fo^2^)+(0.0276P)^2^+8.5052P] where P=(Fo^2^+2Fc^2^)/3'
_atom_sites_solution_primary     intrinsic
_atom_sites_solution_secondary    diffmap
_atom_sites_solution_hydrogens    none
_refine_ls_hydrogen_treatment     none
_refine_ls_extinction_method      none
_refine_ls_extinction_coef        .
_refine_ls_abs_structure_details
;
 Refined as an inversion twin.
;
```

_refine_ls_abs_structure_Flack 0.48(3)
_chemical_absolute_configuration ?
_refine_ls_number_reflns 2238
_refine_ls_number_parameters 146
_refine_ls_number_restraints 2
_refine_ls_R_factor_all 0.0211
_refine_ls_R_factor_gt 0.0204
_refine_ls_wR_factor_ref 0.0521
_refine_ls_wR_factor_gt 0.0517
_refine_ls_goodness_of_fit_ref 1.078
_refine_ls_restrained_S_all 1.078
_refine_ls_shift/su_max 0.001
_refine_ls_shift/su_mean 0.000

loop_
_atom_site_label
_atom_site_type_symbol
_atom_site_fract_x
_atom_site_fract_y
_atom_site_fract_z
_atom_site_U_iso_or_equiv
_atom_site_adp_type
_atom_site_occupancy
_atom_site_site_symmetry_order
_atom_site_calc_flag
_atom_site_refinement_flags_posn
_atom_site_refinement_flags_adp
_atom_site_refinement_flags_occupancy
_atom_site_disorder_assembly
_atom_site_disorder_group
Fe1 Fe 0.6667 0.3333 0.11420(3) 0.00572(14) Uani 1 3 d S T P . .
Ca1 Ca 0.72446(8) 0.85713(7) 0.21332(2) 0.00491(13) Uani 1 1 d . . . . .
Ca3 Ca 0.50988(7) 0.05019(8) 0.17850(2) 0.00503(13) Uani 1 1 d . . . . .
Ca2 Ca 1.14949(8) 0.87308(8) 0.10639(2) 0.01494(16) Uani 1 1 d . . . . .
P2 P 0.47132(11) -0.02015(10) 0.08205(2) 0.00514(17) Uani 1 1 d . . . . .
P1 P 0.86017(10) 0.67945(10) 0.14554(2) 0.00426(16) Uani 1 1 d . . . . .
P3B P 0.3333 -0.3333 0.21379(6) 0.0051(5) Uani 0.761(5) 3 d S T P . .
P3A P 0.3333 -0.3333 0.1932(2) 0.005 Uiso 0.239(5) 3 d DS U P . .
O10A O 0.3333 -0.3333 0.25546(17) 0.0085(12) Uani 0.761(5) 3 d S T P . .
O10B O 0.3333 -0.3333 0.1520(2) 0.009 Uiso 0.239(5) 3 d DS U P . .
O6 O 0.5602(3) -0.0930(3) 0.06843(7) 0.0156(6) Uani 1 1 d . . . . .
O9 O 0.3420(3) -0.1882(3) 0.20178(9) 0.0165(6) Uani 1 1 d . . . . .
O8 O 0.3317(3) -0.0575(3) 0.05945(6) 0.0063(4) Uani 1 1 d . . . . .
O5 O 0.5746(3) 0.1516(3) 0.07811(7) 0.0092(5) Uani 1 1 d . . . . .
O2 O 0.8660(3) 0.7168(3) 0.10543(7) 0.0104(5) Uani 1 1 d . . . . .
O3 O 1.0204(2) 0.7308(3) 0.15797(6) 0.0068(4) Uani 1 1 d . . . . .
O1 O 0.7857(3) 0.7538(3) 0.16568(7) 0.0087(5) Uani 1 1 d . . . . .
O4 O 0.7656(3) 0.5096(3) 0.15229(7) 0.0070(4) Uani 1 1 d . . . . .
O7 O 0.4176(3) -0.0657(3) 0.12080(7) 0.0141(5) Uani 1 1 d . . . . .
Ca4a Ca 0.3333 -0.3333 0.13595(13) 0.0112(13) Uiso 0.296(7) 3 d S . P . .
Ca4b Ca 0.3333 -0.3333 0.1028(3) 0.013(3) Uiso 0.148(7) 3 d S . P . .

loop_
 _atom_site_aniso_label
 _atom_site_aniso_U_11
 _atom_site_aniso_U_22
 _atom_site_aniso_U_33
 _atom_site_aniso_U_23
 _atom_site_aniso_U_13
 _atom_site_aniso_U_12
Fe1 0.00575(19) 0.00575(19) 0.0057(3) 0.000 0.000 0.00288(10)
Ca1 0.0055(3) 0.0056(3) 0.0043(3) -0.0007(2) -0.0001(2) 0.0032(2)
Ca3 0.0040(3) 0.0056(3) 0.0049(3) 0.0016(2) 0.0002(3) 0.0020(2)
Ca2 0.0125(3) 0.0103(3) 0.0089(3) -0.0014(3) 0.0053(3) -0.0041(3)
P2 0.0074(4) 0.0057(3) 0.0037(4) -0.0007(3) -0.0008(3) 0.0043(3)
P1 0.0045(3) 0.0046(3) 0.0038(4) -0.0002(3) -0.0003(3) 0.0024(3)
P3B 0.0025(5) 0.0025(5) 0.0104(13) 0.000 0.000 0.0012(2)
O10A 0.0094(17) 0.0094(17) 0.007(3) 0.000 0.000 0.0047(8)
O6 0.0272(15) 0.0239(14) 0.0095(12) -0.0054(10) -0.0061(10) 0.0231(13)
O9 0.0123(11) 0.0080(11) 0.0320(16) 0.0084(11) 0.0128(11) 0.0071(11)
O8 0.0070(10) 0.0055(10) 0.0046(10) -0.0004(8) -0.0008(8) 0.0017(8)
O5 0.0052(10) 0.0090(12) 0.0126(12) -0.0031(9) -0.0014(8) 0.0030(9)
O2 0.0076(11) 0.0209(13) 0.0040(11) 0.0010(9) -0.0004(9) 0.0080(10)
O3 0.0049(10) 0.0080(10) 0.0052(10) 0.0010(8) -0.0012(8) 0.0016(9)
O1 0.0133(11) 0.0109(10) 0.0057(11) -0.0010(8) 0.0003(9) 0.0089(9)
O4 0.0049(10) 0.0052(11) 0.0100(12) -0.0006(9) -0.0011(8) 0.0018(9)
O7 0.0155(13) 0.0246(14) 0.0053(11) 0.0004(10) -0.0012(9) 0.0123(12)

Fe/Mg-merrillite heat treated open to air

data_FeMgMerrillite_Air_0m_a

_chemical_formula_sum
'Ca9 Fe0.75 Mg0.25 O28 P7'
_chemical_formula_weight 1073.59
_chemical_name_mineral merrillite
_space_group_crystal_system trigonal
_space_group_IT_number 161
_chemical_compound_source 'synthetic'
_symmetry_space_group_name_H-M R3c

loop_
_space_group_symop_operation_xyz
'x, y, z'
'-y, x-y, z'
'-x+y, -x, z'
'-y, -x, z+1/2'
'-x+y, y, z+1/2'
'x, x-y, z+1/2'
'x+2/3, y+1/3, z+1/3'
'-y+2/3, x-y+1/3, z+1/3'
'-x+y+2/3, -x+1/3, z+1/3'

'-y+2/3, -x+1/3, z+5/6'
'-x+y+2/3, y+1/3, z+5/6'
'x+2/3, x-y+1/3, z+5/6'
'x+1/3, y+2/3, z+2/3'
'-y+1/3, x-y+2/3, z+2/3'
'-x+y+1/3, -x+2/3, z+2/3'
'-y+1/3, -x+2/3, z+7/6'
'-x+y+1/3, y+2/3, z+7/6'
'x+1/3, x-y+2/3, z+7/6'

_cell_length_a 10.3301(13)
_cell_length_b 10.3301(13)
_cell_length_c 37.062(5)
_cell_angle_alpha 90
_cell_angle_beta 90
_cell_angle_gamma 120
_cell_volume 3425.1(10)
_cell_formula_units_Z 6
_cell_measurement_temperature 100(2)
_exptl_crystal_density_diffrn 3.123
_exptl_crystal_size_max 0.07
_exptl_crystal_size_mid 0.07
_exptl_crystal_size_min 0.07
_exptl_absorpt_coefficient_mu 3.164
_exptl_absorpt_correction_type multi-scan
_exptl_absorpt_correction_T_min 0.7025
_exptl_absorpt_correction_T_max 0.7466
_exptl_absorpt_process_details "Sadabs"

_diffrn_ambient_temperature 100(2)
_diffrn_radiation_wavelength 0.71073
_diffrn_radiation_type MoK\a
_diffrn_reflns_number 17501
_diffrn_reflns_av_unetI/netI 0.0141
_diffrn_reflns_av_R_equivalents 0.0249
_diffrn_reflns_limit_h_min -14
_diffrn_reflns_limit_h_max 14
_diffrn_reflns_limit_k_min -14
_diffrn_reflns_limit_k_max 14
_diffrn_reflns_limit_l_min -52
_diffrn_reflns_limit_l_max 52
_diffrn_reflns_theta_min 2.528
_diffrn_reflns_theta_max 30.498
_diffrn_reflns_theta_full 25.242
_diffrn_measured_fraction_theta_max 1.000
_diffrn_measured_fraction_theta_full 0.999
_diffrn_reflns_Laue_measured_fraction_max 1.000
_diffrn_reflns_Laue_measured_fraction_full 0.999
_diffrn_reflns_point_group_measured_fraction_max 1.000
_diffrn_reflns_point_group_measured_fraction_full 0.999
_reflns_number_total 2338

```
_reflns_number_gt               2278
_reflns_threshold_expression     'I > 2\s(I)'
_reflns_Friedel_coverage         0.994
_reflns_Friedel_fraction_max     1.000
_reflns_Friedel_fraction_full    1.000
_computing_structure_refinement   'SHELXL-2013 (Sheldrick, 2013)'


_refine_special_details
;
Refined as a 2-component inversion twin.
;
_refine_ls_structure_factor_coef  Fsqd
_refine_ls_matrix_type           full
_refine_ls_weighting_scheme      calc
_refine_ls_weighting_details
'w=1/[\s^2^(Fo^2^)+(0.0314P)^2^+4.3497P] where P=(Fo^2^+2Fc^2^)/3'
_atom_sites_solution_primary     intrinsic
_atom_sites_solution_secondary    diffmap
_atom_sites_solution_hydrogens    none
_refine_ls_hydrogen_treatment     none
_refine_ls_extinction_method      none
_refine_ls_extinction_coef        .
_refine_ls_abs_structure_details
;
Refined as an inversion twin.
;
_refine_ls_abs_structure_Flack    0.49(3)
_chemical_absolute_configuration  ?
_refine_ls_number_reflns         2338
_refine_ls_number_parameters     143
_refine_ls_number_restraints     2
_refine_ls_R_factor_all          0.0178
_refine_ls_R_factor_gt           0.0171
_refine_ls_wR_factor_ref         0.0489
_refine_ls_wR_factor_gt          0.0483
_refine_ls_goodness_of_fit_ref    1.053
_refine_ls_restrained_S_all      1.053
_refine_ls_shift/su_max          0.001
_refine_ls_shift/su_mean         0.000

loop_
_atom_site_label
_atom_site_type_symbol
_atom_site_fract_x
_atom_site_fract_y
_atom_site_fract_z
_atom_site_U_iso_or_equiv
_atom_site_adp_type
_atom_site_occupancy
_atom_site_site_symmetry_order
_atom_site_calc_flag
_atom_site_refinement_flags_posn
```

_atom_site_refinement_flags_adp
_atom_site_refinement_flags_occupancy
_atom_site_disorder_assembly
_atom_site_disorder_group
Fe1 Fe 0.6667 0.3333 0.11488(2) 0.0019(3) Uani 0.754(7) 3 d S T P . .
Mg1 Mg 0.6667 0.3333 0.11488(2) 0.002 Uiso 0.246(7) 3 d S U P . .
Ca1 Ca 0.72255(6) 0.85481(6) 0.21402(2) 0.00404(12) Uani 1 1 d . . . . .
Ca3 Ca 0.50884(6) 0.04511(7) 0.17962(2) 0.00405(12) Uani 1 1 d . . . . .
Ca2 Ca 1.14889(7) 0.87089(6) 0.10713(2) 0.00741(12) Uani 1 1 d . . . . .
P2 P 0.47459(9) -0.01742(9) 0.08372(2) 0.00299(14) Uani 1 1 d . . . . .
P1 P 0.85644(8) 0.67669(9) 0.14577(2) 0.00309(13) Uani 1 1 d . . . . .
P3B P 0.3333 -0.3333 0.21701(4) 0.0047(3) Uani 0.935(4) 3 d S T P . .
P3A P 0.3333 -0.3333 0.1933(5) 0.005 Uiso 0.065(4) 3 d DS U P . .
O10B O 0.3333 -0.3333 0.25863(12) 0.0074(7) Uani 0.935(4) 3 d S T P . .
O10A O 0.3333 -0.3333 0.1511(8) 0.007 Uiso 0.065(4) 3 d DS U P . .
O6 O 0.5677(2) -0.0831(2) 0.06914(5) 0.0065(4) Uani 1 1 d . . . . .
O9 O 0.3436(2) -0.1870(2) 0.20443(6) 0.0093(4) Uani 1 1 d . . . . .
O8 O 0.3356(2) -0.0559(2) 0.06051(5) 0.0053(4) Uani 1 1 d . . . . .
O5 O 0.5762(2) 0.1582(2) 0.08034(5) 0.0045(4) Uani 1 1 d . . . . .
O2 O 0.8613(2) 0.7119(3) 0.10574(6) 0.0070(4) Uani 1 1 d . . . . .
O3 O 1.0161(2) 0.7291(2) 0.15895(5) 0.0059(4) Uani 1 1 d . . . . .
O1 O 0.7800(2) 0.7486(2) 0.16629(6) 0.0067(4) Uani 1 1 d . . . . .
O4 O 0.7623(2) 0.5041(2) 0.15157(5) 0.0046(4) Uani 1 1 d . . . . .
O7 O 0.4222(3) -0.0616(2) 0.12242(6) 0.0078(4) Uani 1 1 d . . . . .

loop_
_atom_site_aniso_label
_atom_site_aniso_U_11
_atom_site_aniso_U_22
_atom_site_aniso_U_33
_atom_site_aniso_U_23
_atom_site_aniso_U_13
_atom_site_aniso_U_12
Fe1 0.0020(3) 0.0020(3) 0.0018(4) 0.000 0.000 0.00099(15)
Ca1 0.0046(3) 0.0041(2) 0.0039(2) -0.00055(19) -0.0001(2) 0.00253(19)
Ca3 0.0039(3) 0.0043(2) 0.0038(2) 0.00076(19) 0.0003(2) 0.00196(19)
Ca2 0.0069(2) 0.0058(3) 0.0060(2) -0.0004(2) 0.0024(2) 0.0006(2)
P2 0.0034(3) 0.0027(3) 0.0031(3) 0.0001(2) -0.0001(3) 0.0017(2)
P1 0.0032(3) 0.0030(3) 0.0030(3) -0.0001(2) 0.0001(3) 0.0015(2)
P3B 0.0026(4) 0.0026(4) 0.0088(7) 0.000 0.000 0.00132(18)
O10B 0.0070(11) 0.0070(11) 0.0083(17) 0.000 0.000 0.0035(5)
O6 0.0075(9) 0.0083(9) 0.0061(8) -0.0004(7) -0.0001(7) 0.0057(8)
O9 0.0087(9) 0.0060(9) 0.0150(10) 0.0045(7) 0.0054(8) 0.0051(8)
O8 0.0052(9) 0.0041(8) 0.0055(8) -0.0005(7) -0.0007(7) 0.0014(7)
O5 0.0031(8) 0.0033(9) 0.0060(9) -0.0006(7) -0.0010(6) 0.0008(7)
O2 0.0089(10) 0.0093(10) 0.0041(9) 0.0000(7) 0.0002(7) 0.0056(8)
O3 0.0042(9) 0.0066(9) 0.0063(8) 0.0009(7) -0.0015(7) 0.0023(8)
O1 0.0084(9) 0.0063(9) 0.0064(8) -0.0009(7) 0.0012(7) 0.0045(8)
O4 0.0047(9) 0.0031(9) 0.0061(9) -0.0003(7) -0.0005(7) 0.0020(7)
O7 0.0106(10) 0.0085(9) 0.0048(8) 0.0012(7) 0.0011(7) 0.0051(8)

Fe/Mg-merrillite heat treated in an SiO_2 sealed tube

```
data_FeMgMerrillite_QTZ_0m_a_a

_chemical_formula_sum
' Ca9.36 Fe0.65 H0.28 Mg0.35 O28 P7'
_chemical_formula_weight         1084.98
_space_group_crystal_system      trigonal
_space_group_IT_number           161
_chemical_name_mineral           merrillite
_chemical_compound_source        'synthetic'
_symmetry_space_group_name_H-M    R3c


loop_
 _space_group_symop_operation_xyz
 'x, y, z'
 '-y, x-y, z'
 '-x+y, -x, z'
 '-y, -x, z+1/2'
 '-x+y, y, z+1/2'
 'x, x-y, z+1/2'
 'x+2/3, y+1/3, z+1/3'
 '-y+2/3, x-y+1/3, z+1/3'
 '-x+y+2/3, -x+1/3, z+1/3'
 '-y+2/3, -x+1/3, z+5/6'
 '-x+y+2/3, y+1/3, z+5/6'
 'x+2/3, x-y+1/3, z+5/6'
 'x+1/3, y+2/3, z+2/3'
 '-y+1/3, x-y+2/3, z+2/3'
 '-x+y+1/3, -x+2/3, z+2/3'
 '-y+1/3, -x+2/3, z+7/6'
 '-x+y+1/3, y+2/3, z+7/6'
 'x+1/3, x-y+2/3, z+7/6'

_cell_length_a                10.3392(7)
_cell_length_b                10.3392(7)
_cell_length_c                37.081(2)
_cell_angle_alpha              90
_cell_angle_beta               90
_cell_angle_gamma              120
_cell_volume                  3432.8(5)
_cell_formula_units_Z          6
_cell_measurement_temperature    100(2)
_exptl_crystal_density_diffrn    3.149
_exptl_crystal_F_000           3225
_exptl_crystal_size_max         0.06
_exptl_crystal_size_mid         0.06
_exptl_crystal_size_min         0.06
_exptl_absorpt_coefficient_mu    3.176
_exptl_absorpt_correction_type   multi-scan
_exptl_absorpt_correction_T_min  0.6997
```

```
_exptl_absorpt_correction_T_max  0.7466
_exptl_absorpt_process_details   "SADABS"

_diffrn_ambient_temperature      100(2)
_diffrn_radiation_wavelength     0.71073
_diffrn_radiation_type           MoK\a
_diffrn_reflns_number            17513
_diffrn_reflns_av_unetI/netI     0.0120
_diffrn_reflns_av_R_equivalents  0.0213
_diffrn_reflns_limit_h_min       -14
_diffrn_reflns_limit_h_max       14
_diffrn_reflns_limit_k_min       -14
_diffrn_reflns_limit_k_max       14
_diffrn_reflns_limit_l_min       -52
_diffrn_reflns_limit_l_max       52
_diffrn_reflns_theta_min         2.526
_diffrn_reflns_theta_max         30.494
_diffrn_reflns_theta_full        25.242
_diffrn_measured_fraction_theta_max  0.997
_diffrn_measured_fraction_theta_full  0.994
_diffrn_reflns_Laue_measured_fraction_max   0.997
_diffrn_reflns_Laue_measured_fraction_full  0.994
_diffrn_reflns_point_group_measured_fraction_max  0.998
_diffrn_reflns_point_group_measured_fraction_full  0.996
_reflns_number_total             2342
_reflns_number_gt                2313
_reflns_threshold_expression     'I > 2\s(I)'
_reflns_Friedel_coverage         0.996
_reflns_Friedel_fraction_max     0.999
_reflns_Friedel_fraction_full    0.999

_computing_structure_refinement  'SHELXL-2013 (Sheldrick, 2013)'


_refine_special_details
;
 Refined as a 2-component inversion twin.
;
_refine_ls_structure_factor_coef  Fsqd
_refine_ls_matrix_type           full
_refine_ls_weighting_scheme      calc
_refine_ls_weighting_details
'w=1/[\s^2^(Fo^2^)+(0.0231P)^2^+5.1052P] where P=(Fo^2^+2Fc^2^)/3'
_atom_sites_solution_primary     none
_atom_sites_solution_secondary   none
_atom_sites_solution_hydrogens   none
_refine_ls_hydrogen_treatment    none
_refine_ls_extinction_method     none
_refine_ls_extinction_coef       .
_refine_ls_abs_structure_details
;
 Refined as an inversion twin.
;
```

```
_refine_ls_abs_structure_Flack    0.49(3)
_chemical_absolute_configuration  ?
_refine_ls_number_reflns         2342
_refine_ls_number_parameters     153
_refine_ls_number_restraints     2
_refine_ls_R_factor_all          0.0160
_refine_ls_R_factor_gt           0.0157
_refine_ls_wR_factor_ref         0.0414
_refine_ls_wR_factor_gt          0.0411
_refine_ls_goodness_of_fit_ref   1.085
_refine_ls_restrained_S_all      1.085
_refine_ls_shift/su_max          0.000
_refine_ls_shift/su_mean         0.000

loop_
 _atom_site_label
 _atom_site_type_symbol
 _atom_site_fract_x
 _atom_site_fract_y
 _atom_site_fract_z
 _atom_site_U_iso_or_equiv
 _atom_site_adp_type
 _atom_site_occupancy
 _atom_site_site_symmetry_order
 _atom_site_calc_flag
 _atom_site_refinement_flags_posn
 _atom_site_refinement_flags_adp
 _atom_site_refinement_flags_occupancy
 _atom_site_disorder_assembly
 _atom_site_disorder_group
Fe1 Fe 0.6667 0.3333 0.11499(2) 0.0037(3) Uani 0.646(6) 3 d S T P . .
Mg1 Mg 0.6667 0.3333 0.11499(2) 0.004 Uiso 0.354(6) 3 d S U P . .
Ca1 Ca 0.72390(6) 0.85662(6) 0.21442(2) 0.00529(10) Uani 1 1 d . . . . .
Ca3 Ca 0.51028(6) 0.05093(6) 0.17944(2) 0.00551(10) Uani 1 1 d . . . . .
Ca2 Ca 1.15060(6) 0.87166(6) 0.10741(2) 0.01588(13) Uani 1 1 d . . . . .
P2 P 0.47248(8) -0.01935(8) 0.08298(2) 0.00539(13) Uani 1 1 d . . . . .
P1 P 0.86006(8) 0.67984(8) 0.14641(2) 0.00467(12) Uani 1 1 d . . . . .
P3B P 0.3333 -0.3333 0.21458(7) 0.0061(5) Uani 0.691(7) 3 d S T P . .
P3A P 0.3333 -0.3333 0.19357(12) 0.0036(11) Uani 0.309(7) 3 d DS T P . .
O10A O 0.3333 -0.3333 0.1523(2) 0.015(3) Uani 0.309(7) 3 d DS T P . .
O10B O 0.3333 -0.3333 0.25597(15) 0.0109(11) Uani 0.691(7) 3 d S T P . .
O6 O 0.5620(2) -0.0909(2) 0.06936(5) 0.0132(4) Uani 1 1 d . . . . .
O9 O 0.3431(3) -0.1876(2) 0.20297(6) 0.0169(4) Uani 1 1 d . . . . .
O8 O 0.3325(2) -0.0579(2) 0.06038(5) 0.0063(3) Uani 1 1 d . . . . .
O5 O 0.5750(2) 0.1529(2) 0.07916(5) 0.0098(4) Uani 1 1 d . . . . .
O2 O 0.8670(2) 0.7198(3) 0.10630(5) 0.0127(4) Uani 1 1 d . . . . .
O3 O 1.02029(19) 0.7311(2) 0.15898(5) 0.0072(3) Uani 1 1 d . . . . .
O1 O 0.7846(2) 0.7528(2) 0.16670(5) 0.0094(3) Uani 1 1 d . . . . .
O4 O 0.7655(2) 0.5093(2) 0.15245(5) 0.0080(3) Uani 1 1 d . . . . .
O7 O 0.4189(2) -0.0650(3) 0.12179(5) 0.0152(4) Uani 1 1 d . . . . .
Ca4B Ca 0.3333 -0.3333 0.13691(12) 0.0067(11) Uani 0.264(6) 3 d S T P . .
Ca4A Ca 0.3333 -0.3333 0.1041(3) 0.019(3) Uani 0.098(6) 3 d S T P . .
```

```
loop_
 _atom_site_aniso_label
 _atom_site_aniso_U_11
 _atom_site_aniso_U_22
 _atom_site_aniso_U_33
 _atom_site_aniso_U_23
 _atom_site_aniso_U_13
 _atom_site_aniso_U_12
Fe1 0.0036(3) 0.0036(3) 0.0038(4) 0.000 0.000 0.00181(15)
Ca1 0.0058(2) 0.0056(2) 0.0052(2) -0.00089(17) -0.00049(17) 0.00340(18)
Ca3 0.0047(2) 0.0061(2) 0.0054(2) 0.00142(17) -0.00002(19) 0.00235(18)
Ca2 0.0135(3) 0.0107(2) 0.0095(2) -0.0019(2) 0.0058(2) -0.0044(2)
P2 0.0068(3) 0.0061(3) 0.0047(3) -0.0005(2) -0.0008(2) 0.0043(2)
P1 0.0051(3) 0.0054(3) 0.0036(3) -0.0003(2) -0.0001(2) 0.0028(2)
P3B 0.0034(5) 0.0034(5) 0.0115(14) 0.000 0.000 0.0017(2)
P3A 0.0052(11) 0.0052(11) 0.000(3) 0.000 0.000 0.0026(5)
O10A 0.022(5) 0.022(5) 0.002(6) 0.000 0.000 0.011(2)
O10B 0.0100(15) 0.0100(15) 0.013(2) 0.000 0.000 0.0050(8)
O6 0.0207(10) 0.0195(9) 0.0097(8) -0.0036(7) -0.0035(7) 0.0177(9)
O9 0.0135(9) 0.0079(8) 0.0319(12) 0.0078(8) 0.0126(8) 0.0074(8)
O8 0.0062(8) 0.0065(7) 0.0052(7) 0.0003(6) -0.0003(6) 0.0023(6)
O5 0.0055(8) 0.0090(9) 0.0143(9) -0.0032(7) -0.0013(6) 0.0033(7)
O2 0.0113(9) 0.0252(11) 0.0045(8) 0.0014(7) 0.0002(7) 0.0112(8)
O3 0.0048(8) 0.0077(8) 0.0069(7) 0.0011(6) -0.0002(6) 0.0014(7)
O1 0.0130(8) 0.0099(8) 0.0077(7) -0.0014(6) 0.0006(6) 0.0075(7)
O4 0.0059(8) 0.0048(8) 0.0122(8) -0.0015(6) -0.0018(6) 0.0019(7)
O7 0.0185(10) 0.0271(11) 0.0056(8) 0.0007(7) 0.0000(7) 0.0157(9)
Ca4B 0.0066(12) 0.0066(12) 0.007(2) 0.000 0.000 0.0033(6)
Ca4A 0.022(4) 0.022(4) 0.013(5) 0.000 0.000 0.011(2)
```

APPENDIX II

SUPPLEMENTARY INFORMATION FOR CHAPTER THREE

Contents

Supplementary Figures

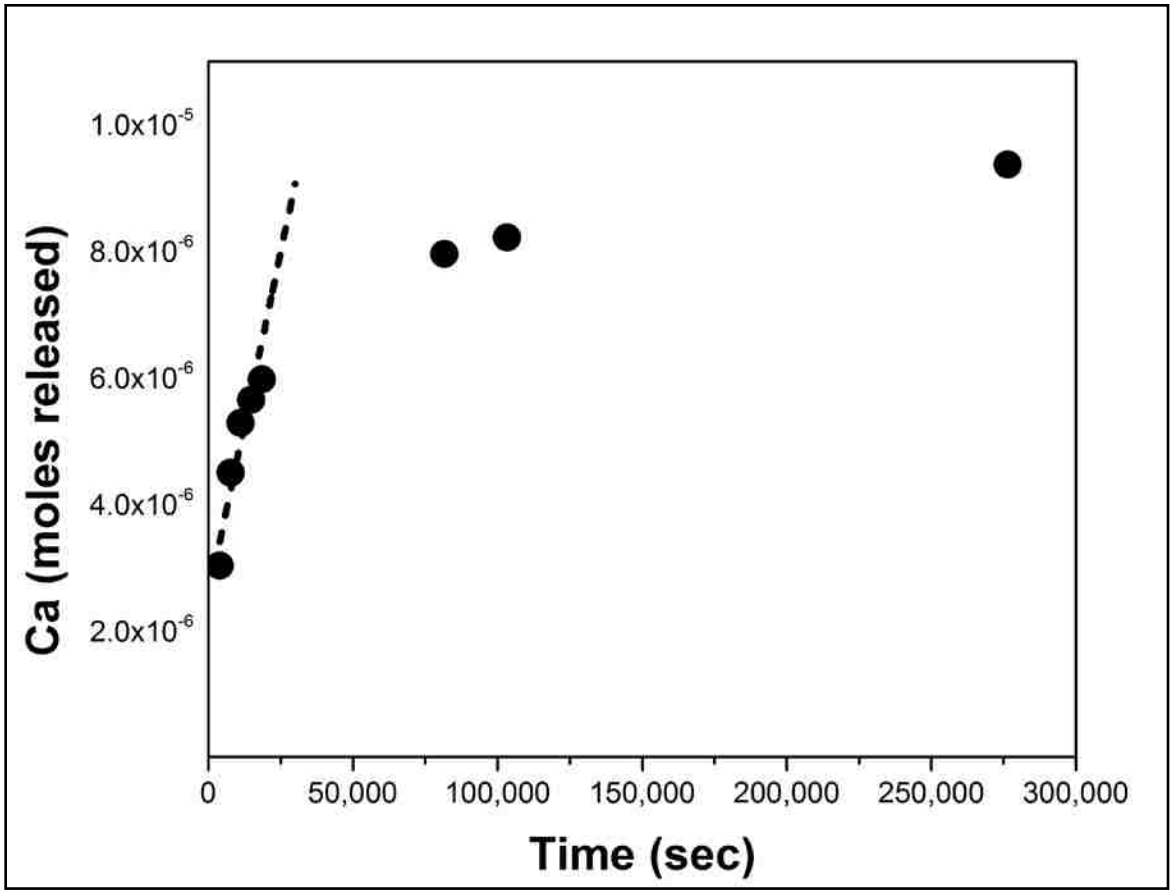

Figure S1. Example of initial rate method batch experiment. At the onset of the experiment while the batch is at far from equilibrium conditions, cumulative moles of Ca released increase sharply in a linear fashion. To calculate a dissolution rate using the initial rate method, regression analysis is applied to measurements taken at the beginning of the experiment during the linear phase (dashed line) before initial conditions change significantly. The slope of the fitted line represents the release rate of Ca which, adjusted for surface area and mineral stoichiometry, represents the dissolution rate of the mineral under the conditions of the experiment. As the experiment continues, concentrations approach steady state. Data in figure is from experiment FAP-P4D.

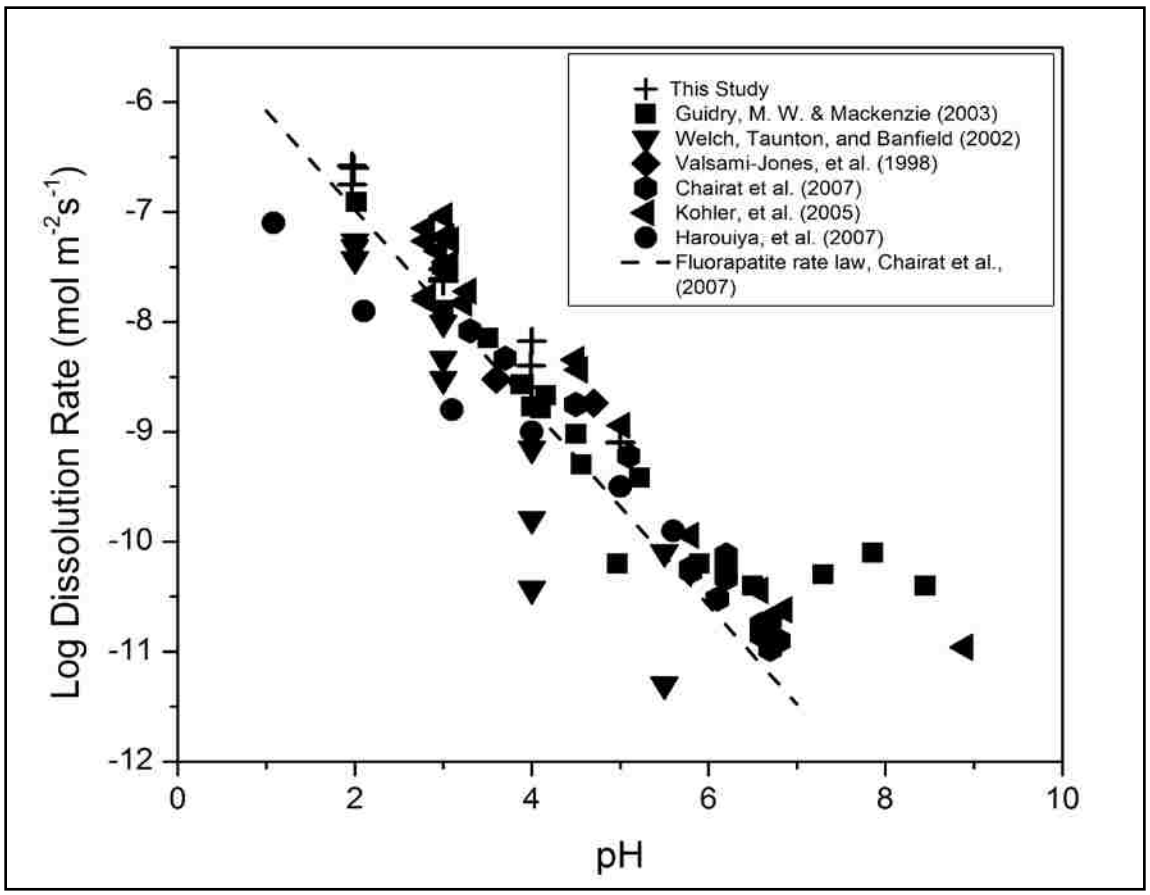

Figure S2. Results of fluorapatite dissolution experiments from this study (+ symbols) plotted with fluorapatite rate data from multiple previous studies. Measured dissolution rates for fluorapatite from this study all fall within half an order of magnitude of previously published data points (Valsami-Jones et al., 1998; Welch et al., 2002; Guidry and Mackenzie, 2003; Köhler et al., 2005; Chaïrat et al., 2007; Harouiya et al., 2007; Bandstra et al., 2008). The intrinsic rate constant (k_H+) for the fluorapatite rate law derived in this study is within error of the intrinsic rate constant for a previously published rate law, and the pH dependence (n) in this study is within 10% of a previously published pH dependence (Chaïrat et al., 2007).

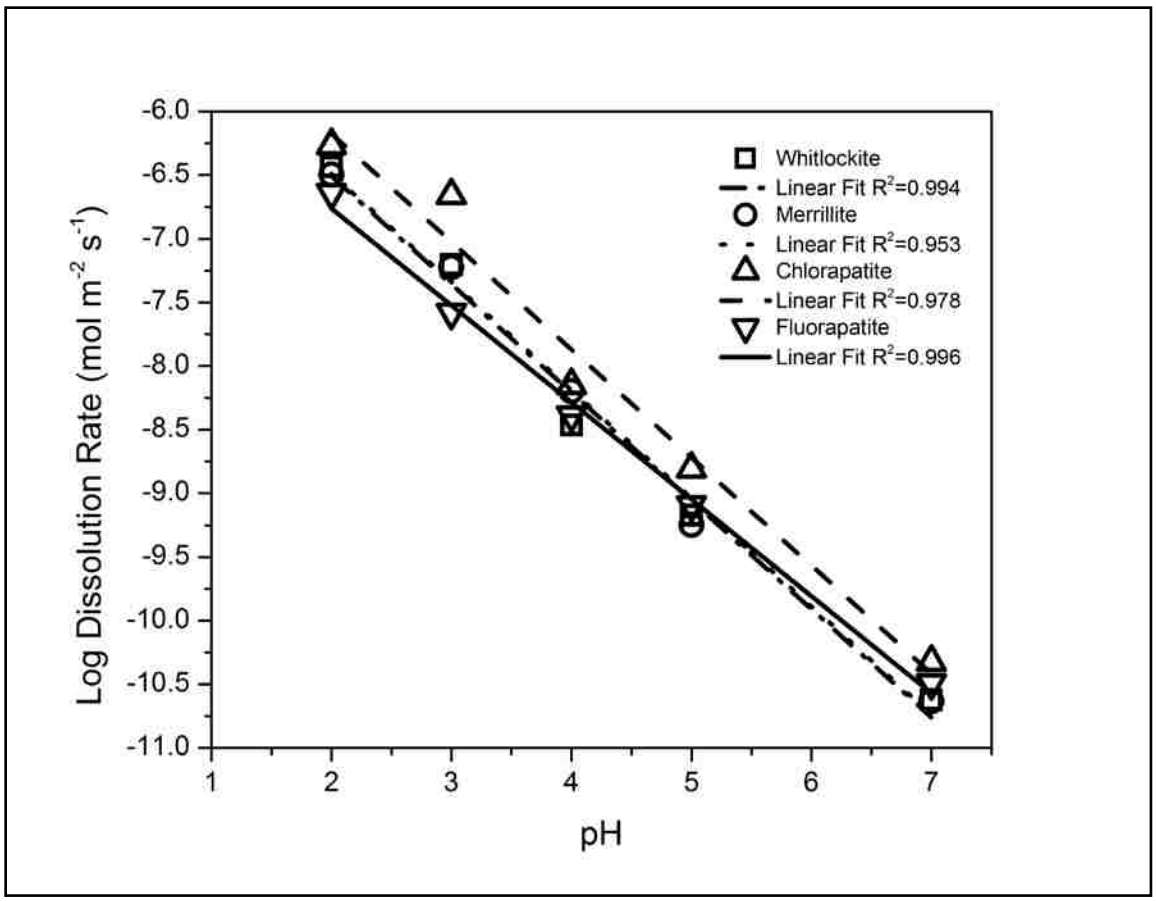

Figure S3. Plot of log dissolution rate law fits incorporating initial rate data from solubility experiments. Plot shows general rate law trends continue into neutral pH range.

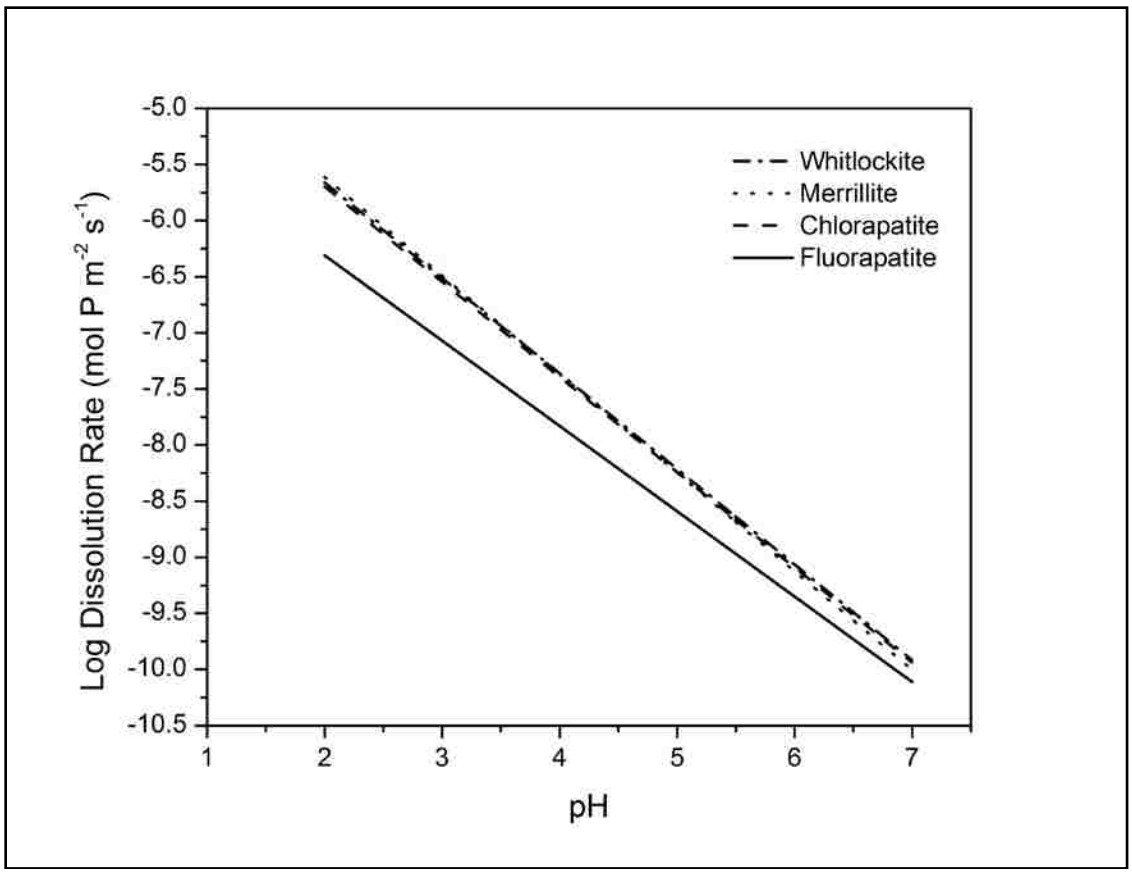

Figure S4. Model of log phosphate release based on mineral stoichiometry and mineral dissolution rates including initial rate data from solubility experiments. Plot shows phosphate release rate from whitlockite, merrillite, and chlorapatite are all higher than fluorapatite over the range of pH 2 to pH 7.

Supplementary Methods

Materials

Chlorapatite was synthesized using previously published methods after (Prener, 1967, 1971; Tacker and Stormer, 1993; Dachs et al., 2010) by heating a mixture of hydroxyapatite and calcium chloride to 1100°C for 24 hours. Whitlockite was synthesized using methods based on Hughes et al. (2008) by combining 1.000 (±0.003) g hydroxyapatite and 0.300 (±0.003) g magnesium nitrate in 90 ml of 18.2 MΩ water, acidifying to pH <2.8 with phosphoric acid, and incubating at 240°C for 6-10 days in a hydrothermal Parr vessel. Merrillite was synthesized by heating whitlockite synthesized as described above to 1060°C for 72 hours after Hughes et al. (2008). Natural fluorapatite from Durango, Mexico, was purchased from Minerals Unlimited of Ridgecrest, California.

Minerals were determined to be pure phases by powder X-ray diffraction (XRD) using a Panalytical X'pert Pro diffractometer using *Cu Kα* radiation(XXL Laboratory, UNLV). Scans were performed over 5-75° 2θ, 0.008˚ step size at 0.06˚ sec^{-1} scan rate, and phase identification was carried out using Panalytical X'Pert High Score Plus software. Mineral compositions were confirmed by electron microprobe analysis (EMP) on a JEOL JXA-8900 microprobe operating at 20keV and 10nA using a 10μm beam (EMiL Facility, UNLV) (see below). With the exception of merrillite, the stoichiometries used in calculations in this study came from the *International Mineralogical Association-CNMNC List of Mineral Names* (IMA)(Nickel and Nichols, 2009) and are $Ca_9Mg(PO_3OH)(PO_4)_6$ (whitlockite), $Ca_5(PO_4)_3Cl$ (chlorapatite) and

$Ca_5(PO_4)_3F$ (fluorapatite). The IMA official formula for merrillite is $Ca_9NaMg(PO_4)_7$. The method of merrillite synthesis used in this study allowed for no sodium. For this reason, the formula $Ca_{9.5}Mg(PO_4)_7$ is used in all required calculations. This formula was confirmed by EMP.

In apatites, a change in structure from P63/m hexagonal structure (fluorapatite) to P21/b monoclinic structure (end-member chlorapatite) can occur at the Cl end-member (Hughes et al., 1989), though hexagonal chlorapatite from high temperature synthesis is documented (Hovis and Harlov, 2010). EMP data indicate our synthetic chlorapatite is end-member or near end-member chlorapatite, and X-ray diffraction confirmed EMP analysis and that the structure is hexagonal.

Minerals were powdered in an agate mortar and pestle, and sieved to obtain the 75-150μm (fluorapatite) or 38-75μm (whitlockite, merrillite, and chlorapatite) size fraction. The retained fractions were cleaned of fine particles by repeatedly sonicating in spectrographic grade ethanol until the supernatant was clear, and then dried at 60°C. A representative sample of each mineral fraction was examined using a JEOL JSM-5610 Scanning Electron Microscope (SEM) (EMiL Facility, UNLV) to confirm the absence of fine particles on mineral surfaces. SEM imaging and analyses of merrillite powder showed very thin (sub-micron) Ca-P features partially covering grains which were not detectable by EMP or XRD. These are likely a product of the dehydrogenation process, and due to the tiny fraction that they make up of the total substrate are assumed to have a negligible effect on the mineral dissolution or solubility.

Surface areas of the cleaned mineral powders were measured by the Brunauer-Emmett-Teller (BET)(Brunauer et al., 1938) method in a Micromeritics ASAP 2020

Accelerated Surface Area and Porosimetry analyzer using Kr as the adsorbate, and are: 0.0536 (± 0.0004) m^2/g (chlorapatite), 0.0321 (± 0.0002) m^2/g (fluorapatite), 0.0516 (±0.0002) m^2/g (whitlockite), and 0.0465 (±0.0003) m^2/g (merrillite).

Dissolution Experimental Setup

Each dissolution experiment consisted of a mineral mass of 0.3000 (±0.0005) g (fluorapatite) or 0.1500 (±0.0005) g (all other minerals) and 180 ml of reacting solution in an acid-washed 250 ml low density polyethylene (LDPE) bottle. Reacting solutions consisted of 0.01M KNO_3 (designed to be similar in ionic strength to a soil solution)(Goyne et al., 2006), adjusted to the required pH of the experiment with trace element analysis grade HNO_3. Batches were immersed in a 25°C shaker bath and agitated at 100 strokes per minute. All batch conditions were run in duplicate, and mineral-free control experiments were run each time experiments were performed. High purity 18.2 MΩ water was used in all solutions, and all equipment was either new or acid washed prior to use.

At time intervals determined through preliminary experiments (10-60 minutes while dissolution rates were being assessed, depending on the pH condition) batches were opened and 10 ml of solution removed by pipette. Between 5 and 9 samples were taken from each batch during the first day to determine dissolution rates by the initial rate method. Subsequent samples of select batches were removed at intervals of days or weeks after the period of initial rate. These samples were to track progress toward steady state, and thus timing was not critical. Solution samples were measured for pH, filtered (0.45 μm filter), and acidified with trace element analysis grade HNO_3 to a pH of <2.

Samples were analyzed for Ca by flame atomic absorption (AA) using a Thermo Scientific iCE 3000 Series AA after adding 0.36 M lanthanum chloride solution to 10% v/v to mitigate interference by phosphorus (Eaton et al., 2005). Samples from batch experiments for each mineral at each pH were additionally analyzed for P by the methyl blue / acetic acid method (Murphy and Riley, 1962) using a Thermo Scientific Genesys 10S UV-Vis.

Moles Ca released into solution at each time interval were calculated using the expression (Welch and Ullman, 2000):

$$m_{(t)} = m_{(t-1)} + (c_{(t)} - c_{(t-1)})V_{(t-1)} \quad \textbf{(Eq. S1)}$$

where $m_{(t)}$ and $m_{(t-1)}$ are the moles of Ca released into solution at time t and t - 1 respectively, $c_{(t)}$ and $c_{(t-1)}$ are measured calcium concentrations (M) at times t and $t - 1$, and $V_{(t-1)}$ is the volume (L) of reaction solution before the sampling event at time t. Moles Ca released were plotted versus time for each batch experiment and fit by linear regression analysis, with the slope of the linear fit representing the rate, r_{Ca}, of Ca release ($mol \cdot s^{-1}$). Linear fits were not forced through zero. Rates were determined using the initial 5-9 points when Ca release was linear with time. Experiments that produced fits with R^2 values of less than 0.900 were rerun and experiments with R^2 values of less than 0.900 not used. Rates of Ca release, r_{Ca}, were then converted to mineral dissolution rates, r_{diss}, using:

$$r_{diss} = r_{Ca}/(A \cdot S) \quad \textbf{(Eq. S2)}$$

where A is the substrate surface area (m^2) used in the experiment and is the product of the BET determined specific surface area (m^2/g) and the mineral mass used in the experiment (g). S is the stoichiometry of the respective mineral in the experiment.

Rate laws for each mineral were developed by applying linear regression to log dissolution rates of averaged batch experiments, as determined above, versus pH (Table 1, Supplementary Data Sheets S1-S35). The resulting pH dependence of mineral dissolution was fit to:

$$\boldsymbol{\log R = \log k_{H+} - npH;} \qquad \textbf{(Eq. S3)}$$

where k_{H+} is the dissolution rate constant and n is the rate dependence on pH.

Solubility Experimental Setup

Solubility experiments were performed using the methods of Zhu, 2009. For each mineral, a mass of 0.2000 grams (+/- 0.0005g) mineral powder was added to a 250ml LDPE vessel along with 200ml of high purity 18.2 MΩ water. Vessels were immersed in a 25°C shaker bath and agitated at 100 strokes per minute. All batch conditions were run in duplicate, and a mineral-free control experiment was included. Sampling consisted of removing 10ml of solution from each vessel at days 5, 10, and 22, every 2 weeks thereafter to day 92, and day 113. Solution samples were measured for pH, filtered (0.20 μm filter), and acidified with trace element analysis grade HNO_3 to a pH of <2. Samples were analyzed for Ca by flame atomic absorption (AA) using a Thermo Scientific iCE 3000 Series AA after adding 0.36 M lanthanum chloride solution to 10% v/v to mitigate interference by phosphorus (Eaton et al., 2005). Samples were additionally analyzed for

P by the methyl blue / acetic acid method (Murphy and Riley, 1962) using a Thermo Scientific Genesys 10S UV-Vis. Once equilibrium concentrations were established, K_{sp} values were calculated from ion concentrations and final pH using PHREEQC (Version 2.15) (Parkhurst and Appelo, 1999) and the included Lawrence Livermore National Laboratory database (llnl.dat) (Johnson et al., 1992) for the reactions in Table 2. Resulting K_{sp} values for fluorapatite from our experiments generally agree with previous studies (Appendix II Table S7) lending confidence to the method.

Table S5. APXS phosphorus of Mars surface rocks and Earth / Mars bulk and crustal abundance.

Gusev Crater (MER Spirit)	P_2O_5 wt%	Meridiani Planum (MER Opportunity)	P_2O_5 wt%	Earth / Mars data	P_2O_5 wt. %
Adirondack_RAT	0.52	McKittrick_RAT	0.99	Earth bulk	0.015
Humphrey_RAT1	0.57	Guadelupe_RAT	0.97	Earth crust	0.2
Humphrey_RAT2	0.56	Mojo2_RAT	1.01	Mars mantle+crust	0.16
Mazatzal_NewYork_RAT1	0.82	BounceROck_Case_RAT	0.92		
Mazatzal _Brooklyn_RAT2	0.65	Golf_Post_RAT_FRAM	0.97		
Pot_of_Gold_RAT	1.08	Lionstone_Numa_RAT	1.01		
WoolyPatch_Sabre_RAT	1.24	Tennessee_RAT	1.03		
WoolyPatch_Mastodon_RAT	1.20	Kentucky_Cubble_Hill2_RAT	1.05		
Clovis_Plano_RAT	1.05	Virginia_RAT	1.07		
Ebenezer_RAT	0.97	Ontario_London_RAT	1.11		
Uchben_Koolik_RAT	0.94	Grindstone_RAT	1.07		
Whishstone_Chisel_RAT	5.19	Kettlestone_RAT	1.03		
Champagne_RAT	5.07	Millstone_Dramensfjord_RAT	1.17		
Champagne_RAT2	5.07	Diamond_Jennes_Homann3_RAT1	1.05		
Peace_RAT1	0.59	Diamond_Jennes_Homann3_RAT2	1.06		
Peace_RAT2	0.49	MacKenzie_Campell_RAT	1.15		
Watchtower_Joker_RAT	4.50	Inuvik_Toroyuktuk_RAT	1.11		
		Bylot_RAT	1.01		
		Escher_Kirchner_RAT	1.01		
		Paikia_RAT	1.13		
		Wharenhui_RAT	1.08		
		Gagarin_RAT	1.07		
		IceCream_RAT	1.04		
		Friutbaskey_Strawberry	0.99		
		LemonRind_RAT	1.05		
		Olympia_Kalavrita	0.98		
Average P2O5	**1.79**		**1.04**		

Rock data compiled from Brukner et al., 2008 and Ming et al., 2008. Earth / Mars bulk and crustal data from Wedepohl, 1995, and Wanke and Driebus, 1988.

Table S6. Individual batch experiment conditions and results.

Exp. ID	Mineral	Initial pH	Final pH	*n*	Dissolution Rate (K_{diss}) (mol m^{-2} s^{-1})	Log K_{diss} (mol m^{-2} s^{-1})	Uncertainty of Fit (mol m^{-2} s^{-1})**	R^2
WHIT-P2DD	Whitlockite	2.00	2.24	9	3.84E-07	-6.42	4.70E-08	0.907
WHIT-P2DDB	Whitlockite	2.00	2.34	9	3.54E-07	-6.45	2.67E-08	0.962
WHIT-P3	Whitlockite	3.00	3.18	6	6.39E-08	-7.19	7.44E-09	0.949
WHIT-P3D	Whitlockite	3.01	3.18	6	6.12E-08	-7.21	3.09E-09	0.990
WHIT-P4D	Whitlockite	3.99	4.81	5	3.43E-09	-8.46	3.60E-10	0.969
WHIT-P4DD	Whitlockite	3.98	4.82	5	3.43E-09	-8.46	6.08E-10	0.915
WHIT-P5D	Whitlockite	5.00	5.38	5	7.26E-10	-9.14	1.27E-10	0.918
WHIT-P5DDB	Whitlockite	4.99	5.67	6	6.29E-10	-9.20	8.59E-11	0.932
MER-P2DDC	Merrillite	2.00	2.16	8	2.86E-07	-6.54	2.03E-08	0.977
MER-P2DD	Merrillite	1.97	2.04	5	3.58E-07	-6.45	3.12E-08	0.983
MER-P3	Merrillite	3.00	3.52	7	5.71E-08	-7.24	3.75E-09	0.983
MER-P3D	Merrillite	3.00	3.17	6	6.26E-08	-7.20	3.15E-09	0.992
MER-P4	Merrillite	4.00	4.59	6	7.47E-09	-8.13	5.70E-10	0.982
MER-P4DD	Merrillite	4.00	4.43	6	5.41E-09	-8.27	4.28E-10	0.981
MER-P5	Merrillite	5.00	5.81	6	5.07E-10	-9.30	1.96E-11	0.995
MER-P5D	Merrillite	4.91	5.65	5	6.28E-10	-9.20	1.27E-10	0.913
CAP-P2	Chlorapatite	1.97	2.06	5	5.99E-07	-6.22	4.57E-08	0.986
CAP-P2D	Chlorapatite	2.00	2.06	6	4.91E-07	-6.31	6.85E-08	0.939
CAP-P3	Chlorapatite	2.95	3.16	5	2.64E-07	-6.58	2.64E-08	0.976
CAP-P3DD	Chlorapatite	3.00	3.33	8	1.82E-07	-6.74	1.18E-08	0.980
CAP-P4	Chlorapatite	3.99	5.06	5	5.78E-09	-8.24	6.97E-10	0.965
CAP-P4D	Chlorapatite	4.00	4.87	5	8.70E-09	-8.06	1.20E-09	0.955
CAP-P5	Chlorapatite	4.97	5.98	6	1.34E-09	-8.87	9.34E-11	0.965
CAP-P5D	Chlorapatite	5.00	5.69	6	1.80E-09	-8.74	2.76E-10	0.914
FAP-P2D	Fluorapatite	1.97	1.95	6	2.67E-07	-6.57	9.20E-09	0.995
FAPM-P2	Fluorapatite	1.97	2.07	6	1.80E-07	-6.74	2.28E-08	0.938
FAP-P2	Fluorapatite	1.99	2.03	6	2.53E-07	-6.60	2.08E-08	0.973
FAPM-P3	Fluorapatite	3.00	3.22	6	2.51E-08	-7.60	1.90E-09	0.977
FAP-P3DD	Fluorapatite	3.00	3.09	9	3.06E-08	-7.51	2.56E-09	0.952
FAPC-P3D	Fluorapatite	3.00	3.02	6	2.38E-08	-7.62	2.04E-09	0.971
FAPC-P4	Fluorapatite	3.99	4.37	5	4.05E-09	-8.39	3.24E-10	0.981
FAP-P4DD	Fluorapatite	4.00	4.82	5	2.55E-09	-8.59	3.04E-10	0.958
FAPM-P4	Fluorapatite	4.00	4.24	6	6.67E-09	-8.18	8.01E-10	0.944
FAPM-P5	Fluorapatite	5.00	5.58	6	8.04E-10	-9.09	8.85E-11	0.953
FAPM-P5D	Fluorapatite	5.00	5.49	5	8.16E-10	-9.09	1.54E-10	0.901

**n = number of points used in linear regression. **Standard error divided by substrate surface area and mineral stoichiometry*

Table S7. Comparison of Log Ksp values from this study to literature

Study	Log Ksp*
Zhu, 2009	-18.95
Jaynes et al., 1998	-21.13
Lindsay, 1979	-21.84
Stumm and Morgan, 1996	-21.95
Chin and Nancollas, 1991	-23.00
Vieillard and Tardy, 1984	-23.09
Amjad et al., 1981(Amjad et al., 1984)	-23.10
Robie et al., 1979	-24.99
Elliot, 1994	-25.45
This study	**-26.50**
Harouiya et al., 2007	-29.40
Stefansson, 2001	-30.94
Valsami-Jones et al., 1989	-32.95

*****$Reaction: Ca_5(PO_4)_3F + 3H^+ = 5Ca^{2+} + 3HPO_4^{2-} + F^-$. *Except for Zhu, 2009, and this study, data are compiled from Oelkers et al, 2009.*

Supplementary Discussion

Mineral Stoichiometry

Stoichiometries calculated from EMP were used to confirm the mineral chemistry and results assume ideal hydrogen and oxygen values. With the exception of merrillite, mineral stoichiometries used for calculations in this study were based on the official conventions of the International Mineralogical Association (IMA). Our synthetic merrillite contained no sodium and EMP analyses confirmed calcium substitution. Thus, for this study a stoichiometry of 9.5 calcium (i.e. $Ca_{9.5}Mg(PO_4)_7$) was used in all calculations.

Whitlockite

IMA convention: $Ca_9Mg(PO_3OH)(PO_4)_6$
EMP results: $Ca_{9.1}Mg_{0.9}(P_{1.0}O_3OH)(P_{1.0}O_4)_6$

Merrillite

IMA convention: $Ca_9NaMg(PO_4)_7$
EMP results: $Ca_{9.0}\ Ca_{0.4}Mg_{1.1}(P_{1.0}O_4)_7$
For this study: $Ca_{9.5}Mg(PO_4)_7$

Chlorapatite

IMA convention: $Ca_5(PO_4)_3Cl$
EMP results: $Ca_{5.0}(P_{1.0}O_4)_3Cl_{1.1}$

Fluorapatite

IMA convention: $Ca_5(PO_4)_3F$
EMP results: $Ca_{5.0}(P_{1.0}O_4)_3F_{1.1}$

Electron Microprobe (EMP) Results

EMP Operating Conditions
Beam diameter: 10 microns
Accelerating Voltage: 20 KeV
Current: 10 nA

Results Summary (*n* represents the number of individual grains analyzed).

Whitlockite:

Element	F	MnO	Cl	P_2O_5	FeO	CaO	MgO	Total
Ave. Wt. %	0.01	0.00	0.01	46.79	0.02	47.57	3.33	97.71*
Std. Dev.	0.02	0.01	0.01	0.26	0.03	0.27	0.37	0.60
n =	17							

**Low totals due to the presence of undetectable/unaccounted for hydrogen within whitlockite* ($Ca_9Mg(PO_3OH)(PO_4)_6$.)

Merrillite:

Element	F	MnO	Cl	P_2O_5	FeO	CaO	MgO	Total
Ave. Wt. %	0.00	0.01	0.01	46.38	0.02	48.89	4.06	99.36
Std. Dev.	0.00	0.01	0.01	0.32	0.03	0.21	0.12	0.36
n =	16							

Chlorapatite:

Element	F	MnO	Cl	P_2O_5	FeO	CaO	MgO	-O = F,Cl	Total
Ave. Wt. %	0.03	0	7.23	40.28	0.14	53.76	0.12	1.64	99.92
Std. Dev.	0.03	0.01	1.18	0.91	0.83	1.21	0.14	-	0.81
n =	40*								

**Analyses were performed on grains from four individual batches of synthetic apatite.*

Fluorapatite:

Element	F	MnO	Cl	P_2O_5	FeO	CaO	MgO	-O = F,Cl	Total
Average	3.75	0.02	0.47	40.91	0.03	54.11	0.02	1.69	97.62*
Std. Dev.	0.17	0.01	0.02	0.19	0.01	0.23	0.01	-	0.44
n =	5*								

**Durango Fluorapatite is well characterized. Low totals reflect ~2.00 wt % undetectable/unanalyzed components including; SrO, REE_2O_3, ThO_2, As_2O_3, V_2O_3, CO_2 , SO_3 (Jarosewich, 1980).*

Supplementary Data

Data Sheets for Individual Batch Experiments

Datasheet S1

Experiment CAP-P2

Mineral: Chlorapatite **Initial pH:** 1.97 **Specific Surf. Area (BET):** 0.0563m²/g
Batch ID: CAP-P2 **Mineral Mass:** 0.1500g **Total Surf. Area (BET):** 0.00845 m²

Batch Results (shaded data = the linear initial rate data shown in the accompanying figure)

Time (*sec*)	Ca (*moles released*)	P (*moles released*)	pH
0	0	NA	1.97
840	5.55E-05	NA	2.06
1380	7.18E-05	NA	2.06
2100	9.22E-05	NA	2.06
2820	1.02E-04	NA	2.07
3600	1.29E-04	NA	2.06
4980	1.26E-04	NA	2.07
9300	1.36E-04	NA	2.12
81360	6.36E-04	NA	2.61

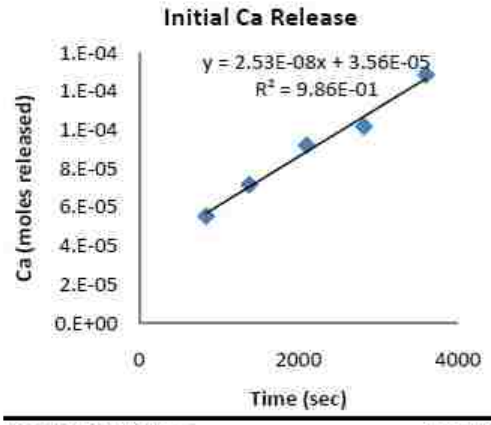

Regression Analysis		*Std.Error*
R Square	0.986	NA
Ca release rate (r_{ca})	2.53E-08	1.76E-09

$K_{diss} = r_{ca}/A \bullet S$, where r_{ca} is the rate of Ca release over time as determined by linear regression, A is the total BET surface area (specific surface area (BET) X mineral mass), and S is the Ca stoiciometric coefficient of the respective mineral.

→ *Diss. Rate Mineral* (K_{diss}) **5.99E-07** mol/m²s

Uncertainty of Fit 4.15E-08 mol/m²s

**Analytical error bars fall within plotted symbols*

Datasheet S2

Experiment CAP-P2D

Mineral: Chlorapatite **Initial pH:** 2.00 **Specific Surf. Area (BET):** 0.0563 m^2/g
Batch ID: CAP-P2D **Mineral Mass:** 0.1500g **Total Surf. Area (BET):** 0.00845 m^2

NA = no analysis

Batch Results (shaded data = the linear initial rate data shown in the accompanying figure)

Time (*sec*)	Ca (*moles released*)	P (*moles released*)	pH
0	0	NA	2.00
660	6.24E-05	4.56E-05	2.01
1380	9.94E-05	6.11E-05	2.03
2220	1.08E-04	6.91E-05	2.09
2880	1.12E-04	7.00E-05	2.01
3600	1.25E-04	7.79E-05	2.03
5220	1.70E-04	1.04E-04	2.06
83280	5.62E-04	NA	2.42
342480	7.08E-04	NA	2.72
7168080	8.78E-04	NA	3.45
7686480	8.75E-04	NA	3.47

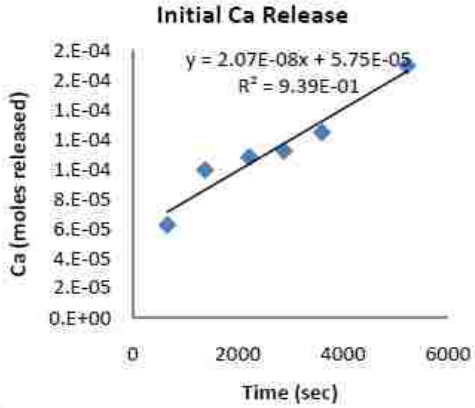

Regression Analysis		*Std.Error*
R Square	0.939	NA
Ca release rate (r_{Ca})	2.07E-08	2.63E-09

$K_{diss} = r_{Ca}/A \bullet S$, where r_{Ca} is the rate of Ca release over time as determined by linear regression, *A* is the total BET surface area (specific surface area (BET) X mineral mass), and *S* is the Ca stoiciometric coefficient of the respective mineral.

Diss. Rate Mineral (K_{diss}) **4.91E-07** mol/m^2s

Uncertainty of Fit 6.2298E-08 mol/m^2s

Stoichiometry

Moles of Mineral Released

Time (*sec*)	Moles Mineral Released (P)	Moles Mineral Released (Ca)
660	1.52E-05	1.25E-05
1380	2.04E-05	1.99E-05
2220	2.30E-05	2.16E-05
2880	2.33E-05	2.24E-05
3600	2.60E-05	2.49E-05
5220	3.45E-05	3.39E-05

Moles mineral released (above) based on P or Ca determined from moles released of P or Ca divided by the appropriate stoichiometric factor of the respective ion.

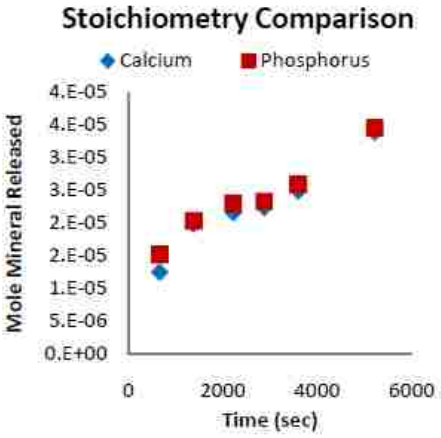

**Analytical error bars fall within plotted symbols*

Datasheet S3

Experiment CAP-P3

Mineral: Chlorapatite	**Initial pH:** 2.95	**Specific Surf. Area (BET):** 0.0563 m^2/g
Batch ID: CAP-P3	**Mineral Mass:** 0.1500g	**Total Surf. Area (BET):** 0.00845 m^2

Batch Results (shaded data = the linear initial rate data shown in the accompanying figure)

Time (*sec*)	Ca (*moles released*)	P (*moles released*)	pH
0	0.00E+00	NA	2.95
900	1.31E-05	NA	3.10
1500	1.63E-05	NA	3.09
2220	2.95E-05	NA	3.10
2940	3.40E-05	NA	3.11
3660	4.29E-05	NA	3.16
5040	3.30E-05	NA	3.21
5760	3.99E-05	NA	3.31
81600	1.20E-04	NA	4.48

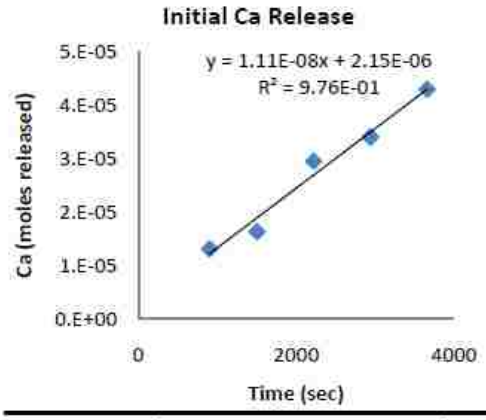

$K_{diss} = r_{ca}/A \bullet S$, where r_{ca} is the rate of Ca release over time as determined by linear regression, *A* is the total BET surface area (specific surface area (BET) X mineral mass), and *S* is the Ca stoiciometric coefficient of the respective mineral.

Regression Analysis		*Std.Error*
R Square	0.976	NA
Ca release rate (r_{Ca})	1.11E-08	1.01E-09

Diss. Rate Mineral (K_{diss}) **2.64E-07** mol/m^2s

Uncertainty of Fit 2.40E-08 mol/m^2s

**Analytical error bars fall within plotted symbols*

Datasheet S4

Experiment CAP-P3DD

Mineral: Chlorapatite **Initial pH:** 2.95 **Specific Surf. Area (BET):** 0.0563 m^2/g
Batch ID: CAP-P3DD **Mineral Mass:** 0.1500g **Total Surf. Area (BET):** 0.00845 m^2

NA = no analysis

Batch Results (shaded data = the linear initial rate data shown in the accompanying figure)

Time (*sec*)	Ca (*moles released*)	P (*moles released*)	pH
0	0	NA	3.00
900	1.89E-05	1.43E-05	3.03
1860	2.39E-05	1.73E-05	3.14
2700	3.11E-05	2.17E-05	3.05
3660	3.76E-05	2.63E-05	3.17
4560	4.14E-05	2.93E-05	3.22
5400	5.34E-05	3.36E-05	3.27
6360	5.63E-05	3.86E-05	3.27
7200	6.90E-05	4.07E-05	3.33

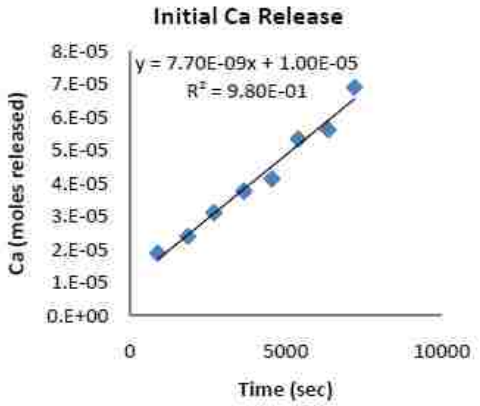

$K_{diss} = r_{ca}/A \bullet S$, where r_{ca} is the rate of Ca release over time as determined by linear regression, *A* is the total BET surface area (specific surface area (BET) X mineral mass), and *S* is the Ca stoiciometric coefficient of the respective mineral.

Regression Analysis		*Std.Error*
R Square	0.976	NA
Ca release rate (r_{ca})	7.70E-09	4.53E-10

Diss. Rate Mineral (K_{diss}) **1.82E-07** mol/m^2s
Uncertainty of Fit 1.07E-08 mol/m^2s

Stoichiometry

Moles of Mineral Released

Time (*sec*)	Moles Mineral Released (P)	Moles Mineral Released (Ca)
900	4.76E-06	3.78E-06
1860	5.77E-06	4.79E-06
2700	7.25E-06	6.22E-06
3660	8.76E-06	7.53E-06
4560	9.76E-06	8.27E-06
5400	1.12E-05	1.07E-05
6360	1.29E-05	1.13E-05
7200	1.36E-05	1.38E-05

Moles mineral released (above) based on P or Ca determined from moles released of P or Ca divided by the appropriate stoichiometric factor of the respective ion.

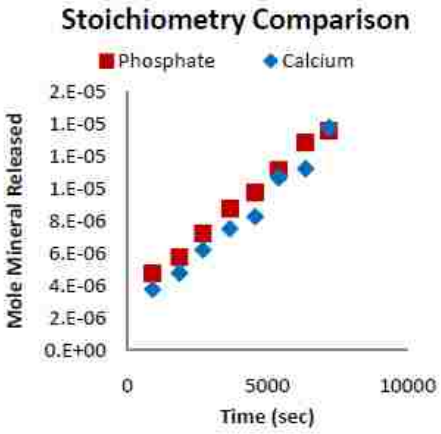

**Analytical error bars fall within plotted symbols*

Datasheet S5

Experiment CAP-P4

Mineral: Chlorapatite **Initial pH:** 3.99 **Specific Surf. Area (BET):** 0.0563 m^2/g
Batch ID: CAP-P4 **Mineral Mass:** 0.1500g **Total Surf. Area (BET):** 0.00845 m^2

NA = no analysis

Batch Results (shaded data = the linear initial rate data shown in the accompanying figure)

Time (*sec*)	Ca (*moles released*)	P (*moles released*)	pH
0	0	NA	3.99
3180	4.88E-06	NA	4.39
6780	6.23E-06	NA	4.55
9360	6.97E-06	NA	4.75
13620	7.73E-06	NA	4.79
16500	8.23E-06	NA	5.06
20220	8.21E-06	NA	5.48
96960	9.38E-06	NA	5.89
1559460	1.14E-05	NA	6.15
8398680	1.26E-05	NA	6.63

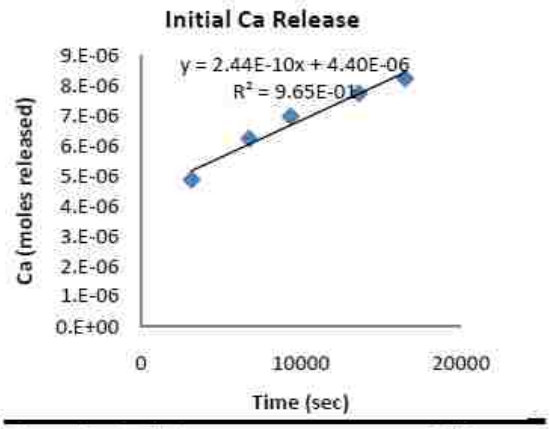

$K_{diss} = r_{ca}/A \bullet S$, where r_{ca} is the rate of Ca release over time as determined by linear regression, *A* is the total BET surface area (specific surface area (BET) X mineral mass), and *S* is the Ca stoiciometric coefficient of the respective mineral.

Regression Analysis		*Std.Error*
R Square	0.965	NA
Ca release rate (r_{ca})	2.44E-10	2.68E-11

Diss. Rate Mineral (K_{diss}) **5.78E-09** mol/m^2s

Uncertainty of Fit 6.33E-10 mol/m^2s

**Analytical error bars fall within plotted symbols*

Datasheet S6

Experiment CAP-P4D

Mineral: Chlorapatite **Initial pH:** 4.00 **Specific Surf. Area (BET):** 0.0563 m^2/g
Batch ID: CAP-P4D **Mineral Mass:** 0.1500g **Total Surf. Area (BET):** 0.00845 m^2

NA = no analysis

Batch Results (shaded data = the linear initial rate data shown in the accompanying figure)

Time (*sec*)	Ca (*moles released*)	P (*moles released*)	pH
0	0	NA	4.00
2880	5.81E-06	3.53E-06	4.63
5460	7.46E-06	4.39E-06	4.79
8160	8.37E-06	5.62E-06	4.84
10860	9.32E-06	5.58E-06	4.86
13440	9.75E-06	6.00E-06	4.87
18780	1.02E-05	6.38E-06	5.08
107280	1.17E-05	7.74E-06	5.86
543120	1.36E-05	NA	6.31

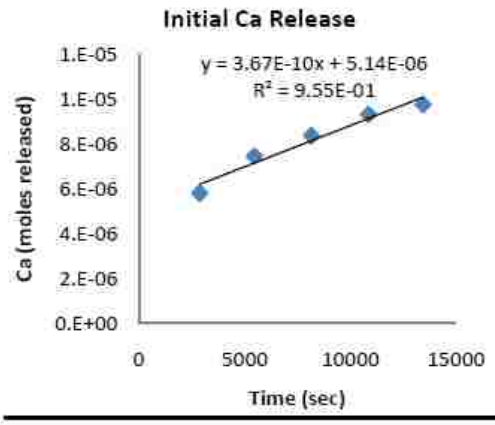

$K_{diss} = r_{ca}/A \bullet S$, where r_{ca} is the rate of Ca release over time as determined by linear regression, *A* is the total BET surface area (specific surface area (BET) X mineral mass), and *S* is the Ca stoiciometric coefficient of the respective mineral.

Regression Analysis		*Std.Error*
R Square	0.955	NA
Ca release rate (r_{ca})	3.67E-10	4.61E-11

Diss. Rate Mineral (K_{diss}) **8.70E-09** mol/m^2s
Uncertainty of Fit 1.09E-09 mol/m^2s

Stoichiometry

Moles of Mineral Released

Time (*sec*)	Moles Mineral Released (P)	Moles Mineral Released (Ca)
2880	1.18E-06	1.16E-06
5460	1.46E-06	1.49E-06
8160	1.87E-06	1.67E-06
10860	1.86E-06	1.86E-06
13440	2.00E-06	1.95E-06

Moles mineral released (above) based on P or Ca determined from moles released of P or Ca divided by the appropriate stoichiometric factor of the respective ion.

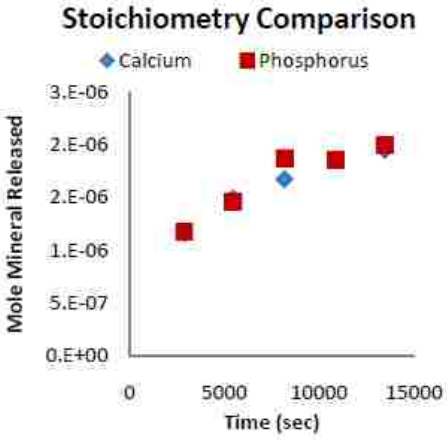

**Analytical error bars fall within plotted symbols*

Datasheet S7

Experiment CAP-P5

Mineral: Chlorapatite **Initial pH:** 4.95 **Specific Surf. Area (BET):** 0.0563 m^2/g
Batch ID: CAP-P5 **Mineral Mass:** 0.1500g **Total Surf. Area (BET):** 0.00845 m^2

NA = no analysis

Batch Results (shaded data = the linear initial rate data shown in the accompanying figure)

Time (*sec*)	Ca (*moles released*)	P (*moles released*)	pH
0	0	NA	4.97
3120	8.56E-07	NA	5.34
6660	1.11E-06	NA	5.46
9300	1.33E-06	NA	5.73
13560	1.50E-06	NA	5.77
16440	1.61E-06	NA	5.78
20160	1.88E-06	NA	5.98
96960	3.14E-06	NA	6.43
1559460	4.84E-06	NA	6.62

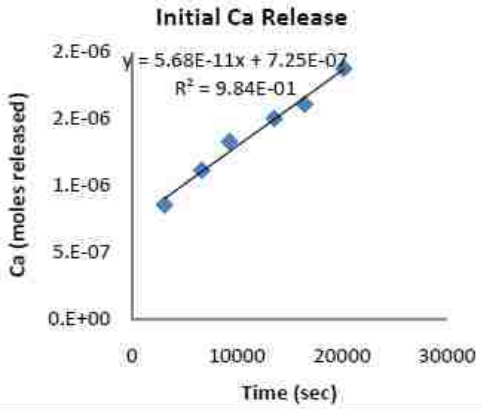

Regression Analysis		*Std.Error*
R Square	0.984	NA
Ca release rate (r_{Ca})	5.68E-11	3.59E-12

$K_{diss} = r_{Ca}/A \bullet S$, where r_{Ca} is the rate of Ca release over time as determined by linear regression, *A* is the total BET surface area (specific surface area (BET) X mineral mass), and *S* is the Ca stoiciometric coefficient of the respective mineral.

Diss. Rate Mineral (K_{diss}) **1.34E-09** mol/m^2s

Uncertainty of Fit 8.49E-11 mol/m^2s

**Analytical error bars fall within plotted symbols*

Datasheet S8

Experiment CAP-P5D

Mineral: Chlorapatite **Initial pH:** 4.95 **Specific Surf. Area (BET):** 0.0563 m^2/g
Batch ID: CAP-P5D **Mineral Mass:** 0.1500g **Total Surf. Area (BET):** 0.00845 m^2

NA = no analysis

Batch Results (shaded data = the linear initial rate data shown in the accompanying figure)

Time (*sec*)	Ca (*moles released*)	P (*moles released*)	pH
0	0	NA	4.95
3000	1.01E-06	5.93E-07	5.48
5580	1.52E-06	5.93E-07	5.65
8340	1.68E-06	6.66E-07	5.40
10980	1.81E-06	6.89E-07	5.84
13560	1.89E-06	7.53E-07	5.88
18960	2.26E-06	9.50E-07	5.69
107460	3.58E-06	1.95E-06	6.37

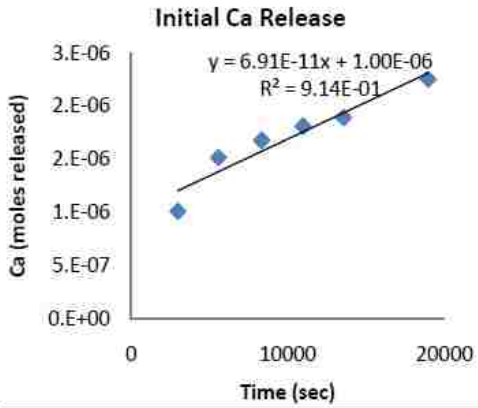

Regression Analysis		*Std.Error*
R Square	0.914	NA
Ca release rate (r_{ca})	6.91E-11	1.06E-11

$K_{diss} = r_{ca}/A \bullet S$, where r_{ca} is the rate of Ca release over time as determined by linear regression, A is the total BET surface area (specific surface area (BET) X mineral mass), and S is the Ca stoiciometric coefficient of the respective mineral.

Diss. Rate Mineral (K_{diss}) **1.64E-09** mol/m^2s

Uncertainty of Fit 2.51E-10 mol/m^2s

Analytical error bars fall within plot symbols

Stoichiometry

Moles of Mineral Released

Time (*sec*)	Moles Mineral Released (P)	Moles Mineral Released (Ca)
3000	1.98E-07	2.03E-07
5580	1.98E-07	3.04E-07
8340	2.22E-07	3.36E-07
10980	2.30E-07	3.63E-07
13560	2.51E-07	3.79E-07
18960	3.17E-07	4.51E-07
107460	6.51E-07	7.17E-07

Moles mineral released (above) based on P or Ca determined from moles released of P or Ca divided by the appropriate stoichiometric factor of the respective ion.

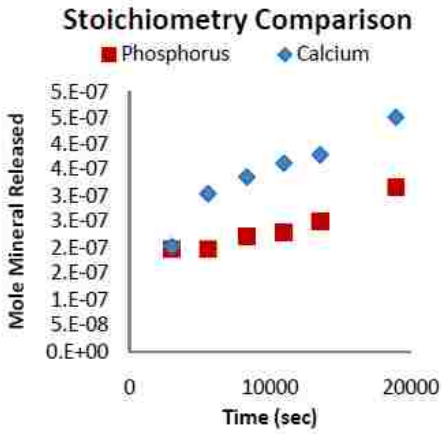

Datasheet S9
Experiment FAP-P2

Mineral: Fluorapatite **Initial pH:** 1.99 **Specific Surf. Area (BET):** 0.0321 m^2/g
Batch ID: FAP-P2 **Mineral Mass:** 0.3000g **Total Surf. Area (BET):** 0.00963 m^2

NA = no analysis

Batch Results (shaded data = the linear initial rate data shown in the accompanying figure)

Time (*sec*)	Ca (*moles released*)	P (*moles released*)	pH
0	0	NA	1.99
600	1.19E-05	1.53E-05	2.02
1260	1.53E-05	1.90E-05	1.99
1800	2.97E-05	2.20E-05	1.98
2460	3.46E-05	2.64E-05	2.03
3120	4.29E-05	3.32E-05	2.03
4140	5.33E-05	NA	2.03
81300	1.40E-04	NA	2.18
242460	2.04E-04	NA	2.21
593220	3.38E-04	NA	2.27
850500	3.47E-04	NA	2.3
1988100	3.61E-04	NA	2.2
2517480	3.62E-04	NA	2.3

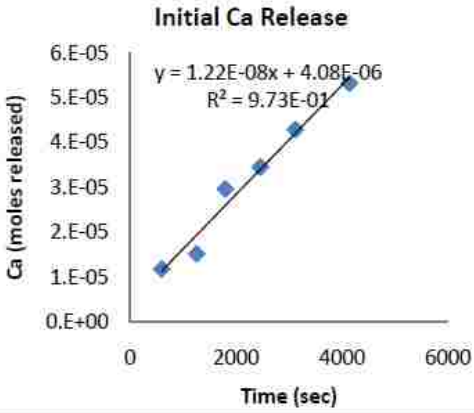

Regression Analysis		*Std.Error*
R Square	0.973	NA
Ca release rate (r_{Ca})	1.2199E-08	1.01E-09

$K_{diss} = r_{ca}/A \bullet S$, where r_{ca} is the rate of Ca release over time as determined by linear regression, *A* is the total BET surface area (specific surface area (BET) X mineral mass), and *S* is the Ca stoiciometric coefficient of the respective mineral.

Diss. Rate Mineral (K_{diss}) **2.53E-07** mol/m^2s

Uncertainty of Fit 2.11E-08 mol/m^2s

Analytical error bars fall within plot symbols

Stoichiometry

Moles of Mineral Released

Time (*sec*)	Moles Mineral Released (P)	Moles Mineral Released (Ca)
600	5.11E-06	2.38E-06
1260	6.32E-06	3.05E-06
1800	7.32E-06	5.94E-06
2460	8.79E-06	6.92E-06
3120	1.11E-05	8.59E-06
4140		1.07E-05

Moles mineral released (above) based on P or Ca determined from moles released of P or Ca divided by the appropriate stoichiometric factor of the respective ion.

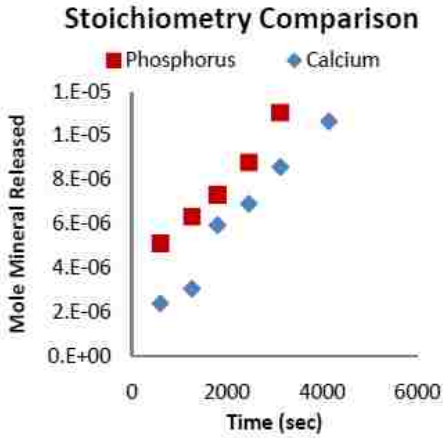

Datasheet S10
Experiment FAP-P2D

Mineral: Fluorapatite **Initial pH:** 1.97 **Specific Surf. Area (BET):** 0.0321 m^2/g
Batch ID: FAP-P2D **Mineral Mass:** 0.3000g **Total Surf. Area (BET):** 0.00963 m^2

NA = no analysis

Batch Results (shaded data = the linear initial rate data shown in the accompanying figure)

Time (*sec*)	Ca (*moles released*)	P (*moles released*)	pH
0	0	NA	1.97
780	1.21E-05	NA	1.98
1380	1.86E-05	NA	1.98
1980	2.76E-05	NA	2.00
2580	3.60E-05	NA	2.02
3300	4.63E-05	NA	2.03
4500	5.84E-05	NA	1.95
11520	6.61E-05	NA	2.01
96060	1.48E-04	NA	2.09

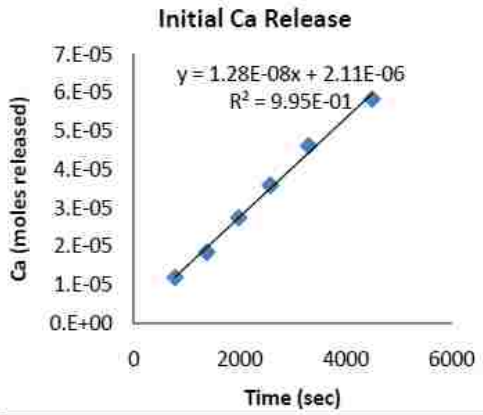

$K_{diss} = r_{ca}/A \bullet S$, where r_{ca} is the rate of Ca release over time as determined by linear regression, *A* is the total BET surface area (specific surface area (BET) X mineral mass), and *S* is the Ca stoiciometric coefficient of the respective mineral.

Regression Analysis		*Std.Error*
R Square	0.995	NA
Ca release rate (r_{ca})	1.28E-08	4.49E-10

Analytical error bars fall within plot symbols

Diss. Rate Mineral (K_{diss} *)* **2.67E-07** mol/m^2s

Uncertainty of Fit 9.31E-09 mol/m^2s

Datasheet S11
Experiment FAPM-P2

Mineral: Fluorapatite **Initial pH:** 1.97 **Specific Surf. Area (BET):** 0.0321 m^2/g
Batch ID: FAPM-P2 **Mineral Mass:** 0.3000g **Total Surf. Area (BET):** 0.00963 m^2

NA = no analysis

Batch Results (shaded data = the linear initial rate data shown in the accompanying figure)

Time (*sec*)	Ca (*moles released*)	P (*moles released*)	pH
0	0	NA	1.97
960	2.46E-05	1.79E-05	1.95
1980	3.14E-05	2.50E-05	1.96
2820	4.05E-05	3.08E-05	1.97
3660	4.43E-05	3.11E-05	1.95
4440	4.75E-05	3.55E-05	2.02
5460	6.71E-05	4.85E-05	2.07
15420	9.52E-05	6.32E-05	2.03
99660	1.56E-04	NA	2.16
1346280	2.64E-04	NA	2.25

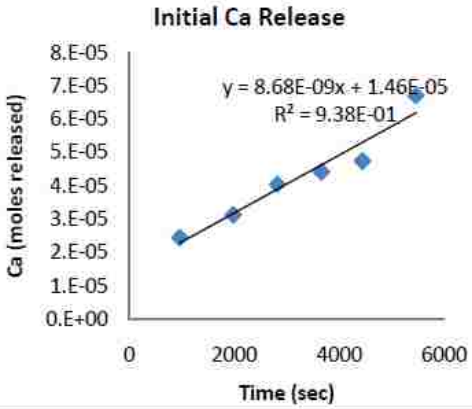

Regression Analysis		*Std.Error*
R Square	0.938	NA
Ca release rate (r_{ca})	8.68E-09	1.11E-09

$K_{diss} = r_{ca}/A \bullet S$, where r_{ca} is the rate of Ca release over time as determined by linear regression, *A* is the total BET surface area (specific surface area (BET) X mineral mass), and *S* is the Ca stoiciometric coefficient of the respective mineral.

Diss. Rate Mineral (K_{diss}) **1.80E-07** mol/m^2s

Uncertainty of Fit 2.31E-08 mol/m^2s

Analytical error bars fall within plot symbols

Stoichiometry

Moles of Mineral Released

Time (*sec*)	Moles Mineral Released (P)	Moles Mineral Released (Ca)
960	5.96E-06	4.91E-06
1980	8.34E-06	6.27E-06
2820	1.03E-05	8.10E-06
3660	1.04E-05	8.86E-06
4440	1.18E-05	9.50E-06
5460	1.62E-05	1.34E-05
15420	2.11E-05	1.90E-05

Moles mineral released (above) based on P or Ca determined from moles released of P or Ca divided by the appropriate stoichiometric factor of the respective ion.

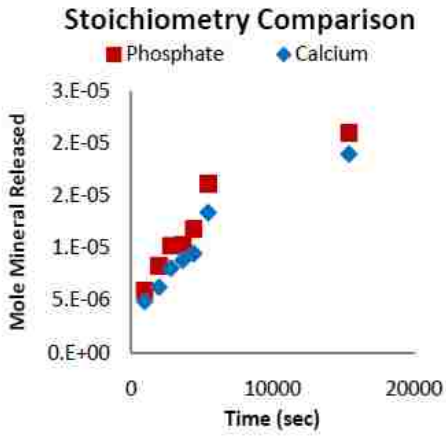

Datasheet S12
Experiment FAPM-P3

Mineral: Fluorapatite **Initial pH:** 3.00 **Specific Surf. Area (BET):** 0.0321 m^2/g
Batch ID: FAPM-P3 **Mineral Mass:** 0.3000g **Total Surf. Area (BET):** 0.00963 m^2

NA = no analysis

Batch Results (shaded data = the linear initial rate data shown in the accompanying figure)

Time (*sec*)	Ca (*moles released*)	P (*moles released*)	pH
0	0	NA	3.00
960	6.363E-06	NA	3.26
1740	7.132E-06	NA	3.08
2700	7.561E-06	NA	3.11
3540	9.348E-06	NA	3.16
4440	1.043E-05	NA	3.20
5700	1.190E-05	NA	3.22
8160	1.311E-05	NA	3.19

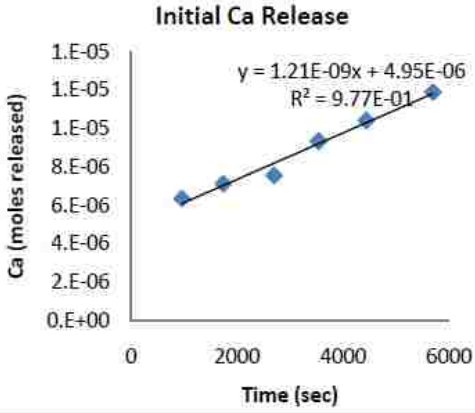

$K_{diss} = r_{ca}/A \bullet S$, where r_{ca} is the rate of Ca release over time as determined by linear regression, *A* is the total BET surface area (specific surface area (BET) X mineral mass), and *S* is the Ca stoiciometric coefficient of the respective mineral.

Regression Analysis		*Std.Error*
R Square	0.977	NA
Ca release rate (r_{ca})	1.21E-09	9.26E-11

Diss. Rate Mineral (K_{diss}) **2.51E-08** mol/m^2s

Uncertainty of Fit 1.92E-09 mol/m^2s

Analytical error bars fall within plot symbols

Datasheet S13
Experiment FAP-P3DD

Mineral: Fluorapatite **Initial pH: 3.00** **Specific Surf. Area (BET):** 0.0321 m^2/g
Batch ID: FAP-P3DD **Mineral Mass:** 0.3000g **Total Surf. Area (BET):** 0.00963 m^2

NA = no analysis

Batch Results (shaded data = the linear initial rate data shown in the accompanying figure)

Time (*sec*)	Ca (*moles released*)	P (*moles released*)	pH
0	0	NA	3.00
1080	6.24E-06	NA	3.10
1920	7.29E-06	NA	3.06
2880	8.23E-06	NA	3.13
3840	9.68E-06	NA	3.07
4860	1.39E-05	NA	3.08
5820	1.37E-05	NA	3.09
6720	1.46E-05	NA	3.06
7620	1.56E-05	NA	3.09
8820	1.71E-05	NA	3.09

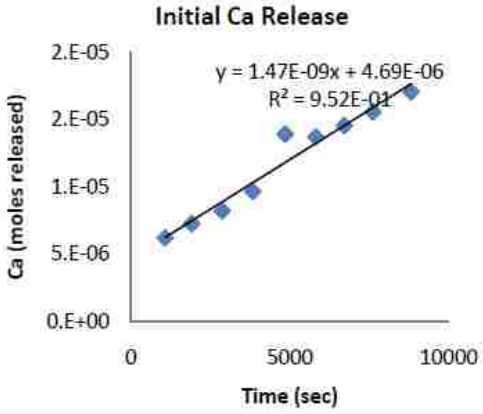

Regression Analysis		*Std.Error*
R Square	0.952	NA
Ca release rate (r_{ca})	1.47E-09	1.25E-10

$K_{diss} = r_{ca}/A \bullet S$, where r_{ca} is the rate of Ca release over time as determined by linear regression, *A* is the total BET surface area (specific surface area (BET) X mineral mass), and *S* is the Ca stoiciometric coefficient of the respective mineral.

→ *Diss. Rate Mineral (K_{diss})* **3.06E-08** mol/m^2s

Uncertainty of Fit 2.59E-09 mol/m^2s

Analytical error bars fall within plot symbols

Datasheet S14
Experiment FAPC-P3D

Mineral: Fluorapatite **Initial pH:** 3.00 **Specific Surf. Area (BET):** 0.0321 m^2/g
Batch ID: FAPC-P3D **Mineral Mass:** 0.3000g **Total Surf. Area (BET):** 0.00963 m^2

NA = no analysis

Batch Results (shaded data = the linear initial rate data shown in the accompanying figure)

Time (*sec*)	Ca (*moles released*)	P (*moles released*)	pH
0	0	0	3.00
1200	4.07E-06	3.48E-06	3.04
1920	5.91E-06	4.74E-06	3.07
2760	6.29E-06	5.09E-06	3.05
3420	6.98E-06	5.55E-06	3.07
4140	7.84E-06	5.69E-06	3.00
5760	9.70E-06	7.10E-06	3.02

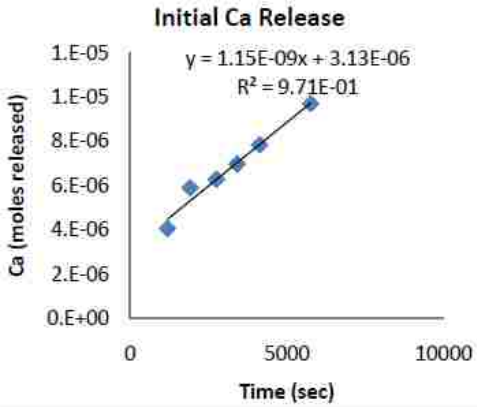

Regression Analysis		*Std.Error*
R Square	0.971	NA
Ca release rate (r_{ca})	1.15E-09	9.95E-11

$K_{diss} = r_{ca}/A \bullet S$, where r_{ca} is the rate of Ca release over time as determined by linear regression, *A* is the total BET surface area (specific surface area (BET) X mineral mass), and *S* is the Ca stoiciometric coefficient of the respective mineral.

Diss. Rate Mineral (K_{diss}) **2.38E-08** mol/m^2s

Uncertainty of Fit 2.07E-09 mol/m^2s

Analytical error bars fall within plot symbols

Stoichiometry

Moles of Mineral Released

Time (*sec*)	Moles Mineral Released (P)	Moles Mineral Released (Ca)
1200	1.16E-06	8.14E-07
1920	1.58E-06	1.18E-06
2760	1.70E-06	1.26E-06
3420	1.85E-06	1.40E-06
4140	1.90E-06	1.57E-06
5760	2.37E-06	1.94E-06

Moles mineral released (above) based on P or Ca determined from moles released of P or Ca divided by the appropriate stoichiometric factor of the respective ion.

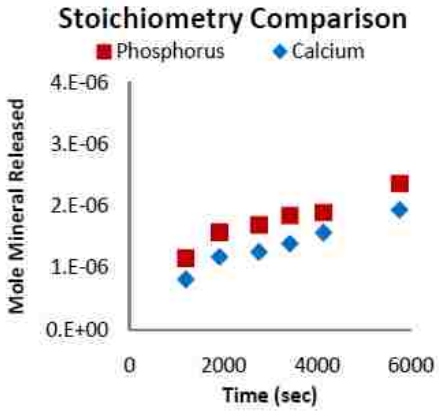

Datasheet S15
Experiment FAPC-P4

Mineral: Fluorapatite **Initial pH:** 3.99 **Specific Surf. Area (BET):** 0.0321 m^2/g
Batch ID: FAPC-P4 **Mineral Mass:** 0.3000g **Total Surf. Area (BET):** 0.00963 m^2

NA = no analysis

Batch Results (shaded data = the linear initial rate data shown in the accompanying figure)

Time (*sec*)	Ca (*moles released*)	P (*moles released*)	pH
0	0	NA	3.99
3540	2.20E-06	NA	4.14
7140	3.18E-06	NA	4.20
9720	3.73E-06	NA	4.26
13980	4.43E-06	NA	4.31
16860	4.84E-06	NA	4.37
20580	5.11E-06	NA	4.41
97260	6.70E-06	NA	4.80

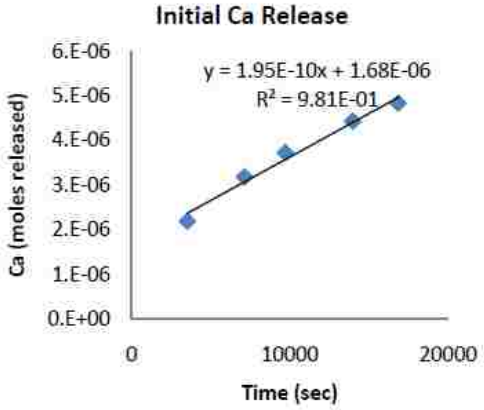

$K_{diss} = r_{ca}/A \bullet S$, where r_{ca} is the rate of Ca release over time as determined by linear regression, *A* is the total BET surface area (specific surface area (BET) X mineral mass), and *S* is the Ca stoiciometric coefficient of the respective mineral.

Regression Analysis		*Std.Error*
R Square	0.981	NA
Ca release rate (r_{Ca})	1.95E-10	1.58E-11

Diss. Rate Mineral (K_{diss}) **4.05E-09** mol/m^2s

Uncertainty of Fit 3.28E-10 mol/m^2s

Analytical error bars fall within plot symbols

Datasheet S16
Experiment FAP-P4DD

Mineral: Fluorapatite **Initial pH:** 3.98 **Specific Surf. Area (BET):** 0.0321 m^2/g
Batch ID: FAP-P4DD **Mineral Mass:** 0.3000g **Total Surf. Area (BET):** 0.00963 m^2

NA = no analysis

Batch Results (shaded data = the linear initial rate data shown in the accompanying figure)

Time (*sec*)	Ca (*moles released*)	P (*moles released*)	pH
0	0	NA	3.98
3660	1.16E-06	NA	4.41
7200	1.22E-06	NA	4.72
10620	1.83E-06	NA	4.45
14160	2.25E-06	NA	4.58
17580	2.78E-06	NA	4.82
83520	3.99E-06	NA	5.60
187140	8.01E-06	NA	5.69
770940	8.64E-06	NA	6.33
1372260	9.00E-06	NA	6.07
1741860	1.03E-05	NA	6.25

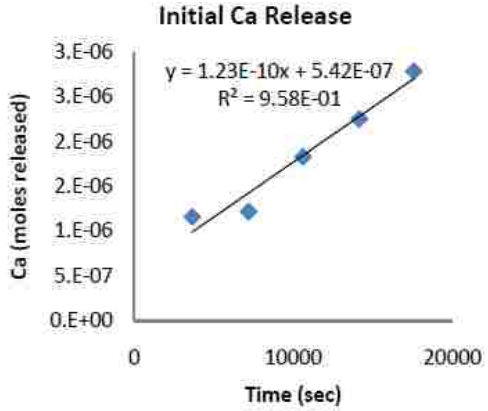

$K_{diss} = r_{ca}/A \bullet S$, where r_{ca} is the rate of Ca release over time as determined by linear regression, A is the total BET surface area (specific surface area (BET) X mineral mass), and S is the Ca stoiciometric coefficient of the respective mineral.

Regression Analysis		*Std.Error*
R Square	0.958	NA
Ca release rate (r_{ca})	1.23E-10	1.48E-11

Diss. Rate Mineral (K_{diss}) **2.55E-09** mol/m^2s

Uncertainty of Fit 3.08E-10 mol/m^2s

Analytical error bars fall within plot symbols

Datasheet S17
Experiment FAPM-P4

Mineral: Fluorapatite **Initial pH:** 4.00 **Specific Surf. Area (BET):** 0.0321 m^2/g
Batch ID: FAPM-P4 **Mineral Mass:** 0.3000g **Total Surf. Area (BET):** 0.00963 m^2

NA = no analysis

Batch Results (shaded data = the linear initial rate data shown in the accompanying figure)

Time (*sec*)	Ca (*moles released*)	P (*moles released*)	pH
0	0	NA	4.00
1320	1.11E-06	4.15E-07	4.13
2400	2.00E-06	6.11E-07	4.07
3840	2.03E-06	8.48E-07	4.05
4980	2.72E-06	9.23E-07	4.18
6300	2.83E-06	1.04E-06	4.10
8700	3.71E-06	1.51E-06	4.24
92460	NA	2.79E-06	4.81

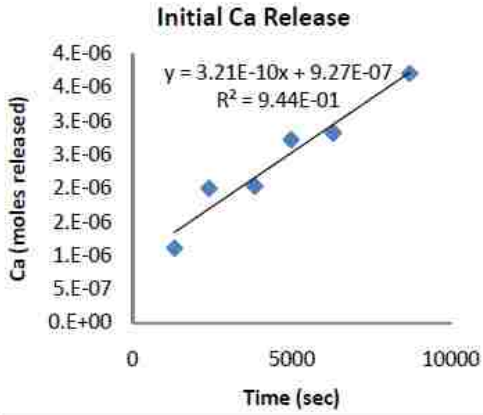

Regression Analysis		*Std.Error*
R Square	0.944	NA
Ca release rate (r_{Ca})	3.21E-10	3.90E-11

$K_{diss} = r_{ca}/A \bullet S$, where r_{ca} is the rate of Ca release over time as determined by linear regression, *A* is the total BET surface area (specific surface area (BET) X mineral mass), and *S* is the Ca stoiciometric coefficient of the respective mineral.

Diss. Rate Mineral (K_{diss}) **6.67E-09** mol/m^2s

Uncertainty of Fit 8.11E-10 mol/m^2s

Analytical error bars fall within plot symbols

Stoichiometry

Moles of Mineral Released

Time (*sec*)	Moles Mineral Released (P)	Moles Mineral Released (Ca)
1320	1.38E-07	2.23E-07
2400	2.04E-07	4.01E-07
3840	2.83E-07	4.07E-07
4980	3.08E-07	5.45E-07
6300	3.46E-07	5.65E-07
8700	5.03E-07	7.41E-07
92460	9.31E-07	NA

Moles mineral released (above) based on P or Ca determined from moles released of P or Ca divided by the appropriate stoichiometric factor of the respective ion.

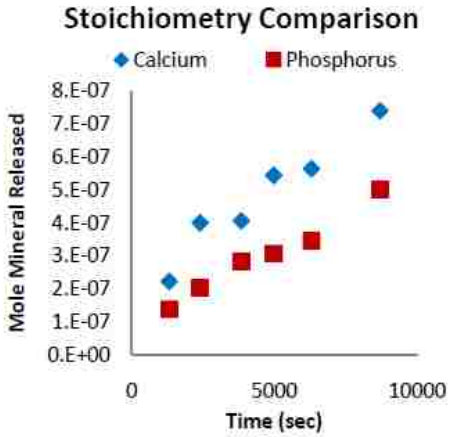

Datasheet S18
Experiment FAPM-P5

Mineral: Fluorapatite **Initial pH:** 5.00 **Specific Surf. Area (BET):** 0.0321 m^2/g
Batch ID: FAPM-P5 **Mineral Mass:** 0.3000g **Total Surf. Area (BET):** 0.00963 m^2

NA = no analysis

Batch Results (shaded data = the linear initial rate data shown in the accompanying figure)

Time (*sec*)	Ca (*moles released*)	P (*moles released*)	pH
0	NA	NA	5.00
3900	5.08E-07	1.88E-07	2.27
7440	5.85E-07	2.76E-07	5.30
11820	8.99E-07	4.41E-07	5.28
14820	9.45E-07	4.41E-07	5.58
18060	1.14E-06	5.14E-07	5.54
24360	1.24E-06	6.48E-07	5.58
103080	2.03E-06	NA	6.05
6319560	2.09E-05	NA	6.20

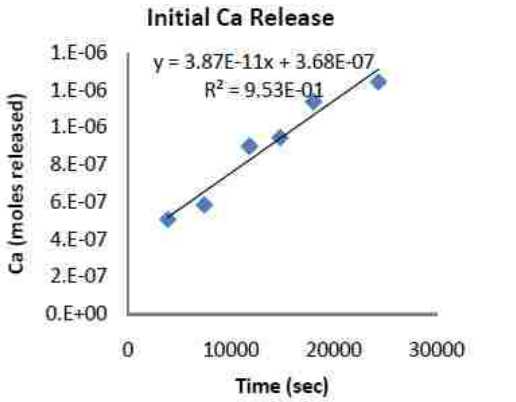

$K_{diss} = r_{ca}/A \bullet S$, where r_{ca} is the rate of Ca release over time as determined by linear regression, *A* is the total BET surface area (specific surface area (BET) X mineral mass), and *S* is the Ca stoiciometric coefficient of the respective mineral.

Regression Analysis		*Std.Error*
R Square	0.953	NA
Ca release rate (r_{ca})	3.87E-11	4.31E-12

Diss. Rate Mineral (K_{diss}) **8.04E-10** mol/m^2s

Uncertainty of Fit 8.9598E-11 mol/m^2s

Analytical error bars fall within plot symbols

Stoichiometry

Moles of Mineral Released

Time (*sec*)	Moles Mineral Released (P)	Moles Mineral Released (Ca)
3900	6.26E-08	1.02E-07
7440	9.19E-08	1.17E-07
11820	1.47E-07	1.80E-07
14820	1.47E-07	1.89E-07
18060	1.71E-07	2.28E-07
24360	2.16E-07	2.49E-07

Moles mineral released (above) based on P or Ca determined from moles released of P or Ca divided by the appropriate stoichiometric factor of the respective ion.

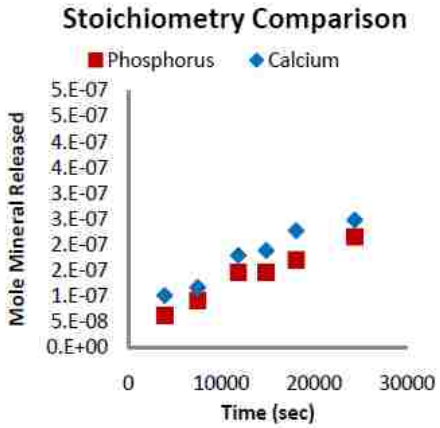

Datasheet S19
Experiment FAPM-P5D

Mineral: Fluorapatite **Initial pH:** 4.91 **Specific Surf. Area (BET):** 0.0321 m^2/g
Batch ID: FAPM-P5D **Mineral Mass:** 0.3000g **Total Surf. Area (BET):** 0.00963 m^2

NA = no analysis

Batch Results (shaded data = the linear initial rate data shown in the accompanying figure)

Time (*sec*)	Ca (*moles released*)	P (*moles released*)	pH
0	0	NA	4.91
3600	7.22E-07	NA	5.14
7080	1.02E-06	NA	5.22
10920	1.11E-06	NA	5.31
14400	1.30E-06	NA	5.41
18420	1.32E-06	NA	5.49
101580	2.38E-06	NA	6.13
522960	3.18E-06	NA	6.15

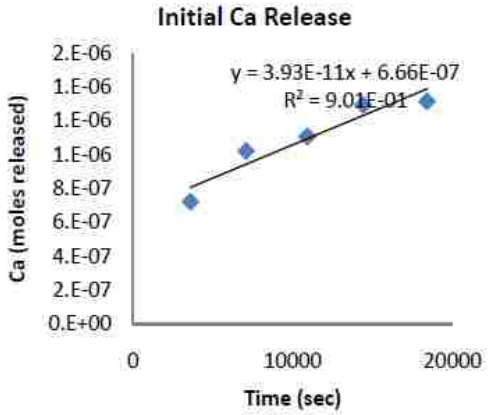

Regression Analysis		*Std.Error*
R Square	0.901	NA
Ca release rate (r_{ca})	3.93E-11	7.51E-12

$K_{diss} = r_{ca}/A \bullet S$, where r_{ca} is the rate of Ca release over time as determined by linear regression, A is the total BET surface area (specific surface area (BET) X mineral mass), and S is the Ca stoiciometric coefficient of the respective mineral.

→ *Diss. Rate Mineral* (K_{diss}) **8.16E-10** mol/m^2s

Uncertainty of Fit 1.56E-10 mol/m^2s

Analytical error bars fall within plot symbols

Datasheet S20
Experiment WHIT-P2DD

Mineral: Whitlockite **Initial pH:** 1.98 **Specific Surf. Area (BET):** 0.0516 m^2/g
Batch ID: WHIT-P2DD **Mineral Mass:** 0.1500g **Total Surf. Area (BET):** 0.00774 m^2

NA = no analysis

Batch Results (shaded data = the linear initial rate data shown in the accompanying figure)

Time (*sec*)	Ca (*moles released*)	P (*moles released*)	pH
0	0	NA	1.98
900	5.04E-05	NA	2.10
1800	5.82E-05	NA	2.07
2760	5.90E-05	NA	2.11
3660	7.29E-05	NA	2.23
4740	8.56E-05	NA	2.10
5640	1.54E-04	NA	2.19
6540	1.59E-04	NA	2.08
7440	2.19E-04	NA	2.20
8700	2.45E-04	NA	2.24
1117680	5.60E-04	NA	3.20
1204080	5.50E-04	NA	3.18
6128880	5.57E-04	NA	3.23

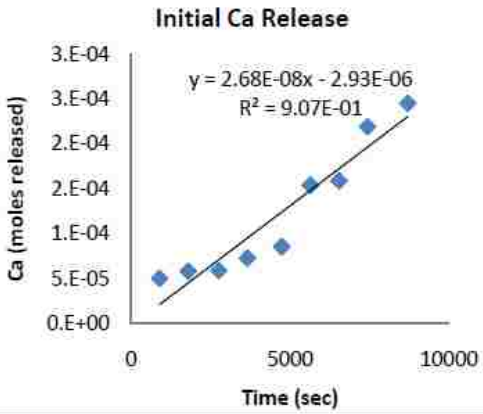

Regression Analysis		*Std.Error*
R Square	0.907	NA
Ca release rate (r_{ca})	2.68E-08	3.246E-09

$K_{diss} = r_{ca}/A \bullet S$, where r_{ca} is the rate of Ca release over time as determined by linear regression, *A* is the total BET surface area (specific surface area (BET) X mineral mass), and *S* is the Ca stoiciometric coefficient of the respective mineral.

Diss. Rate Mineral (K_{diss}) **3.84E-07** mol/m^2s

Uncertainty of Fit 4.6601E-08 mol/m^2s

Analytical error bars fall within plot symbols

Datasheet S21
Experiment WHIT-P2DDB

Mineral: Whitlockite **Initial pH:** 1.98 **Specific Surf. Area (BET):** 0.0516 m^2/g
Batch ID: WHIT-P2DDB **Mineral Mass:** 0.1500g **Total Surf. Area (BET):** 0.00774 m^2

NA = no analysis

Batch Results (shaded data = the linear initial rate data shown in the accompanying figure)

Time (*sec*)	Ca (*moles released*)	P (*moles released*)	pH
0	0	NA	1.98
960	6.48E-05	4.16E-05	2.08
1800	9.11E-05	5.60E-05	2.12
2760	9.27E-05	6.26E-05	2.14
3720	1.04E-04	7.26E-05	2.09
4800	1.50E-04	8.48E-05	2.13
5700	1.67E-04	1.18E-04	2.14
6600	1.87E-04	NA	2.27
7500	2.10E-04	NA	2.13
8700	2.67E-04	NA	2.34
556020	5.58E-04	NA	3.16
599220	5.57E-04	NA	3.21

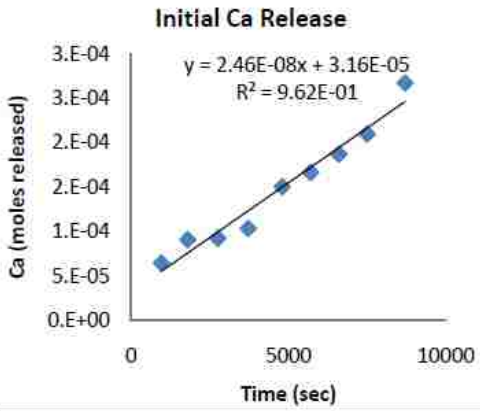

Regression Analysis		*Std.Error*
R Square	0.962	NA
Ca release rate (r_{ca})	2.46E-08	1.85E-09

$K_{diss} = r_{ca}/A \bullet S$, where r_{ca} is the rate of Ca release over time as determined by linear regression, *A* is the total BET surface area (specific surface area (BET) X mineral mass), and *S* is the Ca stoiciometric coefficient of the respective mineral.

Diss. Rate Mineral (K_{diss}) **3.54E-07** mol/m^2s

Uncertainty of Fit 2.65E-08 mol/m^2s

Analytical error bars fall within plot symbols

Stoichiometry

Moles of Mineral Released

Time (*sec*)	Moles Mineral Released (P)	Moles Mineral Released (Ca)
960	5.94E-06	7.20E-06
1800	8.01E-06	1.01E-05
2760	8.94E-06	1.03E-05
3720	1.04E-05	1.15E-05
4800	1.21E-05	1.67E-05
5700	1.68E-05	1.85E-05
6600	NA	2.08E-05
7500	NA	2.33E-05
8700	NA	2.97E-05

Moles mineral released (above) based on P or Ca determined from moles released of P or Ca divided by the appropriate stoichiometric factor of the respective ion.

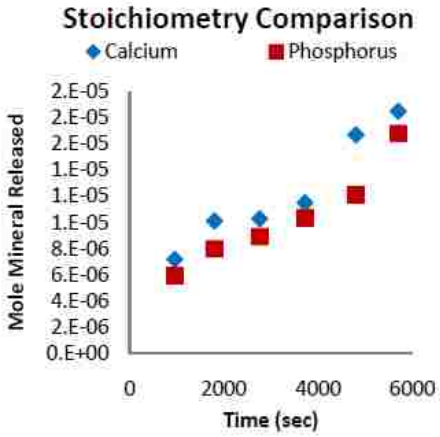

Datasheet S22
Experiment WHIT-P3

Mineral: Whitlockite **Initial pH:** 3.00 **Specific Surf. Area (BET):** 0.0516 m^2/g
Batch ID: WHIT-P3 **Mineral Mass:** 0.1500g **Total Surf. Area (BET):** 0.00774 m^2

NA = no analysis

Batch Results (shaded data = the linear initial rate data shown in the accompanying figure)

Time (*sec*)	Ca (*moles released*)	P (*moles released*)	pH
0	0	NA	3.00
600	1.04E-05	7.96E-06	3.09
1260	1.41E-05	1.35E-05	3.12
1800	1.62E-05	1.45E-05	3.11
2460	1.71E-05	1.50E-05	3.11
3060	2.37E-05	2.13E-05	3.15
4140	2.58E-05	NA	3.18
81300	6.69E-05	NA	3.87
242460	6.63E-05	NA	4.51
593220	6.68E-05	NA	4.69
850500	7.01E-05	NA	4.67
1988580	7.08E-05	NA	4.71

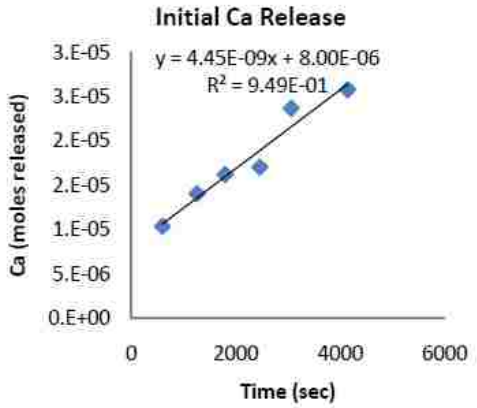

Regression Analysis		*Std.Error*
R Square	0.949	NA
Ca release rate (r_{Ca})	4.4497E-09	5.14E-10

$K_{diss} = r_{ca}/A \bullet S$, where r_{ca} is the rate of Ca release over time as determined by linear regression, *A* is the total BET surface area (specific surface area (BET) X mineral mass), and *S* is the Ca stoiciometric coefficient of the respective mineral.

Diss. Rate Mineral (K_{diss}) **6.39E-08** mol/m^2s

Uncertainty of Fit 7.3799E-09 mol/m^2s

Analytical error bars fall within plot symbols

Stoichiometry

Moles of Mineral Released

Time (*sec*)	Moles Mineral Released (P)	Moles Mineral Released (Ca)
600	1.14E-06	1.16E-06
1260	1.93E-06	1.56E-06
1800	2.08E-06	1.80E-06
2460	2.14E-06	1.90E-06
3060	3.04E-06	2.63E-06

Moles mineral released (above) based on P or Ca determined from moles released of P or Ca divided by the appropriate stoichiometric factor of the respective ion.

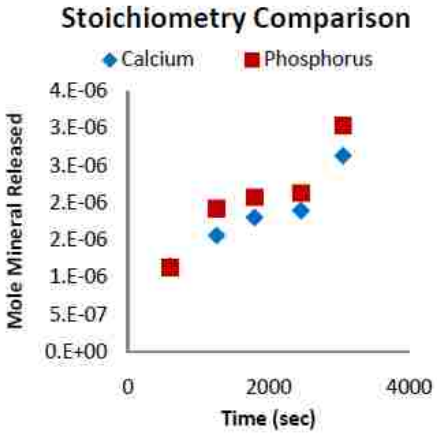

Datasheet S23
Experiment WHIT-P3D

Mineral: Whitlockite **Initial pH:** 3.01 **Specific Surf. Area (BET):** 0.0516 m^2/g
Batch ID: WHIT-P3D **Mineral Mass:** 0.1500g **Total Surf. Area (BET):** 0.00774 m^2

NA = no analysis

Batch Results (shaded data = the linear initial rate data shown in the accompanying figure)

Time (*sec*)	Ca (*moles released*)	P (*moles released*)	pH
0	0	NA	3.01
780	1.60E-05	NA	3.08
1380	1.85E-05	NA	3.12
1920	2.16E-05	NA	3.14
2520	2.27E-05	NA	3.16
3180	2.69E-05	NA	3.19
4440	3.15E-05	NA	3.18
11460	3.31E-05	NA	3.46
96000	7.16E-05	NA	4.16

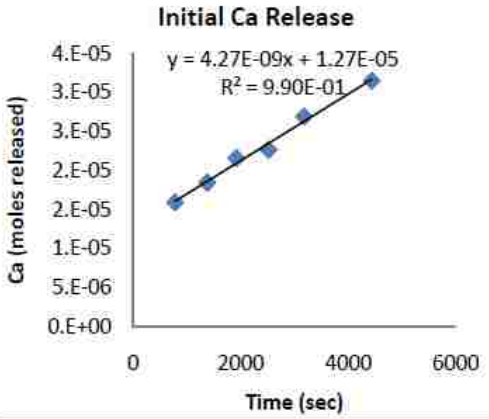

$K_{diss} = r_{ca}/A \bullet S$, where r_{ca} is the rate of Ca release over time as determined by linear regression, *A* is the total BET surface area (specific surface area (BET) X mineral mass), and *S* is the Ca stoiciometric coefficient of the respective mineral.

Regression Analysis		*Std.Error*
R Square	0.990	NA
Ca release rate (r_{ca})	4.27E-09	2.13E-10

Diss. Rate Mineral (K_{diss}) **6.12E-08** mol/m^2s

Uncertainty of Fit 3.06E-09 mol/m^2s

Analytical error bars fall within plot symbols

Datasheet S24
Experiment WHIT-P4D

Mineral: Whitlockite **Initial pH:** 3.99 **Specific Surf. Area (BET):** 0.0516 m^2/g
Batch ID: WHIT-P4D **Mineral Mass:** 0.1500g **Total Surf. Area (BET):** 0.00774 m^2

NA = no analysis

Batch Results (shaded data = the linear initial rate data shown in the accompanying figure)

Time (*sec*)	Ca (*moles released*)	P (*moles released*)	pH
0	0	NA	3.99
3900	4.52E-06	2.70E-06	3.88
7680	5.10E-06	3.73E-06	4.52
11160	6.49E-06	4.41E-06	4.50
14880	7.33E-06	5.32E-06	4.76
18540	7.77E-06	5.64E-06	4.81
81600	9.72E-06	6.95E-06	5.80
103380	1.00E-05	NA	6.01
276480	1.08E-05	NA	6.25

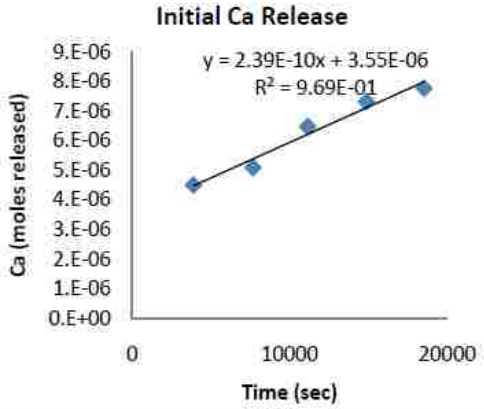

$K_{diss} = r_{ca}/A \bullet S$, where r_{ca} is the rate of Ca release over time as determined by linear regression, *A* is the total BET surface area (specific surface area (BET) X mineral mass), and *S* is the Ca stoiciometric coefficient of the respective mineral.

Regression Analysis		*Std.Error*
R Square	0.969	NA
Ca release rate (r_{ca})	2.39E-10	2.48E-11

Diss. Rate Mineral (K_{diss}) **3.43E-09** mol/m^2s

Uncertainty of Fit 3.57E-10 mol/m^2s

Analytical error bars fall within plot symbols

Stoichiometry

Moles of Mineral Released

Time (*sec*)	Moles Mineral Released (P)	Moles Mineral Released (Ca)
3900	3.85E-07	5.02E-07
7680	5.32E-07	5.67E-07
11160	6.30E-07	7.21E-07
14880	7.60E-07	8.14E-07
18540	8.06E-07	8.64E-07
81600	9.93E-07	1.08E-06

Moles mineral released (above) based on P or Ca determined from moles released of P or Ca divided by the appropriate stoichiometric factor of the respective ion.

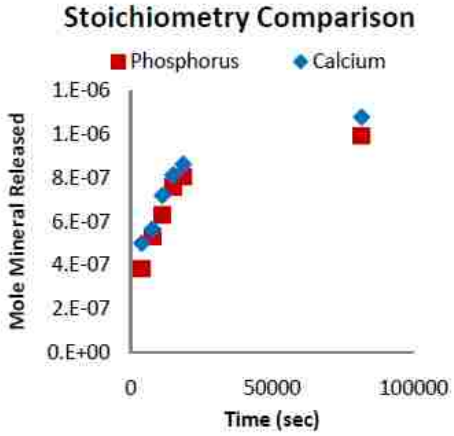

Datasheet S25
Experiment WHIT-P4DD

Mineral: Whitlockite **Initial pH:** 3.98 **Specific Surf. Area (BET):** 0.0516 m^2/g
Batch ID: WHIT-P4DD **Mineral Mass:** 0.1500g **Total Surf. Area (BET):** 0.00774 m^2

NA = no analysis

Batch Results (shaded data = the linear initial rate data shown in the accompanying figure)

Time (*sec*)	Ca (*moles released*)	P (*moles released*)	pH
0	0	NA	3.98
3660	4.03E-06	NA	4.41
7200	5.95E-06	NA	4.72
10620	6.22E-06	NA	4.45
14160	6.78E-06	NA	4.58
17580	7.77E-06	NA	4.82
83520	1.04E-05	NA	5.60
187140	1.03E-05	NA	5.69
770940	1.03E-05	NA	6.33
1372260	1.16E-05	NA	6.07
1741860	1.20E-05	NA	6.25

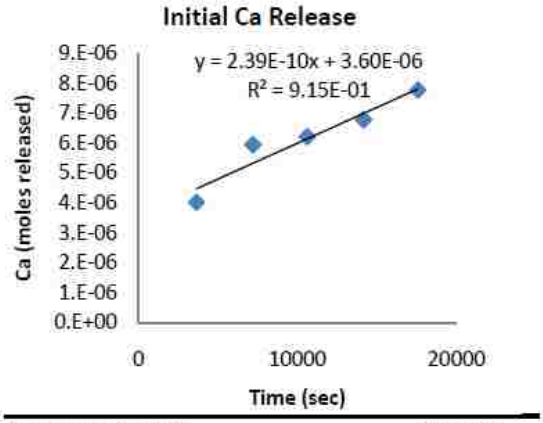

Regression Analysis		*Std.Error*
R Square	0.915	NA
Ca release rate (r_{Ca})	2.39E-10	4.20E-11

$K_{diss} = r_{Ca}/A \bullet S$, where r_{Ca} is the rate of Ca release over time as determined by linear regression, *A* is the total BET surface area (specific surface area (BET) X mineral mass), and *S* is the Ca stoiciometric coefficient of the respective mineral.

→ *Diss. Rate Mineral* (K_{diss}) **3.43E-09** mol/m^2s

Uncertainty of Fit 6.03E-10 mol/m^2s

Analytical error bars fall within plot symbols

Datasheet S26
Experiment WHIT-P5D

Mineral: Whitlockite **Initial pH:** 5.00 **Specific Surf. Area (BET):** 0.0516 m^2/g
Batch ID: WHIT-P5D **Mineral Mass:** 0.1500g **Total Surf. Area (BET):** 0.00774 m^2

NA = no analysis

Batch Results (shaded data = the linear initial rate data shown in the accompanying figure)

Time (*sec*)	Ca (*moles released*)	P (*moles released*)	pH
0	0	NA	5.00
3840	1.12E-06	NA	5.20
7620	1.29E-06	NA	5.31
11100	1.67E-06	NA	5.34
14820	1.69E-06	NA	5.41
18480	1.85E-06	NA	5.38
81540	3.06E-06	NA	6.13
103320	3.22E-06	NA	6.24
276420	4.26E-06	NA	6.34

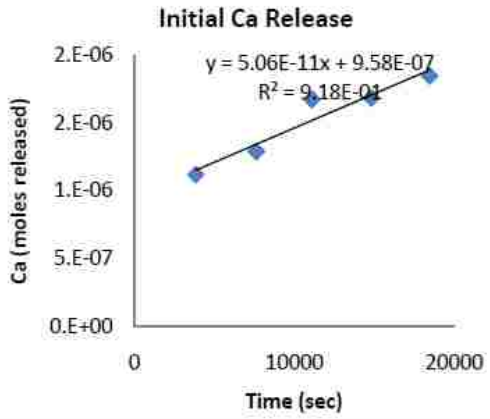

$K_{diss} = r_{ca}/A \bullet S$, where r_{ca} is the rate of Ca release over time as determined by linear regression, *A* is the total BET surface area (specific surface area (BET) X mineral mass), and *S* is the Ca stoiciometric coefficient of the respective mineral.

Regression Analysis		*Std.Error*
R Square	0.918	NA
Ca release rate (r_{ca})	5.06E-11	8.75E-12

Diss. Rate Mineral (K_{diss}*)* **7.26E-10** mol/m^2s

Uncertainty of Fit 1.26E-10 mol/m^2s

Analytical error bars fall within plot symbols

Datasheet S27
Experiment WHIT-P5DDB

Mineral: Whitlockite **Initial pH:** 4.99 **Specific Surf. Area (BET):** 0.0516 m^2/g
Batch ID: WHIT-P5DDB **Mineral Mass:** 0.1500g **Total Surf. Area (BET):** 0.00774 m^2

NA = no analysis

Batch Results (shaded data = the linear initial rate data shown in the accompanying figure)

Time (*sec*)	Ca (*moles released*)	P (*moles released*)	pH
0	0.00E+00	NA	4.99
1320	1.95E-07	4.15E-07	5.19
3840	5.16E-07	6.11E-07	5.33
6300	5.87E-07	8.48E-07	5.31
8700	6.21E-07	9.23E-07	5.40
10980	7.21E-07	1.04E-06	5.55
18720	1.05E-06	1.51E-06	5.67
92460	2.05E-06	NA	6.03

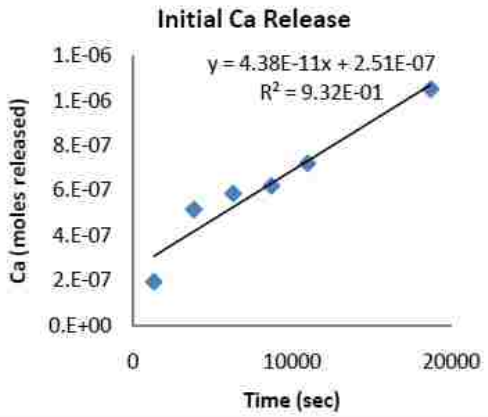

Regression Analysis		*Std.Error*
R Square	0.932	NA
Ca release rate (r_{ca})	4.3799E-11	5.93E-12

$K_{diss} = r_{ca}/A \bullet S$, where r_{ca} is the rate of Ca release over time as determined by linear regression, *A* is the total BET surface area (specific surface area (BET) X mineral mass), and *S* is the Ca stoiciometric coefficient of the respective mineral.

Diss. Rate Mineral (K_{diss}) **6.29E-10** mol/m^2s

Uncertainty of Fit 8.52E-11 mol/m^2s

Analytical error bars fall within plot symbols

Stoichiometry

Moles of Mineral Released

Time (*sec*)	Moles Mineral Released (P)	Moles Mineral Released (Ca)
1320	5.93E-08	2.17E-08
3840	8.73E-08	5.74E-08
6300	1.21E-07	6.53E-08
8700	1.32E-07	6.90E-08
10980	1.48E-07	8.02E-08
18720	2.16E-07	1.17E-07

Moles mineral released (above) based on P or Ca determined from moles released of P or Ca divided by the appropriate stoichiometric factor of the respective ion.

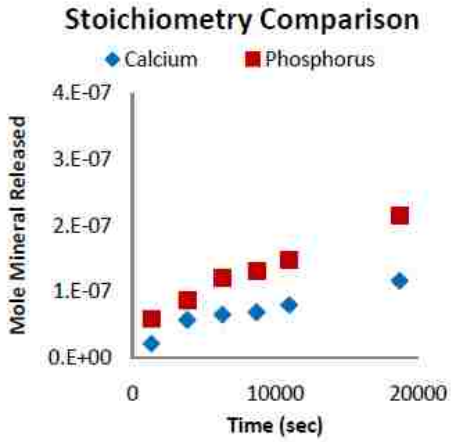

Datasheet S28
Experiment MER-P2DDC

Mineral: Merrillite **Initial pH:** 2.00 **Specific Surf. Area (BET):** 0.0465m²/g
Batch ID: MER-P2DDC **Mineral Mass:** 0.1500g **Total Surf. Area (BET):** 0.00698 m²

NA = no analysis

Batch Results (shaded data = the linear initial rate data shown in the accompanying figure)

Time (*sec*)	Ca (*moles released*)	P (*moles released*)	pH
0	0	NA	2.00
960	1.40E-05	1.87E-05	2.03
1920	2.29E-05	1.97E-05	2.06
2760	4.41E-05	2.26E-05	2.13
3720	6.52E-05	6.89E-05	2.12
4620	7.40E-05	7.98E-05	2.15
5460	8.21E-05	1.03E-04	2.15
6420	1.08E-04	1.09E-04	2.14
7260	1.36E-04	1.17E-04	2.16

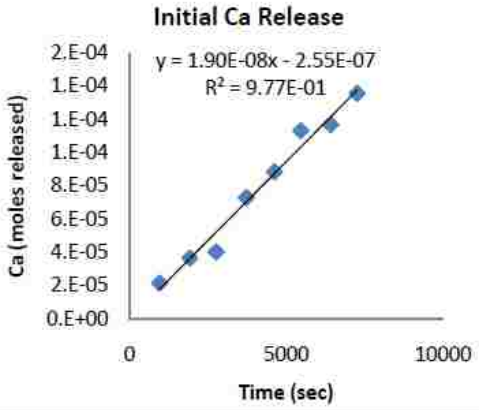

Regression Analysis		*Std.Error*
R Square	0.977	NA
Ca release rate (r_{ca})	1.90E-08	1.18E-09

$K_{diss} = r_{ca}/A \bullet S$, where r_{ca} is the rate of Ca release over time as determined by linear regression, *A* is the total BET surface area (specific surface area (BET) X mineral mass), and *S* is the Ca stoiciometric coefficient of the respective mineral.

Diss. Rate Mineral (K_{diss}) **2.86E-07** mol/m²s

Uncertainty of Fit 1.78E-08 mol/m²s

Analytical error bars fall within plot symbols

Stoichiometry

Moles of Mineral Released

Time (*sec*)	Moles Mineral Released (P)	Moles Mineral Released (Ca)
960	2.67E-06	1.47E-06
1920	2.82E-06	2.42E-06
2760	3.22E-06	4.64E-06
3720	9.85E-06	6.86E-06
4620	1.14E-05	7.79E-06
5460	1.47E-05	8.64E-06
6420	1.56E-05	1.14E-05
7260	1.67E-05	1.43E-05

Moles mineral released (above) based on P or Ca determined from moles released of P or Ca divided by the appropriate stoichiometric factor of the respective ion.

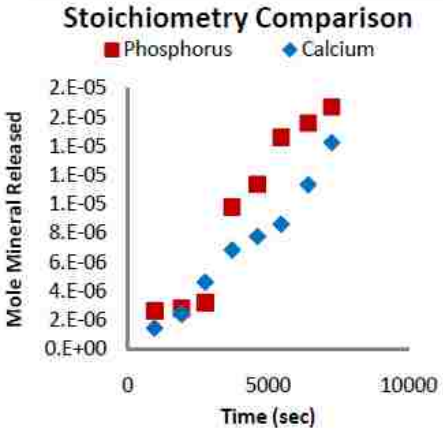

Datasheet S29
Experiment MER-P2DD

Mineral: Merrillite **Initial pH:** 1.97 **Specific Surf. Area (BET):** 0.0465m^2/g
Batch ID: MER-P2DD **Mineral Mass:** 0.1500g **Total Surf. Area (BET):** 0.00698 m^2

NA = no analysis

Batch Results (shaded data = the linear initial rate data shown in the accompanying figure)

Time (*sec*)	Ca (*moles released*)	P (*moles released*)	pH
0	0	NA	1.97
900	1.40E-05	NA	2.06
1440	2.29E-05	NA	2.05
2160	4.41E-05	NA	2.07
2880	6.52E-05	NA	2.07
3600	7.40E-05	NA	2.04
4980	8.21E-05	NA	2.07
9360	1.08E-04	NA	2.14
168060	3.80E-04	NA	2.55

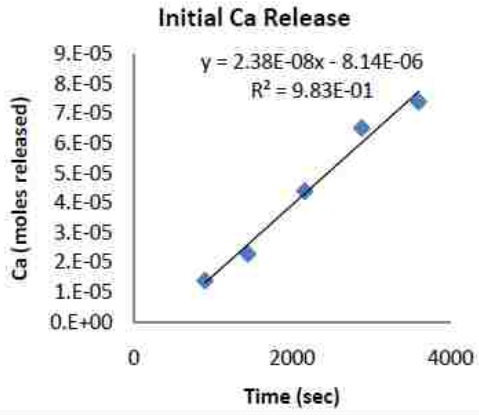

$K_{diss} = r_{ca}/A \bullet S$, where r_{ca} is the rate of Ca release over time as determined by linear regression, *A* is the total BET surface area (specific surface area (BET) X mineral mass), and *S* is the Ca stoiciometric coefficient of the respective mineral.

Regression Analysis		*Std.Error*
R Square	0.983	NA
Ca release rate (r_{ca})	2.38E-08	1.82E-09

Diss. Rate Mineral (K_{diss} *)* **3.58E-07** mol/m^2s

Uncertainty of Fit 2.75E-08 mol/m^2s

Analytical error bars fall within plot symbols

Datasheet S30
Experiment MER-P3

Mineral: Merrillite **Initial pH:** 3.00 **Specific Surf. Area (BET):** 0.0465m^2/g
Batch ID: MER-P3 **Mineral Mass:** 0.1500g **Total Surf. Area (BET):** 0.00698 m^2

NA = no analysis

Batch Results (shaded data = the linear initial rate data shown in the accompanying figure)

Time (*sec*)	Ca (*moles released*)	P (*moles released*)	pH
0	0	NA	3.00
960	1.26E-05	NA	3.50
1800	1.46E-05	NA	2.99
2700	1.78E-05	NA	3.29
3540	2.10E-05	NA	3.26
4440	2.43E-05	NA	3.30
5700	3.22E-05	NA	3.51
8160	3.82E-05	NA	3.52
1165980	5.42E-05	NA	4.81
1209180	5.44E-05	NA	5.27
3671580	5.30E-05	NA	4.92
1504380	5.31E-05	NA	5.45
4578780	5.45E-05	NA	5.49
5226780	5.34E-05	NA	NA

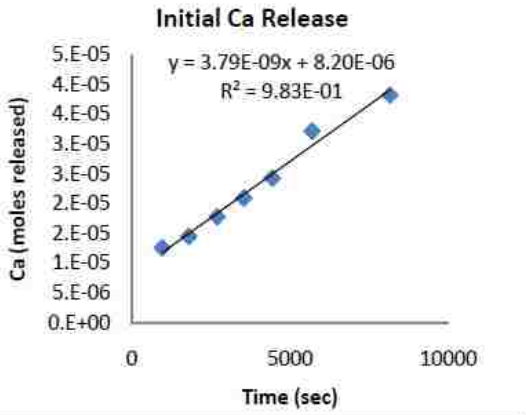

Regression Analysis		*Std.Error*
R Square	0.983	NA
Ca release rate (r_{Ca})	3.79E-09	2.19E-10

$K_{diss} = r_{ca}/A \bullet S$, where r_{ca} is the rate of Ca release over time as determined by linear regression, *A* is the total BET surface area (specific surface area (BET) X mineral mass), and *S* is the Ca stoiciometric coefficient of the respective mineral.

→ *Diss. Rate Mineral (K_{diss})* **5.71E-08** mol/m^2s

Uncertainty of Fit 3.31E-09 mol/m^2s

Analytical error bars fall within plot symbols

Datasheet S31
Experiment MER-P3D

Mineral: Merrillite **Initial pH:** 3.00 **Specific Surf. Area (BET):** 0.0465m^2/g
Batch ID: MER-P3D **Mineral Mass:** 0.1500g **Total Surf. Area (BET):** 0.00698 m^2

NA = no analysis

Batch Results (shaded data = the linear initial rate data shown in the accompanying figure)

Time (*sec*)	Ca (*moles released*)	P (*moles released*)	pH
0	0	NA	3.00
720	6.31E-06	2.89E-06	3.07
1380	9.93E-06	4.57E-06	3.05
2040	1.27E-05	6.37E-06	3.08
2520	1.43E-05	6.64E-06	3.14
3060	1.68E-05	8.53E-06	3.18
3660	1.86E-05	8.71E-06	3.17
7140	2.17E-05	1.72E-05	3.25
101640	6.02E-05	2.81E-05	4.67
523020	6.18E-05	NA	5.00

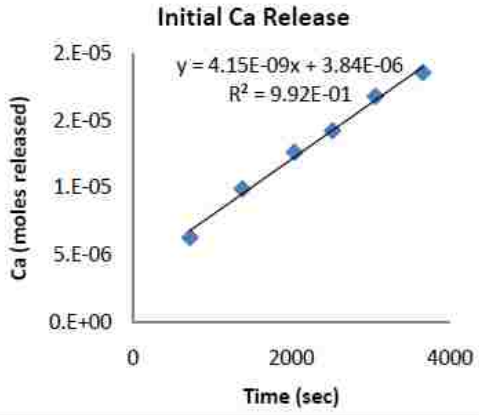

$K_{diss} = r_{ca}/A \bullet S$, where r_{ca} is the rate of Ca release over time as determined by linear regression, *A* is the total BET surface area (specific surface area (BET) X mineral mass), and *S* is the Ca stoiciometric coefficient of the respective mineral.

Regression Analysis		*Std.Error*
R Square	0.992	NA
Ca release rate (r_{ca})	4.15E-09	1.84E-10

Diss. Rate Mineral (K_{diss}) **6.26E-08** mol/m^2s

Uncertainty of Fit 2.77E-09 mol/m^2s

Analytical error bars fall within plot symbols

Stoichiometry

Moles of Mineral Released

Time (*sec*)	Moles Mineral Released (P)	Moles Mineral Released (Ca)
720	4.13E-07	6.65E-07
1380	6.53E-07	1.05E-06
2040	9.10E-07	1.33E-06
2520	9.49E-07	1.50E-06
3060	1.22E-06	1.77E-06
3660	1.24E-06	1.96E-06

Moles mineral released (above) based on P or Ca determined from moles released of P or Ca divided by the appropriate stoichiometric factor of the respective ion.

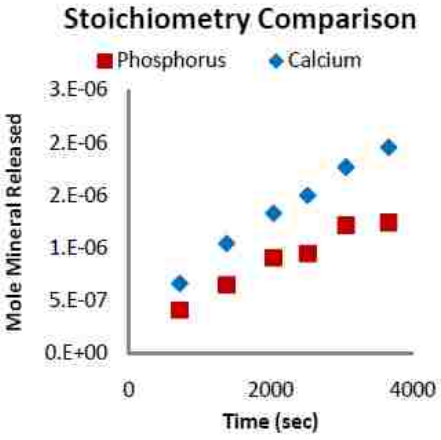

Datasheet S32
Experiment MER-P4

Mineral: Merrillite **Initial pH:** 4.01 **Specific Surf. Area (BET):** 0.0465 m^2/g
Batch ID: MER-P4 **Mineral Mass:** 0.1500g **Total Surf. Area (BET):** 0.00698 m^2

NA =no analysis

Batch Results (shaded data = the linear initial rate data shown in the accompanying figure)

Time (*sec*)	Ca (*moles released*)	P (*moles released*)	pH
0	0	NA	4.01
960	1.76E-06	NA	4.33
1800	2.28E-06	NA	4.34
2700	2.89E-06	NA	4.15
3540	3.15E-06	NA	4.33
4500	3.73E-06	NA	4.53
5700	4.09E-06	NA	4.59
8220	4.95E-06	NA	4.59
101280	6.85E-06	NA	5.83

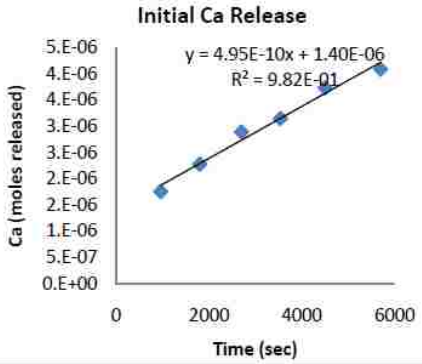

Regression Analysis		*Std.Error*
R Square	0.982	NA
Ca release rate (r_{ca})	4.95E-10	3.33E-11

$K_{diss} = r_{ca}/A \bullet S$, where r_{ca} is the rate of Ca release over time as determined by linear regression, *A* is the total BET surface area (specific surface area (BET) X mineral mass), and *S* is the Ca stoiciometric coefficient of the respective mineral.

Diss. Rate Mineral (K_{diss}) **7.47E-09** mol/m^2s

Uncertainty of Fit 5.03E-10 mol/m^2s

Analytical error bars fall within plot symbols

Datasheet S33
Experiment MER-P4DD

Mineral: Merrillite **Initial pH:** 4.00 **Specific Surf. Area (BET):** 0.0465m^2/g
Batch ID: MER-P4DD **Mineral Mass:** 0.1500g **Total Surf. Area (BET):** 0.00698 m^2

NA = no analysis

Batch Results (shaded data = the linear initial rate data shown in the accompanying figure)

Time (*sec*)	Ca (*moles released*)	P (*moles released*)	pH
0	0	0	4.00
1320	1.20E-06	1.33E-06	4.10
2400	1.71E-06	1.87E-06	4.17
3840	2.31E-06	2.66E-06	4.20
4920	2.82E-06	3.23E-06	4.31
6300	3.20E-06	3.57E-06	4.31
8700	3.83E-06	4.79E-06	4.43
92460	6.95E-06	NA	5.56

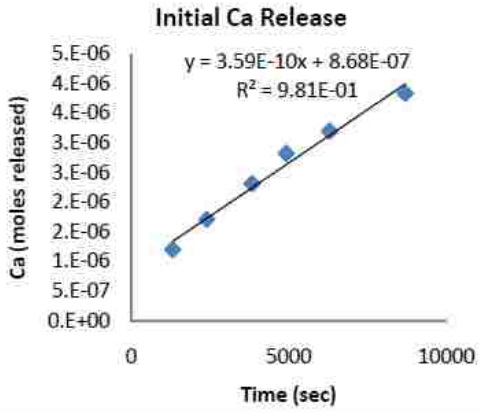

$K_{diss} = r_{ca}/A \bullet S$, where r_{ca} is the rate of Ca release over time as determined by linear regression, *A* is the total BET surface area (specific surface area (BET) X mineral mass), and *S* is the Ca stoiciometric coefficient of the respective mineral.

Regression Analysis		*Std.Error*
R Square	0.981	NA
Ca release rate (r_{ca})	3.59E-10	2.50E-11

Diss. Rate Mineral (K_{diss}) **5.41E-09** mol/m^2s

Uncertainty of Fit 3.77E-10 mol/m^2s

Analytical error bars fall within plot symbols

Stoichiometry

Moles of Mineral Released

Time (*sec*)	Moles Mineral Released (P)	Moles Mineral Released (Ca)
1320	1.91E-07	1.26E-07
2400	2.67E-07	1.80E-07
3840	3.80E-07	2.43E-07
4920	4.61E-07	2.97E-07
6300	5.10E-07	3.36E-07
8700	6.85E-07	4.03E-07

Moles mineral released (above) based on P or Ca determined from moles released of P or Ca divided by the appropriate stoichiometric factor of the respective ion.

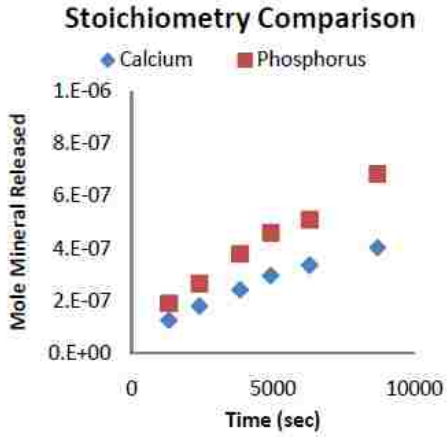

Datasheet S34
Experiment MER-P5

Mineral: Merrillite **Initial pH:** 5.00 **Specific Surf. Area (BET):** 0.0465 m^2/g
Batch ID: MER-P5 **Mineral Mass:** 0.1500g **Total Surf. Area (BET):** 0.00698 m^2

NA = no analysis

Batch Results (shaded data = the linear initial rate data shown in the accompanying figure)

Time (*sec*)	Ca (*moles released*)	P (*moles released*)	pH
0	0	0	5.00
3840	5.74E-07	2.81E-07	5.45
7380	6.95E-07	4.57E-07	5.78
11760	8.08E-07	5.95E-07	5.56
14760	9.10E-07	6.20E-07	5.76
18000	1.05E-06	7.41E-07	5.68
24000	1.25E-06	8.53E-07	5.81
103020	2.03E-06	NA	6.33

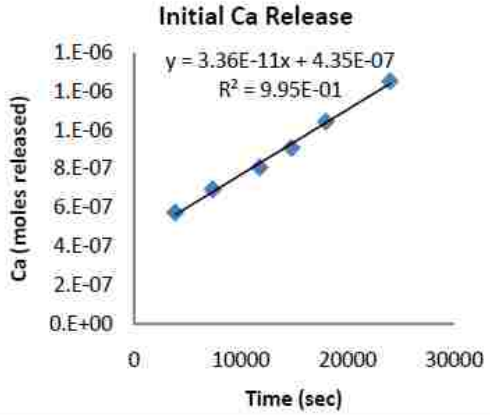

$K_{diss} = r_{ca}/A \bullet S$, where r_{ca} is the rate of Ca release over time as determined by linear regression, *A* is the total BET surface area (specific surface area (BET) X mineral mass), and *S* is the Ca stoiciometric coefficient of the respective mineral.

Regression Analysis		*Std.Error*
R Square	0.995	NA
Ca release rate (r_{ca})	3.36E-11	1.14E-12

Diss. Rate Mineral (K_{diss}) **5.07E-10** mol/m^2s

Uncertainty of Fit 1.73E-11 mol/m^2s

Analytical error bars fall within plot symbols

Stoichiometry

Moles of Mineral Released

Time (*sec*)	Moles Mineral Released (P)	Moles Mineral Released (Ca)
3840	4.01E-08	6.05E-08
7380	6.52E-08	7.31E-08
11760	8.49E-08	8.51E-08
14760	8.86E-08	9.57E-08
18000	1.06E-07	1.10E-07
24000	1.22E-07	1.32E-07

Moles mineral released (above) based on P or Ca determined from moles released of P or Ca divided by the appropriate stoichiometric factor of the respective ion.

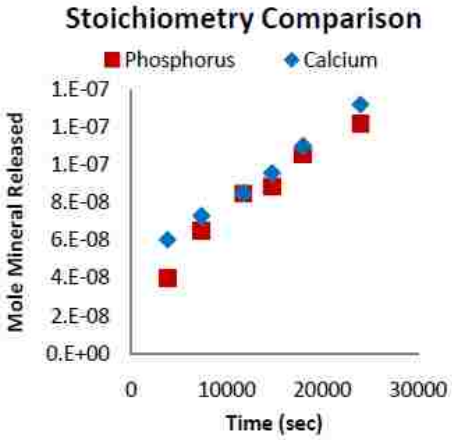

Datasheet S35
Experiment MER-P5D

Mineral: Merrillite **Initial pH:** 4.91 **Specific Surf. Area (BET):** 0.0468m^2/g
Batch ID: MER-P5D **Mineral Mass:** 0.1500g **Total Surf. Area (BET):** 0.00698 m^2

NA = no analysis

Batch Results (shaded data = the linear initial rate data shown in the accompanying figure)

Time (*sec*)	Ca (*moles released*)	P (*moles released*)	pH
0	0	NA	4.91
3840	4.64E-07	NA	5.10
7320	7.02E-07	NA	5.21
11160	9.49E-07	NA	5.25
14640	1.01E-06	NA	5.43
18660	1.08E-06	NA	5.65
101820	2.25E-06	NA	5.95
523200	3.52E-06	NA	6.28

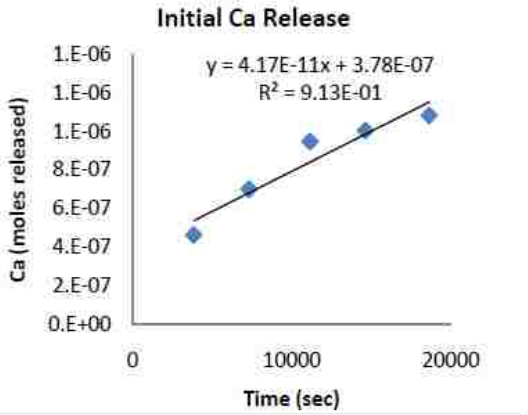

$K_{diss} = r_{ca}/A \bullet S$, where r_{ca} is the rate of Ca release over time as determined by linear regression, *A* is the total BET surface area (specific surface area (BET) X mineral mass), and *S* is the Ca stoiciometric coefficient of the respective mineral.

Regression Analysis		*Std.Error*
R Square	0.913	NA
Ca release rate (r_{ca})	4.17E-11	7.41E-12

Diss. Rate Mineral (K_{diss}) **6.28E-10** mol/m^2s

Uncertainty of Fit 1.12E-10 mol/m^2s

Analytical error bars fall within plot symbols

APPENDIX III SUPPLEMENTARY INFORMATION FOR CHAPTER FOUR

Supplementary Information

Analysis of Weathering Features in Mars Analog Basalts at Craters of the Moon National Monument, Idaho.

Introduction

Craters of the Moon National Monument (COTM) is located on the Snake River Plain of Idaho in the northwestern United States (Figures S5 and S6, this Appendix). The area is the locale of 60 or more alkaline lava flows and 25 cinder cones (Kuntz et al., 1986a; Vaughan, 2008; Vaughan et al., 2011). The first detailed description of the area was conducted by Stearns (1924; 1928) for the Idaho Bureau of Mines and Geology. Stearns (1928) described the biota, geology, geomorphology, and reported the first chemical analysis of COTM basalt, although it is not spatially located or assigned to a specific lava flow. The area receives 240 - 380mm (9.5 - 15") mean annual precipitation moving from south to north (Stearns, 1928; Vaughan, 2008; Kukachka, 2010; Vaughan et al., 2011) making it an arid to semi-arid environment. Average monthly high temperatures range from -1.7 to 29 °C (29 - 84°F) and average lows span -12 to 11 °C (10 to 52°F) with approximately 7 months of lows in the sub-freezing range (Kukachka, 2010). Since the initial reports by Stearns, the chemistry and mineralogy of many COTM flows have been well documented (Leeman et al., 1976; Kuntz et al., 1985; Kuntz et al., 1992; Stout et al., 1994) and a number of flows at COTM have been dated and range in age from ~2,000 to >18,000 years bp (Kuntz et al., 1986b; Kuntz et al., 1992; Vaughan et al., 2011). The flows have experienced various degrees of surface weathering over time, and thus represent an arid to semi-arid environment chronosequence (Vaughan, 2008).

Many of the alkaline basalts at COTM posses high concentrations of FeO, TiO_2, and P_2O_5 (up to 2.9 wt% P_2O_5) (Stearns, 1928; Leeman et al., 1976; Kuntz et al., 1992; Stout et al., 1994). The origins of the high-P basalts at COTM are not conclusively understood. High large-ion lithophile element (LILE) and rare earth element (REE) abundances relative to regionally close olivine basalts of the Snake River Plain suggest they are not formed by crystal fractionation from the same parent magma source of Snake River Plain olivine basalts (Usui et al., 2008). Heterogeneous mantle sources, crustal contamination, or a combination of both have been proposed as possible explanations of the unusual chemistry (Kuntz et al., 1992; Stout et al., 1994; Reid, 1995).

The unusual chemistry of COTM basalts led Usui and others to suggest COTM basalts might serve as useful terrestrial analogs for high-P bearing Wishstone class rocks on Mars (Usui et al., 2008). This martian rock class appears to comprise the dominant population of float rocks encountered by the Mars Exploration Rover (MER) Spirit on Cumberland Ridge and the northwest flank of Husband Hill within Gusev Crater on Mars (Arvidson et al., 2006; Squyres et al., 2006). No source or outcrop for the rocks has been identified. Alpha Particle X-ray Spectroscopy (APXS) analyses by MER Spirit of two Wishstone class rocks (Wishstone and Champagne) showed the rocks, like COTM basalts, to be typified by high Ti (~2.5-3% as TiO_2) and P (~5% as P_2O_5) content (Gellert et al., 2004; Ming et al., 2006). The chemical similarities of terrestrial COTM basalts and martian Wishstone class rocks suggest potential petrogenetic/petrographic similarities between the rocks as well.

As outlined in the accompanying chapter, the high-P chemistry of Wishstone class rocks (much like COTM basalts) make Wishstone petrogenesis and mineralogy of

particular geologic interest in martian studies. Further, these rocks show evidence of both aqueous alteration and the loss of a phosphate mineral through dissolution. Both the water responsible for the alteration of the rock class and the phosphorus released from them have astrobiological implications and may hold insights into the potential for life to have developed and persisted on Mars. In the absence of a physical sample of P-rich Wishstone class martian rocks, investigation of chemically similar rocks of COTM as a Martian analog can lead to insights into phosphate behavior over longer time-scales than can be observed in the laboratory.

In this study, Scanning Electron Microscopy (SEM) using Backscattered Electron (BSE) Imagery, Energy Dispersive Spectroscopy (EDS), and EDS X-Ray mapping was utilized to investigate COTM basalts in thin section. The objective of this study was to use COTM observation and analysis of weathering effects including the development of weathering rinds, porosity, mineral dissolution textures, primary phosphate mineral dissolution, and the abundance of secondary phosphate minerals, to gain insights that might be applicable to Wishstone class rocks on Mars and to inform reactive transport modeling.

Methods

Materials

Fifteen petrographic thin sections were prepared from samples of both buried and exposed material from six COTM flows. Sampled flows ranged in age from 1,670 to 15,100 years before present and Figure S6 documents sample locations and flow ages. Representative pieces of flow samples were broken from the main sample and oriented in

epoxy mounts so that subsequent thin-sectioning would produce sections which included exposed/weathered surfaces. Thin-sections were prepared by Spectrum Petrographics Inc of Vancouver, Washington to 0.3 μm polish using anhydrous cutting and polishing methods and epoxy impregnation in an effort to preserve weathered material and soluble minerals.

Analytical

SEM analyses were performed using a JEOL JSM 5600 (EMiL Facility, UNLV) at 20 kV and 30-40 spot size. Before analyses, thin-sections were carbon coated to 20 nm thickness for conductance. SEM analyses focused on textural evidence of any preferred mineral dissolution, evidence of secondary minerals, development of weathering rinds and porosity development. The chemistry and mineralogy of many COTM flows have been well documented previously (Leeman et al., 1976; Kuntz et al., 1985; Kuntz et al., 1992; Stout et al., 1994) and were not a focus of our study, however, EDS analyses were carried out using an Oxford Instruments detector and Oxford INCA software with semi-quantitative capabilities to confirm the general mineralogy and phases present.

Image analysis

In addition to image analysis performed using Oxford Instruments INCA software installed on the JEOL JSM 5600 SEM, subsequent off-line image analysis was performed using Oxford Instruments INCA and Adobe Photoshop CS6 software. Relative changes in porosity and fracturing with depth were investigated using image BSE mosaics collected from the weathered surface of the samples to unweathered core material. Plots

of porosity with depth were constructed from mosaics by first aligning, rotating, and cropping the mosaic such that 10 μm "slices" of equal areas of the sample image perpendicular to the weathered sample surface could be consecutively isolated, contrast enhanced, and open micro-porosity areas could be determined by histogram. This was done for one mosaic from a sample of each flow to a depth of 1200 μm (well into unweathered corestone). Figure S7 is an example of how mosaics were analyzed. Macro pores (>100 μm on a side) were filled with a color that would not overlap the pore color in the histogram. Histogram pore space was used to obtain a percent porosity value associated with the depth of the particular "slice". The same porosity image analysis techniques were used to get general unweathered porosities of the samples for informing the modeling. The depth of enhanced porosity within samples was determined in three ways. First, subjectively (i.e. "by eye") in BSE mosaics, then subjectively in plotted profiles, and finally the plotted profiles were subjected to more quantitative analysis by determining when three consecutive slices gave measured porosities of less than the average porosity plus the standard deviation of the deepest 300 μm (unweathered corestone). For the Kimama sample, image analysis was applied to measure the grain sizes of minerals in multiple BSE images of unweathered corestone for use in surface area estimates used in reactive transport modeling of the accompanying paper.

Results

Textures in thin section of observed high-P basalts from COTM range from vitrophyric to poikiolitic with the vitrophric textures being restricted to the youngest flows. Figure S8 contains BSE images of textures typical of the 6 flows sampled. In

some samples weathering appeared to favor glassy matrix dissolution over other phases, while in other samples (which also included a glass component) weathered surfaces showed no preferred mineral dissolution. Rinds were present on the exposed surfaces of all samples, but were never continuous and generally never exceeded 100 μm. No conclusive correlation between rind thickness and age was apparent. The youngest sampled flow, Blue Dragon, appears to have weathering-produced porosity (spall type cracks and holes) up to 60 um into the sample and in many places an alteration rind of ~10 μm depth into the glassy matrix has formed (Figure S9). The chemistry of the rind by EDS compared to the unaltered glass does not appear significantly different, thus the lower BSE signal (darker color) in the image may be a density change. This type of rind was unique to the Blue Dragon samples and may play some role in the blue sheen that is characteristic of these basalts in hand sample. Both intermediate aged Lava Point and Pronghorn samples showed variable porosity and weathering textures. Porosity to depth measurements on these samples (discussed further below) were applied to a generally representative area of the samples. Thin-section samples of the oldest flows, Sunset and Kimama show more advanced porosity development than most of the other samples, which was due primarily to the dissolution of the glassy matrix.

Extensive effort focused on detecting any secondary phosphate minerals that were present. A few Al- and Fe-secondary phosphate phases had been previously observed in samples of Pronghorn and Kimama flows (Cornell and Hausrath, 2010). In this study secondary phosphate minerals were found (Figure S10), but were also very rare and restricted to within a few tens of micrometers of the weathered surface.

Part of this study focused on determining if the primary phosphate mineral in COTM samples (fluorapatite) was preferentially dissolving. Though some fluorapatite minerals within samples exhibited a texture that suggested they may be dissolving preferentially, the texture could also be explained as glassy matrix dissolved out of the interior of skeletal apatite (Figure S11). Further, in some cases, relatively pristine fluorapatite crystals were present surrounded by porosity created by the apparent dissolution of glassy matrix. It is of note in regards to the accompanying paper, that fluorapatite is not the expected primary phosphate mineral in martian rocks and has both different kinetics and thermodynamics than Mars-relevant primary phosphate minerals (i.e. Cl-rich apatite and merrillite) (Adcock et al., 2013).

Measurements of porosity from weathered surface to the interiors of samples indicated that increases in fractures and porosity occur to depths well beyond any obvious chemical alteration. Further, a correlation of depth of change in porosity to time does seem apparent, with older flows having enhanced porosity deeper into the rock (Figure S12). For use in informing reactive transport modeling in the accompanying paper, the porosity of unweathered corestone varied from 0.1 % to 1.03 % with an average value of 0.7%. While these values seem low, the technique used here does not measure macroporosity and the value of 0.7% is within range for basalts as measured by others (see Table 9 of accompanying paper). Average porosities of weathered material (surface to 100 μm deep) ranged from 0.6 - 7.5% with an overall average of 3.8%

Reactive transport modeling performed in the accompanying paper requires specific surface areas as mineral dissolution rates are normalized to surface areas. To estimate surface area for this study, grain size measurements taken from COTM Kimama

lava flow thin sections were used to derive grain diameters for the minerals ilmenite, plagioclase, pyroxene, and the primary phosphate mineral fluorapatite. To do this we measured both long and short axes of mineral grains and used them to determine an average geometric diameter (Table S8). These geometric diameters were then used with roughness values from the literature to estimate BET surface area, and estimate total reactive surface area to derive specific surface areas (SSA) for use in modeling. Because Kimama does not contain appreciable pyroxene, we assumed pyroxene grain diameters to be similar to plagioclase, and we assumed that the merrillite and chlorapatite grain sizes would be similar to fluorapatite.

Summary

Despite variations in texture, a correlation between age and depth of weathering-produced porosity in COTM flows is apparent. However, no correlation between age and weathering rind thickness could be confirmed. Secondary phosphate minerals were located in samples but were rare and not a significant phase. Porosity in unweathered corestone (excluding macro porosity) measured in this work is within the range observed in other basalts. With the exception of the glassy matrix of some samples, no preferred mineral dissolution was observed.

Table S8. Long and short axis measurements and averaged diameter of grain in Kimama thin sections (µm). Values were used to obtain geometric surface areas for modeling.

Plagioclase			Ilmenite			Fluorapatite			Enstatite		
x	y	ave	x	y	ave	x	y	ave	x	y	ave
148	123	135.5	172	60	116	20	20	20	114	60	87
132	60	96	73	56	64.5	23	17	20	60	45	52.5
321	99	210	90	50	70	80	30	55	60	40	50
200	60	130	72	30	51	84	46	65	84	48	66
204	50	127	60	60	60	30	25	27.5	108	75	91.5
273	64	168.5	35	35	35	30	22	26	50	50	50
500	82	291	87	78	82.5	48	33	40.5	164	91	127.5
400	100	250	84	40	62	40	29	34.5	136	105	120.5
400	135	267.5	51	35	43	37	23	30	60	52	56
188	30	109	42	24	33	51	24	37.5	90	54	72
Ave. Diameter (µm)		178.45			61.7			35.6			77.3
Radius (µm)		89.225			30.85			17.8			38.65
Radius (m)		8.92E-05			3.09E-05			1.78E-05			3.87E-05

Table S9. Depth of Merrillite front, Chlorapatite front, and the distance between them

Initial pH	Merrillite Front	Chlorapatite Front	Distance between fronts
4	1775	2275	500
5	1475	2075	600
6	1175	1875	**700**
7	825	1475	650

Depths are in micrometers. Data is from models run for 100,000 years of rock water interaction. Distance was measured from the deepest point of the merrillite dissolution front to the deepest point of the chlorapatite dissolution front.

Supplementary Figures

Figure S5. General location of Craters of the Moon National Monument within the state of Idaho

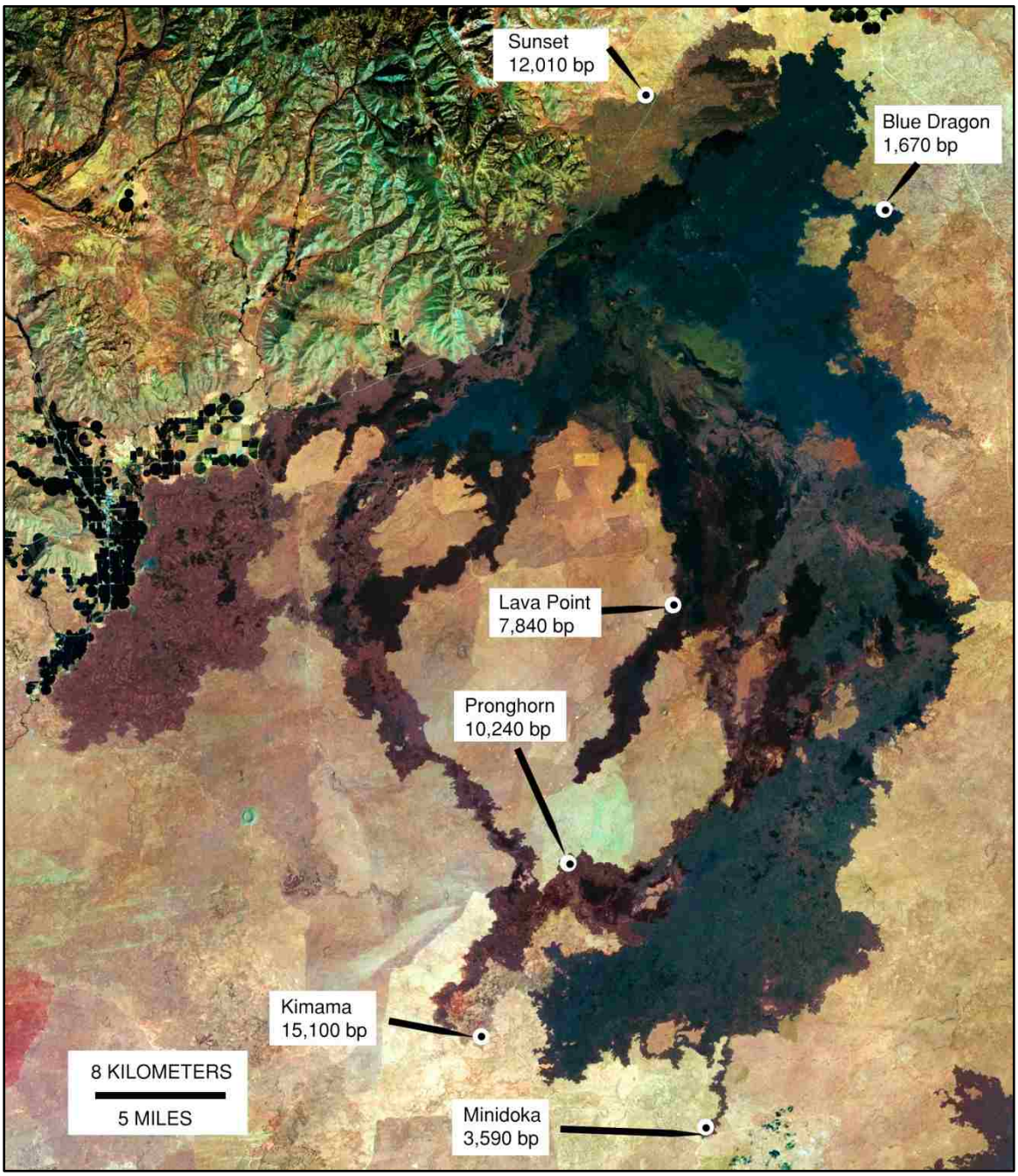

Figure S6. Sampling locations and associated flow and age for Craters of the Moon samples. USGS LANDSAT 8 false color image, bands 7-4-2 displayed as R-G-B. Image color enhanced by the author. Different dark colors in flow field represent different individual flows.

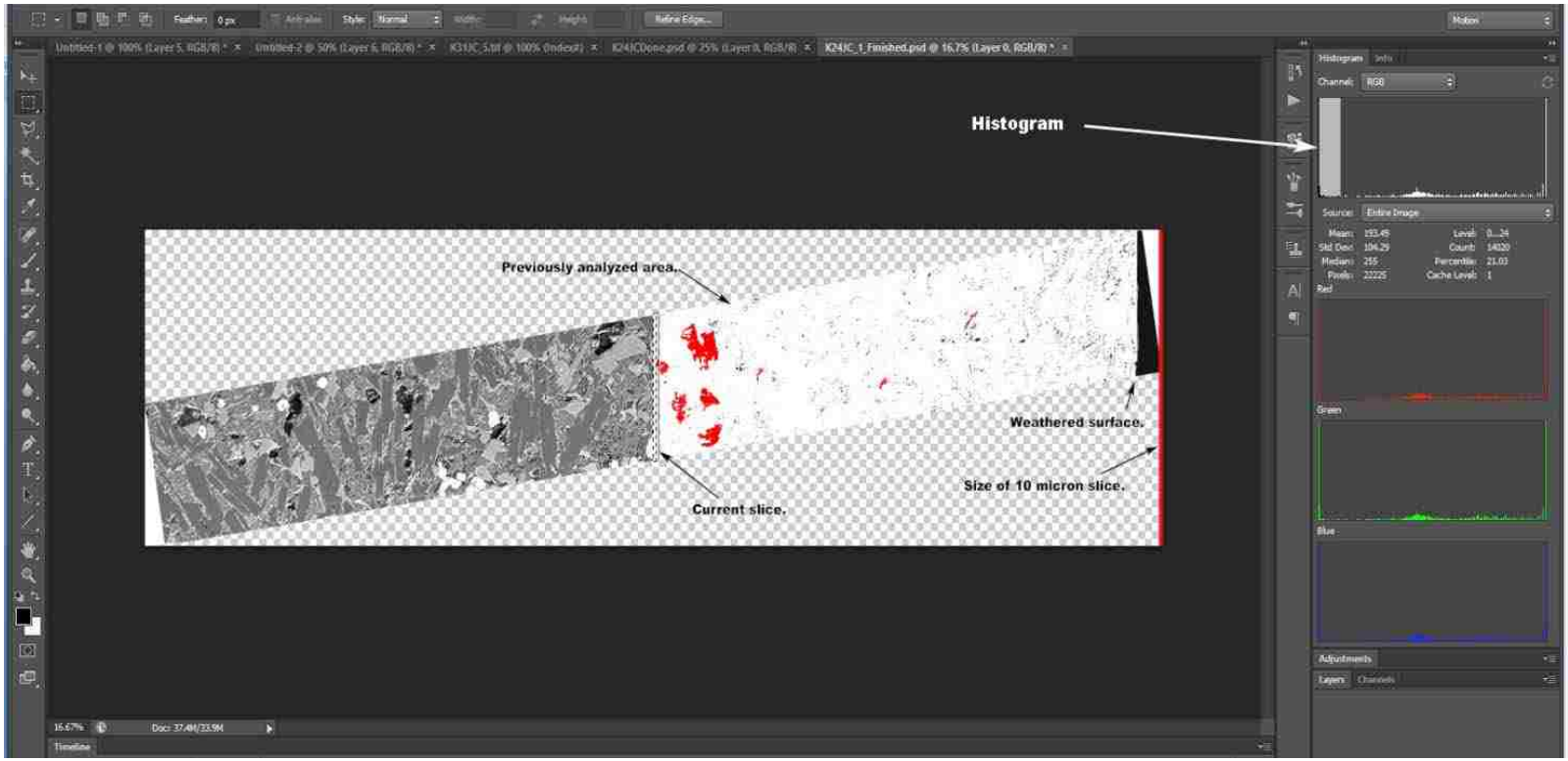

Figure S7. Example of image analysis of cross-section mosaics of COTM samples. This sample was from the Kimama flow.

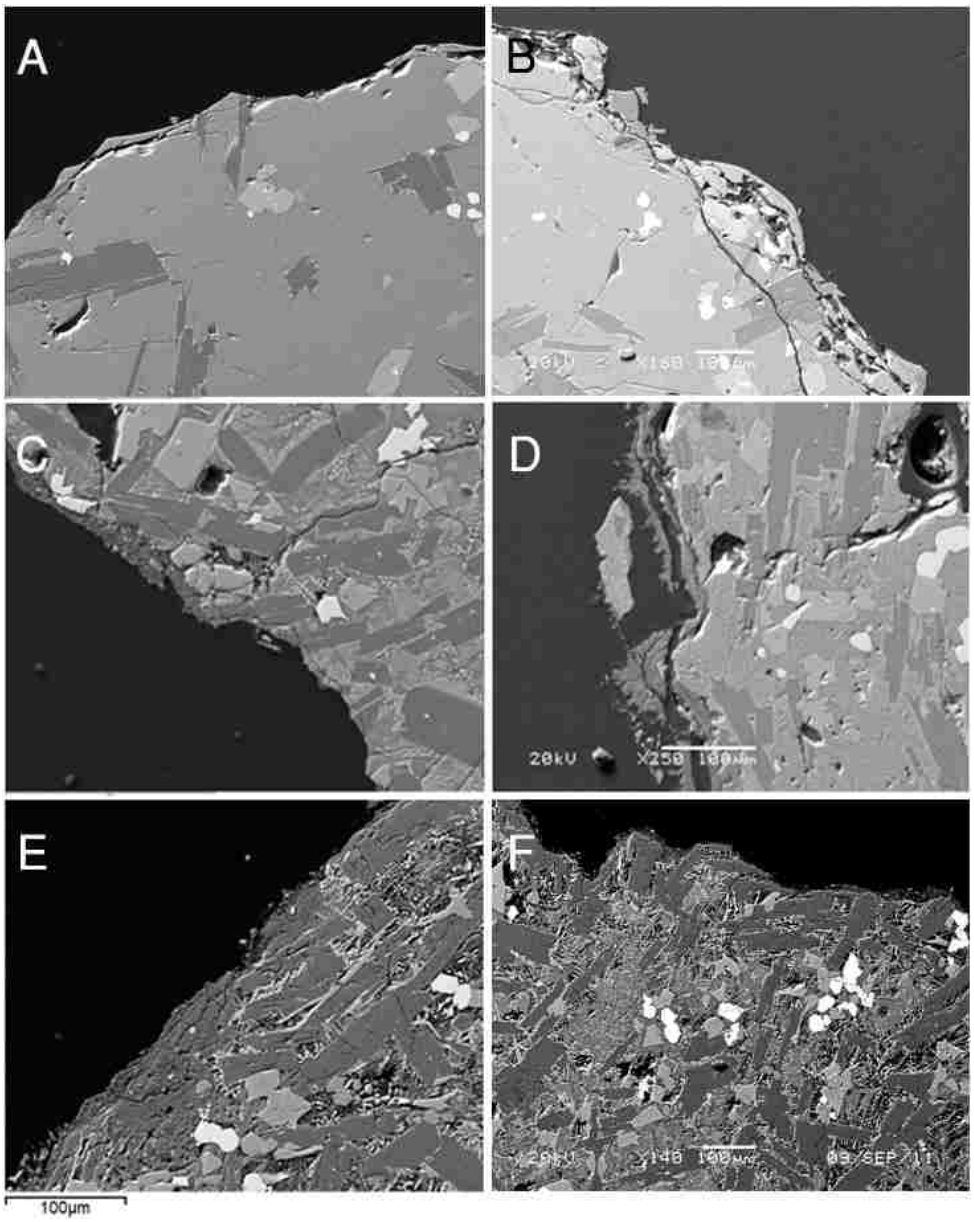

Figure S8. BSE images of textures typical of the six flows sampled. A) Blue Dragon, B) Minidoka, C) Lava Point, D) Prong Horn, E) Sunset, F) Kimama

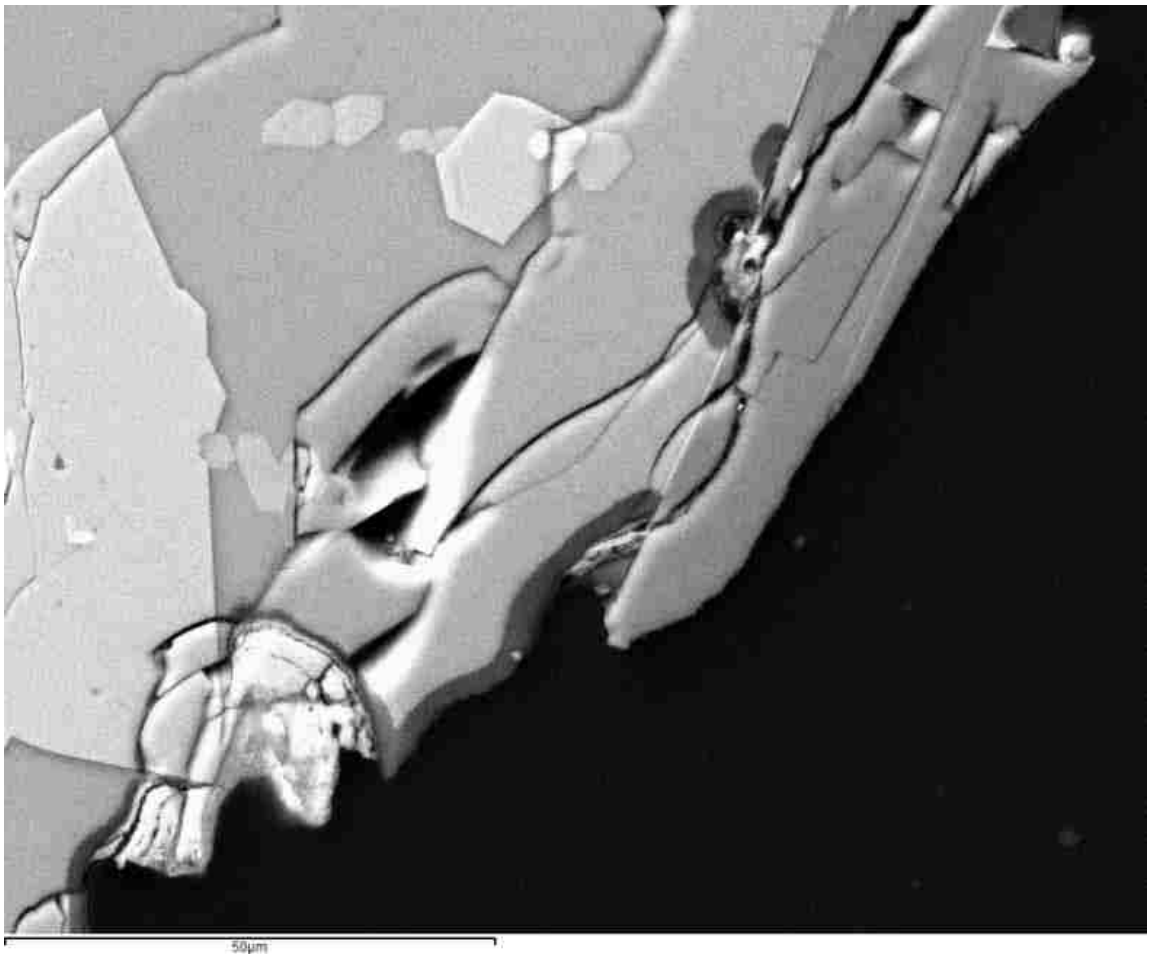

Figure S9. Blue Dragon (1670 bp). Note apparent alteration rind into glassy matrix. Sample BD1BCTA. Scale Bar 50µm

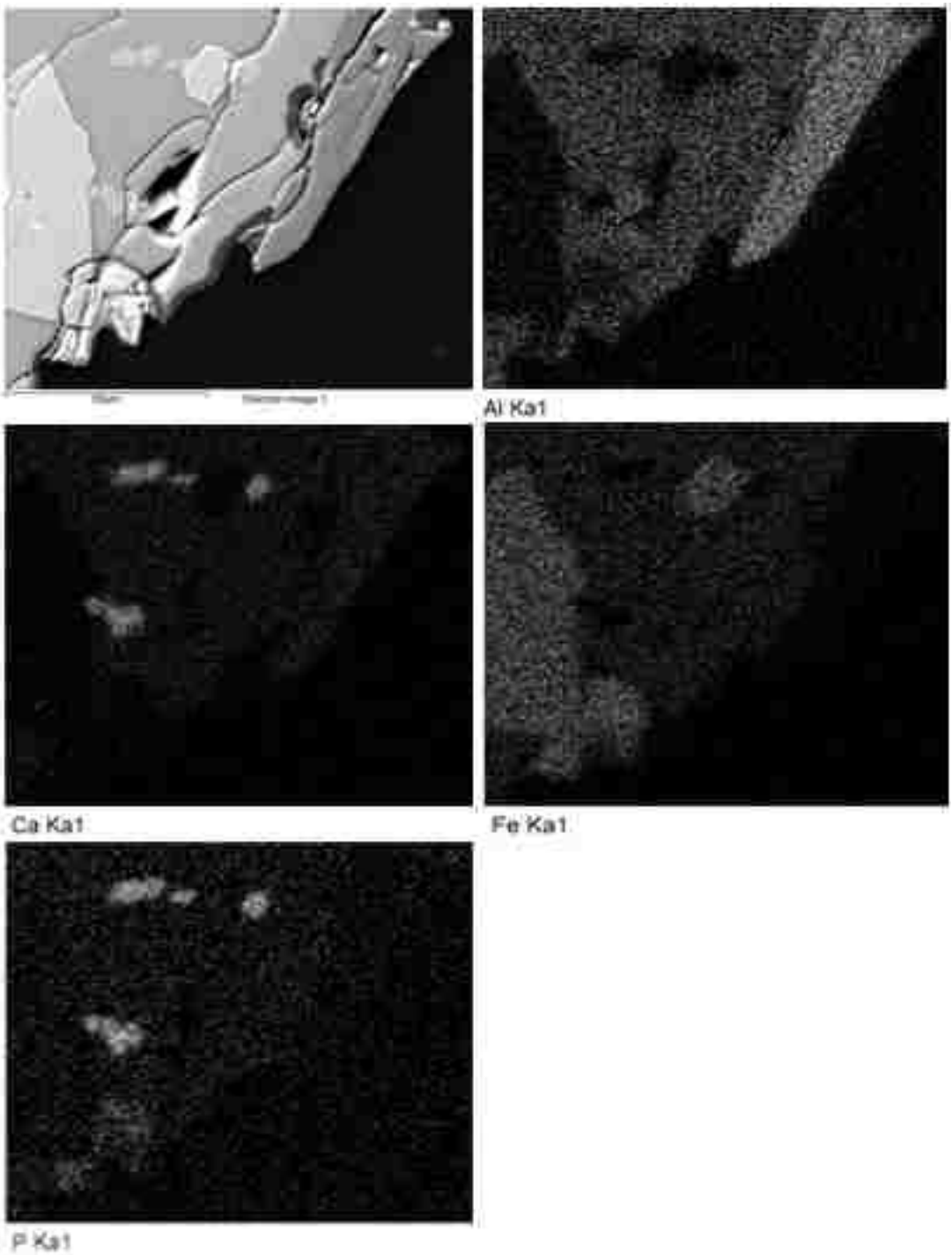

Figure S10. EDS X-ray map of secondary phosphate mineral in Blue Dragon (same location as Figure S9). Note P bearing phase in lower left of P map which has no Ca bearing counter part but does appear to have Fe.

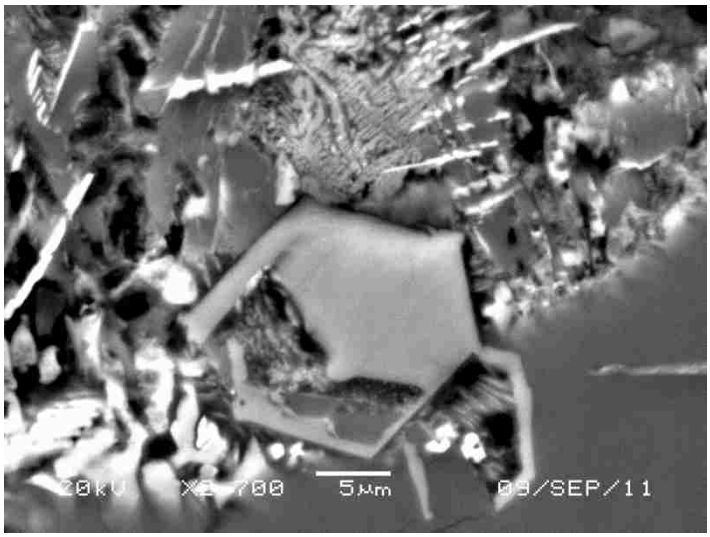

Figure S11. Fluorapatite grains like this one in Kimama appear in some cases to be dissolving fluorapatite, but may also be skeletal with glassy matrix dissolving from within.

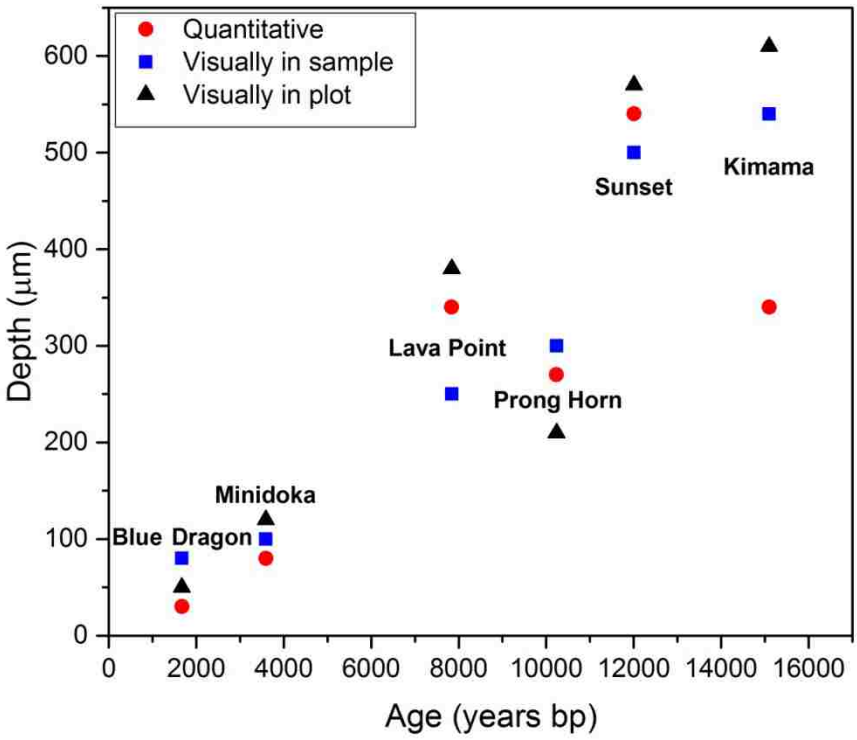

Figure S12. Plot of estimated depth of weathering induced porosity versus time.

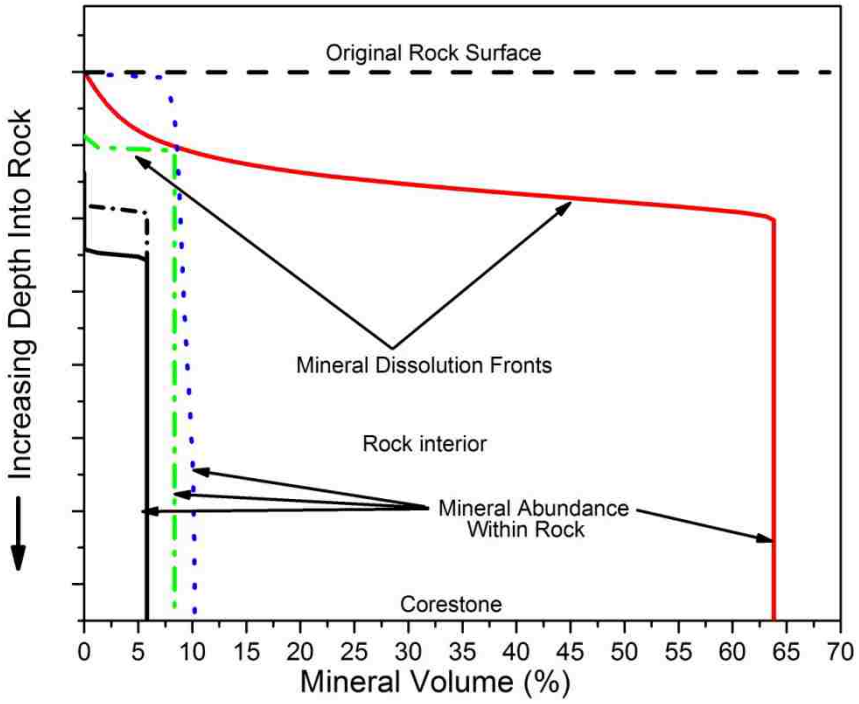

Figure S13. Example of output model profile. Plot shows % mineral volume with depth from the surface of a modeled rock to the interior. Colored lines represents mineral concentration in the rocks as % volume. Dashed line at top represent original surface of modeled rock. Curves in lines are mineral dissolution fronts. At depths above the curves, the mineral has dissolved and the % mineral volume in the rock has decreased. Below the curves the minerals are undissolved and the % mineral volume is that of the parent rock.

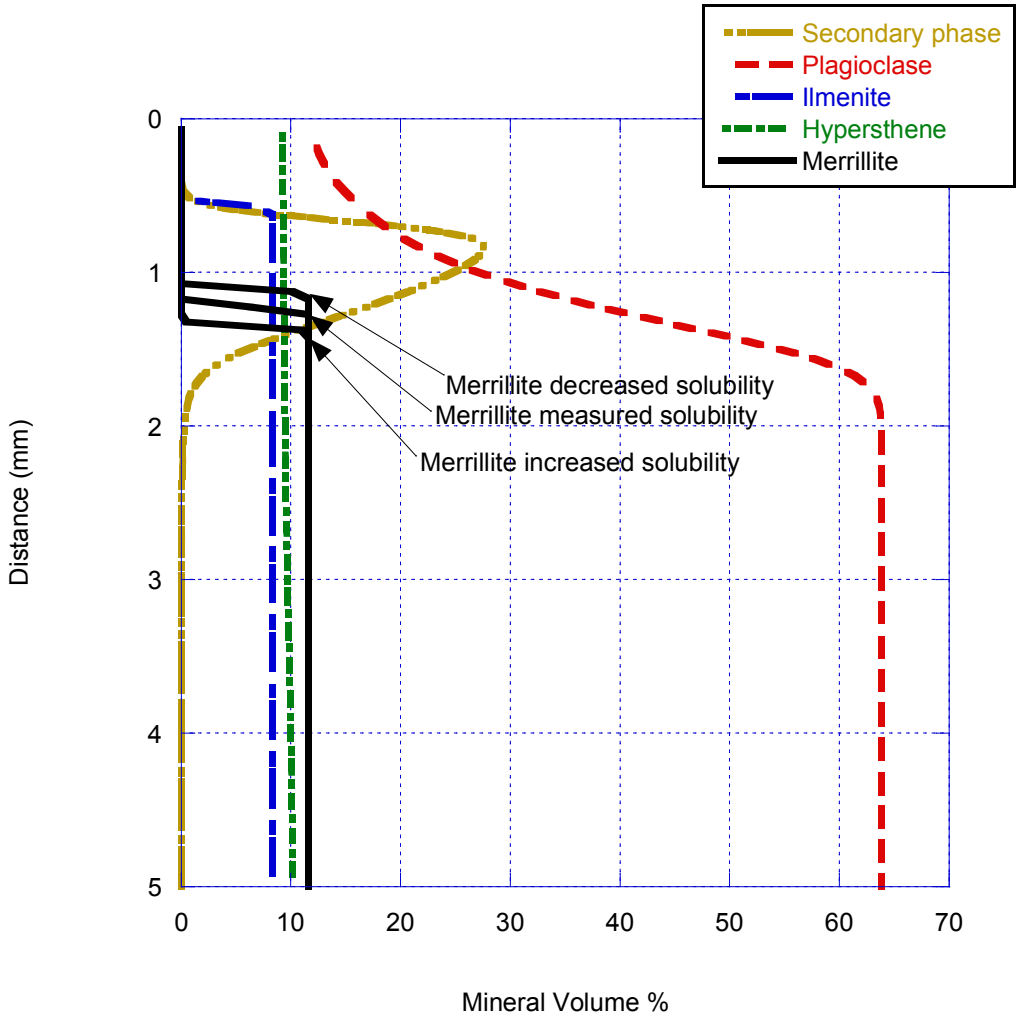

Figure S14. The effects of +/-2 orders of magnitude change in merrillite solubility (pH 6, 100,000 years model time). 1) Merrillite solubility suppressed by 2 orders shows a slightly shallower dissolution depth. **2)** Using the measured value of solubility for merrillite (Adcock et al., 2013). **3)** Depth of dissolution front using merrillite with 2 orders of magnitude enhanced solubility.

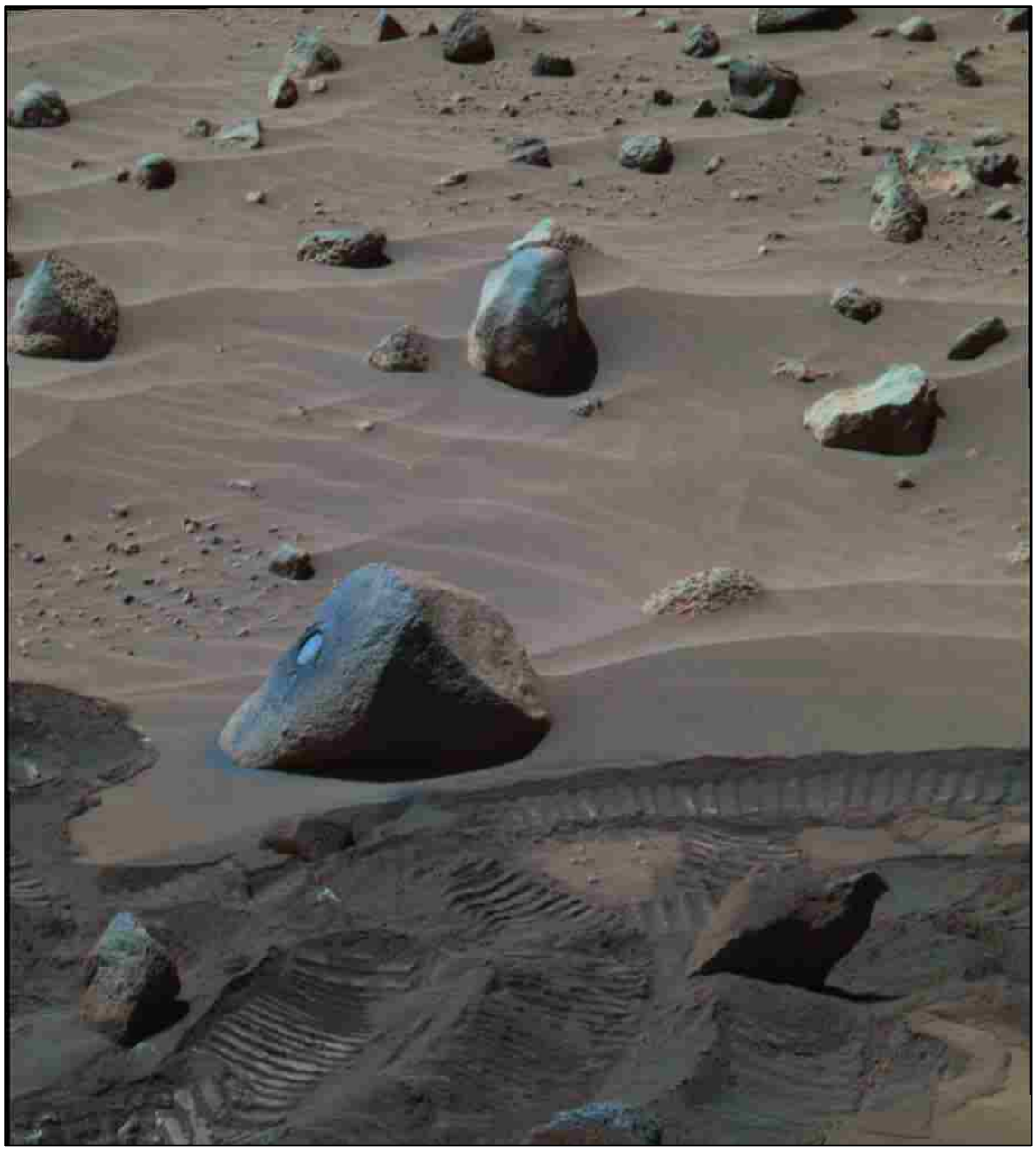

Figure S15. NASA image PIA07191: Spirit view of 'Wishstone' (False Color). Image shows RAT scar on rock. Wishstone has the appearance of rounded edges and evidence of facets that indicate physical erosion has occurred. Image credit: NASA/JPL/Cornell

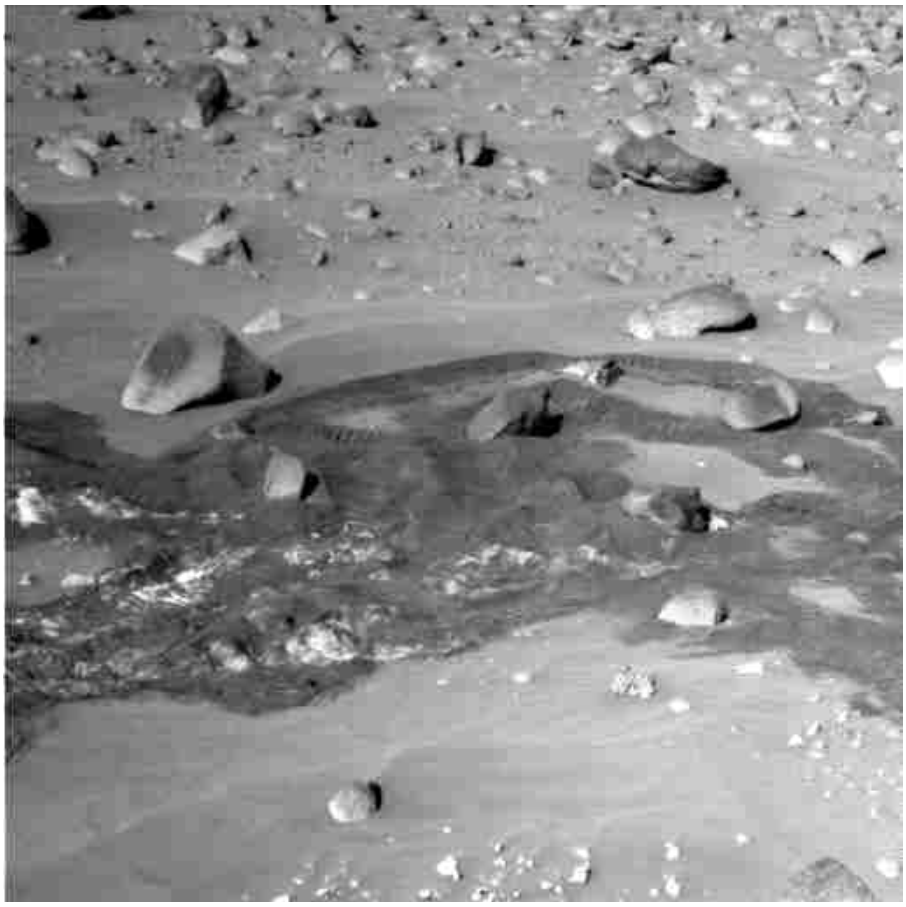

Figure S16. Data from MER Product 2N 156291204 EFF A0 00 P0665 R0 M1. Wishstone appears in the central left and exhibits streaking that developed post RAT operations. Image credit: NASA/JPL/Cornell/USGS

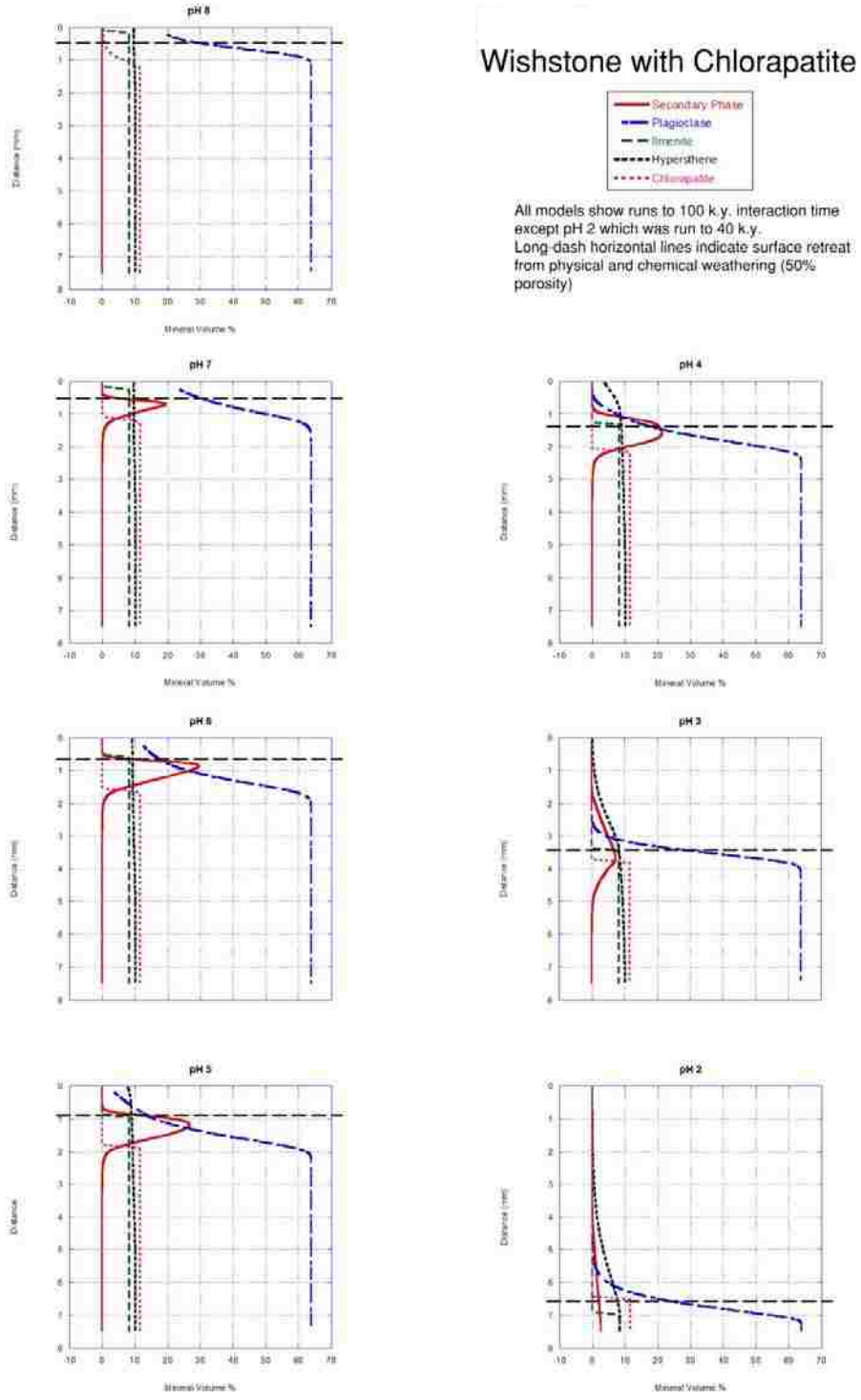

Figure S17. Modeled dissolution profiles for chlorapatite models at pH 2-8.

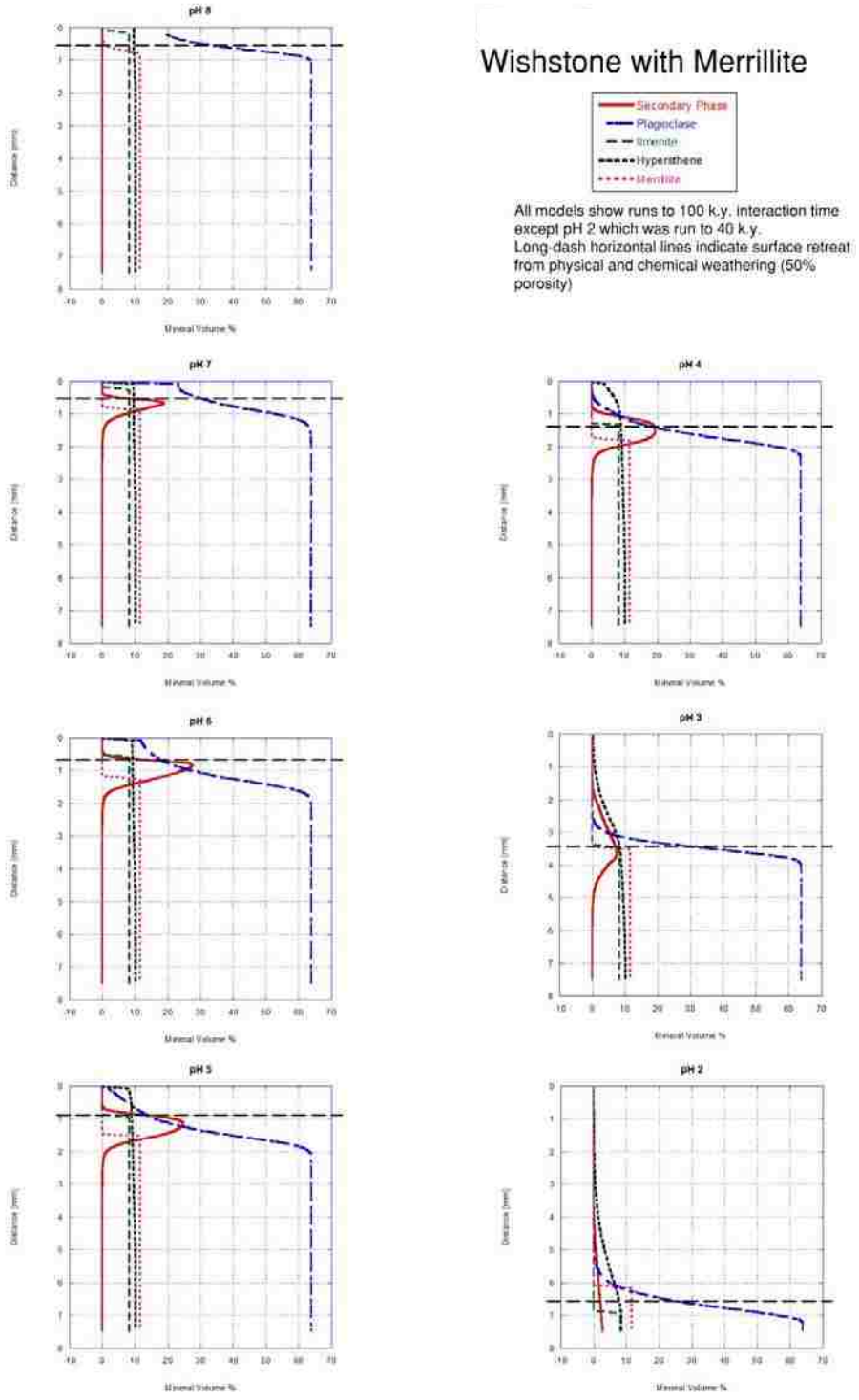

Figure S18. Modeled dissolution profiles for merrillite models at pH 2-8.

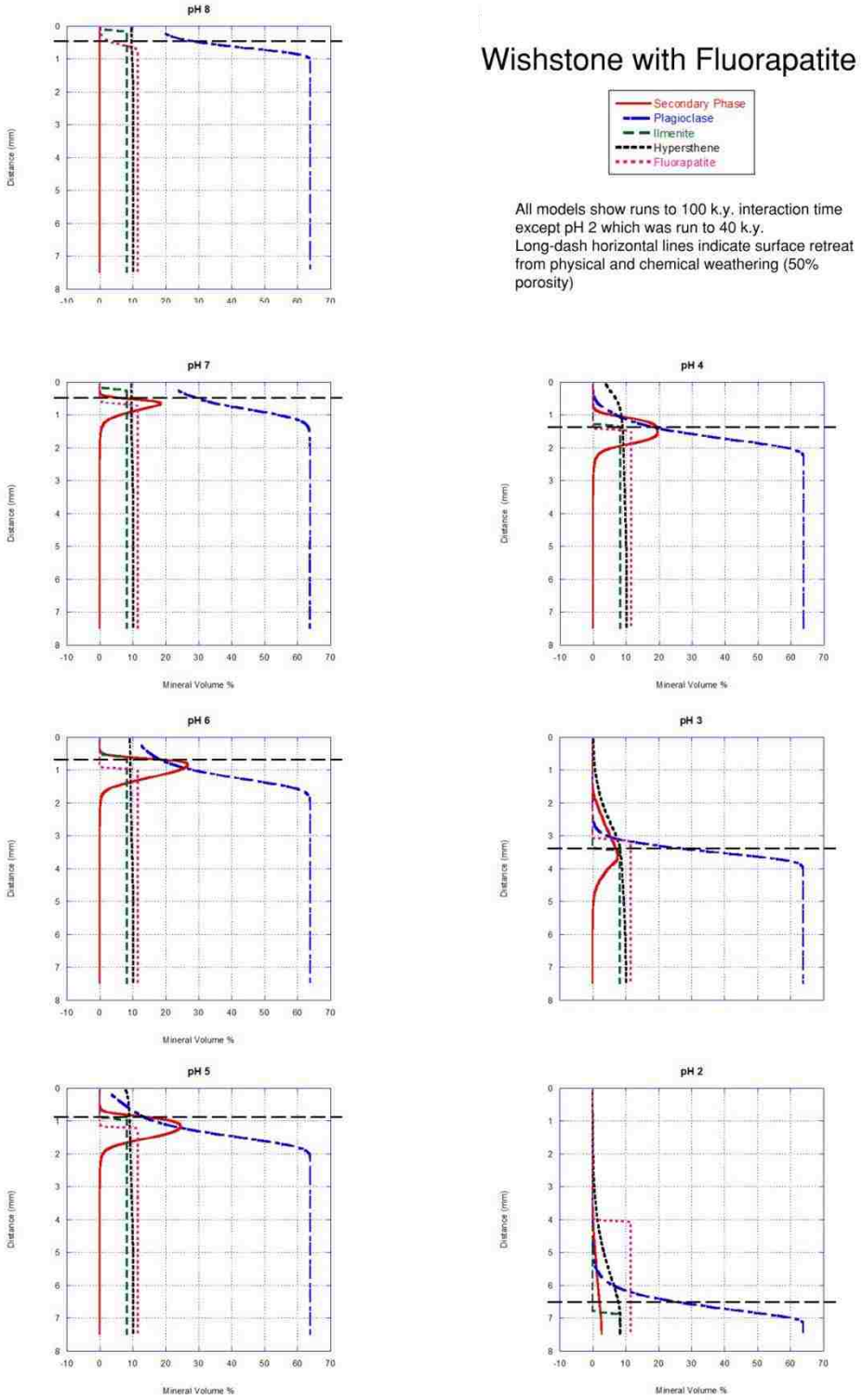

Figure S19. Modeled dissolution profiles for fluorapatite models at pH 2-8.

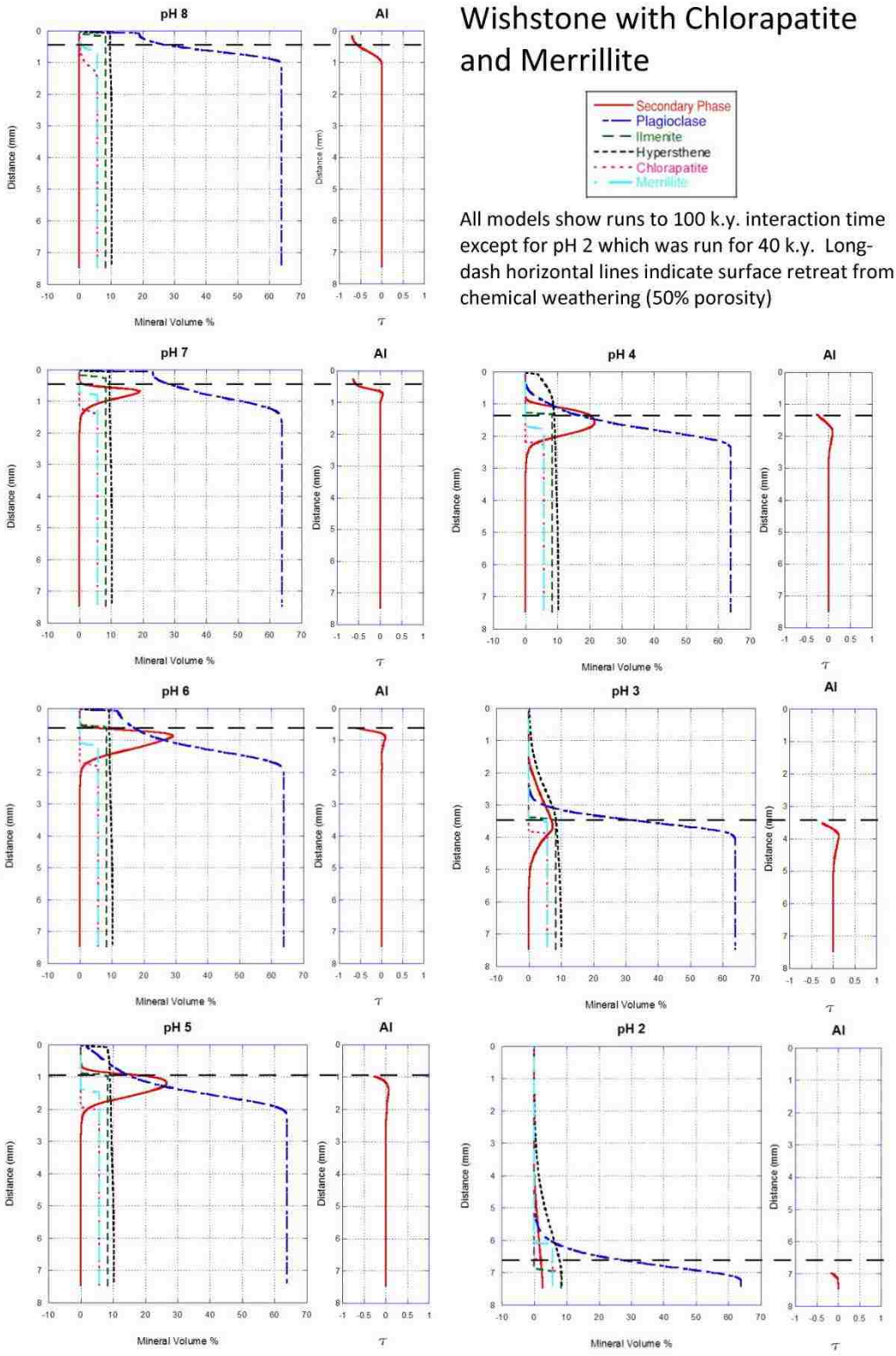

Figure S20. Modeled dissolution profiles and Al τ plots for chlorapatite + merrillite models at pH 2-8.

APPENDIX IV ADDITIONAL SUPPLEMENTARY DATA

This fourth appendix contains data in addition to that associated with the chapter manuscripts.

Though MER Spirit carried and extensive science package capable of chemical and some mineralogical analysis, the unusual chemistry of Wishstone class rocks combined with the fact that they are float rocks has made mineralogical and petrogenetic determinations challenging. Table S10 is a compilation of the many Mars Wishstone rock class mineralogy estimates made based on differing assumptions and data set combinations. The broad range of mineral compositions is both an indicator of the uncertainty in the rock class mineralogy and its petrogenesis, and the interest in the somewhat chemically unusual Wishstone class rocks.

Though the high-P content in Wishstone class is unusual, high-P rocks do exist on Earth and the high-P basalt flows of Craters of the Moon national Monument (COTM) are among the rocks suggested as possible analogs for Wishstone class rock (Usui et al., 2008). Elisabeth Hausrath collected a number of samples from COTM from select lava flows and the author had a total of 15 thin sections of these samples, or sub-samples previously epoxy mounted, from six different lava flows prepared (Table S11). Thin sections were investigated by SEM to help inform modeling of Wishstone class rocks, and likely more than 1000 images were acquired. The images that follow (and occasional EDS spectra) in this appendix were selected from the total catalog of images to document interesting trends that may be helpful to the interpretation of phosphate mobility in arid environments.

Table S10. Mineralogy calculations of Wishstone Class rocks from various studies.

Mineral	Ming et al. Oct. 2005 Wish.[a]	Ming et al. Oct. 2005 Champ.[a]	Ming et al. Oct. 2005 Champ. RAT2[a]	Ming et al. Oct. 2005 "Wishstone Class" combined APSX, Mossbauer, Mini-TES[a]	McSween et al. Sept. 2006 Wish.[b]	McSween et al. Sept. 2006 Champ.[b]	Ruff et al. Dec. 2006 Mini-TES Data[c]	Hurowitz et al. Dec. 2006[d]	McSween et al. May 2008 Wish. CIPW SO_3/Cl corr.[e]	McSween et al. May 2008 Champ. CIPW SO_3/Cl corr.[e]
Feldspars	57.23	57.67	57.57	52	56.7	56.7	55	51.4	55.7	56.1
Albite	43.31	43.76	43.65		42.9	42.9		37.9	42.1	42.5
Anorthite	10.43	10.71	10.72		10.4	10.6	55	10.4	10.2	10.5
Orthoclase	3.49	3.2	3.2		3.4	3.2		3.1	3.4	3.1
Illmenite	5.06	5.82	5.76	1	5.0	5.7		5.6	4.9	5.6
TiO2				1						
Corundum	2.52	2.22	2.22		2.4	2.2		3.1	2.4	2.1
Quartz						0.5		3.4		0.4
Magnetite	1.15	1.24	1.24	1	7.6	9.2		7.8	7.5	9.1
Hypersthene (OPX)	5.08	3.66	3.78	12	13.5	13.0		13.4	13.7	13.0
Enstatite									9.7	9.9
Ferrosilite									4.0	3.1
Merrillite										
Apatite	12.35	12.03	11.98	11	12.5	12.1	10	11.7	12.3	12.0
Olivine*	16.59	17.36	17.45	6	1.9	0.0	15	0	1.5	
Basalt Glass							10			
Secondary Minerals				14			10	2.5		
Totals	99.98	100	100	98	99.6	99.4	100.0	98.9	98.0	98.3

Table S10. Continued

Mineral	McSween et al. May 2008 Wish. $MgSO_4$/NaCl corr.[e]	McSween et al. May 2008 Champ. $MgSO_4$/NaCl corr.[e]	McSween et al. May 2008 Wish. CIPW and recalculated Mossbauer[e]	McSween et al. May 2008 Champ. CIPW and recalculated Mossbauer[e]	Usui et al. Sept. 2008 Wish. CIPW of APXS data[f]	Usui et al. Sept. 2008 Extrapolated Wish. (SO_3 removed)[f]	Usui et al. Sept. 2008 Champ. CIPW of APXS data[f]	Usui et al. Sept. 2008 Extrapolated Champ. (SO_3 removed)[f]	Smith, 2014, Wish. mode[g]	Smith, 2014, Champ. RAT1 mode[g]	Smith, 2014, Champ. RAT2 mode[g]
Feldspars	53.4	51.5	55.7	56.1	63.4	57	63.3	53.1	60.5	60.9	60.8
Albite	39.7	37.9			43.1	41	43.4	37.5	46.4	46.7	46.7
Anorthite	10.3	10.5			16.8	12.4	16.7	12.3	10.6	10.9	10.8
Orthoclase	3.4	3.1			3.5	3.6	3.2	3.3	3.5	3.3	3.3
Illmenite	4.9	5.6	1.9	1.4	5	5.9	5.8	6.3	3.7	4.3	4.3
TiO2											
Corundum	2.9	3.0			0.2	1.2		0.7	2.8	2.5	2.5
Quartz	2.8	5.1						1.6			
Magnetite	7.5	9.1	1.7	1.3	7.7	7.5	9.3	9.1	4.4	4.9	4.6
Hypersthene (OPX)	13.1	10.5	17.0	19.3	5.1	6.7	6.2	7	11.9	12.2	12.4
Enstatite	8.4	7.4									
Ferrosilite	4.7	3.1									
Merrillite					11.4	17.6	11.1	22.1			
Apatite	12.3	12.0	12.3	12.0					11.2	11	11
Olivine*			7.6	7.0	7.3	4	4.2		5.5	4.1	4.2
Basalt Glass											
Secondary Minerals			3.9	2.9							
Totals	96.9	96.8	100.1	100.0	100.1	99.9	99.9	99.9	100	99.9	99.8

[a]Ming et al., 2006, [b]McSween et al., 2006, [c]Ruff et al., 2006, [d]Hurowitz et al., 2006 [e]McSween et al., 2008, [f]Usui et al., 2008, [g]Eugene Smith, 2014, unpublished data calculated using methods after Irvine and Baragar, 1971.

Table S11. Thin section descriptions.

Sample ID	Description	Flow Age
BD1ACTA	Blue Dragon from hand sample	1,670
BD1BCTA	Blue Dragon from hand sample	1,670
BD1CCTA	Blue Dragon from hand sample	1,670
M2CTA	Minidoka from hand sample	3,590
M3CTA	Minidoka from hand sample	3,590
LP2CTA	Lava Point from hand sample	7,840
LP3CTA	Lava Point from hand sample	7,840
P331JC	Pronghorn from Jason Cornell epoxy mount	10,240
P42JC	Pronghorn from Jason Cornell epoxy mount	10,240
P4ACTA	Prong horn from hand sample	10,240
P4BCTA	Prong horn from hand sample	10,240
LC12CTA	Sunset from hand sample	12,010
LC31JC	Sunset from Jason Cornell epoxy mount	12,010
K24JC	Kimama from Jason Cornell epoxy mount	15,100
K31JC	Kimama from Jason Cornell epoxy mount	15,100

Supplementary Figures

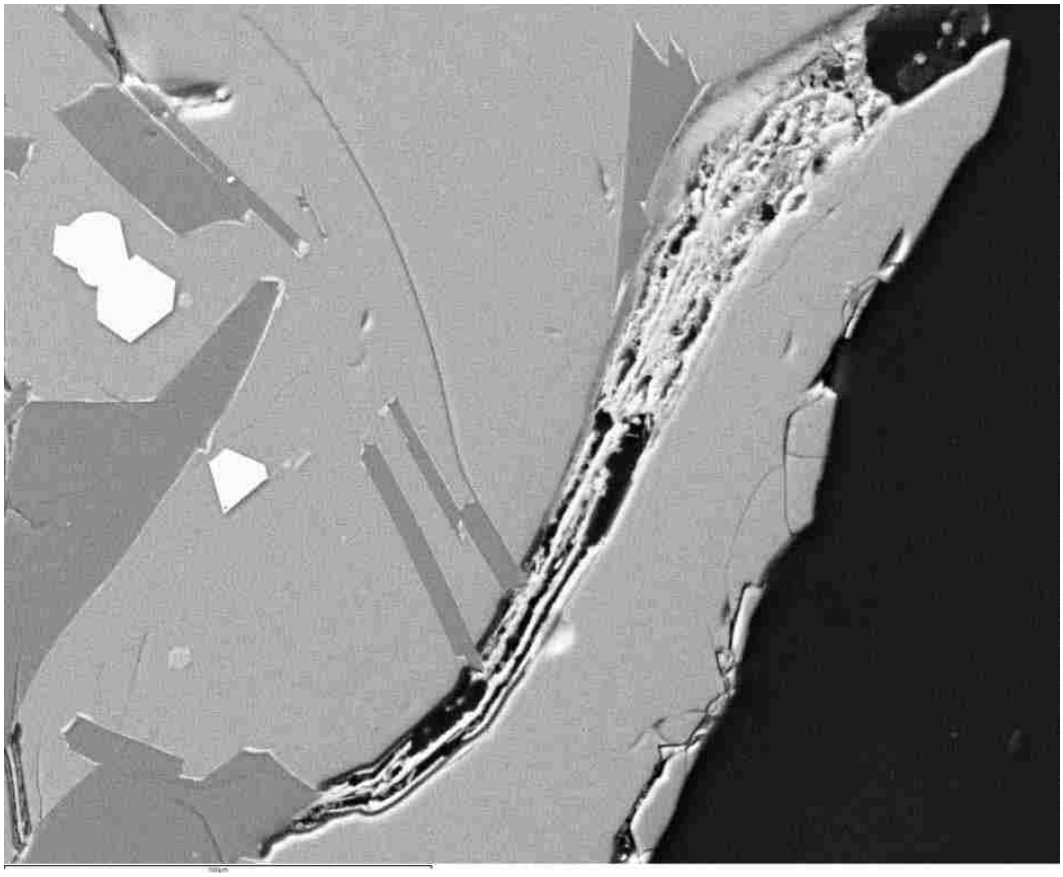

Figure S21. Blue Dragon BD1ACTA weathered edge with a fracture. Scale 100um

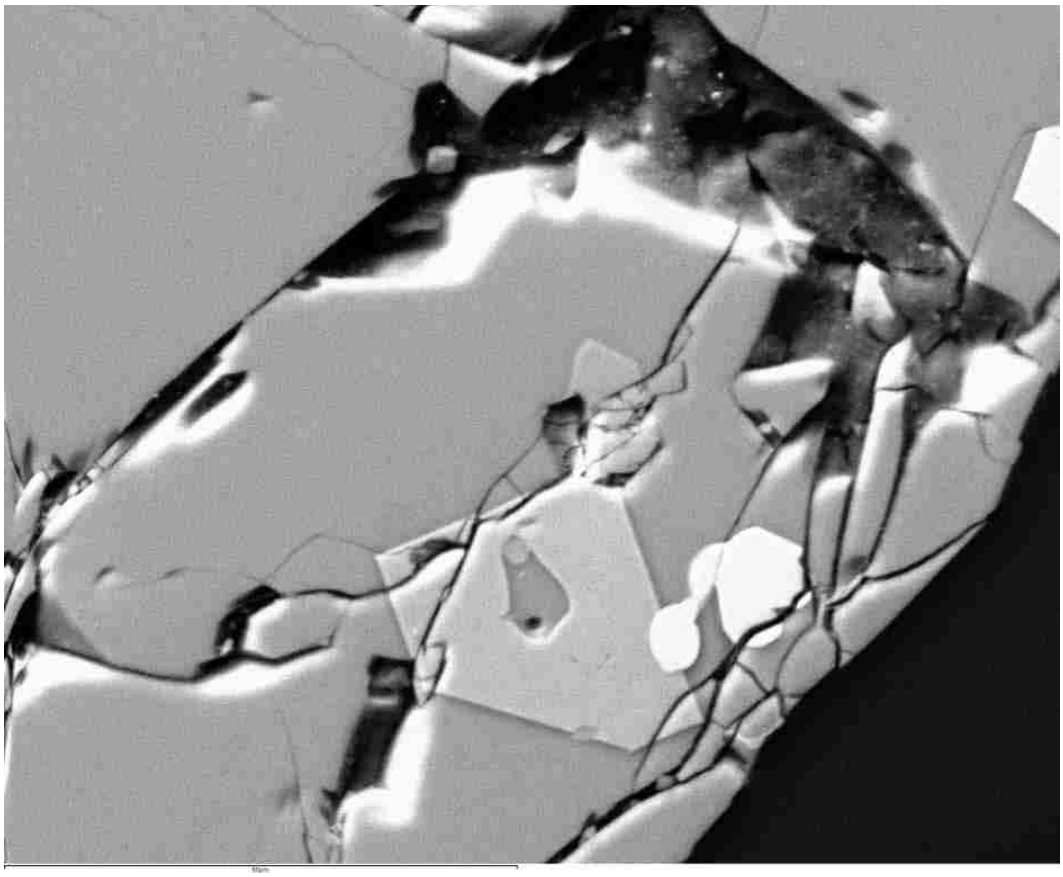

Figure S22. Blue Dragon sample BD1ACTA. An apatite sits inside the inclusion of the olivine in the low-center of the image. Scale 60um.

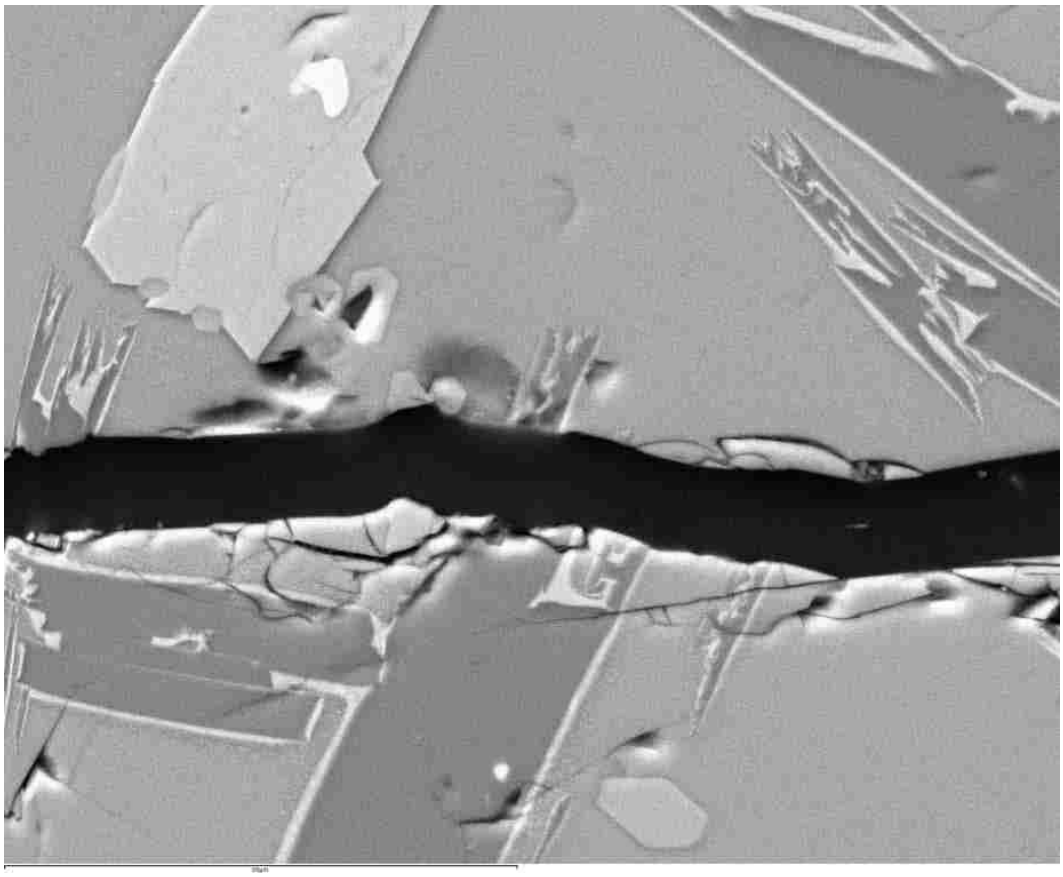

Figure S23. Blue Dragon sample BD1ACTA fracture. This is a fracture that shows some weathering. Note the dissolution texture of the apatite above the fracture and the apatite on the fracture edge showing little sign of weathering. Scale 60um.

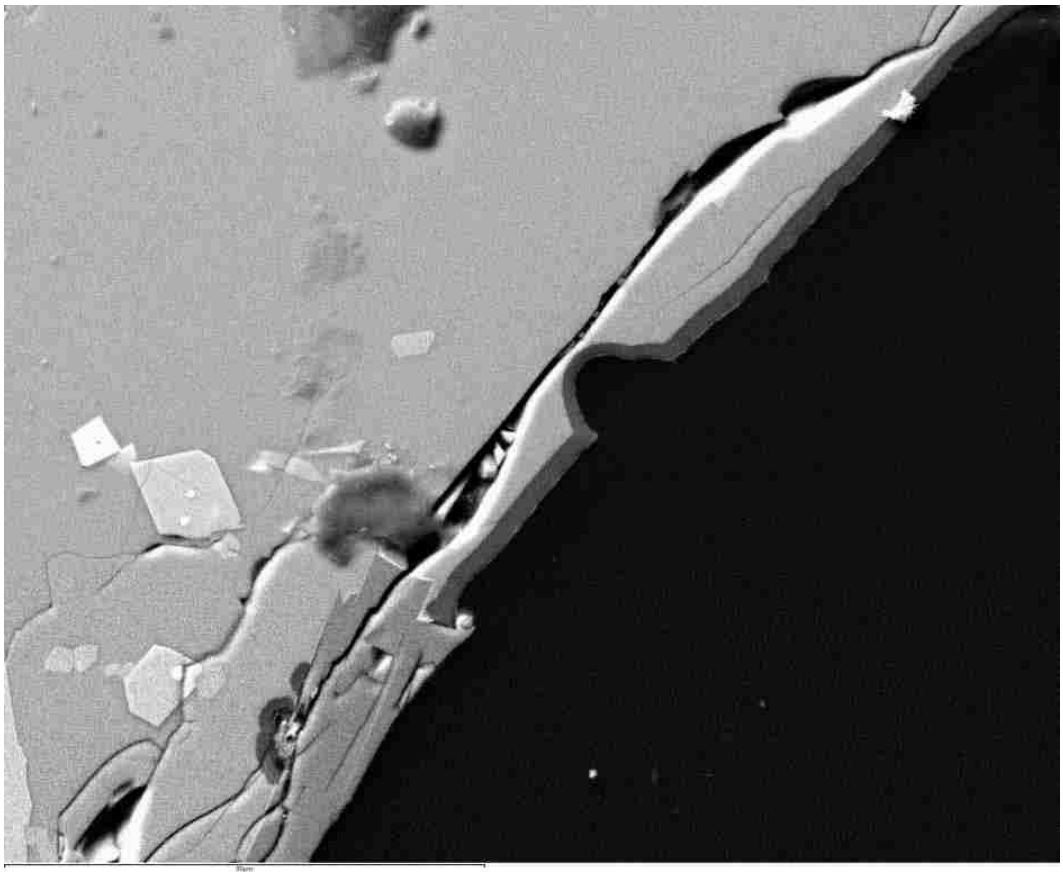

Figure S24. Blue Dragon sample BD1ACTA dark rim. Dark Rim is Si/Al material similar to the glassy matrix but depleted in Ca and Fe compared to interior material. Could this be the “Blue” of Blue Dragon? Scale 90um. The dark "smudges" are contamination of the sample and are not part it.

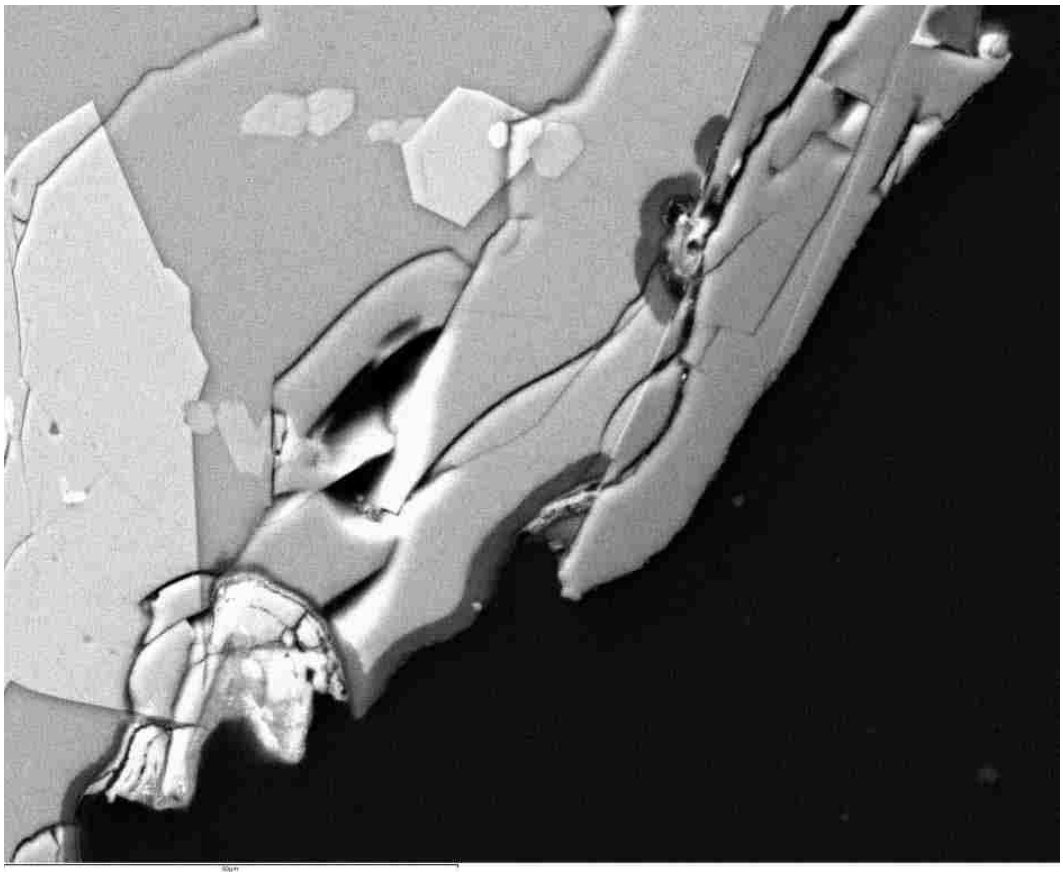

Figure S25. Blue Dragon sample BD1ACTA dark rim. Dark rim is Si/Al material (glass maybe) but depleted in Ca and Fe compared to interior material. Not eroded rind cross cutting olivine. There are secondary phosphates here P/Fe (in rind). What looks like carbonate is the dark rind forming under the rim (under the plag). Scale 50um.

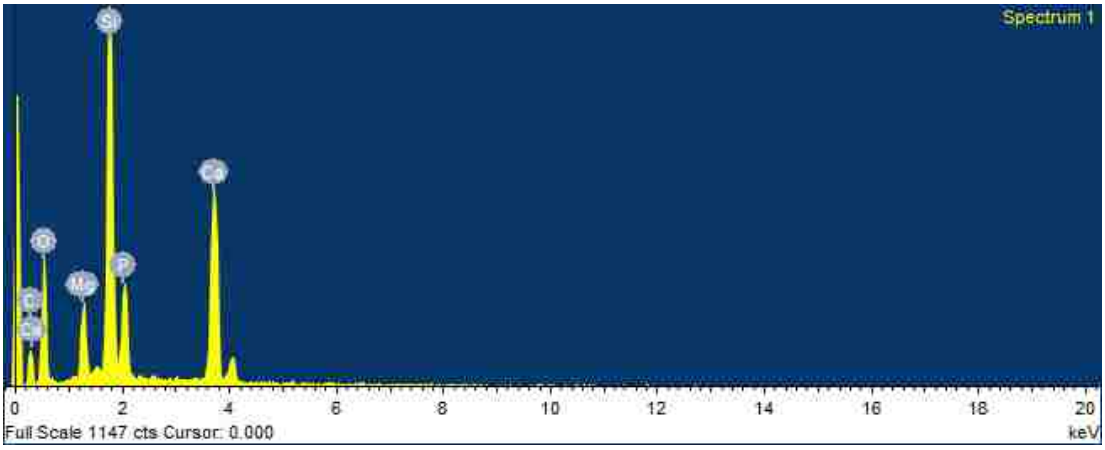

Figure S26. Blue Dragon sample BD1ACTA and EDS. Image, EDS analysis location, and EDS spectra indicating Secondary Phosphates in "pyroxenish" material

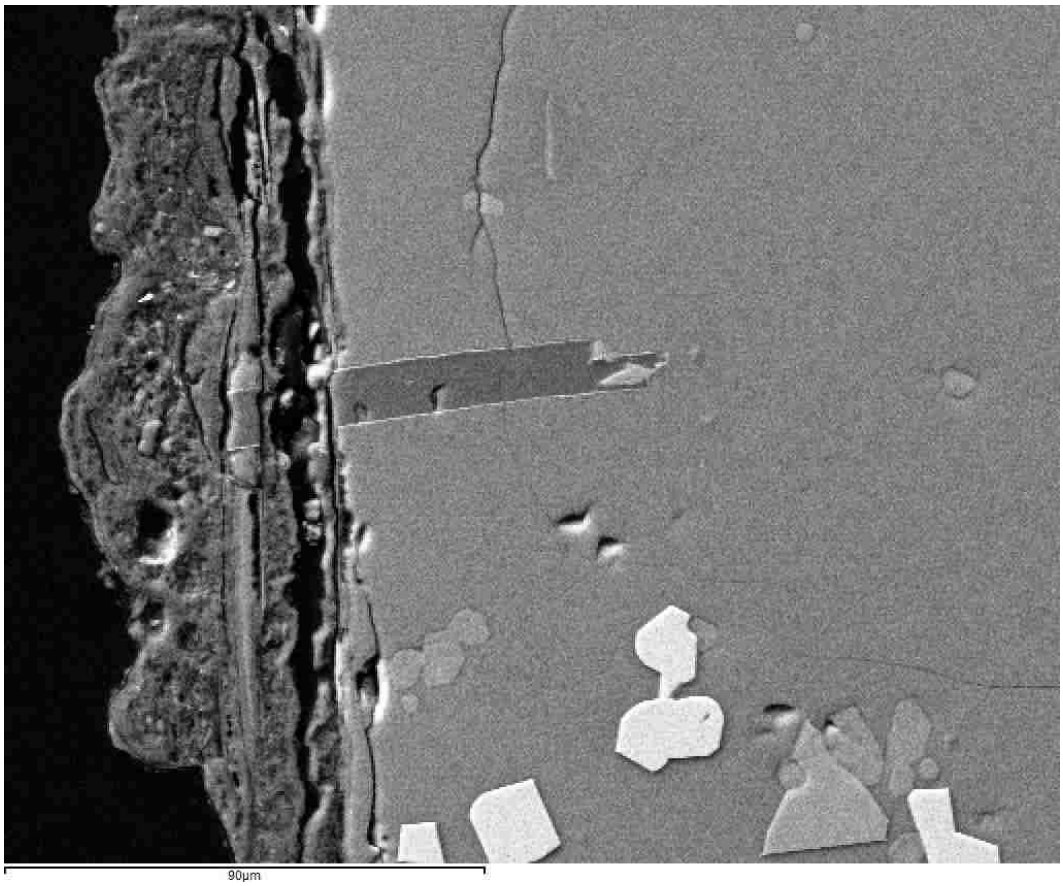

Figure S27. Minidoka Sample M2CTA. Weathering rind, note the cross-cutting. These rinds were discontinuous in samples and varied from 40-100 microns when present. Scale: 90um.

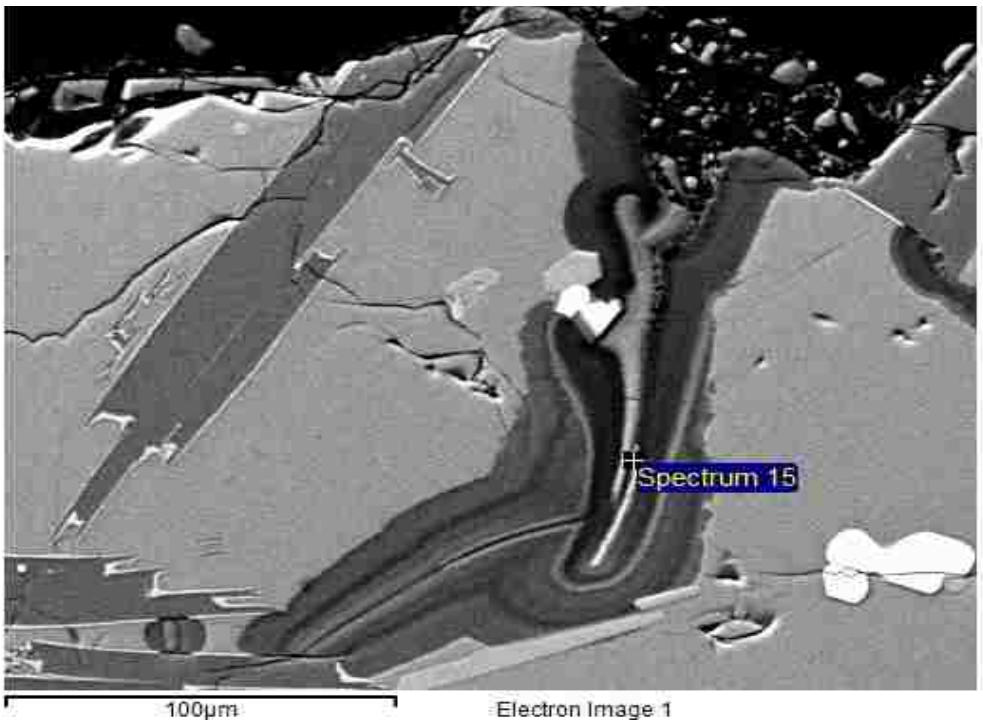

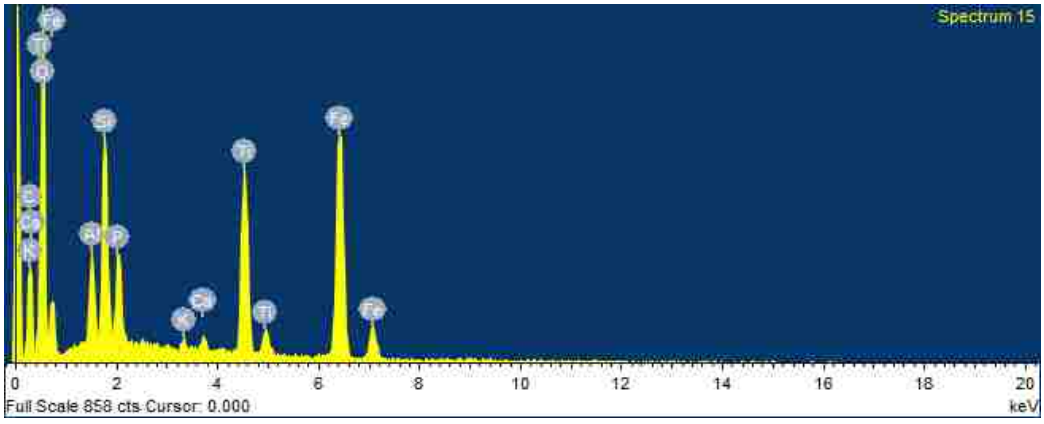

Figure S28. Minidoka Sample M2CTA and EDS. Possible secondary phosphate. This type of texture was rare in the Minidoka samples

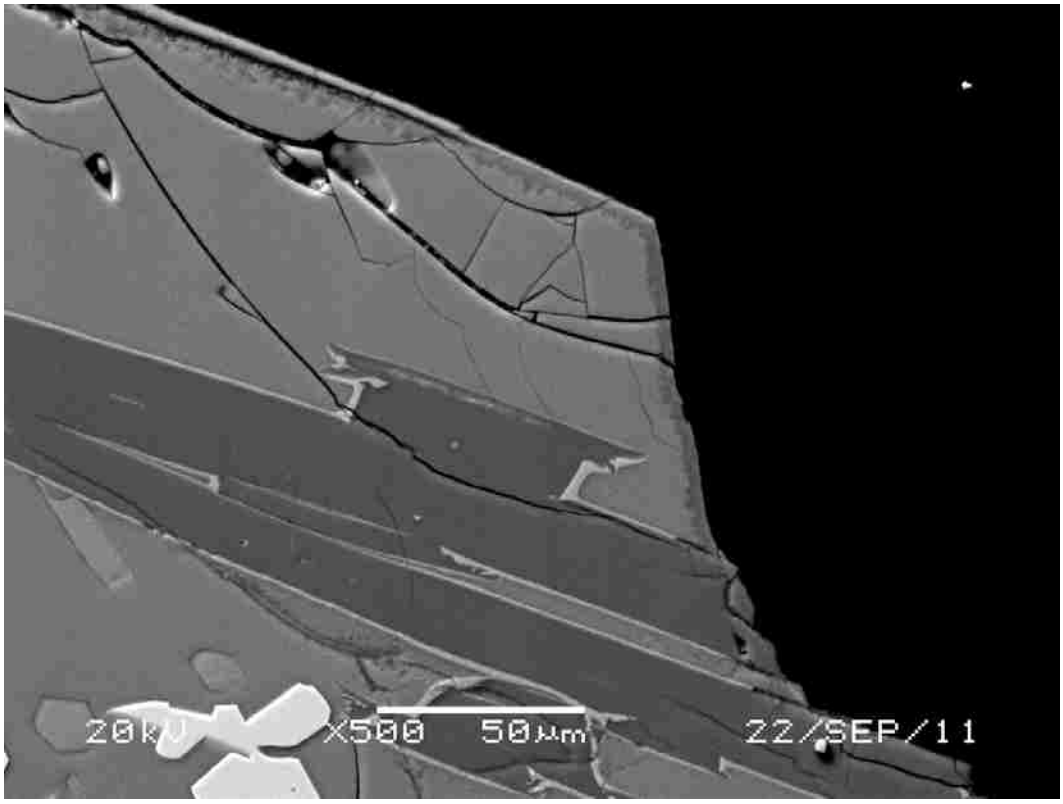

Figure S29. Minidoka Sample M2CTA edge. Note alteration rim on edge.

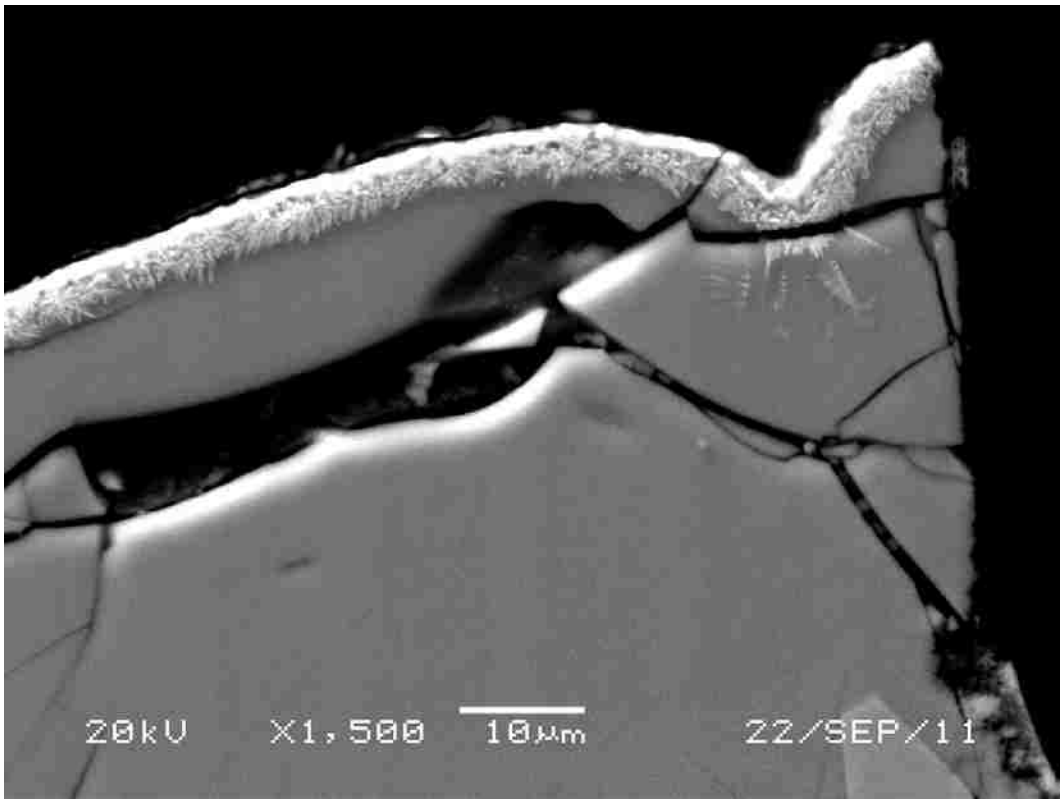

Figure S30. Minidoka sample M2CTA edge. Alteration on exposed edge of sample.

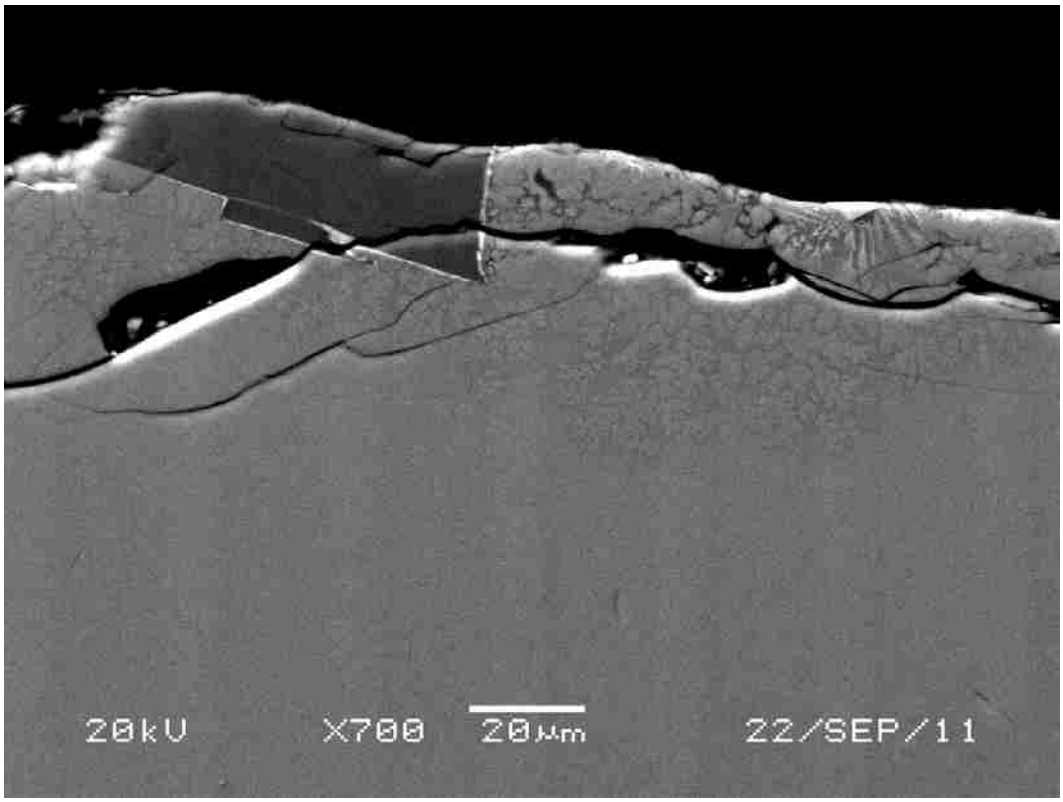

Figure S31. Minidoka sample M2CTA. More alteration textures

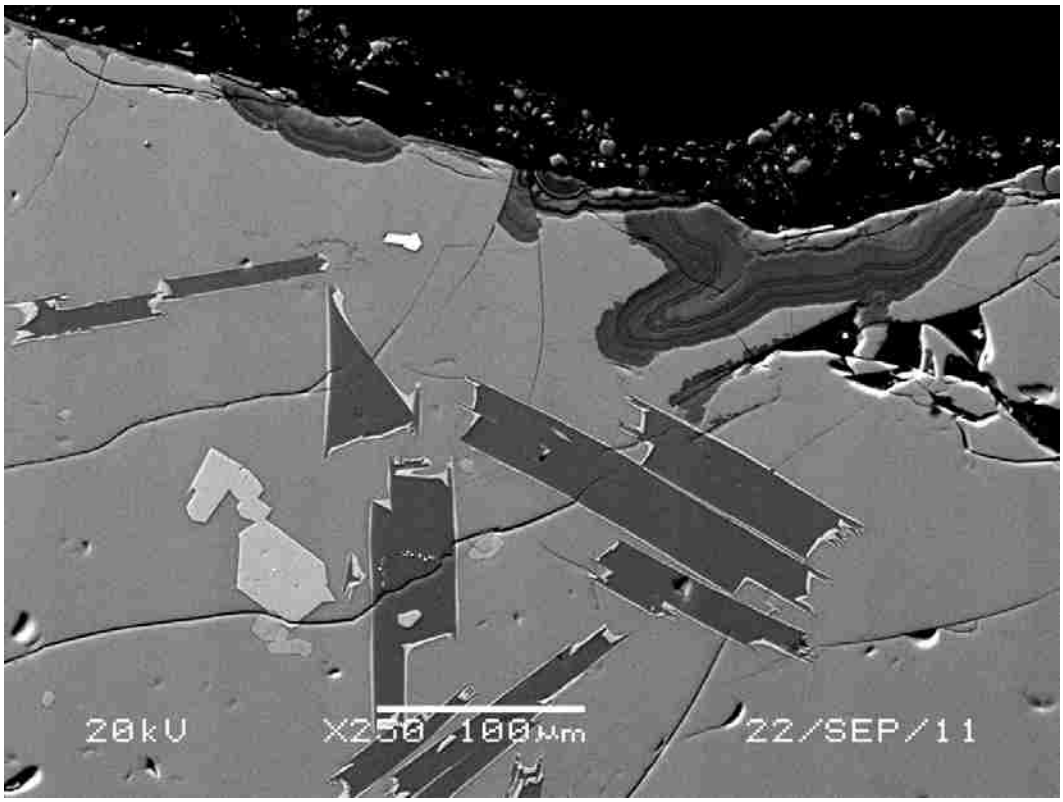

Figure S32. Minidoka sample M2CTA alteration. Alteration textures are on exposed surface.

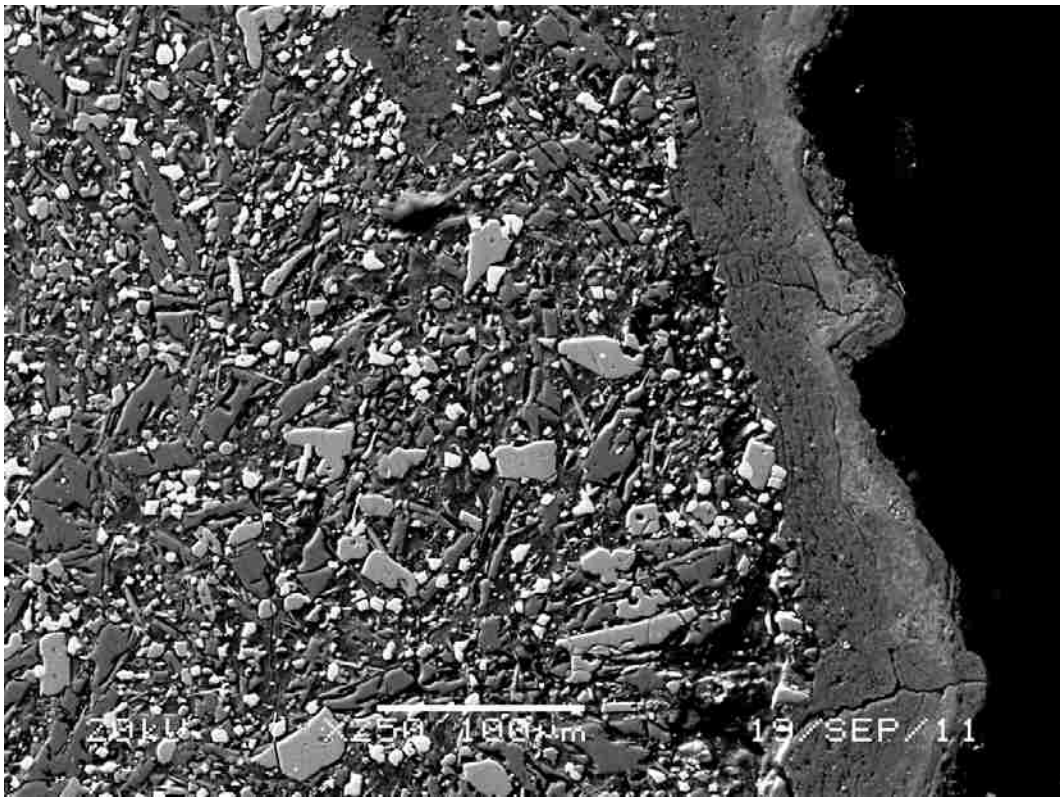

Figure S33. Lava Point sample LP2CTA. Alteration rind and texture indicating increase porosity and dissolution

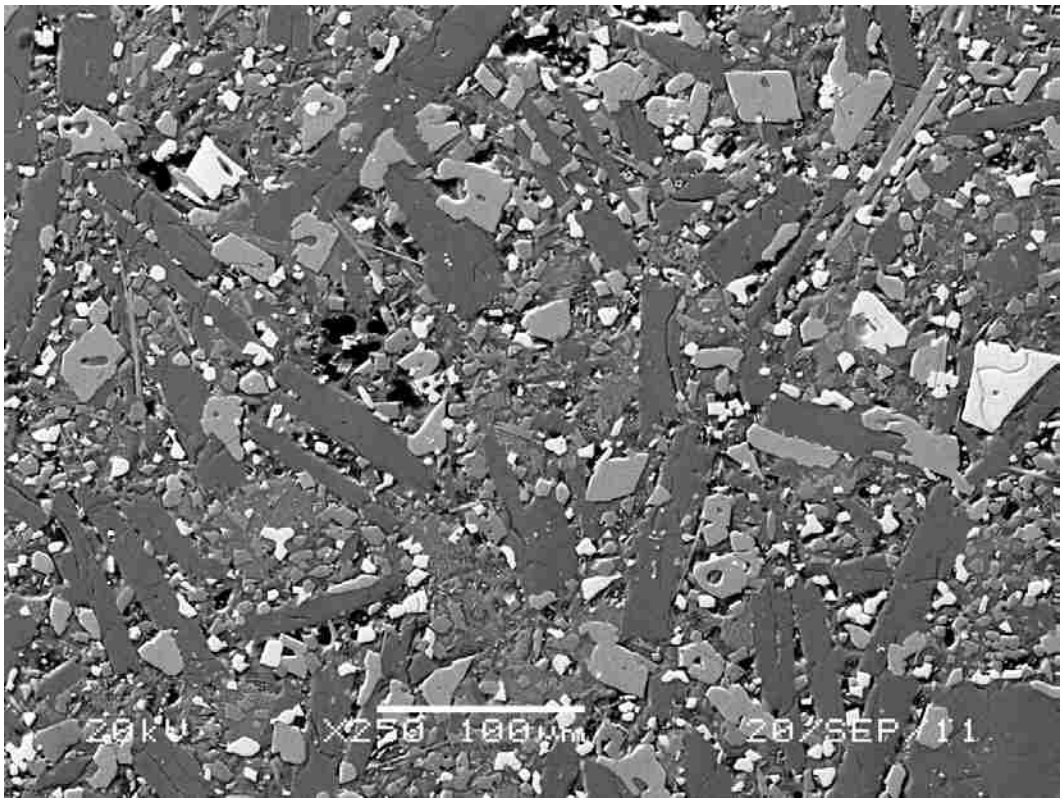

Figure S34. Lava Point sample LP2CTA interior. Possible dissolution textures and increased prosity in the interior of the sample.

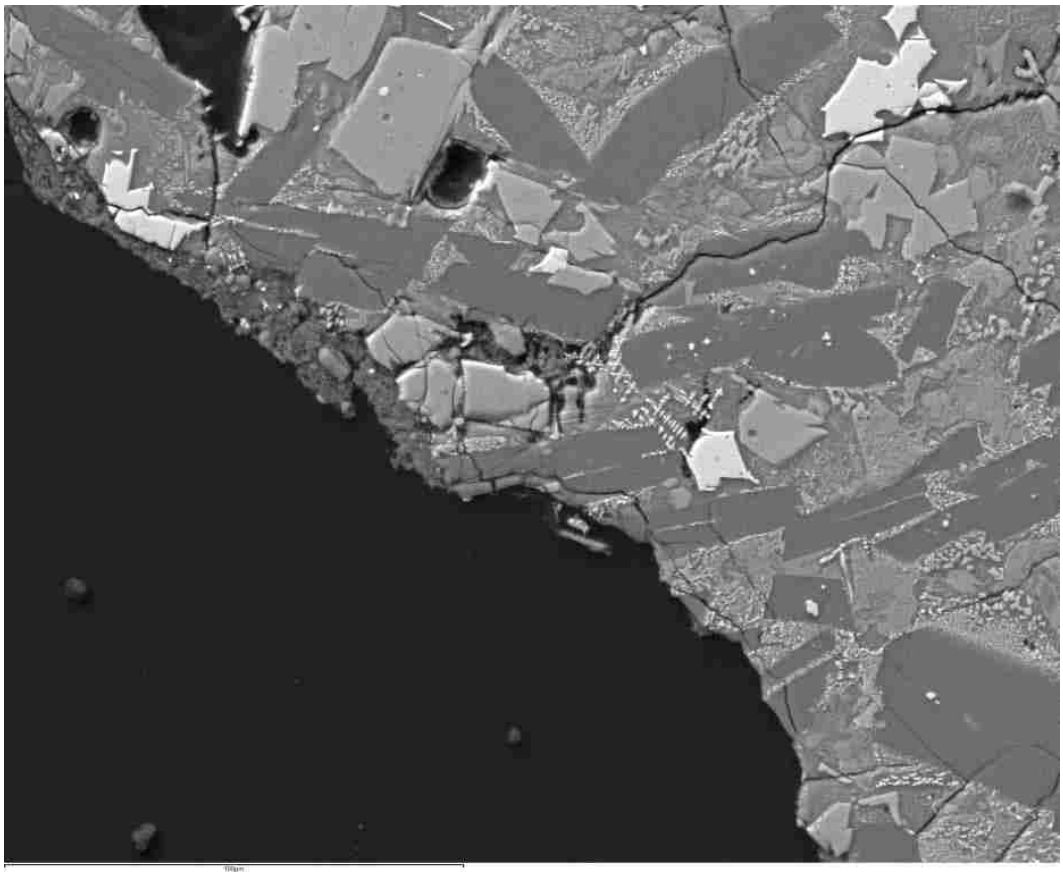

Figure S35. Lava Point sample LP3CTA. Possible alteration rind on exposed egde of sample, however, these same texture could also be surface deposits. Scale: 100um

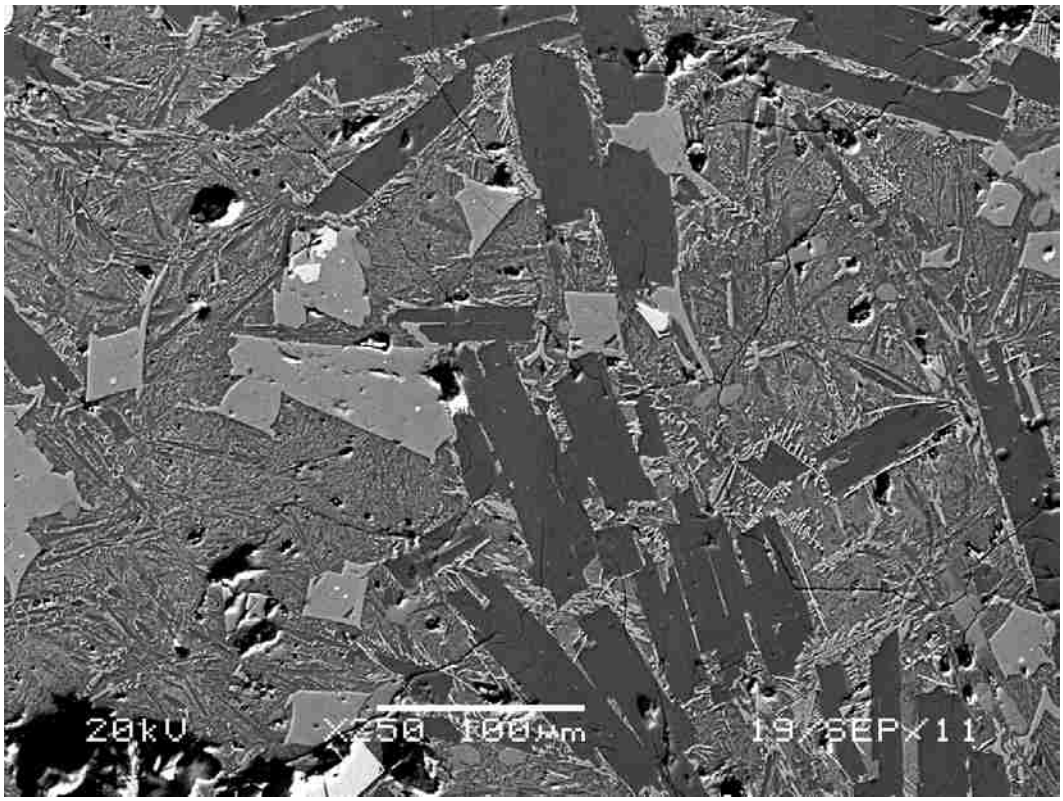

Figure S36. Pronghorn sample P31JC interior. Possible dissolution textures and increased prosity in the interior of the sample.

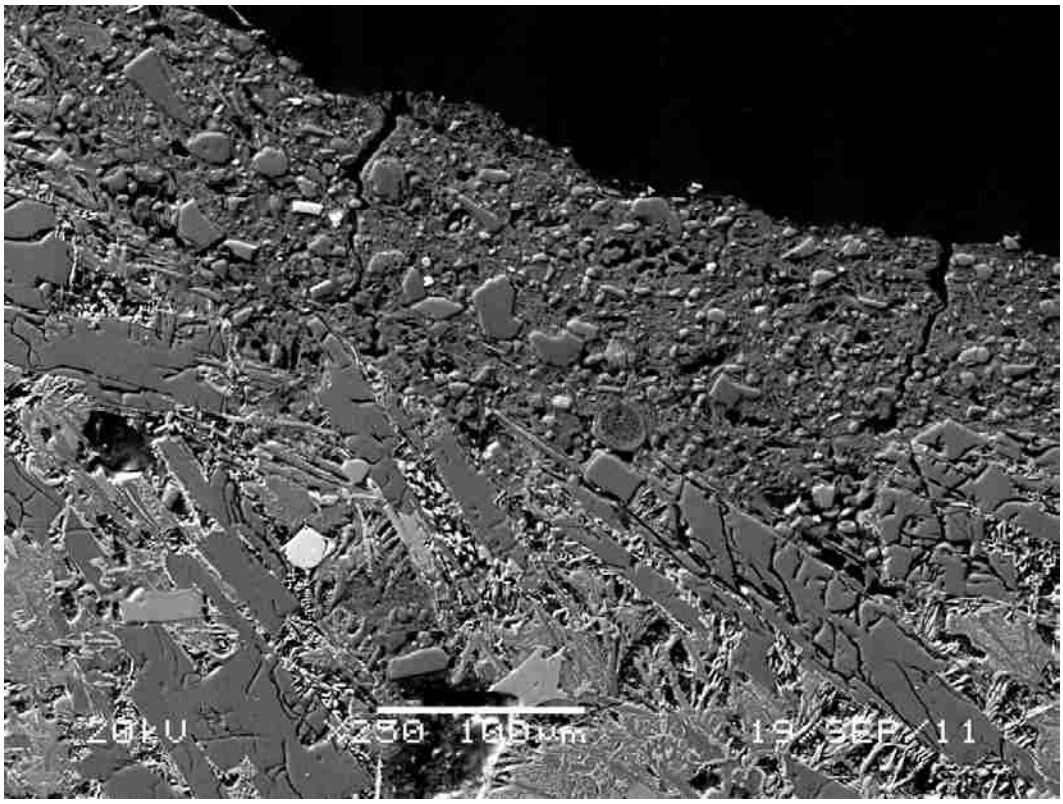

Figure S37. Pronghorn sample P31JC. Possible dissolution textures and increased prosity in the interior of the sample, but also either an alteration rind or a deposit on the original sample surface.

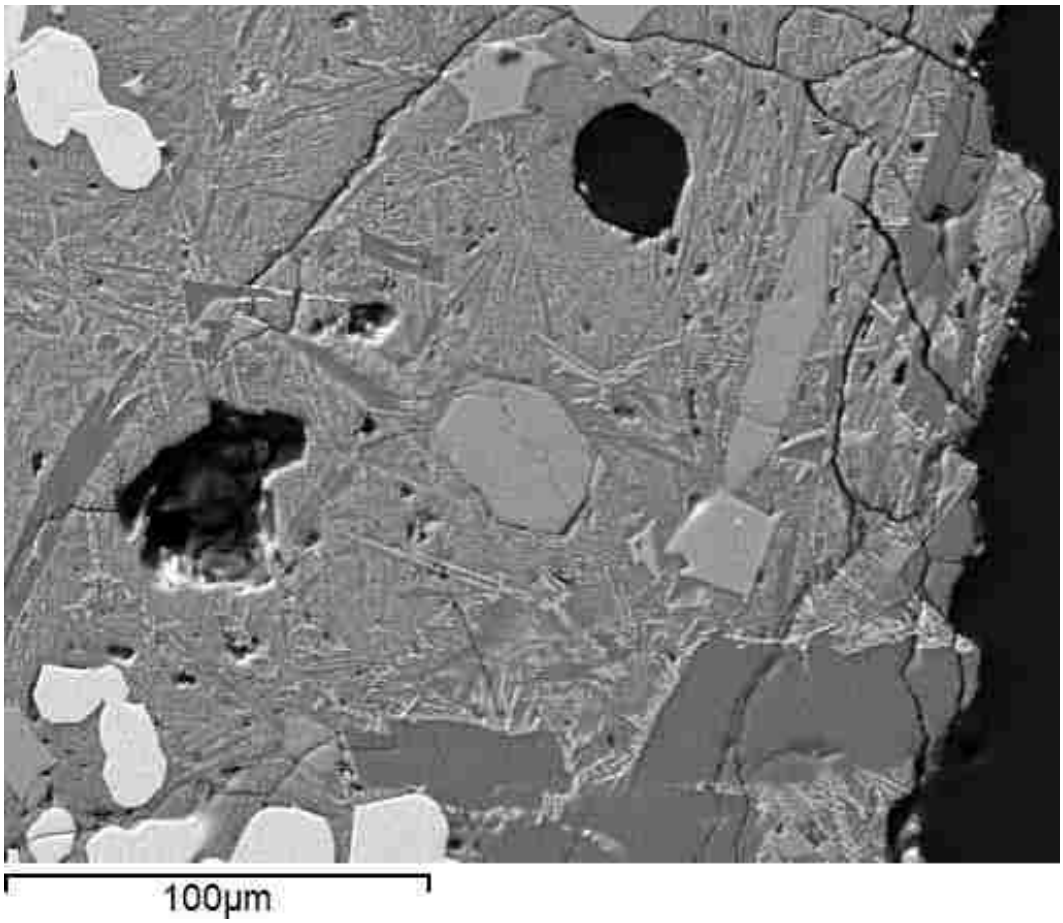

Figure S38. Pronghorn sample P42JC. Fluorapatites (large medium grey grains) near original exposed surface of sample. Long grain in the right of image is a fluorapatite grain with the long C axis near parallel to the thinsectrion surface.

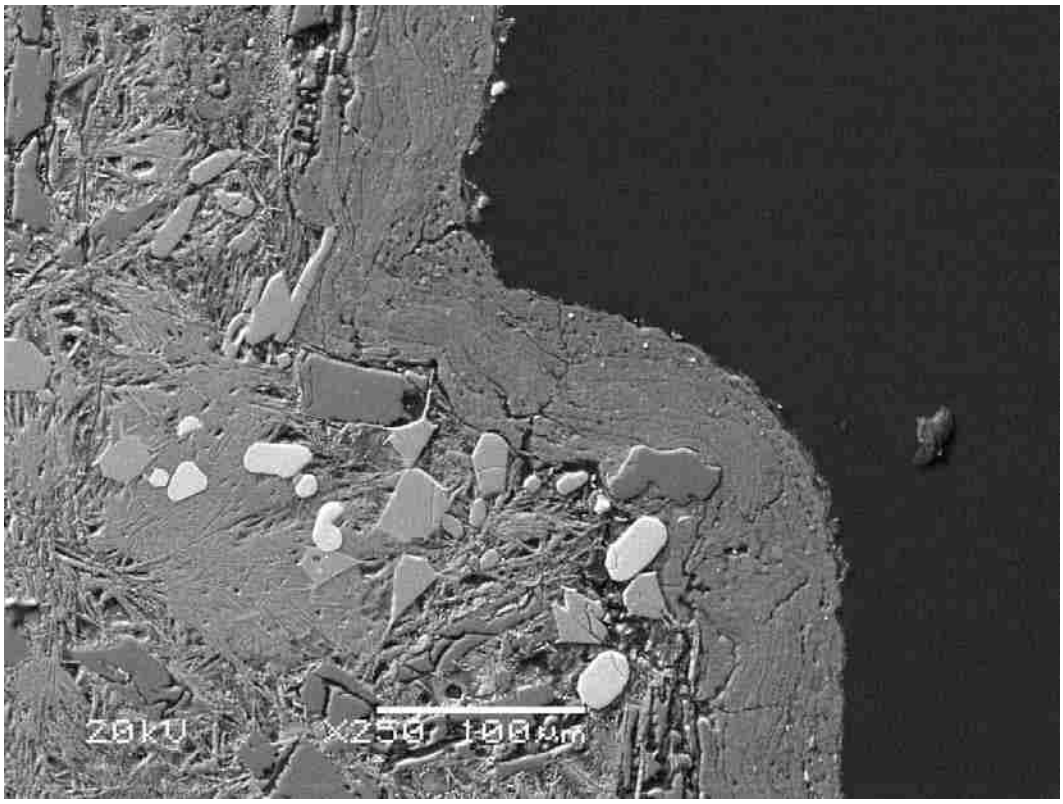

Figure S39. Pronghorn sample P4ACTA. Fluorapatites (medium grey grains) near an altereation rind. Note the dissolutoin texture of the interior of the sample.

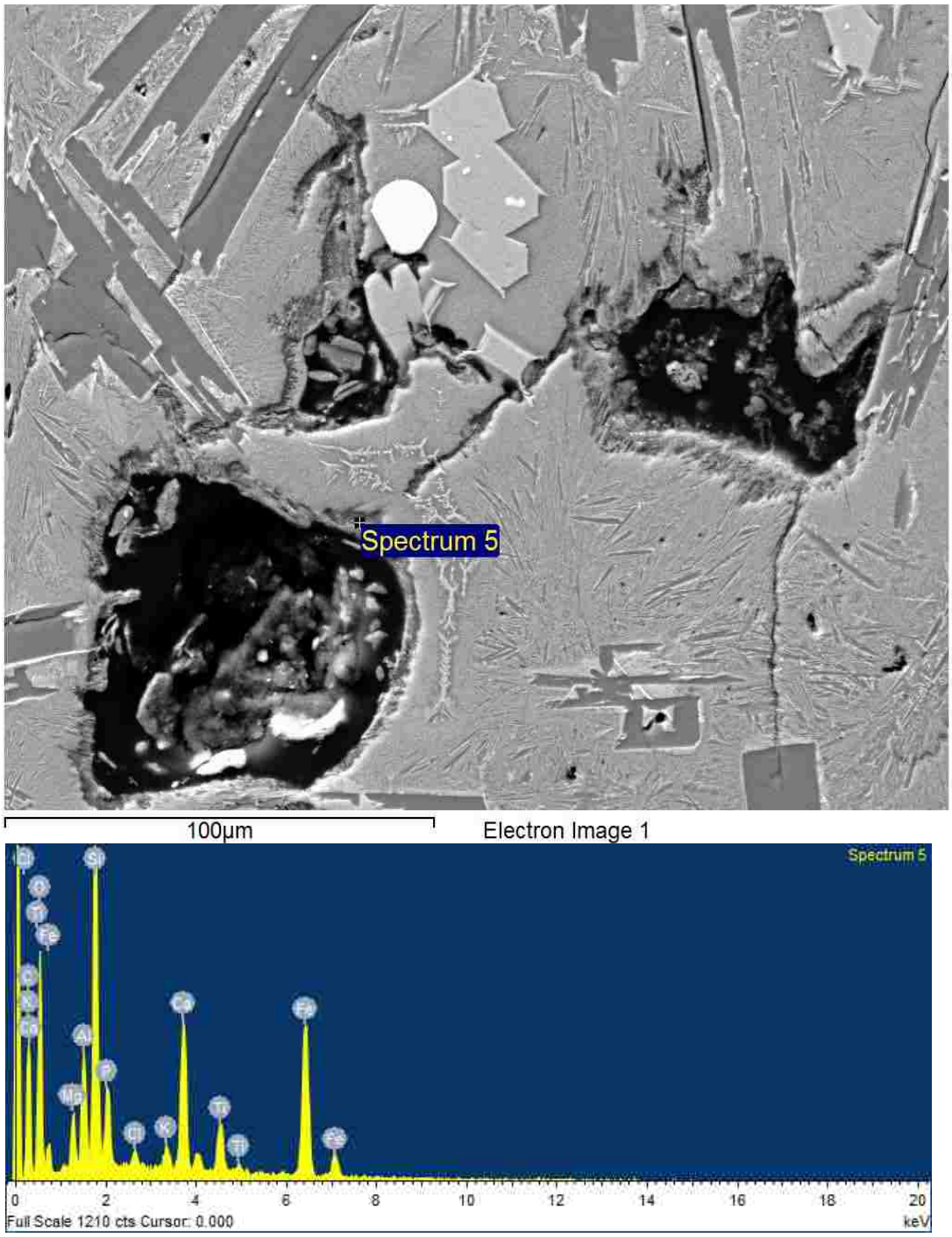

Figure S40. Pronghorn sample P4ACTA and EDS. Image and EDS analysis of rim around porosity. Analysis shows phosphorus.

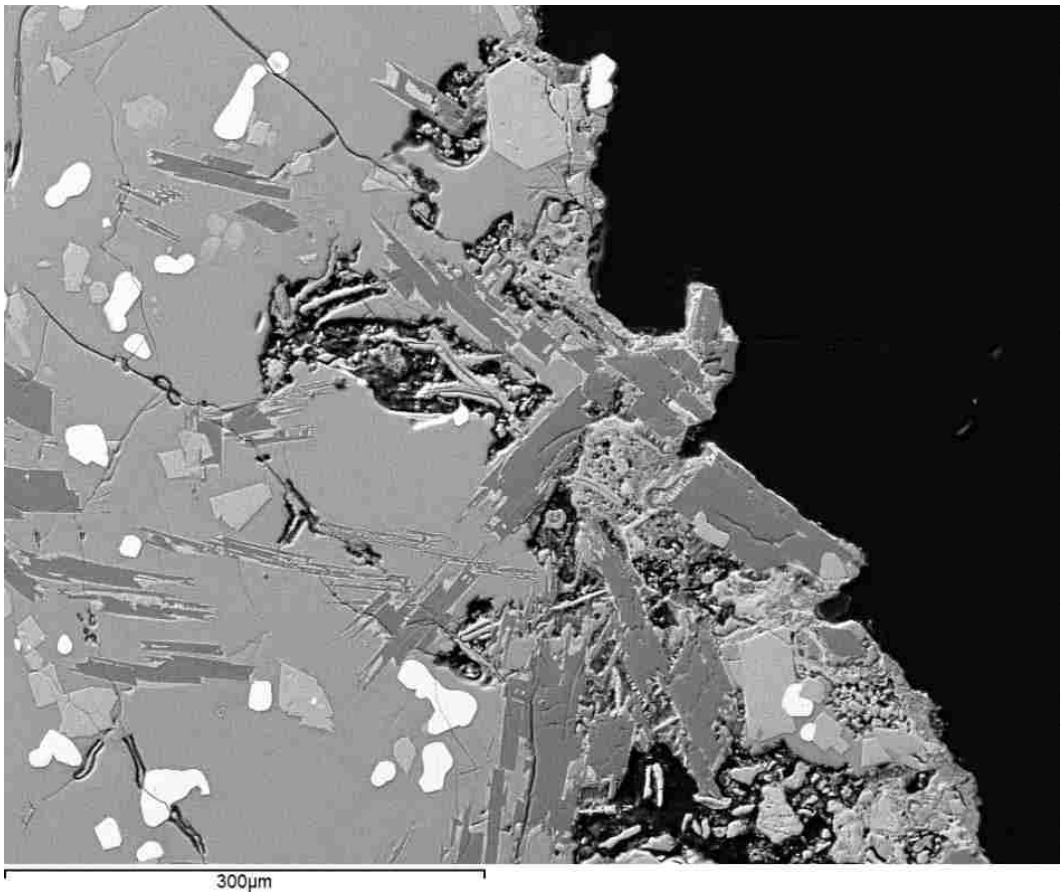

Figure S41. Pronghorn sample P4ACTA dissolution. Dissolution textures near original surface of sample. Not the apatite in the upper center of image (large medium grey grain) which show little sign of dissolution.

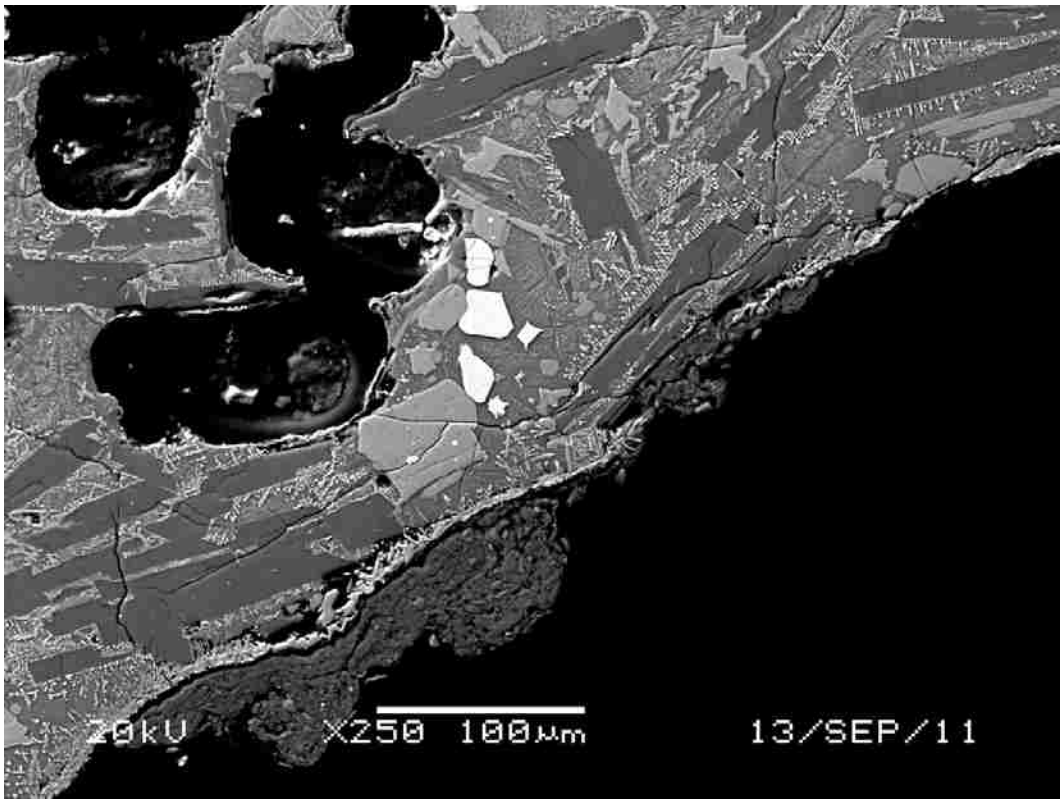

Figure S42. Sunset sample LC12 JC. Possible alteration rind or surface deposit.

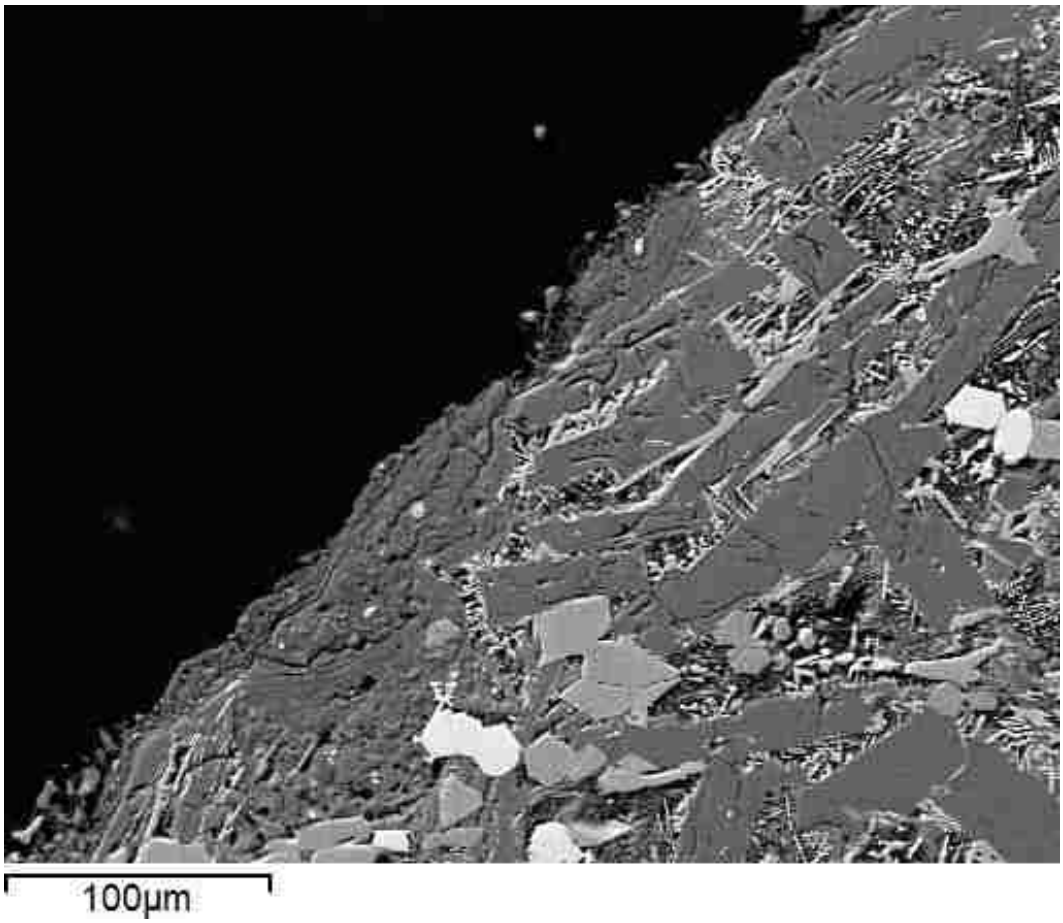

Figure S43. Kimama sample K24JC. Dissolution textures in interior and possible alteration rind or deposit on original mineral surface.

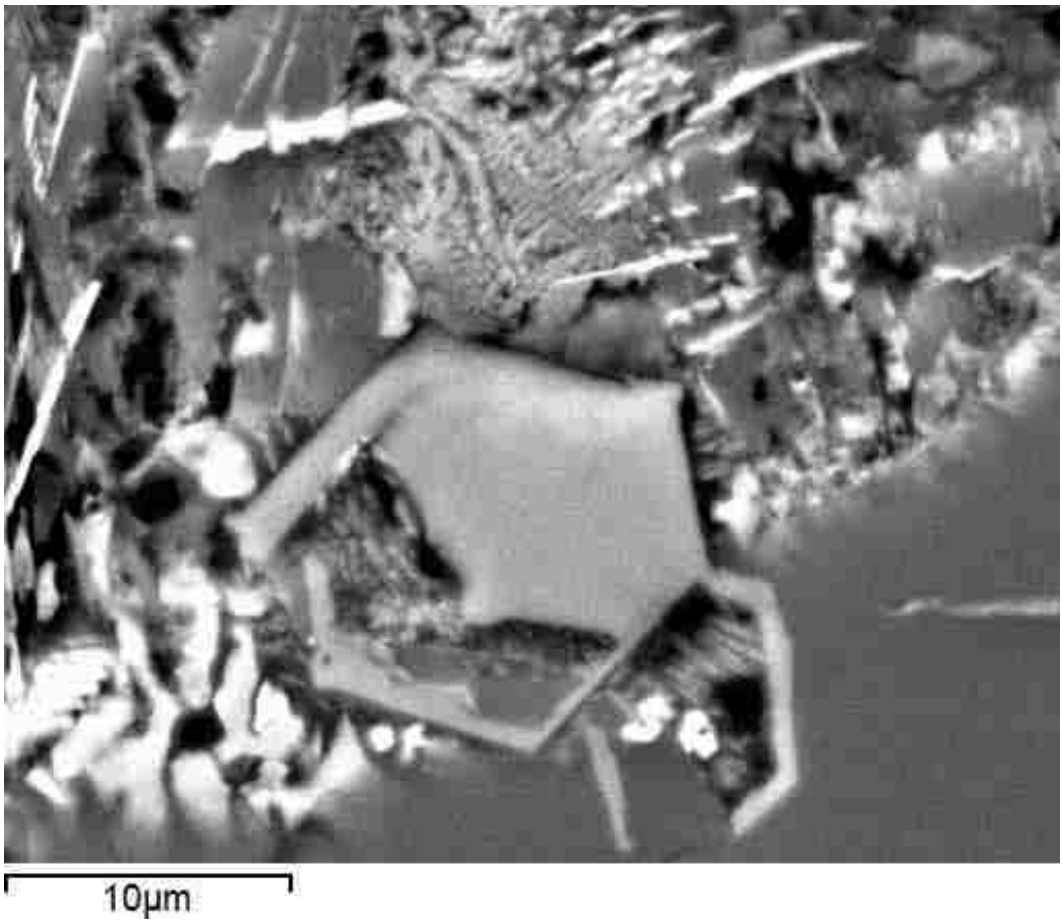

Figure S44. Kimama sample K31JC. Relic Apatite, or more likely skeletal texture.

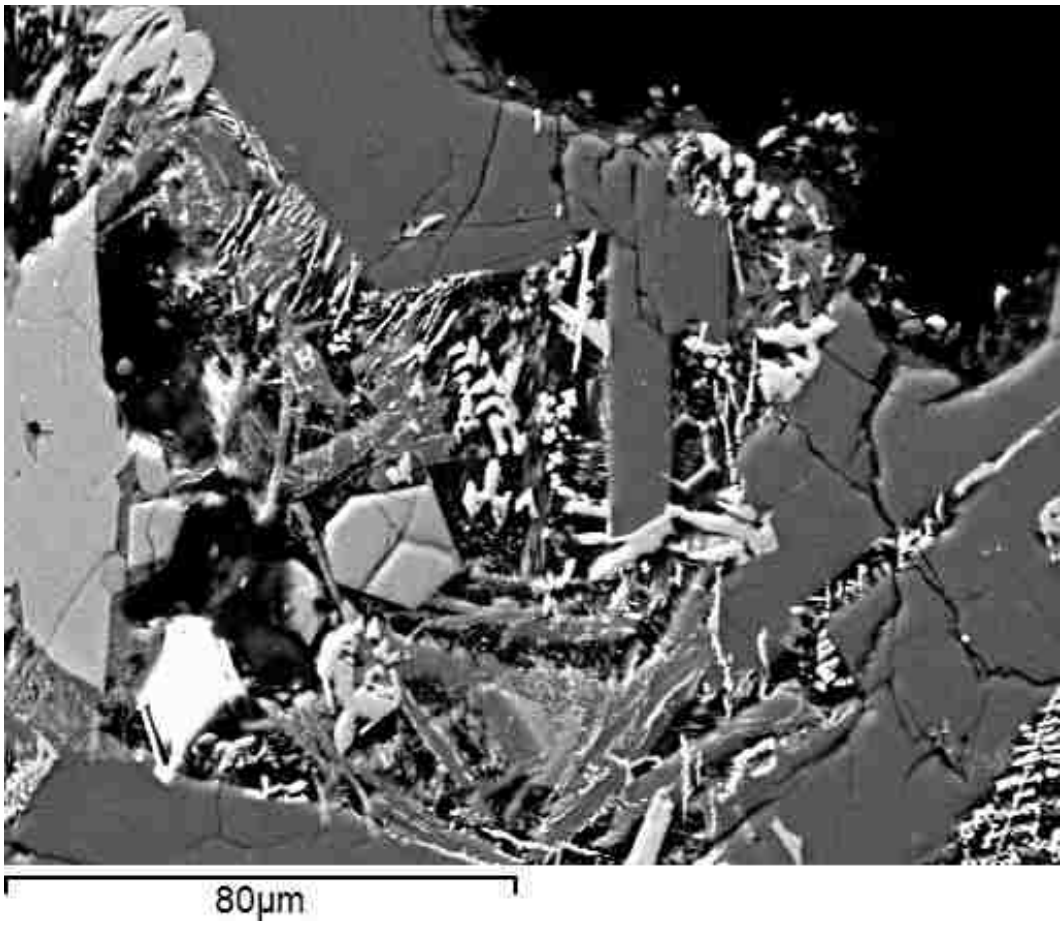

Figure S45. Kimama sample K31JC. Nearly pristine apatite sitting in dissolved matrix zone.

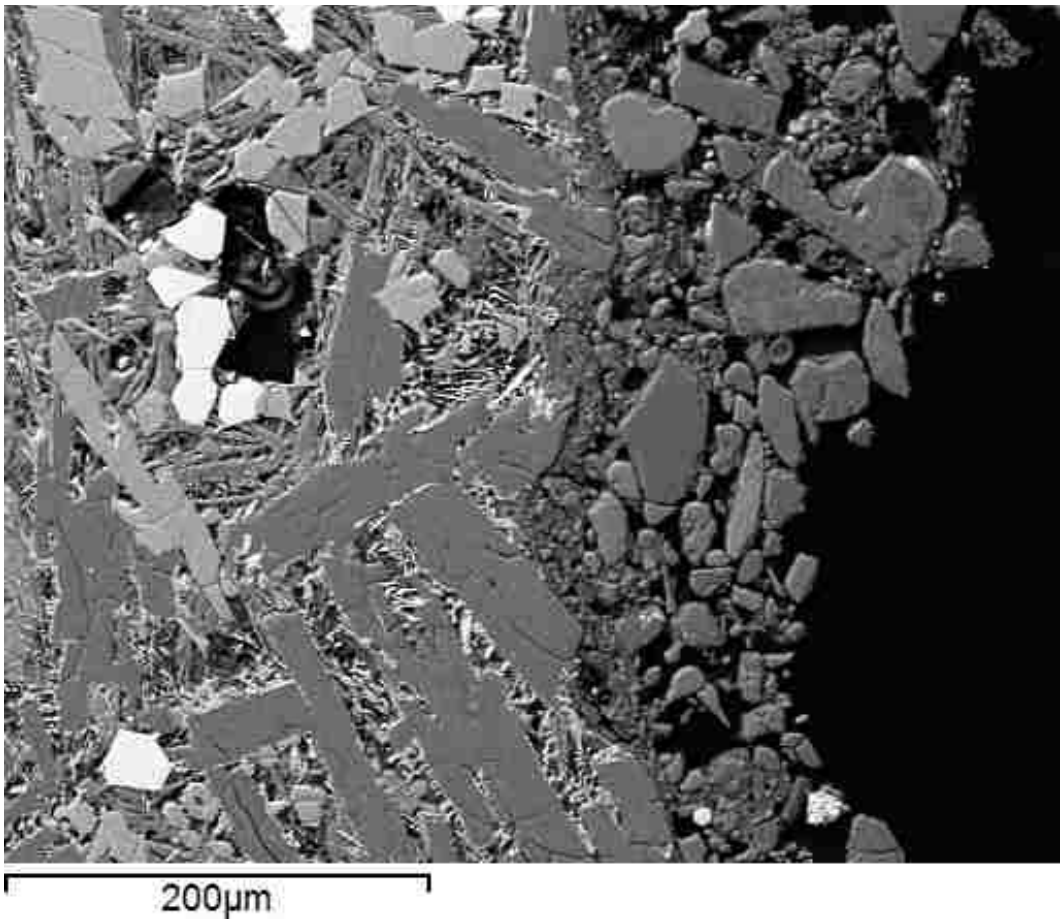

Figure S46. Kimama sample K31JC surface. This is most likely a surface deposit (right side of image) rather than the product of alteration or weathering.

REFERENCES

Adcock, C., Hausrath, E., and Forster, P., 2013, Readily available phosphate from minerals in early aqueous environments on Mars: Nature Geoscience, v. 6, no. 10, p. 824-827.

Adcock, C. T., Hausrath, E. M., Forster, P. M., Tschauner, O., and Sefein, K. J., 2014, Synthesis and characterization of the Mars-relevant phosphate minerals Fe- and Mg-whitlockite and merrillite and a possile mechanism that maintains charge balance during whitlockite to merrillite transformation: American Mineralogist, 99, 1221-1232..

Amjad, Z., Koutsoukos, P., and Nancollas, G., 1984, The crystallization of hydroxyapatite and fluorapatite in the presence of magnesium ions: Journal of Colloid and Interface Science, v. 101, no. 1, p. 250-256.

Amrhein, C., and Suarez, D. L., 1992, Some factors affecting the dissolution kinetics of anorthite at 25oC: Geochim. Cosmochim. Acta, v. 56, p. 1815-1826.

Arvidson, R., Squyres, S., Anderson, R., Bell, J., Blaney, D., Brückner, J., Cabrol, N., Calvin, W., Carr, M., Christensen, P., Clark, B. C., Crumpler, L. A., Des Marias, D. J., de Souza, J. E., d'Uston, C., Economou, T., Farmer, J., Farrand, W. H., Folkner, W., Golombek, M. P., Gorevan, S., Grant, J. A., Greeley, R., Grotzinger, J. P., Guinness, E. A., Hahn, B. C., Haskin, L. A., Herkenhoff, K., Hurowitz, J., Hviid, S., Johnson, J. R., Klingelhoefer, G., Knoll, A. H., Landis, G. A., Leff, C., Lemmon, M. T., Li, R., Madsen, B., Malin, M., McLennan, S. M., McSween, H. Y., Ming, D. W., Moersch, J. E., Morris, R. V., Parker, T., Rice, J. W. J., Richter, L., Rieder, R., Rodionov, D. S., Schroder, C., Sims, M., Smith, M., Smith, P.,

Soderblom, L. A., Sullivan, R., Thompson, S. D., Tosca, N. J., Wang, A., Wanke, H., Ward, J., Wdowiak, T., Wolff, M., and Yen, A., 2006, Overview of the Spirit Mars Exploration rover mission to Gusev crater: Landing site to Backstay rock in the Columbia Hills: Journal of Geophysical Research: Planets (1991–2012), v. 111, no. E2.

Baker, V. R., 2006, Geomorphological Evidence for Water on Mars: Elements, v. 2, no. 3, p. 139-143.

Bandstra, J. Z., and Brantley, S. L., 2008, Data Fitting Techniques with Applications to mineral dissolution kinetics, *in* Brantley, S. L., Kubicki, J. D., and White, A. F., eds., Kinetics of Water-Rock Interaction.

Bandstra, J. Z., Buss, H. L., Campen, R. K., Liermann, L. J., Moore, J., Hausrath, E. M., Navarre-Sitchler, A. K., Jang, J.-H., and Brantley, S. L., 2008, Compilation of Mineral Dissolution Rates, *in* Brantley, S., Kubicki, J., and White, A., eds., Kinetics of Water-Rock Interaction: New York, Springer, p. 737-823.

Banin, A., Han, F., Kan, I., and Cicelsky, A., 1997, Acidic volatiles and the Mars soil: Journal of Geophysical Research: Planets (1991–2012), v. 102, no. E6, p. 13341-13356.

Beisman, J. J., Reed, M., Navarre-Sitchler, A. K., Steefel, C., and Rafa, S. M., High Resolution Reactive Transport: A Poupled Parallel Hydrogeochemical Model, *in* Proceedings Geological Society of America Abstracts with Programs2013, Volume 45, p. 0.

Belik, A., Izumi, F., Stefanovich, S. Y., Lazoryak, B., and Oikawa, K., 2002, Chemical and Structural Properties of a Whitlockite-like Phosphate, Ca9FeD(PO4)7: Chemistry of Materials, v. 14, no. 9, p. 3937-3945.

Benning, J. L., 2008, The effects of scale and spatial heterogeneities on diffusion in volcanic breccias and basalts: Amchitka, Alaska.

Bensalem, A., Ahluwalia, M., Vijayaraghavan, T. V., and Ko, Y. H., 1997, Synthesis of amorphous MgHPO4 · x(R) [R = Ethanol; Ethylene glycol] in anhydrous media: Materials Research Bulletin, v. 32, no. 11, p. 1473-1483.

Bergerhoff, G., and Brown, I., 1987, Crystallographic databases: International Union of Crystallography, Chester, p. 77-95.

Bibring, J.-P., Langevin, Y., Gendrin, A., Gondet, B., Poulet, F., Berthe, M., Soufflot, A., Arvidson, R., Mangold, N., Mustard, J., Drossart, P., and the OMEGA team, 2005, Mars Surface Diversity as Revealed by the OMEGA/Mars Express Observations: Science, v. 307, no. 5715, p. 1576-1581.

Bibring, J.-P., Langevin, Y., Mustard, J. F., Poulet, F., Arvidson, R., Gendrin, A., Gondet, B., Mangold, N., Pinet, P., Forget, F., the OMEGA team, Berthe, M., Gomez, C., Jouglet, D., Soufflot, A., Vincendon, M., Combes, M., Drossart, P., Encrenaz, T., Fouchet, T., Merchiorri, R., Belluci, G., Altieri, F., Formisano, V., Capaccioni, F., Cerroni, P., Coradini, A., Fonti, S., Korablev, O., Kottsov, V., Ignatiev, N., Moroz, V., Titov, D., Zasova, L., Loiseau, D., Pinet, P., Doute, S., Schmitt, B., Sotin, C., Hauber, E., Hoffmann, H., Jaumann, R., Keller, U., Arvidson, R., Duxbury, T., Forget, F., and Neukum, G., 2006, Global

Mineralogical and Aqueous Mars History derived from OMEGA/Mars Express Data 10.1126/science.1122659: Science, v. 312, no. 5772, p. 400-404.

Blum, A. E., and Stillings, L. L., 1995, Feldspar dissolution kinetics, *in* White, A. F., and Brantley, S. L., eds., Chemical Weathering Rates of Silicate Minerals, Volume 31: Washington, D.C., Mineralogical Society of America, p. 291-351.

Brantley, S. L., and Mellott, N., 2000, Specific surface area and porosity of primary silicate minerals: American Mineralogist, v. 85, p. 1767-1783.

Brantley, S. L., and White, A. F., 2009, Approaches to modeling weathered regolith: Reviews in Mineralogy and Geochemistry, v. 70, no. 1, p. 435-484.

Brückner, J., Dreibus, G., Gellert, R., Squyres, S. W., Wänke, H., Yen, A., and Zipfel, J., 2008, Mars Exploration Rovers: chemical composition by the APXS, *in* Bell, J., ed., The Martian Surface - Composition, Mineralogy, and Physical Properties: Cambridge, Cambridge University Press, p. 58-100.

Brunauer, S., Emmett, P. H., and Teller, E., 1938, Adsorption of gases in multimolecular layers: Journal of American Chemical Society, v. 60, p. 309-319.

Carr, M. H., 1996, Water on Mars, New York, Oxford University Press, 229 p.

Casey, W. H., Westrich, H. R., and Holdren, G. R., 1991, Dissolution rates of plagioclase at pH = 2 and 3: American Mineralogist, v. 76, p. 211-217.

Chadwick, O. A., Derry, L. A., Vitousek, P. M., Huebert, B. J., and Hedin, L. O., 1999, Changing sources of nutrients during four million years of ecosystem development: Nature (London), v. 397, no. 6719, p. 491-497.

Chaïrat, C., Schott, J., Oelkers, E. H., Lartigue, J.-E., and Harouiya, N., 2007, Kinetics and mechanism of natural fluorapatite dissolution at 25 °C and pH from 3 to 12: Geochimica et Cosmochimica Acta, v. 71, no. 24, p. 5901-5912.

Chevrier, V., 2006, Thermodynamics of clay minerals on Mars: Insight into the geochemical environment of early Mars, Lunar and Planetary Science Conference: Houston, p. Abstract # 1038.

Chin, K. A., and Nancollas, G. H., 1991, Dissolution of fluorapatite. A constant-composition kinetics study: Langmuir, v. 7, no. 10, p. 2175-2179.

Chou, L., and Wollast, R., 1984, Study of the weathering of albite at room temperature and pressure with a fluidized bed reactor: Geochimica et Cosmochimica Acta, v. 48, p. 2205-2217.

Christensen, P., Bandfield, J., Clark, R., Edgett, K., Hamilton, V., Hoefen, T., Kieffer, H., Kuzmin, R., Lane, M., and Malin, M., 2000, Detection of crystalline hematite mineralization on Mars by the Thermal Emission Spectrometer: Evidence for near-surface water: Journal of Geophysical Research, v. 105, no. E4, p. 9623-9642.

Clark, B. C., Arvidson, R. E., Gellert, R., Morris, R. V., Ming, D. W., Richter, L., Ruff, S. W., Michalski, J. R., Farrand, W. H., and Yen, A., 2007, Evidence for montmorillonite or its compositional equivalent in Columbia Hills, Mars: Journal of Geophysical Research: Planets (1991–2012), v. 112, no. E6.

Corlett, M., and Keppler, U., 1966, Chemische Zusammensetzung des Whitlockits: Naturwissenschaften, v. 53, no. 4, p. 105-105.

Cornell, J. W., and Hausrath, E. M., 2010, Phosphate Mobility in a Mars Analog Environment, LPSC XXXXI: Houston, TX, LPI, p. 2141.

Dachs, E., Harlov, D., and Benisek, A., 2010, Excess heat capacity and entropy of mixing along the chlorapatite–fluorapatite binary join: Physics and Chemistry of Minerals.

Davis, S. N., 1969, Porosity and permeability of natural materials: Flow through porous media, p. 53-89.

Delany, J. M., and Lundeen, S. R., 1990, The LLNL thermochemical database, Lawrence Livermore National Laboratory Report UCRL-21658, 150 p.:

Dolomanov, O. V., Bourhis, L. J., Gildea, R. J., Howard, J. A., and Puschmann, H., 2009, OLEX2: a complete structure solution, refinement and analysis program: Journal of Applied Crystallography, v. 42, no. 2, p. 339-341.

Dontsova, K., 2009, Interactive comment on "Coupled modeling of hydrologic and geochemical fluxes for prediction of solid phase evolution in the Biosphere 2 hillslope experiment" by K. Dontsova et al.

Dorozhkin, S. V., and Epple, M., 2002, Biological and medical significance of calcium phosphates: Angewandte Chemie International Edition, v. 41, no. 17, p. 3130-3146.

Dove, P. M., and Czank, C. A., 1995, Crystal chemical controls on thge dissolutoin kintetics of the isostructural sulfates - Celestite, Anglesite, and Barite.: Geochimica et Cosmochimica Acta, v. 59, no. 10, p. 1907-1915.

Downs, R. T., and Hall-Wallace, M., 2003, The American Mineralogist crystal structure database: American Mineralogist, v. 88, no. 1, p. 247-250.

Dowty, E., 1977, Phosphate in Angra dos Reis: Structure and composition of the Ca3(PO4)2 minerals: Earth and Planetary Science Letters, v. 35, no. 2, p. 347-351.

Drever, J. I., 2005, Surface and Ground Water, Weathering, and Soils: Treatise on Geochemistry, Volume 5: Kidlington, Elsevier Science, p. 626.

Dzombak, D. A., and Morel, F. M., 1990, Surface complexation modeling: hydrous ferric oxide, Wiley New York.

Eaton, A., Clesceri, L., Rice, E., and Greenberg, A., 2005, Standard Methods for the Examination of Waste Water, *in* Mary, F., ed.: Washington, American Public Health Association.

Ehlmann, B. L., Mustard, J. F., Murchie, S. L., Poulet, F., Bishop, J. L., Brown, A. J., Calvin, W. M., Clark, R. N., Marais, D. J. D., Milliken, R. E., Roach, L. H., Roush, T. L., Swayze, G. A., and Wray, J. J., 2008, Orbital Identification of Carbonate-Bearing Rocks on Mars: Science, v. 322, no. 5909, p. 1828-1832.

Elliott, J. C., 1994, Structure and chemistry of the apatites and other calcium orthophosphates, Elsevier Amsterdam.

Elwood Madden, M. E., Bodnar, R. J., and Rimstidt, J. D., 2004, Jarosite as an indicator of water-limited chemical weathering on Mars: Nature, v. 431, no. 7010, p. 821-823.

Elwood Madden, M. E., Madden, A. S., and Rimstidt, J. D., 2009, How long was Meridiani Planum wet? Applying a jarosite stopwatch to determine the duration of aqueous diagenesis: Geology, v. 37, no. 7, p. 635-638.

Filiberto, J., and Treiman, A. H., 2009a, The effect of chlorine on the liquidus of basalt: First results and implications for basalt genesis on Mars and Earth: Chemical Geology, v. 263, no. 1-4, p. 60-68.

-, 2009b, Martian magmas contained abundant chlorine, but little water: Geology, v. 37, no. 12, p. 1087-1090.

Filippelli, G. M., 2002, The Global Phosphorus Cycle: Reviews in Mineralogy and Geochemistry, v. 48, no. 1, p. 391-425.

Freeze, R. A., and Cherry, J. A., 1977, Groundwater, Prentice-Hall.

Frondel, C., 1941, Whitlockite: a new calcium phosphate Ca3 (PO4) 2: American Mineralogist, v. 26, p. 145-152.

Frondel, C., and Prien, E. L., 1946, Deposition of Calcium Phosphates Accompanying Senile Degeneration and Disease: Science, v. 103, no. 2672, p. 326.

Fuchs, L. H., 1962, Occurrence of Whitlockite in Chondritic Meteorites: Science, v. 137, no. 3528, p. 425-426.

Gainey, S. R., Hausrath, E. M., Hurowitz, J. A., and Milliken, R. E., 2014, Nontronite dissolution rates and implications for Mars: Geochimica et Cosmochimica Acta, v. 126, p. 192-211.

Gellert, R., Rieder, R., Anderson, R. C., Bruckner, J., Clark, B. C., Dreibus, G., Economou, T., Klingelhofer, G., Lugmair, G. W., Ming, D. W., Squyres, S. W., d'Uston, C., Wanke, H., Yen, A., and Zipfel, J., 2004, Chemistry of Rocks and Soils in Gusev Crater from the Alpha Particle X-ray Spectrometer: Science, v. 305, no. 5685, p. 829-832.

Gellert, R., Rieder, R., Bruckner, J., Clark, B. C., Dreibus, G., Klingelhofer, G., Lugmair, G., Ming, D. W., Wanke, H., Yen, A., Zipfel, J., and Squyres, S. W., 2006, Alpha Particle X-Ray Spectrometer (APXS): Results from Gusev crater and calibration report: Journal of Geophysical Research, v. 111, no. E02S05, p. doi:10.1029/2005JE002555.

Giambalvo, E. R., Steefel, C. I., Fisher, A. T., Rosenberg, N. D., and Wheat, C. G., 2002, Effect of fluid-sediment reaction on hydrothermal fluxes of major elements, eastern flank of the Juan de Fuca Ridge: Geochimica et Cosmochimica Acta, v. 66, no. 10, p. 1739-1757.

Goetz, W., Bertelsen, P., Binau, C. S., Gunnlaugsson, H. P., Hviid, S. F., Kinch, K. M., Madsen, D. E., Madsen, M. B., Olsen, M., and Gellert, R., 2005, Indication of drier periods on Mars from the chemistry and mineralogy of atmospheric dust: Nature, v. 436, no. 7047, p. 62-65.

Golden, D., Ming, D. W., Morris, R. V., and Mertzman, S. A., 2005, Laboratory-simulated acid-sulfate weathering of basaltic materials: Implications for formation of sulfates at Meridiani Planum and Gusev crater, Mars: Journal of Geophysical Research: Planets (1991–2012), v. 110, no. E12.

Gopal, R., and Calvo, C., 1972, Structural Relationship of Whitlockite and βCa3(PO4)2: Nature, v. 237, no. 71, p. 30-32.

Gopal, R., Calvo, C., Ito, J., and Sabine, W. K., 1974, Crystal-Structure of Synthetic Mg-Whitlockite, Ca18Mg2H2(PO4)14: Canadian Journal of Chemistry-Revue Canadienne De Chimie, v. 52, no. 7, p. 1155-1164.

Goyne, K. W., Brantley, S. L., and Chorover, J., 2006, Effects of organic acids and dissolved oxygen on apatite and chalcopyrite dissolution: Implications for using elements as organomarkers and oxymarkers: Chemical Geology, v. 234, no. 1-2, p. 28-45.

Greeley, R., Arvidson, R., Barlett, P., Blaney, D., Cabrol, N., Christensen, P., Fergason, R., Golombek, M., Landis, G., and Lemmon, M., 2006, Gusev crater: Wind-related features and processes observed by the Mars Exploration Rover Spirit: Journal of Geophysical Research: Planets (1991–2012), v. 111, no. E2.

Greeley, R., Whelley, P. L., Neakrase, L. D., Arvidson, R. E., Bridges, N. T., Cabrol, N. A., Christensen, P. R., Di, K., Foley, D. J., and Golombek, M. P., 2008, Columbia Hills, Mars: Aeolian features seen from the ground and orbit: Journal of Geophysical Research: Planets (1991–2012), v. 113, no. E6.

Greenwood, J. P., and Blake, R. E., 2006, Evidence for an acidic ocean on Mars from phosphorus geochemistry of Martian soils and rocks: Geology, v. 34, no. 11, p. 953-956.

Gross, J., Filiberto, J., and Bell, A. S., 2013a, Water in the martian interior: Evidence for terrestrial MORB mantle-like volatile contents from hydroxyl-rich apatite in olivine–phyric shergottite NWA 6234: Earth and Planetary Science Letters.

Gross, J., Filiberto, J., Herd, C. D., Daswani, M. M., Schwenzer, S. P., and Treiman, A. H., 2013b, Petrography, mineral chemistry, and crystallization history of olivine-phyric shergottite NWA 6234: A new melt composition: Meteoritics & Planetary Science.

Grotzinger, J. P., Sumner, D. Y., Kah, L. C., Stack, K., Gupta, S., Edgar, L., Rubin, D., Lewis, K., Schieber, J., Mangold, N., Milliken, R., Conrad, P. G., DesMarais, D., Farmer, J., Siebach, K., Calef, F., Hurowitz, J., McLennan, S. M., Ming, D., Vaniman, D., Crisp, J., Vasavada, A., Edgett, K. S., Malin, M., Blake, D., Gellert, R., Mahaffy, P., Wiens, R. C., Maurice, S., Grant, J. A., Wilson, S., Anderson, R. C., Beegle, L., Arvidson, R., Hallet, B., Sletten, R. S., Rice, M., Bell, J., Griffes, J., Ehlmann, B., Anderson, R. B., Bristow, T. F., Dietrich, W. E., Dromart, G., Eigenbrode, J., Fraeman, A., Hardgrove, C., Herkenhoff, K., Jandura, L., Kocurek, G., Lee, S., Leshin, L. A., Leveille, R., Limonadi, D., Maki, J., McCloskey, S., Meyer, M., Minitti, M., Newsom, H., Oehler, D., Okon, A., Palucis, M., Parker, T., Rowland, S., Schmidt, M., Squyres, S., Steele, A., Stolper, E., Summons, R., Treiman, A., Williams, R., Yingst, A., and Team, M. S., 2013, A Habitable Fluvio-Lacustrine Environment at Yellowknife Bay, Gale Crater, Mars: Science.

Guidry, M. W., and Mackenzie, F. T., 2003, Experimental study of igneous and sedimentary apatite dissolution: Control of pH, distance from equilibrium, and temperature on dissolution rates: Geochimica et Cosmochimica Acta, v. 67, no. 16, p. 2949-2963.

Gulick, A., 1955, Phosphorus as a Factor in the Origin of Life: American Scientist, v. 43, no. 3, p. 479-489.

Hamad, M., and Heughebaert, J.-C., 1986, The growth of whitlockite: Journal of Crystal Growth, v. 79, no. 1, p. 192-197.

Hamilton, J., 1999, Effects of structure, composition, and pH on the corrosion behavior of Na-aluminosilicate glasses and crystals [Ph.D. thesis]: University Park, PA, Pennsylvania State University.

Hammersley, A., Svensson, S., Hanfland, M., Fitch, A., and Hausermann, D., 1996, Two-dimensional detector software: from real detector to idealised image or two-theta scan: International Journal of High Pressure Research, v. 14, no. 4-6, p. 235-248.

Hargreaves, W., Mulvihill, S., and Deamer, D., 1977, Synthesis of phospholipids and membranes in prebiotic conditions: Nature, v. 266, p. 78-80.

Harouiya, N., Chaïrat, C., Köhler, S. J., Gout, R., and Oelkers, E. H., 2007, The dissolution kinetics and apparent solubility of natural apatite in closed reactors at temperatures from 5 to 50 °C and pH from 1 to 6: Chemical Geology, v. 244, no. 3-4, p. 554-568.

Hausrath, E. M., Golden, D., Morris, R., Agresti, D., and Ming, D., 2013, Acid sulfate alteration of fluorapatite, basaltic glass and olivine by hydrothermal vapors and fluids: Implications for fumarolic activity and secondary phosphate phases in sulfate-rich Paso Robles soil at Gusev Crater, Mars: Journal of Geophysical Research: Planets.

Hausrath, E.M., Navarre-Sitchler, A.K., Sak, P.B., Steefel, C.I., Brantley, S.L., 2008a. Basalt weathering rates on Earth and the duration of liquid water on the plains of Gusev Crater, Mars. Geology 36, 67-70

Hausrath, E. M., Navarre-Sitchler, A., Sak, P., Williams, J., and Brantley, S., 2011, Soil profiles as indicators of mineral weathering rates and organic interactions for a Pennsylvania diabase: Chemical Geology, v. 290, no. 3, p. 89-100.

Hausrath, E. M., and Olsen, A. A., 2013, Using the chemical composition of carbonate rocks on Mars as a record of secondary interaction with liquid water: American Mineralogist, v. 98, no. 5-6, p. 897-906.

Hausrath, E.M., Treiman, A.H., Vicenzi, E., Bish, D.L., Blake, D., Sarrazin, P., Hoehler, T., Midtkandal, I., Steele, A., Brantley, S.L., 2008b. Short- and Long-Term Olivine Weathering in Svalbard: Implications for Mars. Astrobiology 8, 1079-1092.

Hausrath, E. M., and Tschauner, O., 2013, Natural Fumarolic Alteration of Fluorapatite, Olivine, and Basaltic Glass, and Implications for Habitable Environments on Mars: Astrobiology, v. 13, no. 11, p. 1049-1064.

Hecht, M. H., Kounaves, S. P., Quinn, R. C., West, S. J., Young, S. M. M., Ming, D. W., Catling, D. C., Clark, B. C., Boynton, W. V., Hoffman, J., DeFlores, L. P., Gospodinova, K., Kapit, J., and Smith, P. H., 2009, Detection of Perchlorate and the Soluble Chemistry of Martian Soil at the Phoenix Lander Site: Science, v. 325, no. 5936, p. 64-67.

Hodson, M. E., 2003, The influence of Fe-rich coatings on the dissolution of anorthite at pH 2.6: Geochimica et Cosmochimica Acta, v. 67, no. 18, p. 3355-3363.

Holdren, G. R., and Speyer, P. M., 1987, Reaction rate-surface area relationships during the early stages of weathering. II. Data on eight additional feldspars: Geochemica Cosmochimica Acta, v. 51, p. 2311-2318.

Hovis, G. L., and Harlov, D. E., 2010, Solution calorimetric investigation of fluor-chlorapatite crystalline solutions: American Mineralogist, v. 95, no. 7, p. 946-952.

Huertas, F. J., Chou, L., and Wollast, R., 1999, Mechanism of kaolinite dissolution at room temperature and pressure Part II: Kinetic study: Geochimica et Cosmochimica Acta, v. 63, no. 19, p. 3261-3275.

Hughes, J. M., Cameron, M., and Crowley, K. D., 1989, Structural Variations in Natural F, Oh, and Cl Apatites: American Mineralogist, v. 74, no. 7-8, p. 870-876.

Hughes, J. M., Jolliff, B. L., and Gunter, M. E., 2006, The atomic arrangement of merrillite from the Fra Mauro Formation, Apollo 14 lunar mission: The first structure of merrillite from the Moon: American Mineralogist, v. 91, no. 10, p. 1547-1552.

Hughes, J. M., Jolliff, B. L., and Rakovan, J., 2008, The crystal chemistry of whitlockite and merrillite and the dehydrogenation of whitlockite to merrillite: American Mineralogist, v. 93, no. 8-9, p. 1300-1305.

Hurowitz, J. A., McLennan, S., Tosca, N., Arvidson, R., Michalski, J. R., Ming, D. W., Schroder, C., and Squyres, S. W., 2006a, In situ and experimental evidence for acidic weathering of rocks and soils on Mars: Journal of Geophysical Research, v. 111.

Hurowitz, J. A., McLennan, S. M., McSween, H. Y., DeSouza, P. A. J., and Klingelhofer, G., 2006b, Mixing relationships and the effects of secondary alteration in the Wishstone and Watchtower Classes of Husband Hill, Gusev Crater, Mars,: Journal of Geophysical Research, v. 111, no. E12S14, p. doi:10.1029/2006JE002795.

Huygens, C., 1698, Cosmotheoros: Conjectures concerning the inhabitants, plants and productions of the worlds in the planets., London.

Irvine, T., and Baragar, W., 1971, A guide to the chemical classification of the common volcanic rocks: Canadian Journal of Earth Sciences, v. 8, no. 5, p. 523-548.

Jarcho, M., Salsbury, R., Thomas, M., and Doremus, R., 1979, Synthesis and fabrication of β-tricalcium phosphate (whitlockite) ceramics for potential prosthetic applications: Journal of Materials Science, v. 14, no. 1, p. 142-150.

Jarosewich, E., 2002, Smithsonian microbeam standards: Journal of Research - National Institute of Standard and Technology, v. 107, no. 6, p. 681-686.

Jarosewich, E. N., J A; Norberg, J A, 1980, Reference samples for electron microprobe analysis: Geostandards Newsletter, v. 4, no. 1, p. 43-47.

Jaynes, W., Moore, P., and Miller, D., 1999, Solubility and ion activity products of calcium phosphate minerals: Journal of Environmental Quality, v. 28, no. 2, p. 530-536.

Johnson, J., Anderson, G., and Parkhurst, D., 2000, Database thermo. com. V8. R6. 230', Rev. 1.11: Lawrence Livermore Natl. Lab., Livermore, Calif.

Johnson, J. W., Oelkers, E. H., and Helgeson, H. C., 1992, SUPCRT92: A software package for calculating the standard molal thermodynamic properties of minerals, gases, aqueous species, and reactions from 1 to 5000 bar and 0 to 1000 C: Computers & Geosciences, v. 18, no. 7, p. 899-947.

Johnston, J., Daniel, R. J., and University of, L., 1934, James Johnston memorial volume, [Liverpool], University of Liverpool Press, v. x, 348 p., x, 348 p. p.:

Jolliff, B. L., Haskin, L. A., Colson, R. O., and Wadhwa, M., 1993, Partitioning in REE-saturating minerals: Theory, experiment, and modelling of whitlockite, apatite,

and evolution of lunar residual magmas: Geochimica et Cosmochimica Acta, v. 57, no. 16, p. 4069-4094.

Jolliff, B. L., Hughes, J. M., Freeman, J. J., and Zeigler, R. A., 2006, Crystal chemistry of lunar merrillite and comparison to other meteoritic and planetary suites of whitlockite and merrillite: American Mineralogist, v. 91, no. 10, p. 1583-1595.

Keefe, A., and Miller, S., 1995, Are polyphosphates or phosphate esters prebiotic reagents?: Journal of Molecular Evolution, v. 41, no. 6, p. 693-702.

Keller, G., 1960, Physical properties of tuffs of the Oak Spring Formation, Nevada: US Geol. Surv. Prof. Pap, v. 4008, p. 8396-8400.

Keppler, U., 1968, Structural investigation of calciumphosphate and isotypic structures: Bulletin de la Société Chimique de France.

Kiefer, W. S., Macke, R. J., Britt, D. T., Irving, A. J., and Consolmagno, G. J., 2012, The density and porosity of lunar rocks: Geophysical Research Letters, v. 39, no. 7.

Klingelhöfer, G., Morris, R., Bernhardt, B., Schröder, C., Rodionov, D., De Souza, P., Yen, A., Gellert, R., Evlanov, E., and Zubkov, B., 2004, Jarosite and hematite at Meridiani Planum from Opportunity's Mössbauer spectrometer: Science, v. 306, no. 5702, p. 1740-1745.

Knauss, K. G., Johnson, J. W., and Steefel, C. I., 2005, Evaluation of the impact of CO2, co-contaminant gas, aqueous fluid and reservoir rock interactions on the geologic sequestration of CO2: Chemical Geology Geochemical Aspects of CO2 sequestering, v. 217, no. 3-4, p. 339-350.

Knauss, K. G., and Wolery, T. J., 1986, Dependence of albite dissolution kinetics on pH and time at 25°C and 70°C: Geochimica et Cosmochimica Acta, v. 50, p. 2481-2497.

Knoll, A. H., Carr, M., Clark, B., Des Marais, D. J., Farmer, J. D., Fischer, W. W., Grotzinger, J. P., McLennan, S. M., Malin, M., and Schroder, C., 2005, An astrobiological perspective on Meridiani Planum: Earth and Planetary Science Letters, v. 240, no. 1, p. 179-189.

Köhler, S. J., Harouiya, N., Chaïrat, C., and Oelkers, E. H., 2005, Experimental studies of REE fractionation during water–mineral interactions: REE release rates during apatite dissolution from pH 2.8 to 9.2: Chemical Geology, v. 222, no. 3–4, p. 168-182.

Kukachka, F. R., 2010, Soil survey of Craters of the Moon National Monument and Preserve, Idaho.: United States Department of Agriculture, Natural Resources Conservation Service, and United States Department of the Interior, National Park Service.

Kuntz, M. A., Champion, D. E., Spiker, E. C., and Lefebvre, R. H., 1986a, Contrasting magma types and steady-state, volume-predictable, basaltic volcanism along the Great Rift, Idaho: Geological Society of America Bulletin, v. 97, no. 5, p. 579-594.

Kuntz, M. A., Covington, H. R., and Schorr, L. J., 1992, An overview of basaltic volcanism of the eastern Snake River Plain, Idaho, *in* Link, P. K., Kuntz, M. A., and Platt, L. B., eds., Regional Geology of Eastern Idaho and Western Wyoming: Geological society of America Memoir, Volume 179, p. 227-266.

Kuntz, M. A., Elsheimer, N. H., Espos, L. F., and Klock, P. R., 1985, Major-element analyses of latest Pleistocene-Holocene lava fields of the Snake River Plain, Idaho, [Denver, CO], U.S. Dept. of the Interior, Geological Survey, U.S. Geological Survey open-file report ; 85-593., v. Accessed from http://nla.gov.au/nla.cat-vn4000478.

Kuntz, M. A., Spiker, E. C., Rubin, M., Champion, D. E., and Lefebvre, R. H., 1986b, Radiocarbon studies of latest Pleistocene and Holocene lava flows of the Snake River Plain, Idaho: Data, lessons, interpretations: Quaternary Research, v. 25, no. 2, p. 163-176.

Lagier, R., and Baud, C.-A., 2003, Magnesium whitlockite, a calcium phosphate crystal of special interest in pathology: Pathology-Research and Practice, v. 199, no. 5, p. 329-335.

Lane, M. D., Bishop, J. L., Darby Dyar, M., King, P. L., Parente, M., and Hyde, B. C., 2008, Mineralogy of the Paso Robles soils on Mars: American Mineralogist, v. 93, no. 5-6, p. 728-739.

Lasaga, A., 1998, Kinetic Theory in the Earth Sciences, Princeton, NJ, Princeton University Press, Princeton series in geochemistry, 811 p.:

Lazoryak, B., Morozov, V., Belik, A., Khasanov, S., and Shekhtman, V. S., 1996, Crystal Structures and Characterization of Ca 9 Fe (PO 4) 7 and Ca 9 FeH 0.9 (PO 4) 7: Journal of Solid State Chemistry, v. 122, no. 1, p. 15-21.

Le Bail, A., 2005, Whole powder pattern decomposition methods and applications: a retrospection: Powder Diffraction, v. 20, no. 4, p. 316-326.

Lee, G. H., Seo, S. D., Shim, H. W., Park, K. S., and Kim, D. W., 2012, Synthesis and Li electroactivity of Fe2P2O7 microspheres composed of self-assembled nanorods: Ceramics International, v. 38, no. 8, p. 6927-6930.

Leeman, W. P., Vitaliano, C. J., and Prinz, M., 1976, Evolved lavas from the snake river plain: craters of the moon national monument, Idaho: Contributions to Mineralogy and Petrology, v. 56, no. 1, p. 35-60.

Levenspiel, O., 1972, Chemical reaction engineering, Wiley New York etc.

Lindahl, T., 1993, Instability and decay of the primary structure of DNA: Nature, v. 362, no. 6422, p. 709-715.

Lindsay, W. L., 1979, Chemical equilibria in soils, John Wiley and Sons Ltd.

Macke, R., Kiefer, W., Britt, D., Irving, A., and Consolmagno, G., Density and Porosity of Apollo Lunar Basalts and Breccias, *in* Proceedings Lunar and Planetary Institute Science Conference Abstracts2012, Volume 43, p. 1299.

Madigan, M. T., Martinko, J. M., and Parker, J., 2000, Brock Biology of Microorganisms, Upper Saddle River, Prentice Hall, 991 p.:

Maher, K., Steefel, C. I., DePaolo, D. J., and Viani, B. E., 2006, The mineral dissolution rate conundrum: Insights from reactive transport modeling of U isotopes and pore fluid chemistry in marine sediments: Geochimica et Cosmochimica Acta, v. 70, no. 2, p. 337-363.

Maher, K., Steefel, C. I., White, A. F., and Stonestrom, D. A., 2009, The role of reaction affinity and secondary minerals in regulating chemical weathering rates at the Santa Cruz Soil Chronosequence, California: Geochimica et Cosmochimica Acta, v. 73, no. 10, p. 2804-2831.

Malin, M. C., and Edgett, K. S., 2000, Evidence for recent groundwater seepage and surface runoff on Mars: Science, v. 288, no. 5475.

McAdam, A. C., Zolotov, M. Y., Mironenko, M. V., and Sharp, T. G., 2008, Formation of silica by low-temperature acid alteration of Martian rocks: Physical-chemical constraints: J. Geophys. Res., v. 113.

McCubbin, F. M., Hauri, E. H., Elardo, S. M., Vander Kaaden, K. E., Wang, J., and Shearer, C. K., 2012, Hydrous melting of the martian mantle produced both depleted and enriched shergottites: Geology, v. 40, no. 8, p. 683-686.

McCubbin, F. M., and Nekvasil, H., 2008, Maskelynite-hosted apatite in the Chassigny meteorite: Insights into late-stage magmatic volatile evolution in martian magmas: American Mineralogist, v. 93, no. 4, p. 676-684.

McGuire, A. V., Francis, C. A., and Dyar, M. D., 1992, Mineral standards for electron microprobe analysis of oxygen: American Mineralogist, v. 77, p. 1087-1087.

McSween, H., and Treiman, A. H., 1998, Martian Meteorites, *in* Papike, J., ed., Planetary Materials: Washington, DC, Mineral Society of America, p. F1-F53.

McSween, H. Y., Eisenhour, D. D., Taylor, L. A., Wadhwa, M., and Crozaz, G., 1996, QUE94201 shergottite: Crystallization of a Martian basaltic magma: Geochimica et Cosmochimica Acta, v. 60, no. 22, p. 4563-4569.

McSween, H. Y., et al., 2006, Characterization and petrologic interpretation of olivine-rich basalts at Gusev Crater, Mars,: Journal of Geophysical Research, v. 111, no. E02S10, p. doi:10.1029/2005JE002477.

McSween, H. Y., Ruff, S., Morris, R., Bell, J., Herkenhoff, K., Gellert, R., Stockstill, K., Tornabene, L., Squyres, S., and Crisp, J., 2006, Alkaline volcanic rocks from the

Columbia Hills, Gusev crater, Mars: Journal of Geophysical Research: Planets (1991–2012), v. 111, no. E9.

McSween, H. Y., Ruff, S. W., Morris, R. V., Gellert, R., Klingelhofer, G., Christensen, P. R., McCoy, T. J., Ghosh, A., Moersch, J. M., Cohen, B. A., Rogers, A. D., Schroder, C., Squyres, S. W., Crisp, J., and Yen, A., 2008, Mineralogy of volcanic rocks in Gusev Crater, Mars: Reconciling Mossbauer, Alpha Particle X-Ray Spectrometer, and Miniature Thermal Emission Spectrometer spectra: J. Geophys. Res., v. 113.

Merrill, G. P., 1915, On the Monticellite-Like Mineral in Meteorites, and on Oldhamite as a Meteoric Constituent: Proceedings of the National Academy of Sciences, v. 1, no. 5, p. 302-308.

-, 1917, On the calcium phosphate in meteoric stones: American Journal of Science, no. 256, p. 322-324.

Michalski, J. R., and Dobrea, E. Z. N., 2007, Evidence for a sedimentary origin of clay minerals in the Mawrth Vallis region, Mars: Geology, v. 35, no. 10, p. 951-954.

Miller, S. L., and Urey, H. C., 1959, Organic Compound Synthesis on the Primitive Earth: Science, v. 130, no. 3370, p. 245-251.

Milliken, R., Swayze, G., Arvidson, R., Bishop, J., Clark, R., Ehlmann, B., Green, R., Grotzinger, J., Morris, R., and Murchie, S., 2008, Opaline silica in young deposits on Mars: Geology, v. 36, no. 11, p. 847-850.

Milliken, R. E., Grotzinger, J. P., and Thomson, B. J., 2010, Paleoclimate of Mars as captured by the stratigraphic record in Gale Crater: Geophysical Research Letters, v. 37, no. 4, p. L04201.

Ming, D. W., Gellert, R., Morris, R. V., Arvidson, R. E., Brückner, J., Clark, B. C., Cohen, B. A., d'Uston, C., Economou, T., Fleischer, I., Klingelhöfer, G., McCoy, T. J., Mittlefehldt, D. W., Schmidt, M. E., Schröder, C., Squyres, S. W., Tréguier, E., Yen, A. S., and Zipfel, J., 2008, Geochemical properties of rocks and soils in Gusev Crater, Mars: Results of the Alpha Particle X-Ray Spectrometer from Cumberland Ridge to Home Plate: J. Geophys. Res., v. 113, no. E12, p. E12S39.

Ming, D. W., Mittlefehldt, D. W., Morris, R. V., Golden, D. C., Gellert, R., Yen, A., Clark, B. C., Squyres, S. W., Farrand, W. H., Ruff, S. W., Arvidson, R. E., Klingelho¨fer, G., McSween, H. Y., Rodionov, D. S., Schro¨ der, C., de Souza Jr., P. A., and Wang, A., 2006, Geochemical and mineralogical indicators for aqueous processes in the Columbia Hills of Gusev crater, Mars: Journal of Geophysical Research, v. 111, no. E02S12, p. doi:10.1029/2005JE002560.

Murchie, S. L., Mustard, J. F., Ehlmann, B. L., Milliken, R. E., Bishop, J. L., McKeown, N. K., Noe Dobrea, E. Z., Seelos, F. P., Buczkowski, D. L., and Wiseman, S. M., 2009, A synthesis of Martian aqueous mineralogy after 1 Mars year of observations from the Mars Reconnaissance Orbiter: Journal of Geophysical Research: Planets (1991–2012), v. 114, no. E2.

Murphy, J., and Riley, J. P., 1962, A modified single solution method for the determination of phosphate in natural waters: Analytica Chimica Acta, v. 27, no. 0, p. 31-36.

Mustard, J. F., Murchie, S. L., Pelkey, S. M., Ehlmann, B. L., Milliken, R. E., Grant, J. A., Bibring, J.-P., Poulet, F., Bishop, J., Dobrea, E. N., Roach, L., Seelos, F., Arvidson, R. E., Wiseman, S., Green, R., Hash, C., Humm, D., Malaret, E.,

McGovern, J. A., Seelos, K., Clancy, T., Clark, R., Marais, D. D., Izenberg, N., Knudson, A., Langevin, Y., Martin, T., McGuire, P., Morris, R., Robinson, M., Roush, T., Smith, M., Swayze, G., Taylor, H., Titus, T., and Wolff, M., 2008, Hydrated silicate minerals on Mars observed by the Mars Reconnaissance Orbiter CRISM instrument, v. 454, no. 7202, p. 305-309.

Nancollas, G. H., and Marshall, R. W., 1971, Kinetics of Dissolution of Dicalcium Phosphate Dihydrate Crystals: Journal of Dental Research, v. 50, no. 5, p. 1268-1272.

Navarre-Sitchler, A., Steefel, C. I., Sak, P. B., and Brantley, S. L., 2011, A reactive-transport model for weathering rind formation on basalt: Geochimica et Cosmochimica Acta, v. 75, no. 23, p. 7644-7667.

Navarre-Sitchler, A., Steefel, C. I., Yang, L., Tomutsa, L., and Brantley, S. L., 2009, Evolution of porosity and diffusivity associated with chemical weathering of a basalt clast: Journal of Geophysical Research: Earth Surface, v. 114, no. F2, p. F02016.

Nickel, E. H., and Nichols, M. C., 2009, The International Mineralogical Association-CNMNC List of Mineral Names, Volume IMA/CNMNC List of Mineral Names, Materials Data, Inc.

Oelkers, E. H., Bénézeth, P., and Pokrovski, G. S., 2009, Thermodynamic databases for water-rock interaction: Reviews in Mineralogy and Geochemistry, v. 70, no. 1, p. 1-46.

Olsen, A. A., and Rimstidt, J. D., 2007, Using a mineral lifetime diagram to evaluate the persistence of olivine on Mars: American Mineralogist, v. 92, p. 598-602.

Orlova, A. I., Khaĭnakov, S., Loginova, E., Oleneva, T., Granda, S. G., and Kurazhkovskaya, V. S., 2009, Calcium thorium phosphate (Whitlockite-type mineral). Synthesis and structure refinement: Crystallography Reports, v. 54, no. 4, p. 591-597.

Palandri, J. L., and Kharaka, Y. K., 2004, A compilation of rate parameters of water-mineral interaction kinetics for application to geochemical modeling: US Geological Survey, 1068.

Papike, J., Karner, J., and Shearer, C., 2006, Comparative planetary mineralogy: Implications of martian and terrestrial jarosite. A crystal chemical perspective: Geochimica et Cosmochimica Acta, v. 70, no. 5, p. 1309-1321.

Parkhurst, D. L., and Appelo, C. A. J., 1999, User's guide to PHREEQC (ver. 2)—A computer program for speciation, batch-reaction, one-dimensional transport, and inverse geochemical calcu-lations.: USGeol. Surv. Water-Resources Invest. Rept., p. 99–4259.

Pasek, M., and Block, K., 2009, Lightning-induced reduction of phosphorus oxidation state: Nature Geosci, v. 2, no. 8, p. 553-556.

Pasek, M., and Lauretta, D., 2008, Extraterrestrial Flux of Potentially Prebiotic C, N, and P to the Early Earth: Origins of Life and Evolution of Biospheres, v. 38, no. 1, p. 5-21.

Pasek, M. A., and Kee, T. P., 2011, On the Origin of Phosphorylated Biomolecules, Origins of Life: The Primal Self-Organization, Springer, p. 57-84.

Patiño Douce, A. E., and Roden, M., 2006, Apatite as a probe of halogen and water fugacities in the terrestrial planets: Geochimica et Cosmochimica Acta, v. 70, no. 12, p. 3173-3196.

Patiño Douce, A. E., Roden, M. F., Chaumba, J., Fleisher, C., and Yogodzinski, G., 2011, Compositional variability of terrestrial mantle apatites, thermodynamic modeling of apatite volatile contents, and the halogen and water budgets of planetary mantles: Chemical Geology, v. 288, no. 1, p. 14-31.

Powner, M. W., Gerland, B., and Sutherland, J. D., 2009, Synthesis of activated pyrimidine ribonucleotides in prebiotically plausible conditions: Nature, v. 459, no. 7244, p. 239-242.

Prener, J. S., 1967, The Growth and Crystallographic Properties of Calcium- Fluor and Chlorapatite Minerals: Journal of the Electrochemical Society, v. 114, no. 1, p. 77-83.

-, 1971, Nonstoichiometry in calcium chlorapatite: Journal of Solid State Chemistry, v. 3, no. 1, p. 49-55.

Reid, M. R., 1995, Processes of mantle enrichment and magmatic differentiation in the eastern Snake River Plain: Th isotope evidence: Earth and Planetary Science Letters, v. 131, no. 3, p. 239-254.

Rejeki, S., Hadi, J., and Suhayati, I., Porosity Study for Detail Reservoir Characterization in Darajat Geothermal Field, West Java, Indonesia, *in* Proceedings Proceedings2005.

Rimstidt, D. J., Brantley, S. L., and Olsen, A. A., 2012, Systematic review of forsterite dissolution rate data: Geochimica et Cosmochimica Acta.

Rimstidt, J. D., and Newcomb, W. D., 1993, Measurement and analysis of rate data: the rate of reaction of ferric iron with pyrite: Geochimica et Cosmochimica Acta, v. 57, no. 9, p. 1919-1934.

Robie, R. A., Hemingway, B. S., and Fisher, J. R., 1979, Thermodynamic properties of minerals and related substances at 298.15°K and 1 Bar (105 Pascals) pressure and at higher temperatures: United States Geological Survey Bulletin, v. 1452, p. 456.

Rose, N. M., 1991, Dissolution rates of prehnite, epidote, and albite: Geochimica et Cosmochimica Acta, v. 55, no. 11, p. 3273-3286.

Rowles, S., 1968, The precipitation of whitlockite from aqueous solutions: Bull Soc Chim Fr, v. 1968, p. 802.

Rubin, A. E., 1997, Mineralogy of meteorite groups: An update: Meteoritics & Planetary Science, v. 32, no. 5, p. 733-734.

Ruff, S.W., Christensen, P.R., Blaney, D.L., Farrand, W.H., Johnson, J.R., Michalski, J.R., Moersch, J.E., Wright, S.P., Squyres, S.W., 2006. The rocks of Gusev Crater as viewed by the Mini-TES instrument. J. Geophys. Res. 111, doi:10.1029/2006JE002747.

Ruff, S.W., Niles, P.B., Alfano, F., Clarke, A.B., 2014. Evidence for a Noachian-aged ephemeral lake in Gusev crater, Mars. Geology 42, 359-362.

Ruszala, F., and Kostiner, E., 1980, The hydrothermal synthesis and crystal growth of various whitlockites and a manganese containing graftonite: Journal of Crystal Growth, v. 48, no. 3, p. 473-474.

Sak, P. B., Fisher, D. M., Gardner, T. W., Murphy, K., and Brantley, S. L., 2004, Rates of weathering rind formation on Costa Rican basalt: Geochimica et Cosmochimica Acta, v. 68, no. 7, p. 1453-1472.

Sato, H., Shibutani, T., and Yui, M., 1997, Experimental and modeling studies on diffusion of Cs, Ni and Sm in granodiorite, basalt and mudstone: Journal of Contaminant Hydrology, v. 26, p. 119-133.

Schott, J., and Berner, R. A., 1985, Dissolution mechanisms of pyroxenes and olivines during weathering, *in* Drever, J. I., ed., The Chemistry of Weathering, Volume 149: Boston, D. Reidel.

Schroeder, G. K., Lad, C., Wyman, P., Williams, N. H., and Wolfenden, R., 2006, The time required for water attack at the phosphorus atom of simple phosphodiesters and of DNA: Proceedings of the National Acadamy of Sciences, v. 131, no. 11, p. 4052-4055.

Schwartz, A. W., 2006, Phosphorus in Prebiotic Chemistry: Philosophical Transactions: Biological Sciences, v. 361, no. 1474, p. 1743-1749.

Schwenzer, S., and Kring, D., 2008, Inferred impact generated hydrothermal mineral assemblages in basaltic regions of Mars, Lunar and Planetary Science Conference: Houston, p. Abstract 1817.

Settle, M., 1979, Formation and deposition of volcanic sulfate aerosols on Mars: Journal of Geophysical Research: Solid Earth (1978–2012), v. 84, no. B14, p. 8343-8354.

Shearer, C., Papike, J., Burger, P., Sutton, S., McCubbin, F., and Newville, M., 2011a, Direct determination of europium valence state by XANES in extraterrestrial

merrillite: Implications for REE crystal chemistry and martian magmatism: American Mineralogist, v. 96, no. 8-9, p. 1418-1421.

Shearer, C. K., Burger, P. V., Papike, J. J., Sharp, Z. D., and McKeegan, K. D., 2011b, Fluids on differentiated asteroids: Evidence from phosphates in differentiated meteorites GRA 06128 and GRA 06129: Meteoritics & Planetary Science, v. 46, no. 9, p. 1345-1362.

Sheldrick, G. M., 2007, A short history of SHELX: Acta Crystallographica Section A: Foundations of Crystallography, v. 64, no. 1, p. 112-122.

Shen, C., Trebotich, D., Molins, S., Graves, D. T., Straalen, B., Graves, D., Ligocki, T., and Steefel, C., 2011, High performance computations of subsurface reactive transport processes at the pore scale: Proceedings of SciDAC.

Skowron, A., and Brown, I., 1990, Refinement of the structure of robinsonite, Pb4Sb6S13: Acta Crystallographica Section C: Crystal Structure Communications, v. 46, no. 4, p. 527-531.

Smith, E., personal communication, May, 2014, Calculations of mineralogy of Wishstone class rocks, to Adcock, C. T.,: Las Vegas

Squyres, S. W., Arvidson, R. E., Blaney, D. L., Clark, B. C., Crumpler, L., Farrand, W. H., Gorevan, S., Herkenhoff, K. E., Hurowitz, J., Kusack, A., McSween, H. Y., Ming, D. W., Morris, R. V., Ruff, S. W., Wang, A., and Yen, A., 2006, Rocks of the Columbia Hills: Journal of Geophysical Research: Planets, v. 111, no. E2, p. E02S11.

Squyres, S. W., Clifford, S. M., Kuzmin, R. O., Zimbelman, J. R., and Costard, F. M., 1992, Ice in the Martian regolith, *in* Kieffer, H. H., Jakosky, B. M., Snyder, C.

W., and Matthews, M. S., eds., Mars, The University of Arizona Press, p. 523-556.

Squyres, S. W., Grotzinger, J. P., Arvidson, R. E., Bell, J. F., III, Calvin, W., Christensen, P. R., Clark, B. C., Crisp, J. A., Farrand, W. H., Herkenhoff, K. E., Johnson, J. R., Klingelhofer, G., Knoll, A. H., McLennan, S. M., McSween, H. Y., Jr., Morris, R. V., Rice, J. W., Jr., Rieder, R., and Soderblom, L. A., 2004, In situ evidence for an ancient aqueous environment at Meridiani Planum, Mars: Science, v. 306, no. 5702, p. 1709-1714.

Stearns, H. T., 1924, Craters of the Moon National Monument: Geographical Review, v. 14, no. 3, p. 362-372.

-, 1928, Craters of the Moon National Monument: Idaho Bureau of Mines and Geology.

Steefel, C., 2009, CrunchFlow software for modeling multicomponent reactive flow and transport. User's manual: Earth Sciences Division. Lawrence Berkeley, National Laboratory, Berkeley, CA. October, p. 12-91.

Steefel, C. I., 2008, Geochemical Kinetics and Transport *in* Brantley, S. L., Kubicki, J. D., and White, A. F., eds., Kinetics of Water-Rock Interaction: New York, Springer, p. 545-589.

-, 2010, CrunchFlow - Multicomponent Reactive Flow and Transport Software accessed. 2010, April 4th, Software Page,http://www.csteefel.com/.

Steefel, C. I., and Lasaga, A. C., 1994, A coupled model for transport of multiple chemical species and kinetic precipitation/dissolution reactions with application to reactive flow in single phase hydrothermal systems: Am J Sci, v. 294, no. 5, p. 529-592.

Steefel, C. I., and MacQuarrie, K. T., 1996, Approaches to modeling of reactive transport in porous media: Reviews in Mineralogy and Geochemistry, v. 34, no. 1, p. 85-129.

Steefel, C. I., and Van Cappellen, P., 1990, A new kinetic approach to modeling water-rock interaction: The role of nucleation, precursors and Ostwald ripening: Geochimica et Cosmochimica Acta, v. 54, p. 2657-2677.

Stefansson, A., Gislason, S. R., and Arnorsson, S., 2001, Dissolution of primary minerals in natural waters: II. Mineral saturation state: Chemical Geology, v. 172, no. 3-4, p. 251-276.

Stearns, H. T., 1924, Craters of the Moon National Monument: Geographical Review, v. 14, no. 3, p. 362-372.

Stearns, H. T., 1928, Craters of the Moon National Monument: Idaho Bureau of Mines and Geology.

Stillings, L. L., and Brantley, S. L., 1995, Feldspar dissolution at 25°C and pH 3: Reaction stoichiometry and the effect of cations: Geochimica et Cosmochimica Acta, v. 59, no. 8, p. 1483-1496.

Stopar, J. D., Jeffrey Taylor, G., Hamilton, V. E., and Browning, L., 2006, Kinetic model of olivine dissolution and extent of aqueous alteration on mars: Geochimica et Cosmochimica Acta, A Special Issue Dedicated to Larry A. Haskin, v. 70, no. 24, p. 6136-6152.

Stout, M. Z., Nicholls, J., and Kuntz, M. A., 1994, Petrological and mineralogical variations in 2500-2000 yr B.P. lava flows, Craters of the Moon lava field, Idaho: Journal of Petrology, v. 35, no. 6, p. 1681-1681-1715.

Stumm, W., and Morgan, J. J., 1996, Aquatic Chemistry: Chemical Equilibria and Rates in Natural Waters, New York, John Wiley & Sons, Inc., 1022 p.:

Tacker, R. C., and Stormer, J. C., 1993, Thermodynamics of mixing of liquids in the system Ca3(PO4)2- CaCl2-CaF2-Ca(OH)2.: Geochimica Et Cosmochimica Acta, v. 57, no. 19, p. 4663-4676.

Tang, R., Hass, M., Wu, W., Gulde, S., and Nancollas, G. H., 2003, Constant composition dissolution of mixed phases: II. Selective dissolution of calcium phosphates: Journal of Colloid and Interface Science, v. 260, no. 2, p. 379-384.

Terada, K., Monde, T., and Sano, Y., 2003, Ion microprobe U-Th-Pb dating of phosphates in martian meteorite ALH 84001: Meteoritics & Planetary Science, v. 38, no. 11, p. 1697-1703.

Teterskii, A., Stefanovich, S. Y., Lazoryak, B., and Rusakov, D., 2007, Whitlockite solid solutions Ca9− x M x R (PO4) 7 (x= 1, 1.5; M= Mg, Zn, Cd; R= Ln, Y) with antiferroelectric properties: Russian Journal of Inorganic Chemistry, v. 52, no. 3, p. 308-314.

Tosca, N. J., McLennan, S. M., Clark, B. C., Grotzinger, J. P., Hurowitz, J. A., Knoll, A. H., Schroder, C., and Squyres, S. W., 2005, Geochemical modeling of evaporation processes on Mars: Insight from the sedimentary record at Meridiani Planum: Earth and Planetary Science Letters, v. 240, no. 1, p. 122-148.

Tosca, N. J., McLennan, S. M., Lindsley, D. H., and Schoonen, M. A. A., 2004, Acid-sulfate weathering of synthetic Martian basalt: The acid fog model revisited: J. Geophys. Res., v. 109.

Treiman, A. H., 2003, Chemical compositions of martian basalts (shergottites): Some inferences on b; formation, mantle metasomatism, and differentiation in Mars: Meteoritics & Planetary Science, v. 38, no. 12, p. 1849-1864.

-, 2008, Ancient groundwater flow in the Valles Marineris on Mars inferred from fault trace ridges: Nature Geosci, v. 1, no. 3, p. 181-183.

Usui, T., McSween, H. Y., and Clark, B. C., 2008, Petrogenesis of high-phosphorous Wishstone Class rocks in Gusev Crater, Mars: Journal of Geophysical Research, v. 113, no. E12S44, p. doi:10.1029/2008JE003225.

Valsami-Jones, E., Ragnarsdottir, K. V., Putnis, A., Bosbach, D., Kemp, A. J., and Cressey, G., 1998, The dissolution of apatite in the presence of aqueous metal cations at pH 2-7: Chemical Geology, v. 151, no. 1-4, p. 215-233.

Vaughan, K. L., 2008, Pedogenesis at Craters of theMoon National Monument and Preserver, Idaho, USAPh.D]: University of Idaho, 156 p.

Vaughan, K. L., McDaniel, P. A., and Phillips, W. M., 2011, Episodic soil succession on basaltic lava fields in a cool, dry environment: Soil Science Society of America Journal, v. 75, no. 4, p. 1462-1470.

Velbel, M. A., 1993, Constancy of silicate-mineral weathering-rate ratios between natural and experimental weathering: implications for hydrologic control of differences in absolute rates: Chemical Geology, v. 105, no. 1-3, p. 89-99.

Vieillard, P., and Tardy, Y., 1984, Thermochemical properties of phosphates, Photosphate Minerals, Springer, p. 171-198.

Wald, G., 1962, Life in the second and third periods; or why phosphorus and sulfur for high-energy bonds?, *in* Kasha, M., and Szent-Györgyi, A., eds., Horizons in

biochemistry : Albert Szent-Györgyi dedicatory volume: New York, Academic Press, p. 127-142.

-, 1964, The Origins of Life: Proceedings of the National Academy of Sciences of the United States of America v. 52, no. 2, p. 595-611.

Wanke, H., and Dreibus, G., 1988, Chemical Composition and Accretion History of Terrestrial Planets: Philosophical Transactions of the Royal Society of London. Series A, Mathematical and Physical Sciences, v. 325, no. 1587, p. 545-557.

Wedepohl, H. K., 1995, The composition of the continental crust: Geochimica et Cosmochimica Acta, v. 59, no. 7, p. 1217-1232.

Welch, S. A., Taunton, A. E., and Banfield, J. F., 2002, Effect of Microorganisms and Microbial Metabolites on Apatite Dissolution: Geomicrobiology Journal, v. 19, no. 3, p. 343-367.

Welch, S. A., and Ullman, W. J., 2000, The temperature dependence of bytownite feldspar dissolution in neutral aqueous solutions of inorganic and organic ligands at low temperature (5-35 ^{o}C): Chemical Geology, v. 167, p. 337-354.

Westheimer, F. H., 1987, Why Nature Chose Phosphates: Science, v. 235, no. 4793, p. 1173-1178.

Wherry, E., 1917, Merrillite, meteoritic calcium phosphate: American Mineralogist, v. 2, p. 119.

White, A. F., 2002, Determining mineral weathering rates based on solid and solute weathering gradients and velocities: application to biotite weathering in saprolites: Chemical Geology, v. 190, no. 1-4, p. 69-89.

-, 2008, Quantitative Approaches to Characterizing Natural Chemical Weathering Rates, p. 469-543.

White, A. F., Peterson, M. L., and Hochella Jr, M. F., 1994, Electrochemistry and dissolution kinetics of magnetite and ilmenite: Geochimica et Cosmochimica Acta, v. 58, no. 8, p. 1859-1875.

White, R., 1990, Chromatography/Fourier transform infrared spectroscopy and its applications, CRC Press.

Williams, R., Dietrich, W., Grotzinger, J., Gupta, S., Malin, M., Palucis, M., Rubin, D., Stack, K., Sumner, D., and Yingst, R., 2013, Curiosity's Mastcam Images Reveal Conglomerate Outcrops with Water-Transported Pebbles: LPI Contributions, v. 1719, p. 1617.

Wills, A. S., 1999, VaList-bond valence calculation and listing Program, accessed. 2013,www.ccp14.ac.uk.

Wogelius, R. A., and Walther, J. V., 1992, Olivine dissolution kinetics at near-surface conditions: Chemical Geology, v. 97, no. 1-2, p. 101-112.

Wolff-Boenisch, D., Gislason, S.R., Oelkers, E.H., Putnis, C.V., 2004. The dissolution rates of natural glasses as a function of their composition at pH 4 and 10.6, and temperatures from 25 to 74[deg]C. Geochimica et Cosmochimica Acta 68, 4843-4858.

Wray, J. J., Murchie, S. L., Squyres, S. W., Seelos, F. P., and Tornabene, L. L., 2009, Diverse aqueous environments on ancient Mars revealed in the southern highlands: Geology, v. 37, no. 11, p. 1043-1046.

Xie, X., Minitti, M. E., Chen, M., Mao, H.-k., Wang, D., Shu, J., and Fei, Y., 2002, Natural high-pressure polymorph of merrillite in the shock veins of the Suizhou meteorite: Geochimica et Cosmochimica Acta, v. 66, no. 13, p. 2439-2444.

Yamagata, Y., Watanabe, H., Saitoh, M., and Namba, T., 1991, Volcanic production of polyphosphates and its relevance to prebiotic evolution: Nature, v. 352, no. 6335, p. 516-519.

Yang, L., and Steefel, C. I., 2008, Kaolinite dissolution and precipitation kinetics at 22 C and pH 4: Geochimica et Cosmochimica Acta, v. 72, no. 1, p. 99-116.

Yen, A. S., Morris, R. V., Clark, B. C., Gellert, R., Knudson, A. T., Squyres, S., Mittlefehldt, D. W., Ming, D. W., Arvidson, R., McCoy, T., Schmidt, M., Hurowitz, J., Li, R., and Johnson, J. R., 2008, Hydrothermal processes at Gusev Crater: An evaluation of Paso Robles class soils: Journal of Geophysical Research: Planets, v. 113, no. E6, p. E06S10.

Zhu, Y., Zhang, X., Chen, Y., Xie, Q., Lan, J., Qian, M., and He, N., 2009, A comparative study on the dissolution and solubility of hydroxylapatite and fluorapatite at 25 °C and 45 °C: Chemical Geology, v. 268, no. 1-2, p. 89-96.

Zolotov, M. Y., and Mironenko, M. V., 2007, Timing of acid weathering on Mars: A kinetic-thermodynamic assessment: J. Geophys. Res., v. 112.

CHRISTOPHER T. ADCOCK
Graduate College
Department of Geoscience
University of Nevada Las Vegas
4505 S. Maryland Parkway
Las Vegas, NV 89154-4010
702-774-1421 (office)
702-277-4650 (cell)

EDUCATION

University of Nevada Las Vegas, Las Vegas, NV 2010 – 2014 (expect.)
Advisor: Dr. Elisabeth Hausrath
PhD graduate candidate in Geoscience (Planetary geochemistry and astrobiology)

Oklahoma State University, Stillwater, OK 2004
Advisor: Dr. Richard Marston
M.S., Geology, (Planetary geomorphology and martian remote sensing)

University of New Mexico, Albuquerque, NM 1995
B. Sci., Earth and Planetary Sciences with Distributed Sciences minor.

PROFESSIONAL EXPERIENCE

University of Nevada Las Vegas, Department of Geoscience Aug. 2009 – Present
Laboratory Assistant
Research Assistant
Laboratory Teaching Assistant, GEOL 101L

Zenitech Environmental, LLC Feb. 2005 – Aug. 2009
Scientist II/Certified Environmental Manager, Surface processes, geomorphology, geology, and remote sensing research to characterize mining remediation project sites.

Oklahoma State University,
T. Boone Pickens School of Geology Aug. 2002 – Dec. 2004
Teaching Assistant, GEOL 1114L
Research Assistant for the Arkansas/Oklahoma Center for Space and Planetary Sciences
Research Assistant for Research Experience for Undergraduates (REU) program.
Research Assistant (technician, system admin.), Dept. of English, Writing Center.

Sandia National Laboratories (Contracted to SNL by OnSite) Jan. 2001 – Aug. 2002
Senior Technologist, electron / optical microscopist (EMP/SEM)

Isonics Corporation
(formerly Colorado Mineral Research Institute) Jun. 1999 – Jan. 2001
*Senior Research Technician***,** chlorine handling systems development, metal extraction methods from recycled materials, pilot plant operation, development of solvent extraction techniques.

University of New Mexico Institute of Meteoritics May 1993 –April 1999
*Physical Sciences Research Technician V***,** scanning electron and electron microprobe microscopist.

PEER REVIEWED PUBLICATIONS AND THESIS

Adcock, C.T., Hausrath, E.M., Forster, P.M., Tschauner, O., and Sefein, K.J. (2014). "Synthesis and characterization of the Mars-relevant phosphate minerals Fe- and Mg-whitlockite and merrillite and a possible mechanism that maintains charge balance during whitlockite to merrillite transformation." Am. Min., 99, 1221-1232.

Adcock, C., Hausrath, E., Forster, P., 2013. "Readily available phosphate from minerals in early aqueous environments on Mars." Nat. Geosci. 6, 824-827.

Adcock, C.T., 2004. Determining Formative Winds Through Geomorphology: Herschel Crater, Mars. Oklahoma State University, Thesis.

Shearer C.K., Leshin, L.A. and Adcock C.T. (1999). "Olivine in Martian meteorite ALH 84001. Evidence for a high-temperature origin and implications for signs of life." Meteorit. Planet. Sci. 34, 331-340.

J.J. Papike, G.W. Fowler, C.T. Adcock, and C.K. Shearer (1999). "Systematics of Ni and Co in olivine from planetary melt systems: lunar mare basalts." Am. Min., Mar 1999; 84: 392 – 399

Papike, J.J., Spilde, M.N., Adcock, C.T., Fowler, G.W., Shearer, C.K., (1997). "Trace element fractionation by impact-induced volatization: SIMS study of lunar HASP samples" Am. Min., 82, 630-634

EXTENDED ABSTRACTS AND PRESENTATIONS

Adcock, C.T., Hausrath, E.M., 2014. Reactive Transport Modeling of Phosphate Mineral Dissolution in High-P Martian Rocks, 45th Lunar and Planetary Science Conference. Lunar and Planetary Institute, Houston, p. Abstract #2250.

Hausrath, E.M., Adcock, C.T., Elwood Madden, M.E., Gainey, S.R., Olsen, A.A., Steiner, M.H., 2014. Using Geochemical Kinetics to Interpret Potential Habitability, 45th Lunar and Planetary Science Conference. Lunar and Planetary Institute, Houston, p. Abstract #2376

Adcock, C., Hausrath, E., 2013. Interpretation of Phosphate Mobility on Mars Based on Terrestrial Mars- analog Basalts and Reactive Transport Modeling, Lunar and Planetary Institute Science Conference Abstracts, p. 2727.

Adcock, C., Hausrath, E., 2012. The Dissolution Rate of Whitlockite and Implications for the Habitability of Early Mars, Lunar and Planetary Institute Science Conference Abstracts, p. 2446.

Hausrath, E., Adcock, C., Tu, V., 2012. Phosphate Records Environmental Conditions Important to Habitability in Soils and Rocks on Mars, Lunar and Planetary Institute Science Conference Abstracts, p. 2719.

Adcock, C., Hausrath, E., 2011. Dissolution Rates and Mineral Lifetimes of Phosphate Containing Minerals and Implications for Mars, AGU Fall Meeting Abstracts, p. 1708.

Adcock, C., Simon, A., Hausrath, E., 2011. Synthesis of Phosphate Minerals for Use in Dissolution Experiments, Lunar and Planetary Institute Science Conference Abstracts, p. 2300.

Adcock, C., Hausrath, E., 2010. Kinetic Studies of Phosphate Containing Minerals and Implications for Mars, Lunar and Planetary Institute Science Conference Abstracts, p. 2177.

Stinchfield, M. O., Adcock, C. T., (2006) "When Nature Collides: Remediation Complications Due to Natural Presence of Lead and Arsenic" Presentation (Adcock). Air and Waste Management Association, June, 2006, Great Basin Chapter Annual Conference.

B. D. Stanley, C. T. Adcock, R. A. Marston, (2004). "Interpretation of Wind Direction from Eolian Features: Herschel Crater, Mars." Abstract and Poster Presentation. XXXV Lunar and Planetary Sci. Conf., CD-Rom.

C. T. Adcock, B. D. Stanley, R. A. Marston, (2004). "Comparison of Geomorphically Determined Winds with a General Circulation Model: Herschel Crater, Mars." Abstract and Poster Presentation. XXXV Lunar and Planetary Sci. Conf., CD-Rom.

B. D. Stanley, C. T. Adcock, R. A. Marston, (2003). "Interpretation of Wind Direction from Eolian Features: Herschel Crater, Mars." Poster Presentation. Arkansas and Oklahoma Center for Space and Planetary Sciences Summer Research Experience/Experiment for Undergraduates (REU).

Adcock, C. T., (2003) "Characterizing Surface Winds on Mars: Herschel Crater." Poster Presentation. 2003 Meeting of the Southwest Association of American Geographers, Stillwater, Oklahoma, Oct. 23-25, 2003.

Newsom H.E., Hagerty J.J., Spilde M.N., Adcock C.T. and C. Sorge (1999). "Introducing planetary science and technology to students from grades 6-12." Abstract and Poster Presentation. Abstract and Poster Presentation. XXX Lunar and Planetary Sci. Conf., CD-Rom

J.J. Papike, G.W. Fowler, C.T. Adcock, and C.K. Shearer (1999). "Systematics of Ni and Co in olivine from planetary melt systems: lunar mare basalts." Presentation (Papike). XXX Lunar and Planetary Sci. Conf., CD-Rom

Wacker, J., Hildebrand, A., Brown, P., Crawford, D., Boslough, M., Chael, E., Revelle, D., Doser, D., Tagliaferri, E., Rathbun, D., D. Cooke, C. Adcock 1998. The Juancheng and El Paso Superbolides of February 15 and October 9, 1997: Preatmospheric Meteoroid Sizes. Meteoritics and Planetary Science Supplement 33, 160

Shearer C.K. and Adcock C.T. (1998) "A comparison between sulfide assemblages in Martian meteorites Allan Hills 84001 and Governador Valadares" In Workshop on the Issue Martian Meteorites: Where Do We Stand and Where Are We Going? LPI contribution No. 956. Lunar and Planetary Institute, Houston TX. 64 pp.

Shearer, C.K. and C.T. Adcock (1998) "The relationship between the carbonate and shock-produced glass in ALH 84001." Abstract and Poster Presentation. XXIX Lunar and Planetary Sci. Conf., CD-Rom

Shearer, C.K. and C.T. Adcock (1998) "The composition and distribution of shock glass in ALH84001." Presentation (Shearer). XXIX Lunar and Planetary Sci. Conf., CD-Rom

Shearer, C.K. and C.T. Adcock (1998) "The origin of olivine in Martian meteorite ALH 84001. Part 1. The distribution of olivine." Presentation (Shearer). XXIX Lunar and Planetary Sci. Conf., CD-Rom

A.R. Hildebrand, P. Brown, D. Crawford, M. Boslough, E. Chael, D. Revelle, D. Doser, E.Tagliaferri, D. Rathbun, D. Cooke, C. Adcock, and J. Karner; (1998) "The El Paso Superbolide of October 9, 1997." Presentation (Hildebrand). 1998 Hypervelocity Impact Symposium

Papike, J.J., Spilde, M.N., Adcock, C.T., Fowler, G.W., Shearer, C.K., (1997). "Trace element fractionation by impact-induced volatization: SIMS study of lunar HASP glasses" Presentation (Papike). XXVIII Lunar and Planetary Sci. Conf., 1059P

Papike, J.J., Spilde, M.N., Adcock, C.T., Fowler, G.W., Shearer, C.K., (1997). "Trace element fractionation by impact-induced volatization: SIMS study of lunar HASP samples" American Mineralogist, 82, 630-634.

Adcock, C.T., Spilde, M.N., Papike, J.J., (1997). "Automated HASP glass search using the electron microprobe." Abstract and Poster Presentation. XXVIII Lunar and Planetary Sci. Conf., 5A.

INVITED TALKS

Adcock, C. T., Stinchfield, M. O., (2007) "When Nature Collides: Remediation Complications Due to Natural Presence of Metals" Presentation and Fieldtrip (Adcock). Association of Engineering and Environmental Geologists, January, 2007, Southern Nevada Chapter meeting.

GRANTS, HONORS, AND AWARDS

UNIVERSITY OF NEVADA LAS VEGAS

- Nevada Space Grant NASA Fellowship, 2010, 2011, 2012, 2013
- Bernada French Scholarship, 2012
- Geological Society of America Research Grant, 2011
- Edwards & Olswang Geology Scholarship, 2011, 2013, 2014
- Desert Space Foundation Geoscience Award, 2011, 2012, 2013, 2014
- Member of the Phi Kappa Phi Honors Society

OKLAHOMA STATE UNIVERSITY

- Rumsey Bissell Marston Scholarship, 2004
- Oklahoma Space Grant NASA Fellowship 2004
- Invited Attendee of the NASA/JPL Planetary Science Summer School 2004
- Departmental Outstanding Teaching Award 2003-2004
- Member of the Phi Kappa Phi Honors Society, 2004
- Graduate member of the Sigma Gamma Epsilon Honorary Society, 2003-2004

UNIVERSITY OF NEW MEXICO

- Harry and Mabel Leonard Scholarship, 1994
- General Thomas Campell Award, 1993

RECENT WORKSHOPS

Photogrammetric Processing of Planetary Stereo Imagery using ISIS and SOCET SET® December 17-19, 2013, USGS Astrogeology Science Center, Flagstaff. AZ.

ADDITIONAL TRAINING AND EXPERIENCE

State of Nevada Certified Environmental Manager (CEM #1959), 2006-2013; OSHA 40-Hour HAZWOPER (29 CFR § 1910.120), 2005 - Most recent refresher: 2009; US EPA Lead Inspector (Certification #NV-I-16411-1), 2008-2012; Electron Microscopist with operator hours on JEOL 733,

8600, 8200 Electron Microprobes as well as JEOL 840, 5600, 5400, and 6400 series Scanning Electron Microscopes; UV/VIS, Flame AA, and XRD operation experience; Programming experience in Python and FORTRAN.